Spring 2015

Numerical study on scaling effects and decoupled network-based simulation of gaseous explosion

Liang Wang

Department: Mining and Nuclear Engineering

NUMERICAL STUDY ON SCALING EFFECTS AND DECOUPLED NETWORK-BASED SIMULATION OF GASEOUS EXPLOSION

by

LIANG WANG

A DISSERTATION

MISSOURI UNIVERSITY OF SCIENCE AND TECHNOLOGY

In Partial Fulfillment of the Requirements for the Degree

DOCTOR OF PHILOSOPHY

in

MINING ENGINEERING

2015

Approved
Jerry C. Tien, Advisor
Nassib Aouad, Co-advisor
Kwame Awuah-Offei
Jason Baird
Maochen Ge
Deyi Jiang

ABSTRACT

This research seeks to improve the prediction efficiency of gaseous explosions realized by numerical simulations in a full-scale underground network using a decoupled method. To provide quick predictions of overpressure distribution of methane explosions in underground airway networks, a two-section theory is employed. The explosion space is divided into a driver section and a blast-wave section. Governing equations including conservation of mass, momentum, and energy, together with chemical reaction and turbulence models are solved for the driver and the blast-wave sections using computational fluid dynamics (CFD) solver *ANSYS Fluent* (3D-based) and *Flowmaster* (1D-based) respectively. The three dimensional (3D) and one dimensional (1D) numerical analyses are preceded separately (decoupled). In the driver section, the numerical calculation results with three variables (FLSF, HDSF, and concentration) considering the size of explosion space and methane concentration level for the driver section are stored in a database tool *Microsoft SQL Server Express* aims to generate a methane explosion source database. To validate the selected combustion and turbulent models, a series of lab-scale methane explosion experiments were conducted. In the blast-wave section, the influences of geometric changes are quantified by using 2D Euler equations, whereas the simulation results are used to adjust the 1D network-based modeling. The decoupled method is applied in two case studies and proved capable to predict the pressure distribution of methane explosions that occurs in a complex airway network.

ACKNOWLEDGMENTS

There are many people I would like to thank. Without their help, this work cannot be accomplished.

I owe many thanks to my advisor, Dr. J. C. Tien who introduced me to the Mining and Nuclear Engineering Department at the Missouri University of Science and Technology. Without his effort and funding, I may not enter the department and start the research. His guidance and teaching gave me the original idea of this study and provided a firm support during the process. His time spent on editing makes this work complete.

I also want to thank my co-advisor Dr. N. Aouad who provided numerous constructive suggestions to the structure of this research. His advising on my comprehensive exam strengthened my presentation. In addition, I appreciate his generosity for funding me in the last two semesters which allowed this work to be accomplished.

Other committee members also deserve great acknowledgment. Dr. Awuah-Offei, Dr. Ge, Dr. Jiang, and Dr. Baird provided so much time on this work and support on my personal life. I would like to thank them here for their selfless hard work. In addition, I would like to thank my colleagues who made contributions to this work. Dr. B. Y. Jiang provided great help on the experiment conduction in CUMT; Dr. T. Magesh's suggestions pertaining the numerical method are helpful and constructive.

My family's contribution to this work is great. I would like to thank my wife S.S. Que who provided great support as a Ph.D. student at Missouri S & T. Without her endless sacrifices, this work would not been finished smoothly.

Finally, the credit of this work also belongs to all the people who supported my study and research during the three years in Rolla.

TABLE OF CONTENTS

Page

LIST OF ILLUSTRATIONS

LIST OF TABLES

1. INTRODUCTION

1.1. BACKGROUND

Methane explosions are one of the most dangerous mining accidents that can cause tens, even hundreds of deaths per incident, resulting in devastating loss of life as well as financial loss to the mining industry. In 1906, 1,099 miners were killed in the Courrieres Coal Mine explosion in France. In December 1907, the Monongah Numbers Six and Eight explosions in West Virginia, USA, claimed 362 lives, the worst American mine disaster. Moreover, in May 1928, 195 miners were killed in the Mather Number One mine explosion in Pennsylvania, USA. The most catastrophic explosion ever recorded was the Honkeiko Colliery disaster of 1942, in China, in which 1,549 miners lost their lives (McPherson, 1993). Despite the attention to mining safety brought by methane explosions, accidental deaths in the coal industry continued through the mid-20th Century. For example, in December 1951, a methane explosion in Orient Number Two Mine, Illinois, resulted in 119 fatalities. From 1900 to 2010, 10,390 miners lost their lives in 420 explosions in USA alone. Methane explosions continue to be the number one killer amongst all mining accidents (Brnich and Kowalski, 2010).

With the development of detection and prevention techniques, the number of methane explosion events decreased sharply since 1970. The enactment of the *Federal Coal Mine Health and Safety Act of 1969* also contributed to this improvement. However, in 2006, the Sago Mine disaster in West Virginia rocked the mining industry with 12 fatalities. The exact source of ignition is still under debate (McAteer, et al., 2006). This and several subsequent mine explosions renewed research interests in explaining and preventing mine explosions.

Methane explosions will probably never be completely eliminated, but they must be better understood and controlled through effective detection and prediction methods, as well as more stringent regulations. It is the intent of this study to improve current prediction methods through a more practical approach to the problem.

1.2. DEVELOPMENT OF METHANE EXPLOSION RESEARCH

Significant efforts have been made to understand methane explosion mechanisms over the past one hundred years. The period of high rates of deaths due to explosions, sometimes considered to be the Dark Age in US mining, occurred in the early-to-mid 20th century. In 1907 alone, more than 600 miners were killed by gas explosions in US coal mines (Taylor and Karacan, 2012). In 1910, the US Bureau of Mines (USBM) was created to conduct research on mine accidents and improve mining safety. Its major goal was to mitigate methane explosion occurrence. Since then, researchers from USBM and other organizations methodically explored the nature of methane explosions and developed techniques to mitigate its destructiveness, with emphasis on four major aspects: (1) ignition sources, (2) methane concentration and degasification, (3) methane monitoring, and (4) understanding explosion mechanisms. The majority of this research can be categorized into aspect (4), the understanding of explosion mechanisms, but both ignition processes and methane concentration control are also involved. Each aspect will be described in details below.

1.2.1. Control Ignition Sources. Early understanding of ignition control can be traced back to the early 20th century. It was believed that quantity of airflow from ventilation is commonly enough to serve as an ignition source. The control of the ignition source was often considered to be the most effective way to decrease the possibility of methane explosions until the mechanical fan was widely employed by the mining industry.

The most critical ignition source before the 1950s was flame lighting (also called open flame). The early electric cap lamp could not provide as much light as did flame light; yet its usage was not regulated. Consequently, the usage of flame became a potential hazard in gassy mines. The flame light provides enough energy to ignite a methane/air mixture when its concentration falls within explosion limits (between 5% to 15%). Despite its danger, this ignition source could not have been eliminated until the development of a new generation electric cap lamp and relevant legislative action prohibited the usage of open flame lamp in coal mines (Fieldner, 1950).

With the introduction of continuous mining equipment (CM), the resultant frictional heating became a new ignition source. Researchers recognized this issue and

sought to understand the antecedents of explosions related to CM. In the process of continuous mining it was found that the cutting bits on a rotational drum could become heated during normal operation. Ignition could then occur when heated air came into contact with a methane/air mixture. Frictional ignition can be mitigated by two measures. First, use of bits with larger carbide inserts reduce contact between bits and rock and thereby reduce friction. Second, the rock surface can be cooled with directional water spray. Documented mining applications show that frictional ignition has been effectively controlled with the use of either method, or by a combination of the two measures in the CM cutter head design (Courtney, 1990).

After 2000, studies on ignition sources focused on the influences of ignition energy and the location of ignition sources. The major ignition source at that time became an electric spark accidentally exposed to a methane/air mixture. Kindracki (2007) conducted an explosion experiment in a closed-end vessel and found that the position of the ignition affected maximum combustion pressure and the rate of pressure rise. In Zhang's (2011) similar research, it was noted that maximum deflagration overpressure, maximum deflagration temperature, and maximum rate of deflagration pressure rise with the increase of spark durations. In his later study, minimum ignition energy of a methane/air mixture was found to be at a volumetric concentration around 8.5%, which deviated from the stoichiometric concentration of 9.5% (Zhang and Li, 2013).

In addition to experimental research into the phenomenon, with the development of personal computers and numerical theories, research on ignition processes became feasible through the application of numerical techniques. The spark model, designed to simulate the ignition process of internal combustion engines, was successfully employed to simulate an ignition process in a methane explosion (Heywood, 1988; Alla, 2002; Bayraktar & Durgun, 2003; 2004). Research on the nature of ignition sources will remain an important aspect in predicting and preventing gaseous explosions. Numerical tools will be an effective alternative to the traditional experiment for exploring its mechanism.

1.2.2. Ventilation and Degasification. Methane/air mixture has lower and upper explosion limits between 5% and 15%. Therefore, keeping the methane concentration off this range is an effective way to prevent explosions. To meet this goal, providing adequate ventilation for effective dilution as well as use of a degasification system to

lower methane emissions are common techniques used by the coal industry. Mine ventilation is effective in reducing methane concentration in working places and gob areas. Coalbed methane can also be degasified through extensive methane drainage system effectively controlling methane emissions.

1.2.2.1 Ventilation. In the early 1900s, ventilation as an effective methane control measure did not receive enough attention. Because of a lack of mechanical ventilation equipment available at that time, only limited air quantity was provided. Ventilation provided, in fact, barely enough air to sustain mining operations. With the introduction of the mechanical fan, air quantity significantly increased and much more airflow could be provided to the working faces (Taylor & Karacan, 2012). The dilution of methane became feasible with increased airflow.

In the 1970s, research on ventilation had been focused on leakage prevention and efficiency of airflow patterns. Consequently, plastic materials were applied to the ventilation curtain to reduce porosity. During that time, auxiliary fans were introduced to ventilate the face with tubing, to increase vent efficiency in face area (Dalzell, 1966; Peluso, 1968). Both blowing and exhausting systems were investigated with a result that blowing systems were found to be more efficient in diluting methane in the face area (Luxner, 1969). The exhausting method, on the other hand, left "blind region" (or pockets) in which methane tended to accumulate. The introduction of *Federal Coal Mine Health and Safety Act of 1969* highlighted the importance of mine ventilation for combating methane and respirable dusts underground. With the increase in required air quantity by *ACT of 1969*, methane can be more effectively diluted.

After 1980, the study on ventilation and dilution mainly focused on operations in the face area, especially in longwall mines. This research suggested that a narrower entry will cause methane concentration to increase and a water spray system will facilitate the face ventilation, if the airflow is directed towards return-air side (Taylor, 1997; Chilton, 2006).

As numerical techniques became more sophisticated, research after year 2000 tended to be more often model-based rather than experimental. Flow patterns in working panels and faces were detailed in simulation using Computational Fluid Dynamics (CFD) methods. The transient methane concentration distribution and its variation can be

simulated and recorded with the help of CFD tools (Brechtel and Thimons, 1989; Petrov & Wala, 2013).

1.2.2.2 Degasification. Degasification is another means to control the risk of methane explosion. At an early stage, boreholes were drilled directly into the coalbed and/or roof above the seam in gassy mines to release methane pressure. However, the amount of methane removed in this manner was limited (Lawall & Morris, 1934). It was found in the 1960s that, degasification efficiency could be significantly improved by hydraulic stimulation operation (Maksimovic, Elder, & Kissell, 1977; Spindler & Poundstone, 1960). Despite this, hydraulic stimulation approaches have had only a small impact in longwall panel studies (Maksimovic, Elder & Kissell, 1977). This problem was solved by adding foam and proppant sands into boreholes, which significantly reduced methane emission in longwall face areas (Steidle, 1978).

In the past decade, the most important improvements in degasification have become numerical modeling of methane emissions using a variety of borehole patterns and the employment of directional drilling (Schwerer, et al., 1984; Karacan, Diamond, & Schatzel, 2007; Karacan, 2007; Ruban, Zaburdyaev, & Kharchenko, 2011). The contribution of better understanding of methane dynamics and more accurate drilling supported by advanced equipment has made degasification more effective.

1.2.3. Methane Monitoring. The methane concentration should always be kept out of the known explosion ranges and be under continuous monitoring. Methane monitoring systems are indispensable for protecting miners' safety. Before the 1950s, a safety lamp was widely used for methane detection. At that time, survey and monitoring instruments were unsophisticated; and the ventilation condition was mainly based on observation (Taylor & Karacan, 2012). This condition was not improved until 1958, when USBM initiated a program to provide continuous monitoring of methane in face areas (James, 1959). From the regulator's standpoint, all mining machines were mandated to mount methane sensors by 30 CFR § 75.342(a). The new procedure allows ventilation effectiveness to be evaluated by analyzing the data collected by monitors.

Research in the last decade of the 20th century recommended that methane sensors be placed in the return side of the mining machine, and stated that they also should be mounted on roof bolting machines as well (Taylor, 1997; 2001).

Around the year 2000, research demonstrated that the response time of the existing methane monitoring systems were too slow to capture accurate methane peak values. In most cases, methane concentration was found to fluctuate quickly, rising and falling rapidly during mining. A potential risk of a methane explosion exists when the methane monitor is not able to respond to a rapid change in methane concentration, allowing it to quickly reach the explosive range without being detected. The dust cap was later redesigned to improve the system so that higher methane peak values could be detected during monitoring (Taylor, 2008). In addition to methane monitoring on the mining machines, a personal monitoring system was developed to provide local methane concentration information. An alarm system was embedded in the personal methane monitoring system that could alert the user when concentration approached or and/or exceeded the safety limit (Chilton, 2005). A modern methane monitor, with its improved sophistication of detection technology, provides an early and continuous warning. Therefore, the emphasis today should be on the practice of periodical maintenance and stringent execution of existing monitoring strategies.

1.2.4. Explosion Characteristics. A method that brings clarity to an understanding of explosion characteristics is through an actual methane explosion experiment. Early explosion tests conducted at the Experimental Mine in Bruceton (Taylor & Karacan, 2012), though interesting, do not contribute much to the accurate understanding of explosion mechanisms. There is a gap in knowledge, in that the process and its specific mechanism of methane explosion is still not completely clear. A thorough study through a series of explosion experiments can be expected to provide valuable information that will enable researchers to gain clarity on explosion characteristics and add to the body of knowledge, building towards a fuller understating of this complex event.

Research methods on explosion characteristics can be categorized into theoretical, experimental, and numerical approaches. All three, at varying degrees, will be included in this study. Out of necessity, all theories on interrelationships of explosion parameters have been based on assumptions and simplifications. Chapman and Jouguet (1905) described a simplified model called CJ detonation theory with an infinitesimally thin detonation front propagating at a local sound velocity. All flow parameters downstream

of the shock front are the same as the shock. Twenty years later, Zel'dovich, Neumann, and Döring's (ZND detonation theory) provided physical exploitation of the detonation process. In the ZND theory, the reactant (explosive) is compressed by the infinite thin shock front and forms a high density, high pressure layer. The layer is called the Von Neumann Spike. Exothermic reactions start at the Von Neumann Spike and shock wave propagates at local sound speed. Afterward, the products expand back to CJ state (Zel'dovich & Ya, 1940; Neumann, 1963; Döring, 1943). Details of the CJ theory will be described in detail in Section 2.

The experiment-based body of research is extensive, and seeks to develop empirical relationships that can be used directly for engineering purposes. Explosion tests were carried out by numerous researchers after the Bruceton test. These explosion tests sought to reveal the flame acceleration mechanism and measure the impact of site conditions (e.g. environmental temperature, pressure, and site geometry) on the representative explosion parameters such as peak overpressure and arrival time (Zipf, et al., 2010; Jia & Lin, 2009; Jia, Liu & Jin, 2011; Kordylewski & Wach, 1988; Lin, Zhou, & Zhang, 1999).

Due to the advent of computing technology and increasingly powerful and reliable computers available over the last two decades, the emphasis of research has shifted to a numerical approach. With increasing numbers of turbulent and combustion modeling techniques being developed, CFD codes based on fluid dynamics and chemical equivalence theories have become capable of providing greater detail than can experimental methods. The cost of numerical modeling has decreased, and is now lower than the cost of traditional, physical experimentation in a lab environment. Increasingly, since numerical methods provide greater detail and are less expensive, they are commonly used for studying shock wave propagation, flame acceleration mechanism, site geometric influences, deflagration to detonation transition (DDT), and other aspects of methane explosion (Dai, et al., 2011; Jia & Lin, 2009; Jiang, et al., 2011; Lea, 2002; Lin, Jiang, & Zhou, 2003; Makarov, Verbecke, & Molkov, 2007).

1.3. MODELING OF TURBULENT COMBUSTION AND INFLUENCES OF GEOMETRIC CHANGES

As described in Section 1.2, the trend in methane explosion research is to apply more numerical techniques. Therefore, numerical techniques will be a major approach of this study as well, and will be used to model turbulent combustion and site geometric influences.

1.3.1. Turbulence Modeling. The selection of turbulence modeling is critical when simulating a turbulence reactive flow such as methane explosion. There are two major categories of a turbulence model: time-averaged and filtered, with the former being more common. The time-averaged turbulence model is also referred to as the Reynolds-averaged turbulent model; and is a two-equation standard k-ε model. The rationale of this model is to treat the randomly fluctuating fluid parameter as a combination of a mean value and a fluctuation value. Standard k-ε model has been widely used within the computational fluid research field for many years, due to its stability and high computational-efficiency. This model has also been employed by the majority of research to simulate a gaseous explosion (Makarov, Verbecke, & Molkov, 2007). However, time-averaged models have an inherent drawback in resolving transient turbulent structures.

The Large Eddy Simulation (LES) method, on the other hand, is a reasonable alternative to the time-averaged approach. Eddy structures and the associate fluid parameters can be better predicted when turbulence is highly time dependent, such as in turbulent combustion (Makarov, Verbecke, & Molkov, 2008). The LES method has proven efficient to simulate hydrogen combustion, but has thus far had very few applications in methane combustion. The capability of LES to simulate methane/air combustion in underground coal mines is yet unknown, and needs to be investigated to fill a gap in theoretical body of knowledge. Methods and applications of the two models will be described in detail in Section 2.

1.3.2. Geometric Change Influences. In this research, two major geometric influences on a methane explosion are known as scaling effect and geometric change effect. The control and implementation of a full-scale experiment underground is often difficult and expensive to conduct (Catlin, 1991; Zhang, Pang, & Zhang, 2011); therefore, numerical methods and lab-scale experiments are good alternatives. However, there are uncertainties regarding numerical models, such as that numerical model need to be

validated. In addition, it is not yet known if the results of lab-scale experiments are statistically representative of larger scale studies. Therefore, efforts are now being made to investigate effects of scale during a gaseous explosion.

In Van Wingerden's (1989) work, scale effect is related to normalized flame speed. However, this relationship breaks when turbulence is incorporated in the analysis. Catlin and Johnson explored feasibility for compensation of the scale effect by enriching oxygen concentration in air (1991, 1992). The results are theoretically correct when the turbulence Reynolds number is smaller than 10,000. However, this Reynolds number is smaller than typical cases in practical problems. Zhang, et al. (2011) on the other hand, tested the scale effect on methane explosion using a CFD commercial package, AutoReaGas, in which three scales (1:1, 1:10, and 1:100) were tested (Zhang, Pang & Zhang, 2011; Zhang, Pang & Liang, 2011).

It was found that when the length to diameter ratio is less than 80, the explosion parameters do not yield the geometric similarity law, which means the explosion overpressure is promotional to the explosion diameter. In addition to the scaling effect, geometric changes along an airway could have significant impact on the propagation of blast wave as well. The influences should be understood and quantified when investigating an explosion in an underground ventilation system (airway network). The most representative geometric changes in longwall or room-and-pillar operations are bends, branches, obstacles, and cross-sectional changes (Jia & Lin, 2009). Some experimental studies have provided qualitative data on the influences brought by geometrical changes (Jia, Liu, & Jin, 2011; Kordylewski & Wach, 1988; Lin, Zhou & Zhang, 1999). Prior studies demonstrated that the bend of a duct would result in two opposite effects on the overpressure produced by an explosion. It could increase the overpressure if it is located in a gas-filled region and otherwise attenuates it (Lin and Zhu, 2009). Branching of a duct and sudden area increase in cross-sections will decrease the flame speed induced by the methane explosion, as well as overpressure (Lin, et. al., 2008). The impacts of obstacles are similar to bends; hence, the presence of obstacles in a methane-filled site could increase overpressure, but decreases it during blast-wave propagation (Lin, Zhou, & Zhang, 1999). In summary, geometrical changes at an explosion site will either accelerate the flame or attenuate it and, in turn, affect its

overpressure. A model using an unsteady 2D compressible Euler Scheme has been developed to quantify these influences will be illustrated in details in Section 5.

1.4. MOTIVATIONS AND OBJECTIVES

1.4.1. Motivations. An accurate prediction of methane explosion is essential in providing a safe working environment for miners underground. To be effective, this prediction must be considered from both the mine planning and emergency planning perspectives. The prediction will provide an influencing region of a methane explosion. Continuing emissions of methane into the airways and the presence of coal dust on the ground could ignite a secondary explosion with a higher severity causing even more damage. A knowledgeable understanding of methane emission patterns could also assist mine rescue teams in identifying and assessing possible atmospheric conditions underground, enabling a more efficient rescue plans, in advance. However, most available predictions methods are either slow in producing alerts or time extensive depending on the complexity of the mine. Therefore, only a geometric model, or simplified local explosion geometry, can be managed. An efficient prediction tool that can cover the entire explosion region is therefore needed.

As stated in Section 1.3, either numerical tools or experimental methods can be used to characterize a methane explosion. The experimental methods are used to obtain empirical relationships between explosion parameters and experimental conditions. However, outcomes are commonly limited to a specific experimental condition and are therefore difficult to extrapolate to describe different situations with different parameters (Jing, Shi, & Jia, 2011). Meanwhile CFD tools have become sophisticated and been widely used in many engineering practices. There are some commercial codes available on the market for combustion simulation such as *AutoReaGas* and *SCOPE* (Jiang, et al., 2011). The available commercial packages currently available lack the flexibility needed, and only limited sub-models are available that can be used to simulate given circumstances.

CFD packages are commonly used among popular programs there are *ANSYS CFX* and *Fluent*. These codes take advantage of the latest numerical techniques and the computational power of modern computers, which provides significant flexibility and

speed for user-defined algorithms. However, simulations using these general codes are computationally demanding. Hence, the cost is excessive when an entire mine is considered. In addition to cost, general code requires meshing of a computational domain, which could be time consuming, on the front end of conducting a simulation. These deficiencies of available numerical methods call for a new numerical method that can model methane explosion in a relatively short time with awareness of each of the considerations described above.

1.4.2. Objectives. The overall objective of the current research is to develop an accurate and efficient prediction model without losing sentential details. To achieve this objective, the strategy is to consider two different sections of a methane explosion separately. The first section is physically complex and model simplification is necessary. Thus, in this section a database will be developed to cover a wide range of explosion sources. The second section is relatively simple in nature where turbulence and chemical reaction are neglected. A One-Dimensional (1D) simplification in this section allows simulations of geometry with higher complexity possible. The details of the two-section approach will be introduced and discussed in details in Section 2.

Based on this strategy approach, the research is broken down into five main Objectives/steps, which are as follows:

(1) To establish a basic methane explosion model and explosion mechanism

(2) To investigate and validate numerical formulation of turbulence and combustion models using ANSYS Fluent

(3) To develop a methane explosion source database based on 3D simulations

(4) To characterize influence on blast-wave propagation due to geometric changes

(5) To establish a 1D-3D decoupling prediction method based on explosion source database and the result of geometric influence study

Methane explosion is a rapid combustion that can be described by Navier-Stokes equations coupled with turbulence and chemical reaction equations. Customizations of these equations are necessary before they can be used in this study. The detailed hypotheses will be discussed in Objective (1) and detailed in Section 2. After the governing equations are determined, a commercial package *ANSYS Fluent* will be used to solve numerically this set of equations. *ANSYS Fluent* provides a platform that

incorporates numerical techniques capable of modeling computational fluid problems. Gaseous combustion is one of its major applications. In this study, the turbulence and combustion models used will be validated by experiments. Therefore, a set of lab-scale methane explosion experiments have been conducted with the intention to evaluate the selected numerical models. In Objective (2), the accuracy of the numerical schemes, when specific turbulence and combustion models are employed, will be investigated. The most accurate numerical scheme will be used in the research that follows validation. After the validation, 3D numerical simulations will be conducted using different explosion conditions, such as site-dimensions and methane concentration. The database in Objective (3) will both record and compile the simulation results. Objective (4) aims to investigate the impact of geometrical changes on the blast-wave propagation within the second section. The results of both objectives (3) and (4) will be used in Objective (5) to simulate a whole mine, using a one-dimensional (1D) model complemented by the results of a three-dimensional (3D) simulation and geometric change study.

1.5. STRUCTURE OF RESEARCH

According to the five objectives stated above, the structure of this research is summarized with the technology roadmap shown in Figure 1.1. The Figure 1.1 illustrates the sequence and interrelationships among three main parts of this research: lab experiments, explosion source database development, and geometric influence investigation. Each of these research categories will occupy three independent sections, which are Sections 3, 4, and 5, respectively. Section 2, 6, and 7 will cover numerical theory derivation, one-dimensional (1D) simulation and case study parameters, and conclusions, respectively.

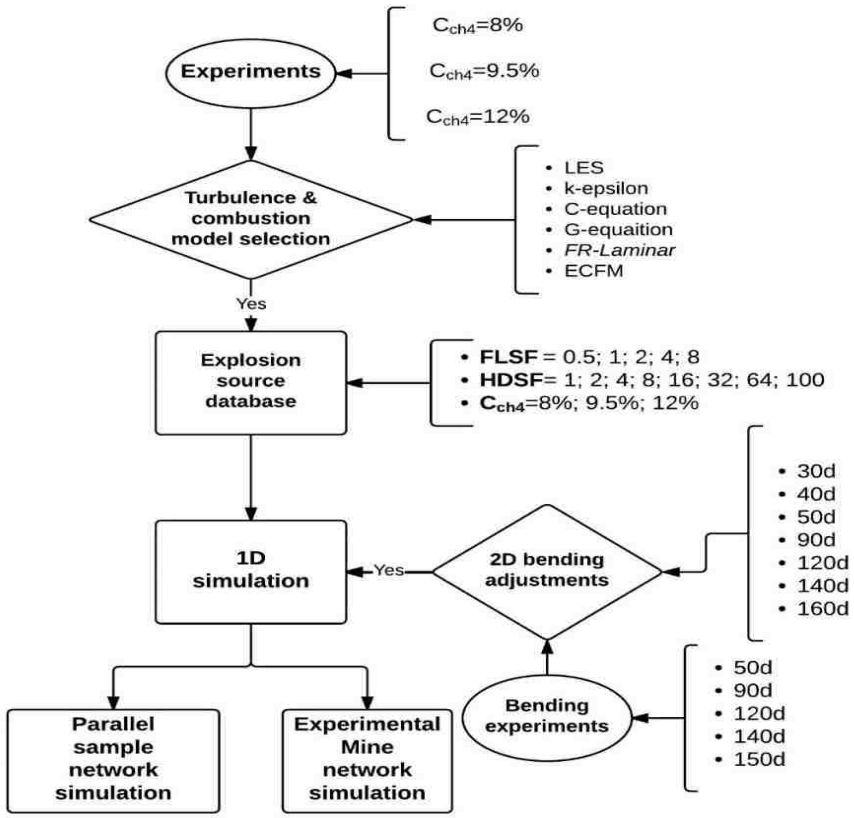

Nomenclature

C_{ch4}	L_f (m)	D_h (m)	FR-Laminar
methane concentration	gas-fill length	hydraulic diameter	finite-rate laminar
P_{max}	V_{max}	d	LES
maximum overpressure	maximum velocity	degrees	large-eddy simulation
ECFM	FLSF	HDSF	
Extended Coherent Flamelet Model	Gas-fill Length Scaling Factor	Hydraulic Diameter Scaling Factor	

Figure 1.1. Technology Roadmap

2. METHANE EXPLOSION MODELING

2.1. PROBLEM STATEMENT

According to Needham and Dai, the methane explosion influence region can be divided into two sections (Needham, 2010; Dai, et al., 2011): *driver section* and *blast-wave section*, as represented in Figure 2.1. This research will be based on a two-section theory where the characteristics of each section will be discussed in details in this Section.

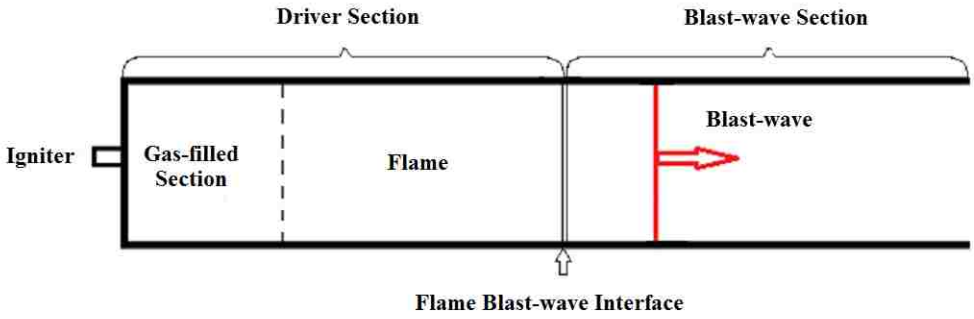

Figure 2.1. Regions of methane explosion process in a duct (Dai et al., 2011)

2.1.1. Driver Section. The *Driver section* extends from the explosion source to the interface between the flame and the blast-wave edge where the flame dies, as shown in Figure 2.1. In this region, which is filled with gases, methane/air mixture can be ignited by a high energy source to initiate chemical reactions. As unburned gas downstream the flame keeps feeding into the flame, the reaction is exacerbated where the flame becomes self-sustained. Blast-wave transmit from the source of ignition to the space is filled with unburned gases. After fuel is exhausted, the flame quenches, but the blast-wave will keep propagating forward in the blast-wave section.

2.1.2. Blast-wave Section. The *Blast-wave section* shares the same boundary with the *driver section*, it is also assumed to be separate from the flame front at the flame blast-wave interface, and propagates forward independently in the airflow. In this section, a simplified one-dimensional (1D) model will be used. As Rankine-Hugoniot relationship suggests, explosion parameters differ between two sides of the blast-wave front, which propagates at the local sound speed D as illustrated in Figure 2.2.

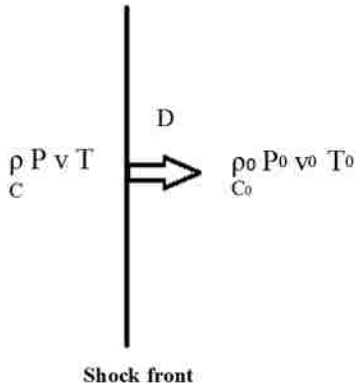

Figure 2.2. Propagation of a shock wave

Following this relationship, undisturbed properties downstream the wave front, are typically known. If the overpressure at the shock front *P* is also known, the rest of shock characteristics could be calculated (Needham, 2010). Therefore, the overpressure is a key index to express a methane explosion in the blast-wave section.

Based on the two-section theory (Needham, 2010; Dai, et al., 2011), different numerical techniques will be applied in two sections. In the *driver section*, interaction between chemical reactions and turbulence is important, a three-dimensional (3D) numerical model with turbulent and combustion subroutines are used in this section. A methane explosion source database will be developed to record overpressure/time relationships (overpressure histories) of an explosion in different conditions. These conditions can be the gas-filled length in an airway, the scale of explosion tube, the

methane concentration, etc... A series of lab-scale experiments will be conducted to validate the selected numerical results.

In the blast-wave section, however, 1D assumption will be applied as turbulence, and combustion can be safely neglected (Qu, et al., 2008). The pre-developed database can provide the initial and boundary conditions, such as overpressure histories, to the 1D model, in order to analyze the pure blast-wave propagation and the overpressure distribution in the blast-wave section. Attributing to the 1D simplification applied in the blast-wave section, the computational cost is lower, which allows the researchers to use a complex geometry in conducting simulations. Thus, a complex airway network, which can be commonly found in underground mines, can be simulated. Another reason for applying a network-based simulation model is the availability of geometric data. The 1D-based ventilation network models are commonly employed by mine operations for ventilation planning purpose and can be used in the 1D simulation. A ventilation network model also offers such information as airway layouts, location of blast source, air velocity, and methane concentration; which can be used as initial conditions for the 1D model.

Within a ventilation network, the presence of geometric changes (e.g. bend, branching, or obstacles) on the explosion tube has considerable influence on peak overpressure of a methane explosion. Therefore, these influences must be investigated.

This research seeks to provide an explosion source database in a *driver section* and a network-based 1D model of methane explosions considering the presence of geometric changes. Although these two sections will be modeled simultaneously and independently, they are coupled and functioned as one combined unit. The governing equations and numerical techniques relevant to this approach will be discussed in the following sections.

2.2. FLUID GOVERNING EQUATIONS

As stated in Section 2.1, the space (region) where methane explosion occurs can be separated into a *driver section* and a *blast-wave section*. Chemical reactions and turbulence dominate in the former section, whereas blast-wave propagation plays a key role in the *blast-wave section*. This research includes three main parts corresponding to

the three objectives listed in Section 1.4.2: Objective (3) explosion source database for the *driver section*, Objective (4) geometric attenuation factor identification, and Objective (5) 1D entire mine compressible flow analysis for the *blast-wave section*.

In Objective (3), a methane explosion source database is required based on the 3D Computational Fluid Dynamics (CFD) simulation results. This database is designed to provide a set of initial and boundary parameters for the 1D compressible flow analysis mentioned in Objective (5). Detailed simulations will be conducted using commercial CFD package *ANSYS Fluent*. These simulations are based on conservation equations including conservation of mass, momentum, energy, and species. Turbulence and combustion models used in this research will be described in details in Sections 2.3 and 2.4, respectively. The last section of this section will discuss in details the numerical solution for the governing equations.

2.2.1. Governing Equations in the Driver Section. The methane explosion is highly time dependent, the fluid field in the *driver section* should therefore be treated as transient and compressible flow where the Mach number could reach as high as 4 (Needham, 2010; Anon, 2011). As a result, the general form of Navier-Stokes and energy equations with changing density are employed (Equations (2.1) ~ (2.3)). Equation (2.1) is the general form of conservation of mass.

$$\frac{\partial \rho}{\partial t} + \nabla \cdot (\rho \vec{v}) = S_m \tag{2.1}$$

where ∇ is divergence operator, ρ denotes density, $\vec{v}$ is velocity vector, t is time, and S_m is mass increment due to phase interchanges.

Equation (2.2) represents the conservation of momentum where p is pressure, while $\bar{\tau}$ denotes stress tensor due to molecular viscosity, $\rho\vec{g}$ and $\vec{F}$ are gravitational force and body force, respectively.

$$\frac{\partial}{\partial t}(\rho \vec{v}) + \nabla \cdot (\rho \vec{v}\vec{v}) = -\nabla \mathrm{p} + \nabla \cdot (\bar{\tau}) + \rho\vec{g} + \vec{F} \tag{2.2}$$

Equation (2.3) is the conservation of energy equation where E is total energy, k_{eff} is the effective conductivity, ∇T is the temperature change. $h_j\overrightarrow{J_j}$, and $\bar{\bar{\tau}}_{eff} \cdot \vec{v}$ are species diffusion and viscous dissipation, S_h is the heat generation of chemical actions.

Note that S_h is the source term that contributes to the temperature increment of methane/air combustion.

$$\frac{\partial}{\partial t}(\rho E) + \nabla \cdot \left(\vec{v}(\rho E + p)\right) = \nabla \cdot \left(k_{eff}\nabla \mathrm{T} - \sum_j h_j \overrightarrow{J_j} + \left(\bar{\bar{\tau}}_{eff} \cdot \vec{v}\right)\right) + S_h \qquad (2.3)$$

In addition to the governing equations above, the contribution of turbulence and combustion also need to be included in the analysis in the *driver section*. Additional equations are required to address turbulence and combustion, both of which will be discussed separately in Sections 2.3 and 2.4.

2.2.2. Governing Equations in the Blast-wave Section. The main task of Objective (5) in Section 1.4.2, is the development of a 1D model used to predict blast-wave propagations within the blast-wave section where the flame has been quenched within this region. However, the disturbances (overpressure discontinuity) will keep propagating until the blast-wave is attenuated to a sound-wave. The major reason for using the 1D simplification is to reduce computational time and thus cost significantly. In this section, the behavior of the blast-wave overwhelms chemical reactions and turbulence; thus, the contribution of turbulent acceleration and reaction-turbulence interaction on the overpressure can be neglected without causing much error (Qu, et al., 2008). Therefore, only the fluid parameters and their gradient on stream-wise direction are included. The Overpressure change along the airflow direction is greater than the pressure in in the transverse direction. For practical purposes, the cross-section of underground mine airways can be treated as either constant or as a function of distance along the direction of airways. Thus, the behavior of the blast-wave in this region can be simplified into a 1D problem (Needham, 2010).

The 1D simulation will be conducted using CFD code *Flowmaster* where the flow is considered transient, compressible, inviscid (flow of ideal fluid that is assumed to have no viscosity) and is one-dimensional. Therefore, the tailored governing equations are used in the 1D simulation. Specifically, from Equations (2.1) to (2.3), all divergence operators ∇ are replaced by the partial derivative respects to x direction, $\frac{\partial}{\partial \mathrm{x}}$. The two viscous terms, i.e. $\bar{\tau}$ in Equation (2.2) and $\bar{\bar{\tau}}_{eff}$ in Equation (2.3) are neglected. Turbulence equations and chemical reaction will also be excluded from the 1D simulation analysis.

Since pressure drops due to geometrical changes along an airway, it must be included in a 1D simulation. Thus, quantitative analyses of the pressure drops will be investigated in Objective (4). The most representative geometrical changes of a longwall or a room-and-pillar mine are bends, branches, obstacles, and cross-sectional changes (Jia & Lin, 2009). A 2D numerical model has been developed to quantify these influences. The results are used to validate geometric change effects in the 1D simulation. The modeling and calculations of the geometric changes influences will be shown in details in Section 5.

2.3. TURBULENCE FORMULATIONS

In a methane explosion process, turbulence tends to stretch and wrinkle the flame front. Thus these effects significantly accelerate the flame and, in turn, result in large overpressure and temperature incremental change. Therefore, turbulent modeling is one of the most important factors for a successful methane explosion simulation.

Turbulence will not be directly modeled because the computational cost of direct numerical simulation (DNS) is prohibitive. One feasible way is to use time-averaged or filtered values to represent the actual unsteady flow parameters. Standard *k*-ε and Large Eddy Simulation (LES) models are the most representative of time-averaged and filtered models, respectively.

The introduction of turbulence to both models adds a new term to the right hand side of the momentum (shown in Equation (2.2)) called turbulent stress. Both, the LES and the standard *k*-ε are turbulence viscous models, which yield to the Boussinesq hypothesis (Tannehill, Anderson, & Pletcher, 1997). According to this hypothesis, turbulent stress is related to velocity vectors of the flow field by turbulent viscosity μ_T. The difference between time-averaged model and LES model lays in different expressions of μ_T in addition to their averaging operation. The standard *k*-ε model has been widely used within computational fluid research field for many years, due to its stability and high computational efficiency. This model has also been employed by the majority of researchers to simulate a gaseous explosion (Makarov, Verbecke, & Molkov, 2007). However, time-averaged models have an inherent drawback when resolving transient turbulent structures (eddies). The LES model, on the other hand, is a reasonable

alternative for time-averaged schemes. This model has also been employed by majority vast number of researchers to simulate a gaseous explosion (Makarov, Verbecke, & Molkov, 2008). The LES method has only been applied in research areas such as hydrogen combustion, whereas few applications have been found in methane combustion In hydrogen combustion simulations, the LES model was found to better predicts the peak overpressure rather than the time-averaged models (Moureaua, Fiorinab, & Pitscha, 2009). Therefore, the capability of LES to simulate methane/air combustion in underground coal mines need to be validated. The current study seeks to broaden the application of LES method while providing an alternative tool to simulate a methane explosion. Thus, the formulation of standard *k-ε* and LES models will be demonstrated in details later in this section.

2.3.1. Standard *k-ε* Model. The most commonly used time-averaged (also called Reynolds-averaged) model is the two-equation, standard *k-ε* model. The rationale for this model is to treat the randomly fluctuating fluid parameter as a combination of a mean value and a fluctuation value.

According to the Boussinesq hypothesis, the contribution of turbulence momentum in standard *k-ε* model is adding a new term $\partial/\partial \mathrm{x}\left(\overline{-\rho u_i u_j}\right)$ on the right hand side of the momentum Equation (2.2). Since $\overline{-\rho u_i u_j}$ cannot be solved directly, the turbulence viscosity μ_T can be related to the strain rate $\bar{S}_{ij}$ ($\bar{S}_{ij} = 1/2\left(\partial \bar{u}_i/\partial x_j + \partial \bar{u}_j/\partial x_i\right)$) by:

$$-\overline{\rho u_i u_j} = 2\mu_T S_{ij} - \frac{2}{3}\delta_{ij}\left(\mu_T \frac{\partial u_k}{\partial x_k} + \rho\bar{k}\right) \tag{2.4}$$

The μ_T can be solved by Equations (2.5) to (2.7) below. (Tannehill, Anderson, & Pletcher, 1997):

$$\rho\frac{D\bar{k}}{Dt} = \frac{\partial}{\partial x_j}\left[\left(\mu + \mu_T/1.3\right)\frac{\partial \bar{k}}{\partial x_j}\right] + \left(2\mu_T S_{ij} - \frac{2}{3}\rho\bar{k}\delta_{ij}\right)\frac{\partial u_i}{\partial x_j} - \rho\varepsilon \tag{2.5}$$

$$\rho\frac{D\varepsilon}{Dt} = \frac{\partial}{\partial x_j}\left[\left(\mu + \mu_T\right)\frac{\partial \varepsilon}{\partial x_j}\right] + 0.09\frac{\varepsilon}{\bar{k}}\left(2\mu_T S_{ij} - \frac{2}{3}\rho\bar{k}\delta_{ij}\right)\frac{\partial u_i}{\partial x_j} - 1.8\rho\frac{\varepsilon^2}{\bar{k}} \tag{2.6}$$

$$\mu_T = 0.09\rho\bar{k}^2 / \varepsilon \quad . \tag{2.7}$$

where k is turbulence kinetic energy and ε is turbulent dissipation rate. δ_{ij} denotes Kronecker delta , $\bar{S}_{ij} = 1/2\left(\partial\bar{u}_i/\partial x_j + \partial\bar{u}_j/\partial x_i\right)$, and turbulent viscosity μ_T.

2.3.2. Large Eddy Simulation (LES). Another turbulent closure used in this research is LES, which seeks to resolve a large eddy structure and model the sub-grid eddy using turbulent viscosity theory. The contribution of turbulence can be represented by a new term $\partial/\partial x\left(\tau_{ij}\right)$ in right hand side of momentum Equation (2.2). Based on the Boussinesq hypothesis, τ_{ij} can be related to strain-rate $\bar{S}_{ij}$ by (Anon, 2011):

$$\tau_{ij} - \frac{1}{3}\tau_{kk}\delta_{ij} = -2\mu_{TSGS}\bar{S}_{ij} \tag{2.8}$$

where $\bar{S}_{ij}$ is sub-grid scale (SGS) strain rate and μ_{TSGS} is sub-grid scale turbulent viscosity.

Smagorinsky (1963) proposed an expression to solve μ_{TSGS} that is shown below.)

$$\mu_{TSGS} = \rho {L_s}^2 \sqrt{2\bar{S}_{ij}\bar{S}_{ij}} \tag{2.9}$$

where L_s is the SGS mixing length in meter and can be computed by $L_s = min\left(\kappa d, C_s \triangle\right)$. κ represents K árm án constant; d is the normal distance to the nearest wall in meter and C_s is Smagorinsky constant, respectively. Δ is the characteristic volume of cells which equines to cubic root of the a cell volume, in meter (Anon, 2011). The universal constant κ is assigned as 0.41 and C_s is 0.12 in this research.

2.4. COMBUSTION FORMULATIONS

To incorporate chemical reaction formulation into the methane explosion simulation, a combustion model should be developed. The eddy-breakup and premixed c-equation models were used in this research, and will be explained in detail, in the section below.

2.4.1. Eddy-breakup Model. The chemical reaction incorporated in a methane explosion yields conservation of species. Therefore, species transport equation (conservation of species) should be used as shown in Equation (2.10). Combining the proceeding mentioned governing equations and the turbulent closure model, the turbulent reaction flows can be modeled by applying finite volume method (FVM) using *ANSYS Fluent*.

$$\frac{\partial}{\partial t}(\rho Y_i) + \nabla \cdot (\rho \vec{v} Y_i) = -\nabla \cdot \vec{J}_i + R_i + S_i \tag{2.10}$$

where Y_i is mass fraction of species *i*, R_i is production of species, and S_i is user-defined source term.

For a turbulent flow, $\vec{J}_i$ in equation (2.10), which is the diffusion flux of species *i*, yields:

$$\vec{J}_i = -\left(\rho D_{m,i} + \frac{\mu_T}{S_{ct}}\right)\nabla Y_i - D_{T,i}\frac{\nabla T}{T} \tag{2.11}$$

where S_{ct} is turbulent Schmidt number equals to 0.7, $D_{m,i}$and $D_{T,i}$ are mass diffusivity and thermal diffusivity for species *I*, respectively.

For the standard *k*-ε model, the production rate R_i in Equation (2.10) can be obtained by the smaller of the two Equations (2.12) and (2.13):

$$R_{i,r} = \nu_{i,r}' M_{w,i} A \rho \frac{\varepsilon}{k} min R \left(\frac{Y_R}{\nu_{R,r}' M_{w,R}}\right) \tag{2.12}$$

$$R_{i,r} = \nu_{i,r}' M_{w,i} A B \rho \frac{\varepsilon}{k} \frac{\sum_P Y_P}{\sum_j^N M_{w,j} \nu_{j,r}''} \tag{2.13}$$

where Y_P is the mass fraction of product species *P* and Y_R is the mass fraction of a specific reactant *R*. A and B are model constants equal to 4.0 and 0.5, respectively. These equations indicate that the chemical reaction rate is governed by the large eddy mixing time scale, as in the eddy-breakup model of Spalding (1970). For the LES model, $\frac{\varepsilon}{k}$ is required to be replaced by sub-grid mixing rate:

$$\tau_{SGS}^{-1} = \sqrt{2 S_{ij} S_{ij}} \tag{2.14}$$

2.4.2. Premixed C-equation Model. Premixed assumption can be used as reasonable assumptions for modeling methane explosion in a wide range of conditions. This leads to the spices transport equation incorporating the progress variable c, which c=0 for unburnt and c=1 for burnt gas:

$$\frac{\partial}{\partial t}(\rho c) + \nabla \cdot (\rho \vec{v} c) = \nabla \cdot \left(\frac{\mu_t}{S_{ct}} \nabla c\right) + \rho S_c \tag{2.15}$$

The TFC mean reaction rate $\rho S_c = \rho_u U_t |\nabla c|$. Where ρ_u and U_t are density of unburnt gas and turublent flame speed, respectively (Zimont, et al., 1998). In Ewald's work, $U_t = U_l(1 + \sigma_t)$ (2006). U_l represents the laminar flame speed related to equvilence ratio of fuel/air (Londoño, et al., 2013). and for LES model:

$$\sigma_t = -\frac{b_3^2}{2b_1 C_{t\Delta} S_{ct}} \frac{l_f}{\delta} + \left[\left(\frac{b_3^2}{2b_1 C_{t\Delta} S_{ct}} \frac{l_f}{\delta}\right)^2 + \frac{b_3^2}{2C_{t\Delta} S_{ct}} \frac{{l_f}^2}{U_l \delta \mu_t}\right]^{1/2} \tag{2.16}$$

where $C_{t\Delta}$ is schemit number modifier which equals to 0.7. and b_1 and b_3 are constant equal to 2.0 and 1.0, respectively. δ is laminar flame thickness equals to $\sqrt{(\lambda/c_p)/U_l \rho}$; where l_f is the flame brush thickness equals to $\sqrt{(C_s \Delta / u')/(\mu_{eff}/\rho S_{ct})}$; u' and μ_{eff} are the turbulent velocity scale and the effective viscosity, respectively (Anon, 2011).For highly compressible detonations, Favre averaged flow parameters should be applied as $\tilde{\phi} = \overline{\rho\phi}/\bar{\rho}$ in which ϕ can be any flow parameter except density itself. The over-bars represent the SGS filtered values.

2.5. CJ-DETONATION THEORY

Although over 90% of methane explosion incidents in underground mines are deflagration, and in some extreme cases, deflagration to detonation transformation (DDT) would still be triggered (Zhou, Wu and Xu, 2002). This calls for a criterion to judge if detonation occurs rather than deflagration. Chapman-Jouguet (CJ) detonation theory provided the criterion to define the minimum overpressure generated by a detonation. The derivation of CJ detonation pressure is illustrated below.

According to the CJ detonation theory, the flow parameters upstream state ρ_1; u_1; $p_1$of the blast front and downstream state ρ_2; u_2; p_2. The density and pressure downstream are also the detonation density ρ_{CJ} and pressure $p_{CJ}$when detonation occurs. ρ_{CJ} and p_{CJ}can be calculated with the following relationships (Needham, 2010; Zeldovich, 1940):

$$\rho_{CJ} = \frac{p_2/\rho_2 + c^2}{C^2} \tag{2.17}$$

$$p_{CJ} = 2(\gamma - 1)\rho_1 e \tag{2.18}$$

where C is speed of sound and γ is the gas-specific heat ratio which is considered a constant of 1.4 in both deflagration and detonation scenarios. e denotes energy per unit mass of explosives. The speed of sound downstream a detonation front C_{CJ} can be obtained using $c_{CJ} = \sqrt{\gamma p_{CJ}/\rho_{CJ}}$. Subsequently, the minimum CJ-detonation overpressure can be calculated by:

$$p(\zeta_0) = p_{CJ}\frac{(-s + C_{CJ})(1+\gamma)}{2} + s \tag{2.19}$$

where ζ_0 is initial detonation speed can be obtained by $0.5(-s + c_{CJ})(1 + \gamma) + s$; s is the shock speed which equals to $c(\rho_2/\rho_1)$.

As observed from Equations (12.17) to (12.19), the CJ-detonation theory is a general rule that does not take into considerations geometric effects, and therefore cannot provide accurate predictions. The scenarios that have a larger overpressure than CJ-detonation overpressure were investigated by CFD simulations, and are presented using the eddy-breakup combustion model, introduced in Section 2.4.1.

2.6. NUMERICAL SOLUTION OF GOVERNING EQUATIONS

The equations introduced in previous sections cannot be solved analytically due to the presence of non-linear terms. Therefore, spatial discretization techniques must be employed to transfer the integral of governing equations used in control volumes into a discrete form. The change of fluid variables over a continuous time duration and is considered in a time-dependent problem (in differential forms), which also needs to be

separated into a finite number of time-steps. This operation is called temporal discretization. After both discretization operations are completed, the discrete equation system can then be solved by a liner mathematical process.

In this current research, a second-order upwind scheme is used for the convection terms governing equations. A least squares cell-based scheme is used for the gradient treatment. Also, a second-order upwind scheme is used in diffusion terms for the governing equation and an implicit scheme is used for temporal discretization. These discretization techniques will be discussed in the following section.

2.6.1. Finite Volume Method. The spatial numerical discretization and linearization technique used by *ANSYS Fluent* is based on the finite volume method (FVM). This method seeks to segment the entire fluid domain into a finite number of small control volumes or cells, in a process called meshing. Each of the control-volumes or cells yields a set of governing equations as illustrated in Sections 2.2 to 2.4. The governing equations are in integral form and can be expresses in a universal form as follows:

$$\int_V \frac{\partial \rho \phi}{\partial t} dV + \oint \rho \phi \vec{v} \cdot d\vec{A} = \oint \Gamma_\phi \nabla \phi \cdot d\vec{A} + \int_V S_\Phi \, dV \qquad (2.20)$$

where ϕ represents a specific fluid scalar (such as density or enthalpy) which is stored in the centroid of a small control volume. Γ_ϕ and S_Φ are diffusivity and source term of the scalar ϕ. This equation needs to be discretized into a discrete control equation, as shown in Equation (2.21):

$$\frac{\partial \rho \phi}{\partial t} V + \sum_f^N \rho \phi_f \vec{v} \cdot \vec{A} = \sum_f^N \Gamma_\phi \nabla \phi \vec{v} \cdot \vec{A} + S_\Phi V \qquad (2.21)$$

The first term on the right hand side (RHS) of Equation (2.21), called an unsteady term, needs temporal discretization to transform it from differential form into algebraic form. The second term, RHS, is a convection term. The variable ϕ_f in this formula denotes a value of a fluid variable on a cell face. It is a new unknown and needs to be related to given center values ϕ of the cell itself and its neighbors. This operation can be done by using a second-order upwind scheme. The first term on the LHS, called the diffusion term, includes a gradient of a scalar $\nabla\phi$, another new unknown. To obtain $\nabla\phi$, a

gradient treatment is required. In addition to the diffusion term, a scalar gradient is also needed in the second-order upwind scheme. The discretization process of each term will be introduced in following section.

2.6.2. Temporal Discretization. The differential form of $\frac{\partial \phi}{\partial t}$ is set equal to a function of all of the special discretization terms (move the convection term to the LHS) $F(\phi)$:

$$\frac{\phi^{n+1}-\phi^{n}}{\Delta t} = F(\phi) \tag{2.22}$$

where n+1 represents the value of ϕ at the next time interval; and, $t + \Delta t$ and n represents the value of ϕ at the current time t. In this research, both explicit and implicit temporal discretization techniques are used. For the explicit method, the RHS of Equation (2.22) becomes $F(\phi^n)$ which represents function relates to current time level. For implicit method, on the other hand, the LHS is $F(\phi^{n+1})$.

2.6.3. Second-Order Upwind Scheme. As stated in Section 2.6.1, the facial value ϕ_f is unknown and needs be calculated. In a second-order upwind scheme, ϕ_f is expressed as (Barth & Jespersen, 1989):

$$\phi_f = \phi + \Delta\phi.\vec{r} \tag{2.23}$$

where $\vec{r}$ is the displacement vector point from the cell centroid to the face centroid. Note that the gradient, $\Delta\phi$, is still unknown and that therefore, gradient treatment is required.

2.6.4. Least-Square Gradient Treatment. The gradient of a fluid scalar $\Delta\phi$ needs to be solved by the gradient treatment operation. Node-based methodology and the least-square gradient treatment are the most common methods utilized. However, the least-square model is less expensive computationally, and thus will be selected. The gradient term can be expressed by the least-square gradient treatment shown as below:

$$(\nabla\phi)_{c_0} \cdot \Delta r_i = \left(\phi_{c_i} - \phi_{c_0}\right) \tag{2.24}$$

where the subscript of the scalar terms represents the cell centroid of the cell selected, c_0 and its neighbor c_i (Figure 2.3). r_i is the displaced vector from the selected cell at a centroid point to its neighbor's centroid.

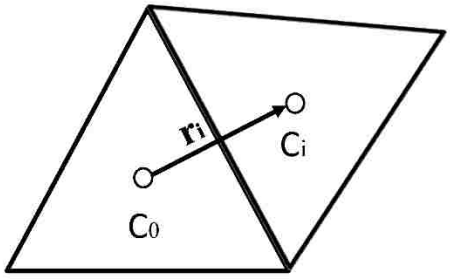

Figure 2.3. Least square gradient treatment

After the above mentioned discretization operations are done, a set of algebraic governing equations are solved in each cell belonging to the computational domain selected. As the transportation nature of the governing equations themselves, the fluid scalars can propagate with mass flux, called conviction, and the scalars' gradient called diffusion. Diffusion can be categorized into thermal diffusion and mass diffusion, which attribute to temperature and density gradient, respectively.

The governing equations introduced in this Section will be applied in numerical studies in Section 4, 5, and 6 and will be revisited many times. Section 3, on the other hand, will provide experimental validations for the numerical models used to predict methane explosions in explosion duct. Details of the design, conduction, and results of the methane explosions will be illustrated in Section 3.

3. EXPERIMENT

3.1. INTRODUCTION

As described in the statement of Objective (2) in Section 1.4.2, numerical models used in both 3D and 2D simulations must be validated. Therefore, an experiment based on the methane explosion limits and the two-section theory was designed and conducted. Details of the design of this experiment, facilities, procedure, and results are provided in this Section.

3.1.1. Explosion Limit Theory. Methane is a known flammable gas that has both a lower-explosive-limit (LEL) and an upper-explosive limit (UEL). LEL refers to the lowest concentration of flammable gas that can be ignited by either an ignition source of flame, sparks or heat.

For a flammable gas mixture with a concentration lower than LEL, the fuel will be too lean to be ignited. As for the upper limit, the oxygen will be too lean to support combustion with a concentration higher than UEL. In such case the methane/air mixture has a LEL of 5% and UEL of 15% (Zhou, Xu & Wu, 2002). However, if methane/air mixtures were mixed with other flammable gases, LEL and UEL will change accordingly. The LEL can be calculated using Le Chatelier's mixing rule (Hustad & Sonju, 1988):

$$LEL_{mix} = \frac{1}{\sum \frac{x_i}{LEL_i}} \tag{3.1}$$

where x_i is volume fraction of flammable gas which is added to the original mixture. The UEL of a mixture can be calculated by substituting LEL_i for UEL_i in Equation (3.1). The combustibility of the methane/air mixture is also affected by oxygen concentrations which yield to the explosive triangle theory. The conditions of the methane/air mixture in different regions in the methane to oxygen concentration relationship map are shown in Figure 3.1 (Anon., 1994).

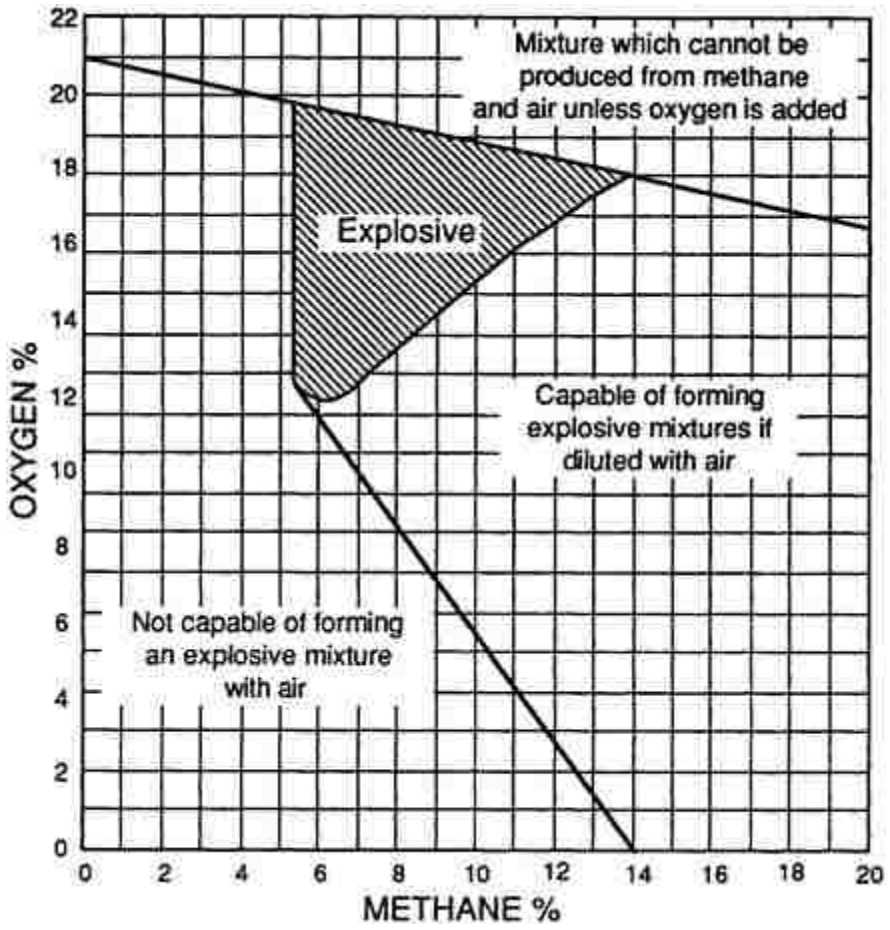

Figure 3.1. Explosive triangle of methane/air mixture (Anon., 1994)

As Figure 3.1 illustrates, the methane/air mixture is not combustible when the oxygen concentration is lower than 12.5% or higher than 19.5%. As a result, controlling the methane and oxygen concentration will be an effective way to prevent or mitigate gaseous explosions.

In the USA, the methane concentration for underground mines is closely monitored and controlled, as required by *30 CFR § 75.323*. The regulations require that when 1.0 percent or more methane is present in a working place, all electronically powered equipment in the affected area shall be de-energized, and other mechanized equipment shall be shut off, except for the intrinsically safe atmospheric monitoring systems (AMS)". If the methane concentration is higher than 1.5%, all personnel shall be withdrawn from the affected area except for persons listed in §104(c) of the Act, and all

electrically powered equipment shall be disconnected at the power source (30CFR§75.323(1) and (2)).

In the current study, three methane concentrations are planned in the experimental design: 8%, 9.5%, and 12% which represent fuel lean, stoichiometric, and fuel rich conditions, respectively. Mixtures made with other flammable gases are beyond the scope of this research.

3.1.2. Environmental Conditions. It is known that both LEL and UEL are affected by environmental factors such as ambient temperature and pressure (Chen & Hou, 2008). Based on previous studies, the LEL decreases while UEL increases as the ambient temperature increases. The experimental relationship among ambient temperature, LEL, and UEL are shown in Table 3.1 below.

Table 3.1. LEL and UEL vary with ambient temperature (Chen & Hou, 2008)

Ambient Temperature (℃)	LEL(%)	UEL(%)
20	6.00	13.4
100	5.45	13.5
200	5.05	13.8
300	4.40	14.2
400	4.00	14.7
500	3.65	15.3
600	3.35	16.4
700	3.25	18.7

As can concluded from Table 3.1, LEL and UEL remain relatively independent of ambient temperatures in a normal experimental environment (no outside heat sources). UEL is sensitive to initial pressure while LEL is not. Moreover, UEL increases as the increment of initial pressure as summarized in Table 3.2.

Table 3.2. LEL and UEL vary with initial pressure (Chen & Hou, 2008)

Initial Pressure (KPa)	LEL(%)	UEL(%)
101.3	5.6	14.3
1013	5.9	17.2
5,065	5.4	29.4
12,662	5.7	45.7

Although the impact of ambient temperature and pressure on combustibility of a methane mixture is insignificant, they were still measured and recorded during each test conducted. The average ambient temperature and pressure were 38 ℃ and 101.5 KPa, respectively; both were used in the numerical modeling.

3.1.3. Effect of Geometric Changes. Presence of geometric changes, such as bends or branches have significant influence on overpressure. Therefore, this influence should not be neglected during simulations. A 2D CFD model will be developed to quantify this influence. The code used in the model is also validated through experimentation, providing an excellent overpressure variation history of impact due to geometric changes. The results of this analysis are described in details in Section 3.5, below.

3.2. EXPERIMENTAL DESIGN

3.2.1. Experimental Scenarios. In this study, a detailed plan for the experiment is developed to characterize methane explosion characteristics under different geometric configurations along with varying methane concentrations. Two factors are chosen within the driver section, methane concentration, and airway blockage condition (geometric change). Three methane concentrations of 8%, 9.5%, and 12% were chosen to represent fuel-lean, stoichiometric, and fuel-rich conditions, respectively. Under each concentration, nine groups of tests were conducted with and without geometrical changes. The geometric changes tested include four major types of bends with four bending angles, obstacles with three Blockage Rations, a t-branch, and a cross-sectional

change component, respectively. Tests with methane concentration of 9.5% were repeated with an “acceleration spiral” used to characterize the explosion in airways with obstructions within the gas-filled section. The flame could be accelerated due to a further stretching of the flame front in the vicinity of the obstacles (Zhou, Wu, & Xu, 2002). The results of the experiments with the presence of an acceleration spiral will not be included, but will be used as a reference to the 2D numerical simulations. Table 3.3 summarizes the experimental scenarios where each scenario was repeated three times to increase accuracy.

Table 3.3. Experimental Scenarios

Methane	8%	9.5%	12%	
Blockage ratios (BR)	25%	50%	75%	
Bending	50°	90°	120°	140°
Cross-sectional change	80mm×80mm to 145mm×145mm			
**Repeat the tests with acceleration spiral for* 9.5% cases				

3.2.2. Experimental Layout. The experiment was conducted at the Institute of Methane Safety Control and Utilization, China University of Mining and Technology (CUMT), Xuzhou, Jiangsu Province, China. The instruments used in the experiments were customized and specifically re-configured for the purpose of this research. The experimental system consisted of six main parts: igniter, main explosion ducts, detachable duct with geometric change, gas source, sensors, and data collection system (Figure 3.2). The explosion test duct has a square cross-section of 80 mm × 80 mm, and a length of 11.35 m. The duct was built to withstand a maximum overpressure of 20 MPa. The data collection system (model: CS20182-32) was connected to the pressure and light-sensitive sensors, which are used to capture overpressure and flame signals along the duct.

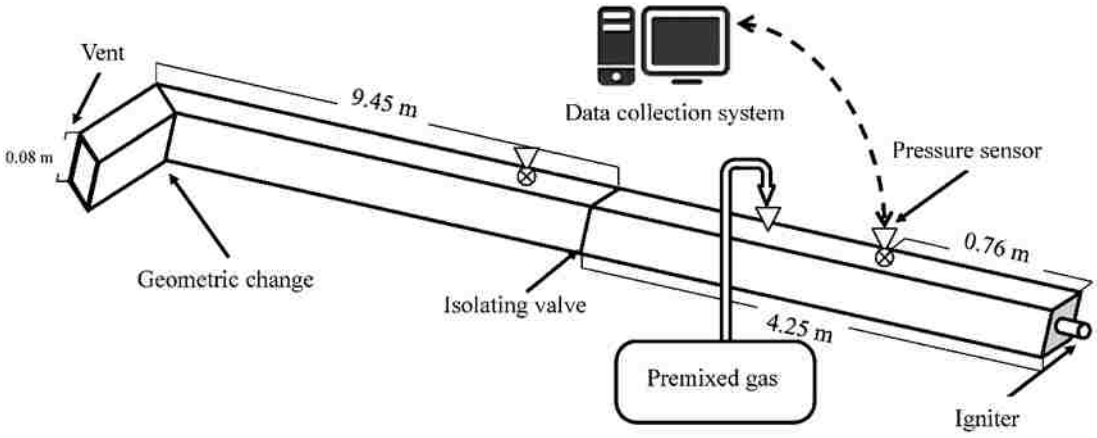

Figure 3.2. Schematic of the methane explosion experimental system (Not to scale)

3.2.3. Experimental Equipment. The experimental system is illustrated in Figure 3.2. The main experimental components are shown in Figure 3.3. These components are a gas bag (Figure 3.3 (a)), an igniter (Figure 3.3 (b)); an explosion duct with geometric change (Figure 3.3 (c)); a pressure sensor (Figure 3.3 (d)); and the data collection system (model: CS20182-32) (Figure 3.3 (e)), respectively.

(a) (b)

Figure 3.3. Instruments used in the explosion experiment; (a) gas bag, (b) igniter, (c) explosion duct with t-branching, (d) pressure sensor and (e) data collection unit

(c)

(d)

(e)

Figure 3.3. Instruments used in the explosion experiment; (a) gas bag, (b) igniter, (c) explosion duct with t-branching, (d) pressure sensor and (e) data collection unit (cont.)

3.2.4. Experimental Procedure. The experiment setup consisted of six major steps: (1) install the duct with various different duct configurations (e.g., bend, branch, obstacle, and duct expand); (2) premix methane and air in gas bag; (3) fill the mixture into the gas-filled section through a pressure valve; (4) setup the data collection system; (5) ignite the mixture, and (6) collect data. Each test occurred over 30 minutes; and more than 120 tests were conducted and tests were repeated when there were unexpected experimental failures.

3.3. EXPERIMENTAL RESULTS

Roughly 1.3 sec (seconds) of overpressure histories were collected by the data collection system for each of the scenarios. The time duration of the collection system which was 0.5 ms (milliseconds), which generated more than 600,000 data points per test. The unprocessed overpressure histories of six pressure sensors (the first channel initialized the collection) for the three concentration levels in a straight airway are shown in Figures 3.4 to 3.6. The layout of pressure sensors (14 Channels in total for each test, 8 channels on the straight duct) may be found in Appendix A.

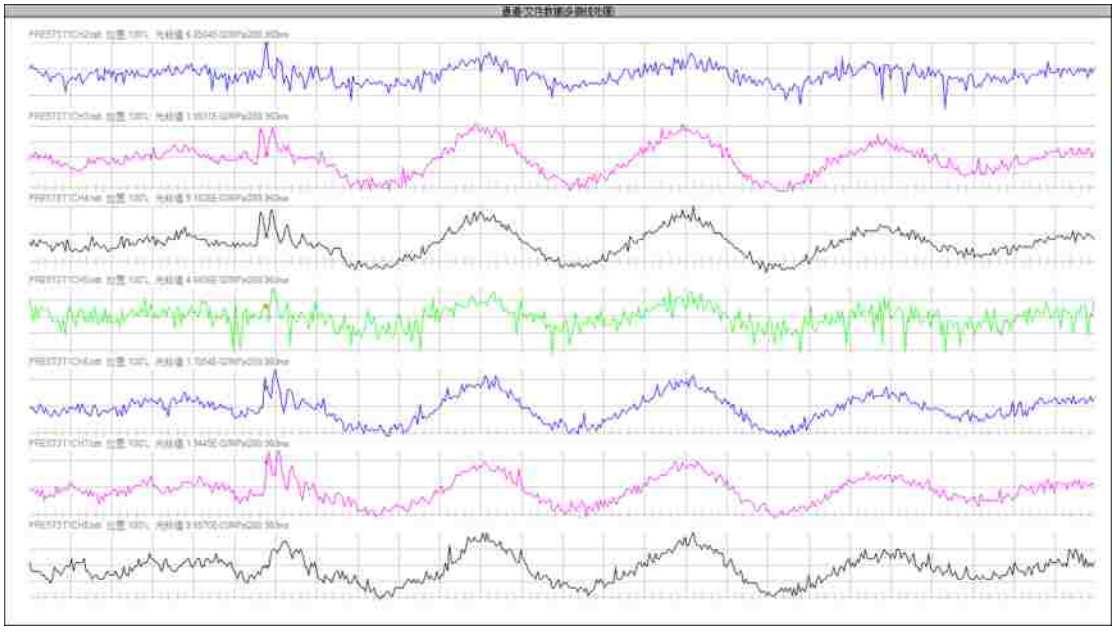

Figure 3.4. Raw data of overpressure for #2 methane explosion test, 8%

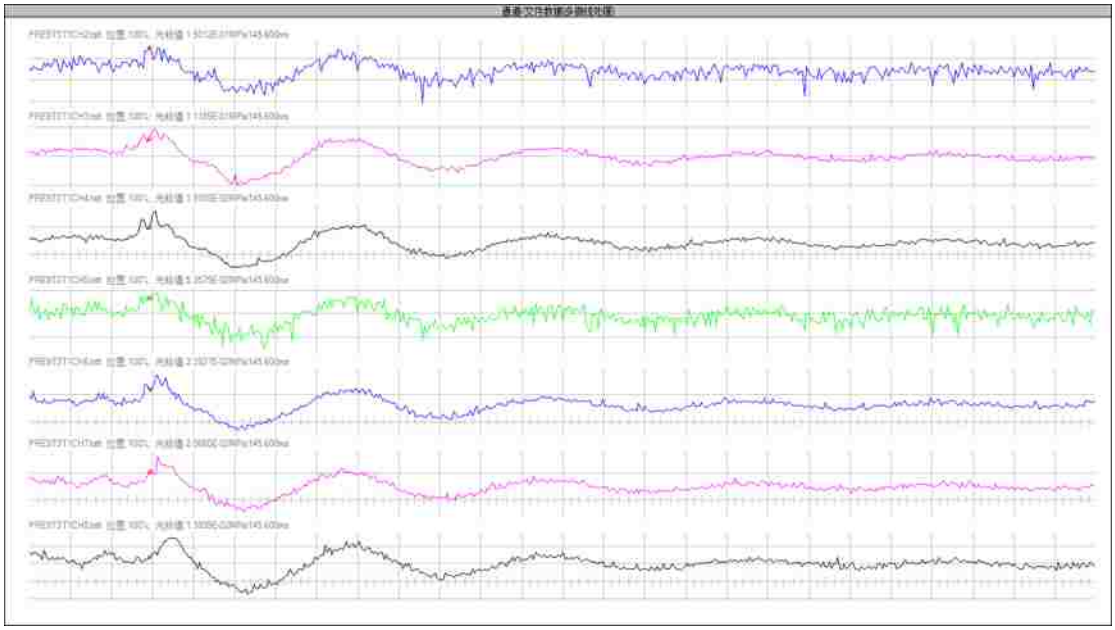

Figure 3.5. Raw data of overpressure for #3 methane explosion test, 9.5%

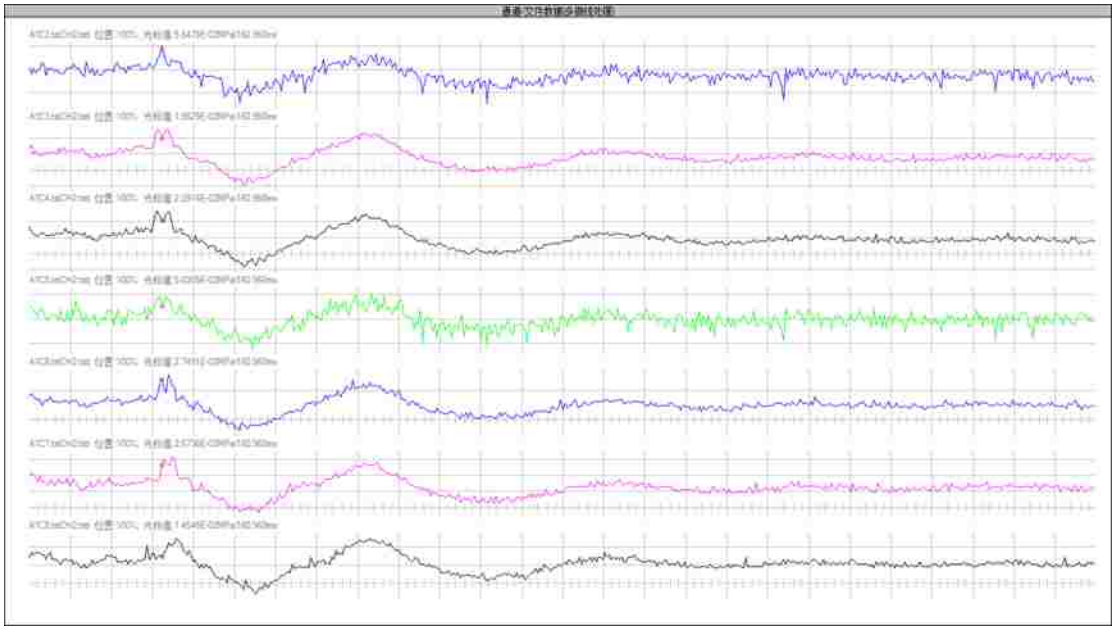

Figure 3.6. Raw data of overpressure for #2 methane explosion test 12%

As Figures 3.4 to 3.6 illustrate, in a comparison between the three concentration levels, faster wave propagation and earlier blast-wave arrival were observed in the 9.5% case compared to the 8% and 12 % cases. However, the 8% and 12% cases have a higher peak overpressure compared to the 9.5% case. Furthermore, because Channel 1 is used to initialize the data capturing, Channel 2 which is located closer to explosion source was observed to have the highest level of reporting among all channels. Thus it will be used to validate the selected numerical models in the corresponding location for future models. In all tests, the overpressure values were adjusted by subtracting their arithmetic mean, in order to eliminate the background noise and systematical deviations.

In the experiment, data collected before the eliminations of the background noise and after it are referred to as "global values" and "adjusted values", respectively. These values are shown in Table 3.4. The peak overpressure was recorded when methane concentration are at 8%, and found to be the greatest among the three concentration levels. The peak overpressure recorded in the same setup when methane concentration was equal to 12% is close to that of 9.5%. The result leads to a conflict with Hjertager's 50 m^3 explosion (tube) test and Zhang's 10 m^3 vessel test, which for instance reported that a 12% concentration explosion has lower peak overpressure than both 8% and 9.5% concentration levels (Hjertager, 1984; Zhang et al., 2014). This contradiction might be due to the scale effect of the explosion tube. In smaller tubes such as the one in this experiment, the peak overpressures might be less sensitive to the concentration. The absolute energy difference among the three selected concentrations of the methane/air mixture is relatively small when an explosion occurs in a smaller accumulative volume. This assumption was supported by the observations of simulation results when larger dimensions of a duct were used. The details of simulations will be discussed in Section 4.

Table 3.4. Global and adjusted global values for three concentrations

	8%	9.5%	12%
Global max (Pa)	68,800	158,200	66,700
Global min (Pa)	-26,900	57,900	-32,500
Global mean (Pa)	5,229	98,611	3,593
Adj. global max (Pa)	63,570	59,588	61,887
Adj. global min (Pa)	-32,130	-40,711	-37,313

3.4. INFLUENCE OF GEOMETRIC CHANGES

As stated in Objective (4) of Section 1.4.2, impact of geometric changes on the blast-wave overpressure must be quantified. Experiments have been conducted based on the configuration shown in Section 3.1. A comparison study has been done between numerical results and measured data to validate the numerical code. More scenarios have been examined using numerical prediction. Results of impacts of geometric change on overpressures during an explosion using numerical simulation will be provided in detail in Section 5.

In the geometric change study, only 9.5% level of methane/air mixture was used. The overpressure captured by pressure sensors located both upstream and downstream with a selected set of different geometrical configurations were recorded. In the case of a t-branch configuration (Figure 3.7), methane is ignited at the dead end of a pre-duct. The blast-wave propagates to the location of pressure sensor P12. The arrows in Figure 3.7 demonstrated the direction of the blast-wave propagation. In this case, pressure sensor P12 was assigned to capture the overpressure history upstream of the t-branch. The red block represents the high overpressure region. The overpressure history downstream was recorded continuously by two other pressure sensors, P13 and P14, at two arms of the branch downstream. For the bend, cross-sectional change, and blockage-ratio (BR) cases, only one downstream overpressure sensor was assigned. The locations of all pressure sensors for all other geometrical changes are shown in Appendix A.

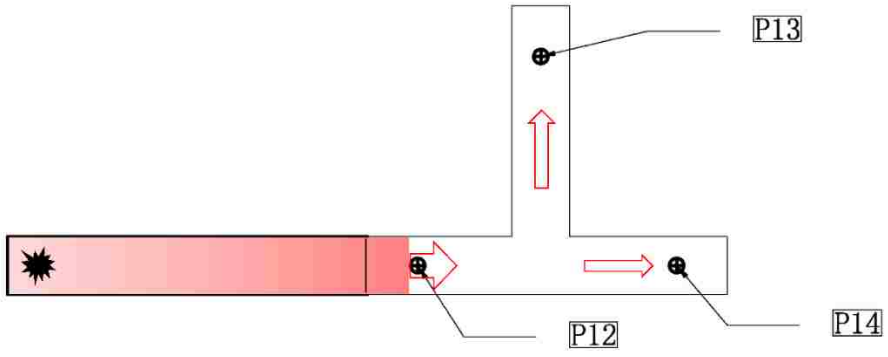

Figure 3.7. Locations of pressure sensor for airway with a t-branching

Attenuation Factor η in Equation 3.2 is used to quantify the influence from these geometrical changes (Jia, Liu, & Jing, 2011).

$$\eta = \frac{\Delta P_0}{\Delta P_1} \tag{3.2}$$

where P_0 and P_1 are overpressures upstream and downstream of a specific geometrical change. The peak overpressures recorded by sensors located upstream and downstream of the selected geometric changes are listed in Table 3.5.

Table 3.5. Experimental and predicted overpressure and Attenuation Factors (Pa/Pa)

	Upstream	Downstream	η
50 °Bending	90,604	50,098	1.726
90 °Bending	43,037	41,284	1.131
120 °Bending	213,920	304,181	0.703
140 °Bending	76,571	85,128	0.945
T-branching	105,899	59,248 (top)	1.615
		103,828 (bottom)	0.998
BR 25%	99,981	90,871	1.1
BR 50%	93,003	70,116	1.326
BR 75%	33,224	18,878	1.759
Cross-section change	73,244	59,439(within expansion)	1.232
		74,458	0.984
*η refers to Attenuation Factor defined in Equation 3.2 BR represents Blockage-ratio			

As shown by the experimental Attenuation Factor (η) for bends in Table 3.5, this factor is observed to be inversely proportional to bending, with ranges between 0° and 120°. The blockage effect is more obvious in smaller angles, and the Attenuation Factor drops below one in bending angles of 120° and 140°, before it increases back to one at 180°. The maximum Attenuation Factor value of 1.726 is observed at a 50° bend, since the blast-wave can hardly go through it, and reflections are also constrained by this geometry.

For obstacles with different blockage ratios (BR), the trend of Attenuation Factor change is simpler than those found in bends, it increases with the BR monotonically. The largest η is 1,759, which is obtained when BR is equal to 75%. The observation suggests that larger blockage ratios tend to attenuate a blast-wave more significantly.

In the case of t-branching, overpressure distributed to the main arm (at the bottom) is higher than the branch arm (on the top) which has a relatively larger Attenuation Factor due to having more energy transported through the main arm than the branch arm. As shown on Table 3.5, the Attenuation Factor downstream of the selected cross-sectional change is 0.984, which is close to one; therefore it does not have notable impact on the propagation of the blast-wave. Further future work investigation needs to be conducted for cases having a larger ratio of the expanded to original area, which is beyond the scope of this research.

Figure 3.8 illustrates the change of the Attenuation Factor with bending angles and blockage ratios, and provides a clear view for the relationship bends and obstacles and their impact on the Attenuation Factor.

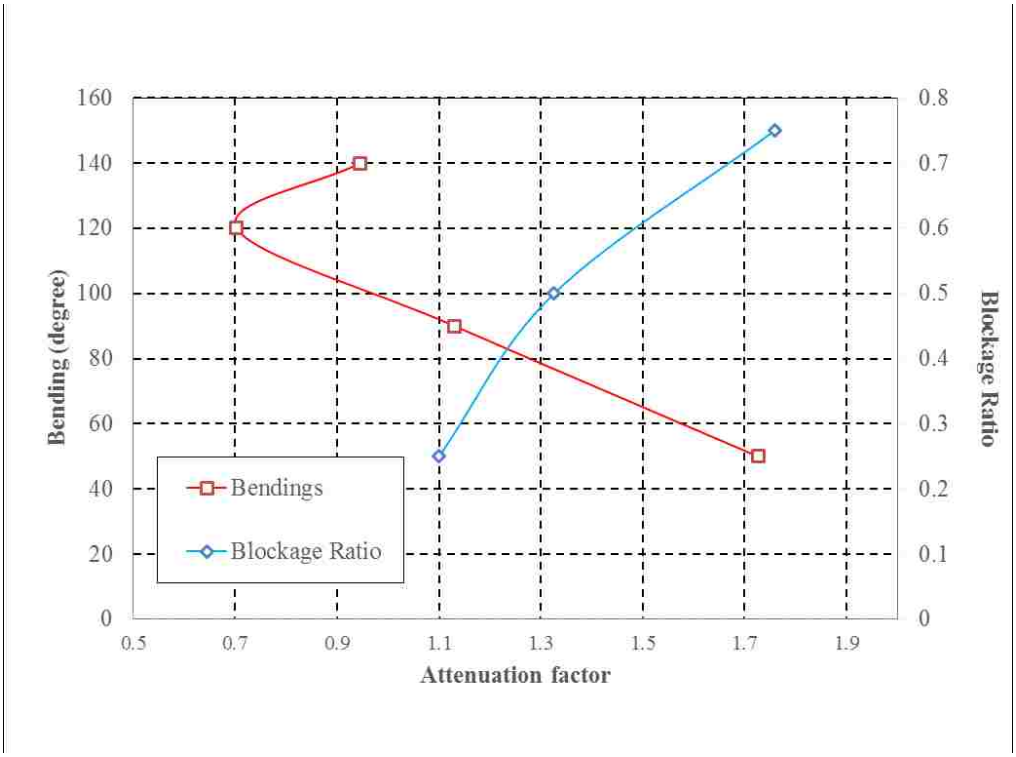

Figure 3.8. Attenuation Factor change with bending angles and blockage ratios

Figure 3.8 suggests smaller bending angle and larger BRs can greater mitigate a blast-wave. The cross point of the two curves implies that a 80° bending angle has an equivalent attenuation effect as an obstacle with 40% area blocked.

3.5. SUMMARY

The maximum overpressure recorded in explosion tube experiments are 63,570 Pa., 59,589 Pa, and 61,887 Pa for 8%, 9.5%, and 12% concentrations, respectively. Note that there are contradictions with Hjertager's 50 m^3 explosion tube and Zhang's 10 m^3 vessel tests at the 12% concentration level. This contradiction might be due to the scale effect of the explosion tube. In quantifying the effect of geometrical changes, four main conclusions are drawn from the discussions in Section 3.4. These conclusions are: (1) Attenuation Factor decreases with the angle of bend, ranging between 0° and 120° and increases close to one at 140°;. The maximum Attenuation Factor is obtained when bending is 50° with a value of 1.726, and the minimum is obtained at 120° with a value of 0.703; (2) in t-branching, overpressure distributed to the bottom branch is higher than the top branch; (3) Attenuation Factor increases with BR for obstacles; (4) cross-sectional change has an insignificant impact on the propagation of blast-wave.

These experiments have been conducted to validate the numerical models. The same results presented in this section will be revisited in the following three sections.

4. NUMERICAL MODELING IN DRIVER SECTION

4.1. INTRODUCTION

For effective network-based modeling, an explosion source database is highly recommended. The database must include overpressure histories and blast-wave arrival time under a wide range of explosion site conditions. In the *driver section*, two major factors that characterize an explosion site are the methane concentration and the geometry of a gas-filled region. Scenarios with three selected methane concentrations and forty different geometries for each concentration of the gas-filled region are investigated.

The governing equations of the driver section introduced in Sections 2.2, 2.3 and 2.4 are used to conduct the numerical simulations. In this Section, both spatial and temporal discretization of the selected governing equations will be introduced. The applied numerical models, namely, turbulence and combustion models were also validated by the experimental results introduced in Section 3 when a methane explosion falls in the deflagration range. A set of literature data was used to validate the numerical model used for methane detonations. After the validations, the selected numerical models were utilized to provide predictions of methane explosions for different methane concentrations and accumulation geometries. The simulation results will be demonstrated in Section 4.4.

4.1.1. Contributions of Turbulence and Combustion. The driver section consists of a gas-filled section and the part of the blast-wave propagation region where flames can reach (refer to Figure 2.1). In this current research, the driver section was isolated from other sections due to its complexity of turbulence fluid dynamics and chemical reactions. As introduced in Section 2.2, the dynamics of the reactants and products in the driver section are governed by three conservation laws, namely, conservation of mass, momentum, and energy. To account for turbulence and combustion phenomena, turbulence and combustion models are needed in addition to the basic conservation equations, all of which have been described in details in Sections 2.3 and 2.4.

Turbulence has two opposite effects on the combustion rate. The first effect is that turbulence could facilitate the mixing of fuel and air while enlarging the total reaction

and the contacting face area, which, in turns increases the combustion rate. The second effect referred as turbulent quenching, is the shear stress generated by turbulence that could quench the flame when combustion rate or reaction rate are relatively low. The size of the *reaction zone* has great impact over turbulent quenching. The quenching effect is less significant in larger scale explosions since a smaller strain rate will be generated (Catlin, 1991). In this research, the quenching effect only appears in a few extreme cases when the combustion rate of the selected scenarios is high enough to sustain combustion.

Combustion also plays a key role when simulating a methane explosion in the driver section. Section 2.4 introduced a combustion formulation based on premixed and general assumptions where the fuel and air are perfectly mixed before ignition; but caution should be taken when using these two models as they are based on a simplified one-step chemical reaction formula. The elementary chemical reaction formula consists of thirty-two steps which is too complicated to be used in numerical simulation directly (Zhen & Chow, 2006). To apply the combustion model appropriately, the following simplified one-step formula is used:

$$CH_4 + 2O_2 = CO_2 + 2H_2O \tag{4.1}$$

A total of 891 KJ of heat is generated in the combustion of 1 mole of CH_4. The heat generation will be accounted for by the source term S_h in the Equation (2.3).

4.1.2. Averaged Flow Variables. Turbulence is a highly transient phenomenon, thus the flow parameters are highly unstable with the respect of time. Averaged variables are used for the turbulence flow modeling throughout the analysis. In Equations (2.1) to (2.3), scalar and vector variables are substituted with three main types of averaging operations depending on the turbulent formulation used.

For the standard *k-ε* model, time averaged variables are used. The expression of a time averaged value is shown as Equation (4.2).

$$\bar{\phi}(x) = \frac{1}{\Delta t}\int_{\Delta t} \phi(x)\, dt \tag{4.2}$$

where $\bar{\phi}$ represents time-averaged variables (ϕ can be any fluid variables). Δt is the increment of time which normally expressed as time step size in numerical calculations.

For Large-Eddy-Simulation (LES) model, filtered variables are used which have universal form as (Tannehill, Anderson, & Pletcher, 1997):

$$\bar{\phi}(x) = \frac{1}{V}\int_V \phi(x_{SGS})\, dx_{SGS} \tag{4.3}$$

where x_{SGS} represents Sub-Grade values. V is the volume of the filter size which is the mesh size for the Finite Volume Method (FVM) used by *ANSYS Fluent*.

When considering a compressible flow field as in the driver section, Faver-averaged values, $\widetilde{\phi}$ can simplify in a numerical formulation process and can be expressed as a filtered or time-averaged of the product of density and a flow variable divided by the filtered or time-averaged value of the density expressed as below (Anon, 2011):

$$\tilde{\phi} = \frac{\overline{\phi\rho}}{\bar{\rho}} \tag{4.4}$$

where $\bar{\phi}$ is time-averaged or filtered value expressed in Equation (4.2) or (4.3)

In the following sections, the time-averaged Faver-averaged flow variables will be used for standard *k-ε* modeling and the Filtered Faver-averaged variables will be applied in LES modeling.

4.1.3. Numerical Tool. *ANSYS Fluent* is selected as the CFD package for the simulations in the driver section. *ANSYS* is an engineering simulation software company located in Pittsburgh, Pennsylvania, founded in 1970. *ANSYS* acquired *Fluent* Inc. in 2006 and integrated it into *ANSYS* code package. *ANSYS Fluent* contains multiple physical modeling modules are capable of simulating turbulence, heat transfer, and chemical reactions. The cortex version used in this research is *ANSYS 14.5.0* released in September, 2012.

ANSYS Fluent has been widely used in the aerospace industry, engineering design, and the energy/safety disciplines (Anon, 2012). It can provide abundant turbulent and chemical reaction subroutines and sophisticated User Defined Functions (UDFs) based on the popular *C language*. In a flow modeling process, the definition of the initial or boundary conditions are highly flexible. Varying the spatial and temporal discretization methods are also part of *ANSYS Fluent* features. The software is stable and robust with sophisticated advancing algorithms.

ANSYS Fluent has also been used in the numerical study of geometrical change influences in Section 5. However, *ANSYS Fluent* does not support the one-dimensional (1D) modeling that is used in simulations of a blast-wave section. A 1D CFD code *flowmaster* is selected for the one dimensional study instead.

4.2. NUMERICAL DETAILS

4.2.1. Discretization. The solution of governing equations requires both temporal and spatial discretization processes, which are discussed in details in the following sections.

4.2.1.1 Meshing. The spatial discretization (meshing) process is accomplished by a pre-processing tool called Gambit, the graphing platform of *ANSYS*. As the base geometrical model, a duct with dimensions of 4.25 m in length and 0.08 m by 0.08 m cross section is used with both Gas-fill Length Scaling Factor (FLSF) and Hydraulic Diameter Scaling Factor (HDSF) are equal to one, Figure 4.1 represents the base geometric model for this study.

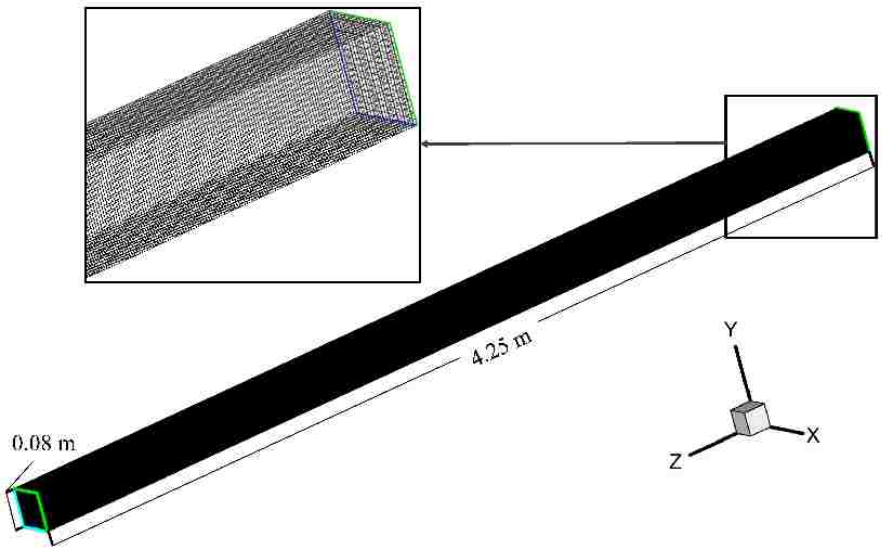

Figure 4.1. Mesh of the geometrical model of base case

Resolution analysis on the base case (FLSF=1 and HDSF=1) under the methane concentration of 8% was conducted to investigate the influence of the mesh size to the predicted overpressures. The mesh with cells size of 2 mm width is assumed to give the most accurate prediction, with the relative error equal to zero. This mesh size is the highest mesh density among all selected and tested meshes. The relative error is expressed by the following statement, $2(P - P_0)/(P + P_0)$; where P and P_0 are the predicted peak overpressures of coarsened meshes (cell width of 4 mm, 6 mm, 8 mm, and 16 mm) and the mesh cell width of 2 mm, respectively. Compared to the mesh with cells of 2 mm width, the relative error is found to increase as the cell number decreases.

Table 4.1 illustrates the comparison of the mesh size and its cells number versus the relative errors. The mesh with 4 mm cell width has a relative error of 4% and a lower cell number compared to the finer mesh (2 mm). Thus, the 4 mm cell width mesh is selected for the analysis. The selected meshed geometrical model shown in Figure 4.1 has 245,939 nodes and 217,600 hexahedral cells. As the FLSF or/and HDSF increase or decrease, the relative mesh size will not change, and the error is proven to be acceptable up to the scale of 1:100 in both longitudinal and horizontal directions (Zhang, Pang, & Zhang, 2011). The mesh dimensions change with scaling factors; e.g. for a geometry with FLSF equals 2 and HDSF equals 4, the mesh size will be 0.8 mm by 1.6 mm by 1.6 mm. The combined effect of eight HDSFs (1, 2, 4, 8, 16, 32, 64, and 100), and five HDSFs (0.5, 1, 2, 4, and 8), were investigated and will be introduced in Section 4.4.

Table 4.1. Influence of cell size on simulation result

Width of Cell (mm)	2	4	6	8	16
Cell Size (mm^3)	8	64	216	512	4,096
Number of Cells	1,740,800	217,600	119,652	53,100	6,650
Number of Nodes	1,852,389	245,939	138,964	64,372	9,612
Relative Error (%)	0	4	28	85	138

4.2.1.2 Time step size. Since methane explosion is highly transient, the time step size must be investigated. Figure 4.2 shows the peak overpressure and the time step size relationship of explosions with the 9.5% methane concentration level that occurred in the base model. In these calculations, twenty iterations were assigned per time step and the residuals are averaged at e^{-5} level.

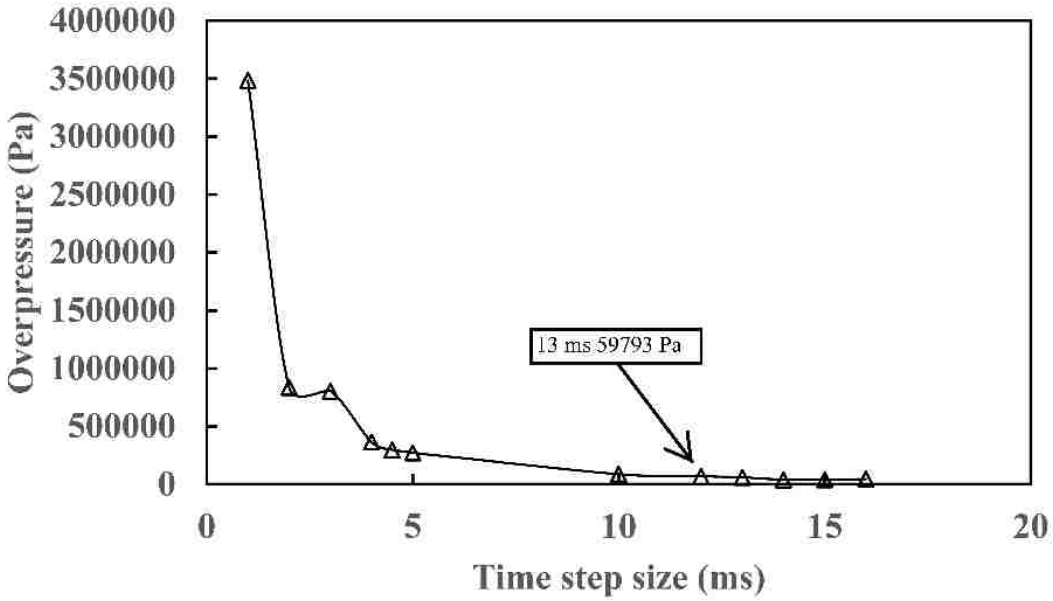

Figure 4.2. Time step size analysis

As observed in Figure 4.2, the peak overpressure decreases monotonically as the time step size increases. The peak overpressure starts to stabilize when the time step size approaches 13 ms. The Courant-Friedrichs-Lewy number ($CFL = \Delta tu/\Delta x$; u is the characterastic flame speed) is around 1.3 for the base case; when $\Delta t = 0.013\ sec$. During modeling of the driver section, the numerical solutions are unconditionally stable since an implicit temporal discretization scheme is used (Tannehill, Anderson, & Pletcher, 1997). In addition, the converged peak overpressure prediction is in agreement with experimental result under the same scenario.

4.2.2. Numerical Details. To simulate methane deflagration in the driver section, the numerical solver *ANSYS Fluent* (Cortex Version 14.5.0) was used. Smagorinsky-Lily LES model and C-equation model were adapted as the turbulence and combustion models, respectively, based on comparison studies detailed later in Section 4.3. For the governing equations, bounded central-difference scheme was used in the convection term and second order upwind scheme was applied in the diffusion terms. SIMPLE velocity/pressure correction method was incorporated and least squares cell based scheme was used for gradient treatment in the deflagration cases. On the other hand, the presence of turbulence can be safely neglected in the detonation cases (Escanciano, et al., 2011). Instead, phenomena as blast-wave generation and propagation are critical for the analysis. The detonation scenarios, which have peak overpressure greater than the calculated CJ-detonation overpressure, will be calculated using the compressible solver with explicit time matching. The detonation modeling is similar to deflagration model except the absence of the turbulence factor and the change of temporal discretization approach.

In addition, the computers used in this research are INTEL quad-core i7 3770K and 16 Gb raw. Eight parallel processes were used for *ANSYS Fluent*. The residuals in this part of numerical study after 800 iterations for the continuity equation, x-velocity, y-velocity, z-velocity, and C-equation (progress variable) are in e^{-2}, e^{-4}, e^{-4}, e^{-4}, and e^{-3} levels, respectively. The residual of the continuity equation is relatively high because there is a closed end to the geometry. Reversed flow is observed on the open boundary, which is connected to the atmosphere.

4.3. BENCHMARCH OF SUBMODELS AND VALIDATION

4.3.1. Benchmark of Turbulence Models. The scenarios with the base geometric model were validated by experiments where the experimental instruments have been described in details in Section 2. The customized experimental system for turbulence model validation in the driver section is shown in Figure 4.3. The system consists of five main parts: igniter, main explosion duct without geometric change, gas bag, pressure sensors, and a data collection system. Note that the study of geometric changes will use the same system with geometric change components installed at the vent (outlet).

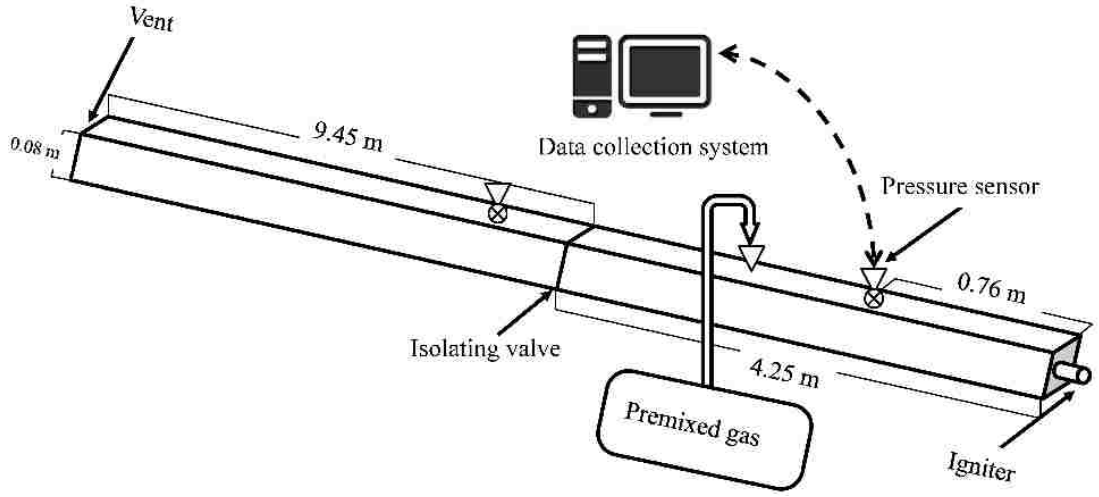

Figure 4.3. Schematic of the methane explosion experiment system (Not to scale)

Experimental results could be helpful in the selection process of an appropriate turbulence model for methane explosion simulations. The governing equations used for each turbulence model were introduced in Sections 2.2 and 2.3. Proper peak overpressure, impulse arrival time, and duration of impulse were selected as criteria to evaluate the turbulence models (Makarov, Verbecke, & Molkov, 2011; Zhou, Xu, & Xu, 2012). A record of actual overpressure history at a scaled distance (distance from ignition source to divide diameter) of 9.5 was used to compare with the predicted results using different turbulence models.

Figure 4.4 illustrates the comparison of overpressure histories predicted by the standard k-ε, LES model combined with the C-equation combustion model and Zimont turbulent flame speed, which is the default premixed combustion model for *ANSYS Fluent*. The simulation results were compared to the filtered experimental results by a 2 KHz signal filter.

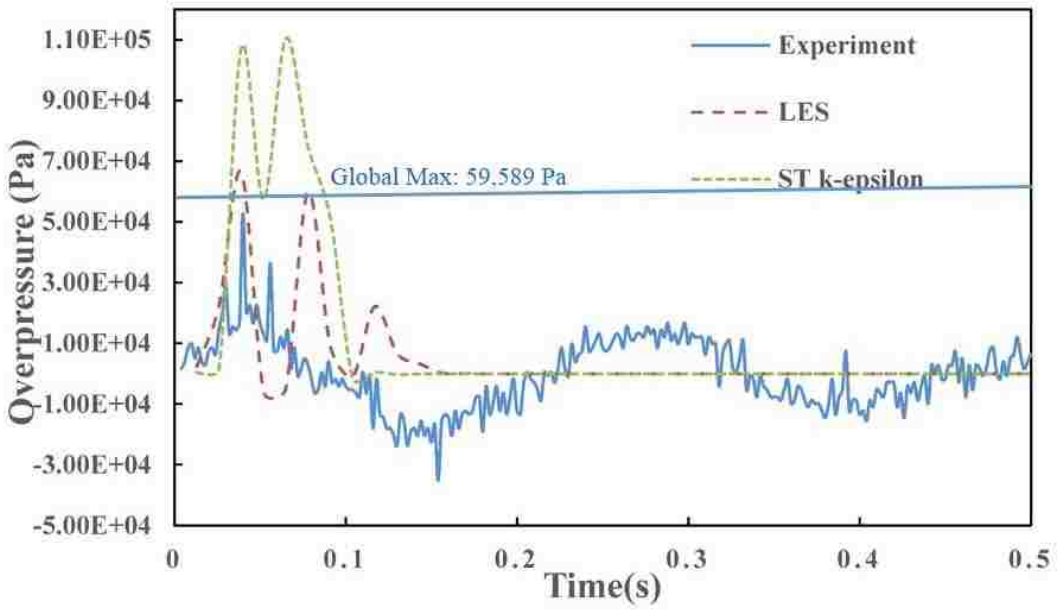

Figure 4.4. Overpressure histories at D/L of 9.5 from ignition source using selected turbulent models, data shows the comparison of overpressure histories of experimental results and two selected turbulence models

The filtered experimental results are used to demonstrate the wave arrive-time and shape. The global maximum overpressure was used for comparison purposes and shown as a blue horizontal line in the figure above. As clearly shown, the LES model gives a better prediction than standard *k-ε* model. This could be due to the inherent drawback for time-averaged turbulence models to resolve a highly transient flow and the requirement of resolving boundary layer is more stringent in the standard *k-ε* model than the LES model (Sarli, Benedetto & Russo, 2010). A finer boundary layer mesh for the *k-ε* model could help increasing the prediction accuracy; but as a tradeoff, it would be computationally expensive. Both the standard *k-ε* model and the LES model failed to resolve the negative phase and the instabilities after the main impulse. The LES model provides a predicted peak overpressure of 63,553 Pa compared to 59,663 Pa in the experiment; a difference of around 7%. The LES model also gives a reasonable prediction of arrive-time of overpressure impulse. However, an approximate 30% relative error was found in predicting the duration of the positive phase by comparing experimental and prediction data using the LES model. According to the comparison

analysis, the LES has a better performance on both the peak overpressure and the arrival time than the standard k-ε model. As a consequence, the LES model will be applied in future studies throughout this research.

In the Moureaua, Fiorinab, and Pitscha's study (2009), the LES model was also proven to have a better prediction on flame structures. Figure 4.5 provides the static temperature contours of 9.5% methane explosion using the LES model. The flame propagating away from the ignition source is clearly shown as time advances. The flame front is irregular at the developing regime and becomes almost fully-developed toward the far end of the domain.

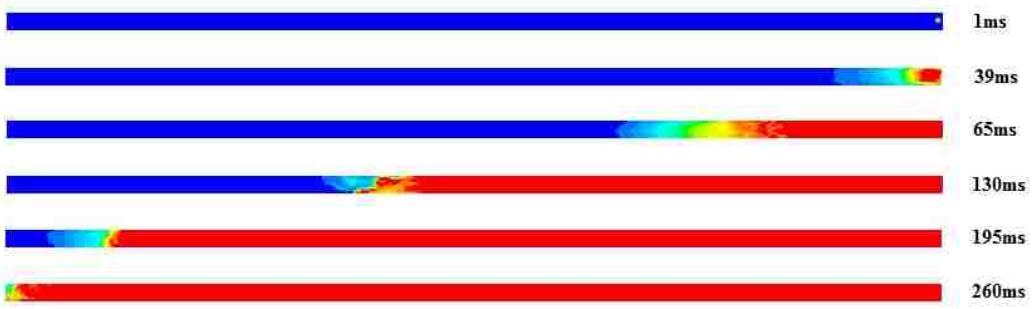

Figure 4.5. Propagation of flame in explosion tube for 9.5% methane using LES model data shows the evolution of the flame through the explosion duct in different time instants

4.3.2. Benchmark of Combustion Models. The governing equations of selected combustion models were introduced in Section 2.4. In this section, the premixed models C-equation and G-equation describing a gas chamber with premixed methane/air mixture combined with Peters and Zimont's turbulent combustion formulations were compared. In addition, another process-variable-based combustion model called Extended Coherent Flamelet Model (ECFM) was also used. ECFM is theoretically more accurate than the C-equation and G-equation models but less robust, which is more difficult to converge. The transport equation of ECFM model is shown as:

$$\frac{\partial \Sigma}{\partial t} + \nabla \cdot (\vec{v}\Sigma) = \nabla \cdot \left(\frac{\mu_t}{S_{ct}} \nabla \left(\frac{\Sigma}{\rho} \right) \right) + (P_1 + P_2 + P_3)\Sigma + P_4 - D \quad (4.5)$$

where Σ is mean flame area density, P_1 is source due to turbulence/flame interaction, P_2 is source due to dilatation in the flame, P_3 is source due to expansion of burned gas, P_4 is source due to normal propagation, and D is flame dissipation area (Candel & Poinsot, 1990).

Turbulent flame speed is required to be modeled by both C-equation and G-equation for the premixed combustion models. The Zimont model is the default option of *ANSYS Fluent*. Turbulent flame speed in the Zimont model is calculated as (Zimont, et al., 1998):

$$U_t = A(u')^{3/4} {U_l}^{1/2} \alpha^{-1/4} {l_t}^{1/4} \quad (4.6)$$

where A is a model constant, u' is root-mean-square (RMS) velocity, $\alpha = k/\rho c_p$, and l_t is turbulent length scale equals to $C_D\ (u')^3/\varepsilon$.

The Zimont turbulent flame speed can be substituded into the transport equations for both C-equation and G-equation models. The comparison of overpressure hsitories among the five premixed combustion schemes are demonstrated in Figure 4.6. As was also found in the comparison study of turbulence models, overpressure is recorded at length to diameter (L/D) scaled distance of 9.5 (m/m) from ignition source. A 9.5% methane concentration level and 100J ignition energy are used.

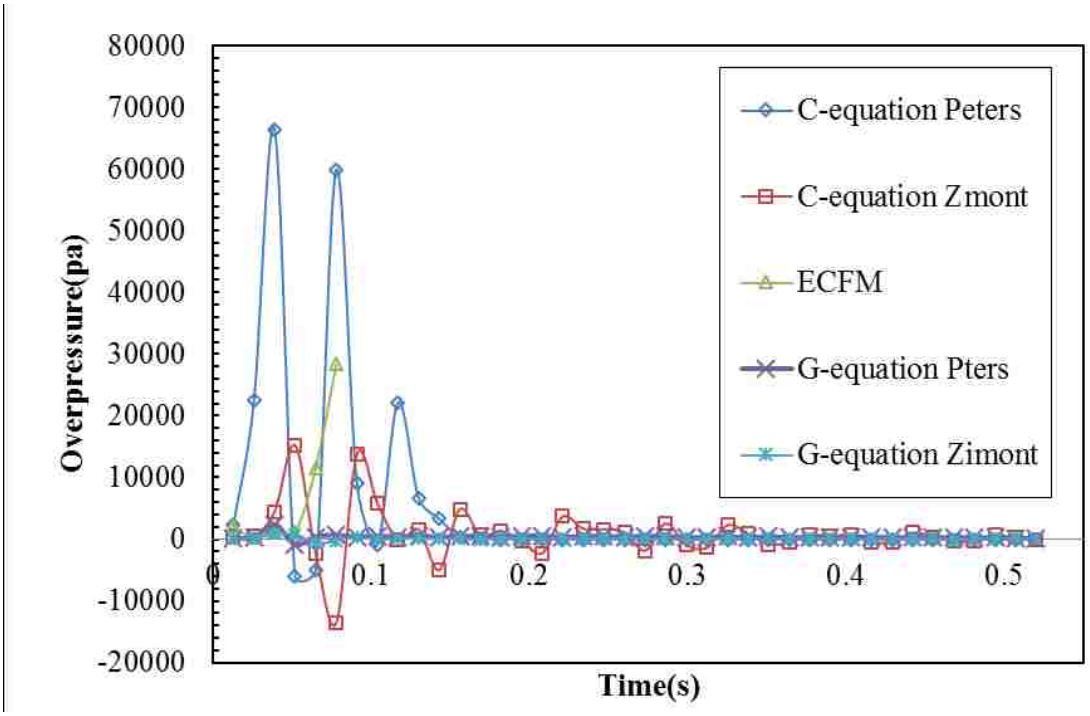

Figure 4.6. Overpressure histories at D/L of 9.5 from ignition source using selected combustion models

Figure 4.6 illustrates that the C-equation model combined with the Peters turbulent flame speed provides the best prediction of the peak overpressure which is the closest to the measured value of 59,589 Pa. At the given initial and boundary conditions, models using the G-equation significantly underestimates the peak overpressure while ECFM model diverged after around 0.08 sec. ECFM and G-equation did not perform as well as the C-equation model using the selected spatial or temporal discretization. As a result, C-equation combined with Peters turbulent flame speed provided a prediction with reasonable accuracy (within a 10% range) and will be used in this study.

4.3.3. Validation of Detonation in a Large Scale Explosion. For the scenarios with peak overpressure lager than CJ-detonation overpressure, the Finite-rate chemical reaction solver was employed because of the limitation of the premixed combustion models which should not be used in modeling detonation (Anon, 2011). The LES turbulence model and Eddy-break-up combustion model introduced in Sections 2.3.2 and 2.4.1 were used instead.

Another objective for this research study was to investigate the performance of the selected numerical models in large scale explosions; therefore, literature with experimental results from a large scale experiments with detonation cases were chosen. The literature data was collected from experiments conducted by NIOSH (National Institute of Occupational Safety and Health) at the Lake Lynn Laboratory (Zipf, et al., 2010). The detonation tube used in the experiment was cylindrical with 73 m long and 1.05 m in diameter. One end of the tube was closed. The test gas was 97.5% methane with about 1.5% ethane. Thirty-eight methane concentrations ranging from 4% to 19% were tested. The experimental layout with baffles (GETF system) is shown in Figure 4.7 (Zipf, et al., 2013).

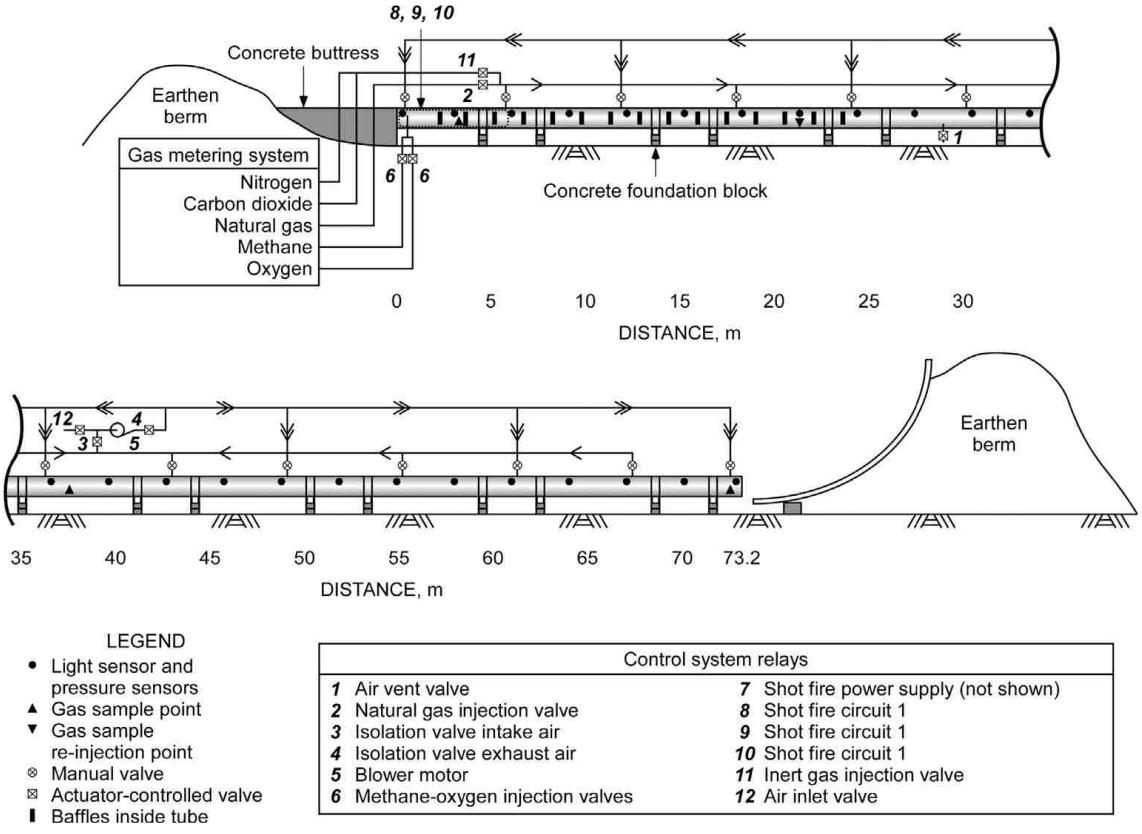

Figure 4.7. Schematic of GETF with baffles (Zipf, et al., 2013)

A numerical model with the same dimensions and baffle layout was developed to evaluate the behavior of the Euler Solver without considering the effects of fluid viscosity terms in the governing equations. These terms were used to predict the detonation scenarios with greater peak overpressures than CJ-detonation overpressure. The meshed geometric model based on the LLL GETF system was developed shown in Figure 4.8. A total of 15 transverse baffles are present in the model as shown inside the explosion tube.

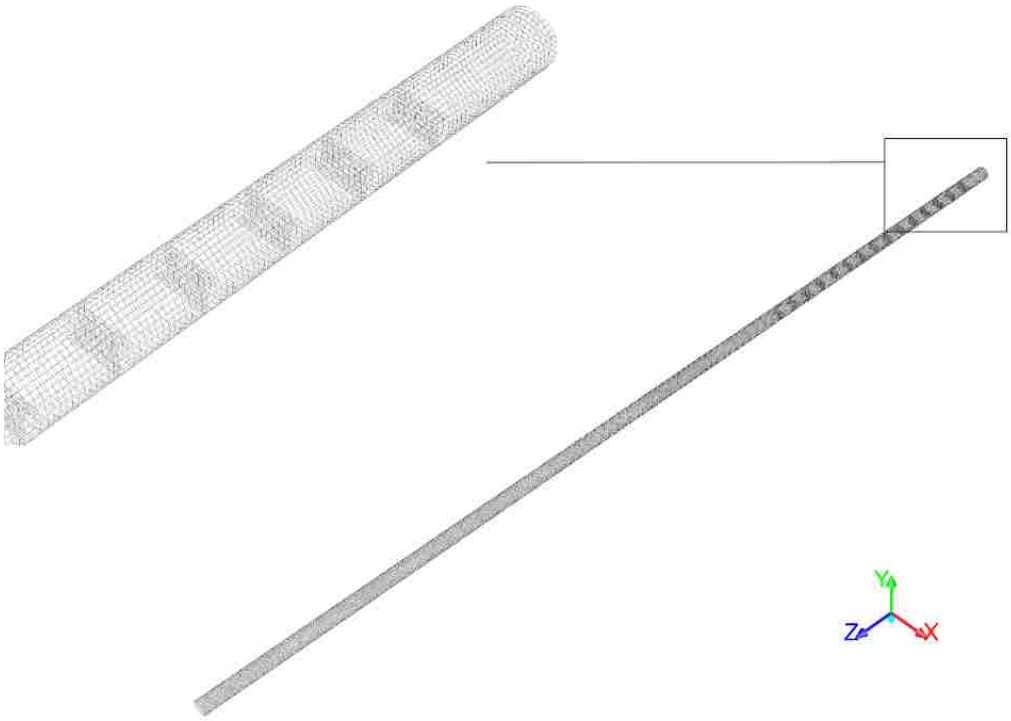

Figure 4.8. Geometric model and mesh for LLL detonation test

When conducting a methane detonation simulation, the initial computational field used laminar flow with a finite-rate-laminar (FRL) combustion closure based on Arrehenius Chemical Reaction Rate theory, as required. Since FRL is only used to calculate an initial field, its theoretical details are beyond the scope of the analysis and will not be stated. The formulations can be referred to in Section 5.1.5 of the book:

Computational Fluid Mechanics and Heat Transfer (Tannehill, Anderson, & Pletcher, 1997).

The simulated propagation of flames along the explosion tube is shown in Figure 4.9:

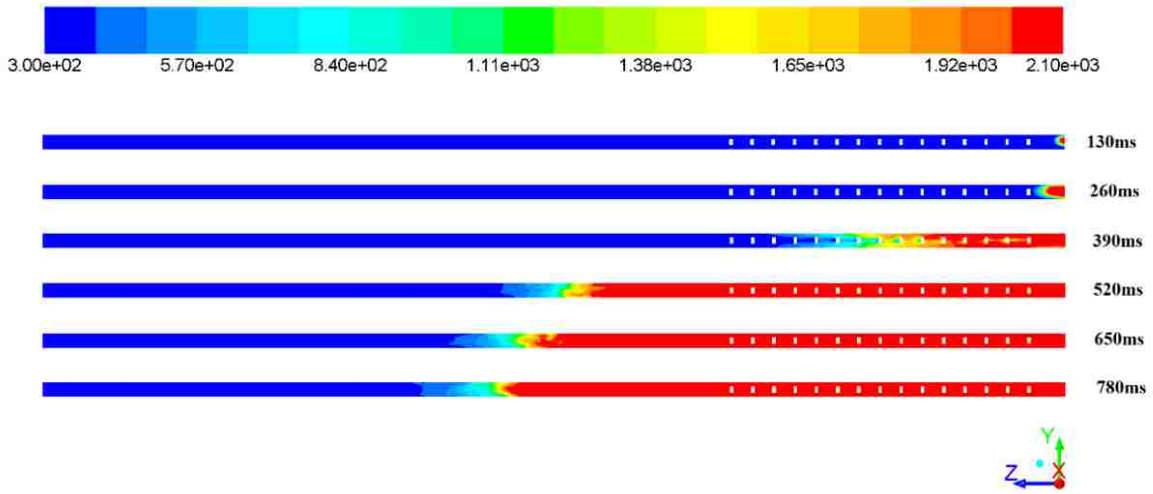

Figure 4.9. Flame propagation in the explosion tube in different time instants

As shown in Figure 4.9, the flame speed is relatively slow at the beginning, with acceleration starting after 260 ms (milliseconds) and then slowing down again after 520 ms. Acceleration is due to the turbulence generated by the baffles which wrinkle the flame, increase the reaction surface area, and therefore accelerate its propagation. This effect disappeared after the flame front had gone through the baffle area. The impact of baffles on the flame propagation can be shown more clearly in Figure 4.10:

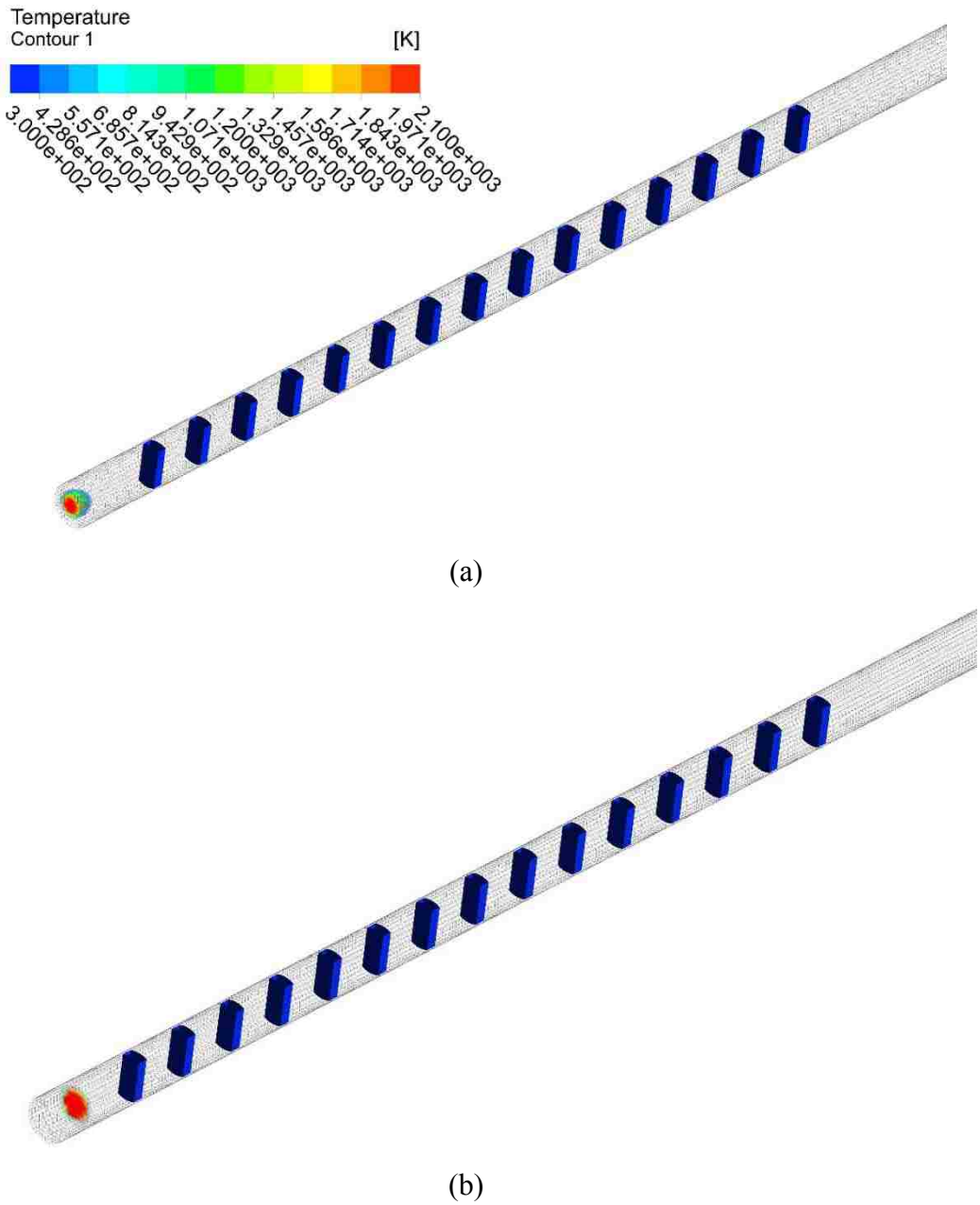

(a)

(b)

Figure 4.10. Effect of baffles on flame propagation at (a)130 ms, (b) 260 ms and (c) 390 ms

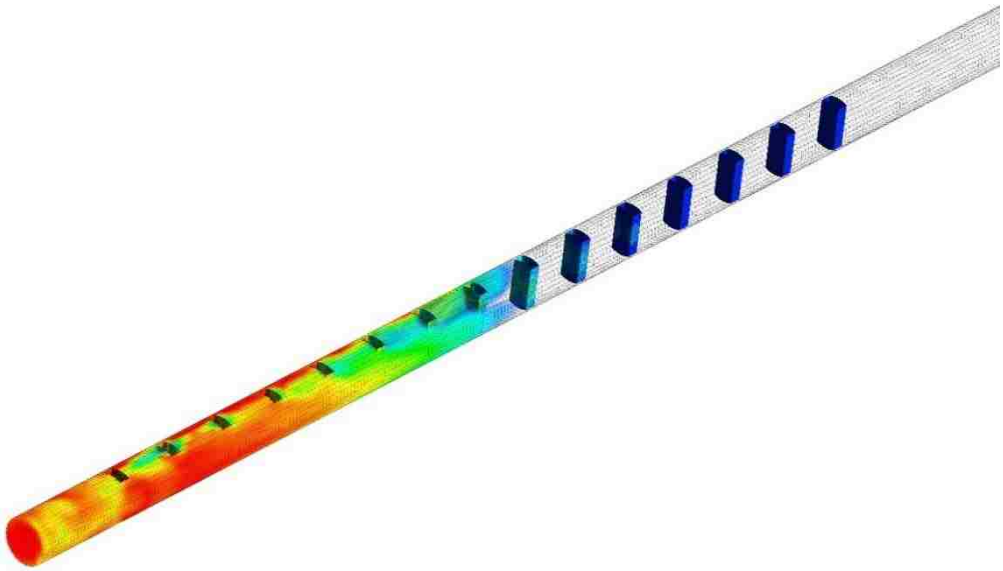

(c)

Figure 4.10. Effect of baffles on flame propagation at (a)130 ms, (b) 260 ms and (c) 390 ms (cont.)

Figure 4.11 illustrates the comparison overpressure history between the LLL experimental and predicted values immediately after the fifteenth baffle.

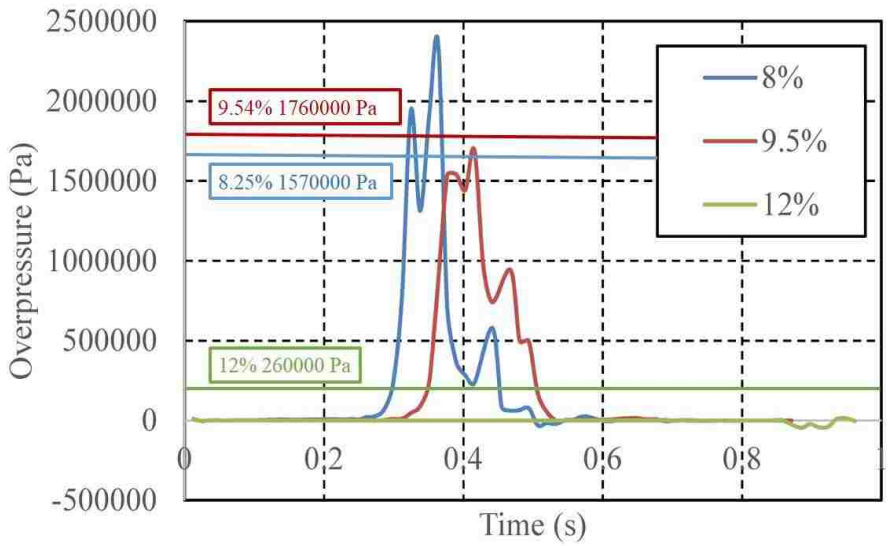

Figure 4.11. Comparison between simulation and LLL experiment, three horizontal lines represent peak overpressure measured in LLL experiments at three methane concentrations

In Figure 4.11, three horizontal lines in red, blue, and green represent peak overpressure measured in LLL experiments at 9.54%, 8.25%, and 12%, respectively. Three curves with the corresponding colors represent the predicted overpressure histories. A comparison study between the peak of the curves and the measured peak values are preceded. It can be observed that the predicted peak overpressure (the peak of red curve with 1,690,628 Pa) has an excellent agreement with the LLL experiment result (1,760,000 Pa) for the 9.5% case and the relative error is 3.9%. With a methane concentration of 8%, however, a relative error over 30% is detected by comparing the peak of blue curve and line in Figure 4.11. The experimental value around 8% of methane explosion is more unstable, a peak overpressure as high as 7.6 MPa was obtained under 8% and 8.8% when blockage ratio of baffles equal to 25%. In these two cases, sustainable detonations other than normal detonation were triggered. However, this trend is in agreement with Hjertager's and Zhang's experiments (Hjertager, 1984; Zhang, et al., 2014) in which explosions with 8% methane have a greater peak overpressure than the 9.5% methane concentration. In the LLL test, scenarios were not repeated for a same configuration. A higher peak overpressure could be obtained closer to the predicted value for 8% methane. In the 12% case, detonation failed to be triggered in all LLL tests and simulation cases. All experimental tests and simulations are in deflagration regime. In the LLL test, the peak overpressure reached as large as 0.26 MPa while the predicted maximum value was 0.0137MPa. This suggests the weakness of Eddy-break-up model to simulate a deflagration. As a result, all scenarios under deflagration are simulated using premixed combustion models in Sections 4.2 and 4.3.2.

4.4. SCALING EFFECT

To develop an explosion source database, a reasonable range of geometric dimensions in an explosion site is necessary. In this section, the scale effect of the driver section of an explosion tube is simulated using the LES turbulence model combined with the premixed C-equation model for deflagration cases and the EDM combustion model for detonation cases. Meanwhile, three representative methane concentrations, 8%, 9.5%, and 12%, were selected to examine the combined effect of scale and concentration which are considered as the two major factors affecting methane explosion.

4.4.1. Introduction. Methane explosion incidents could occur in both unconfined space, such as combustion due to flammable gas leakage; and confined spaces, such as an inner-combustion in process equipment or in underground airways. The destruction of a confined gaseous explosion is much greater than the destruction of explosions in an unconfined space. According to Catlin's research, the size of a confined space has significant impacts on the explosion strength and explosion characteristics (Catlin & Johnson, 1992). Research pertaining the scaling effect of an explosion site is therefore necessary. In addition, the experimental study on explosions with large scale parameters would be costly and dangerous. Numerical methods and lab-scale studies are effective and viable alternatives. However, whether the lab-scale experiments results still hold for larger scales must be investigated. CFD is a sophisticated technique to evaluate such scaling effect on gaseous explosions, and it has already been applied extensively in other studies, especially on hydrogen combustion which has a higher reactivity than does methane (Bauwens, Chaffee, & Dorofeev, 2002; Kindracki, et al., 2007).

Efforts have been made to investigate the scale effects of gaseous explosions. In Van Wingerden's work, scale effect is related to the normalized flame speed. However, the relationship breaks when turbulence is incorporated (1989). Catlin and Johnson (1991, 1992) were looking for feasibilities to compensate the scale effect by enriching the oxygen component of air in their experiments. The results are theoretically correct when the turbulence Reynolds number is less than 10,000, which is often not the case in practical problems. Zhang, et al., tested the scale effect on methane explosion using a CFD commercial package *AutoReaGas* in which three scales (1:1, 1:10, and 1:100) were tested (Zhang, Pang, & Zhang, 2011; Zhang, Pang, & Liang, 2011). Therefore, there is a need to further study the scaling effect for scenarios of lower longitudinal to horizontal ratio. This research provided a wider range of geometries and shed some light on the scaling effect on DDT with all three selected methane concentrations (8%, 9.5%, and 12%). The Gas-fill-length Scaling Factor (FLSF) and Hydraulic Diameter Scaling Factor (HDSF) were used to adjust dimensions of an explosion site in longitudinal and horizontal directions, respectively. The FLSF represents the factor equals to the gas-fill length tested divided by the base model, which is 4.25 m. Similarly, HDSF is the factor equal to the tested hydraulic diameter divided by the base model, which is 0.08 m. The

results of methane explosion simulations with all FLSF-HDSF combinations for each methane concentration are demonstrated in the following sections below.

4.4.2. Results and Discussion - 9.5% Concentration. The first methane concentration analyzed was the 9.5% level which represents the stoichiometry of a methane/air reaction. Peak overpressure/time relationships at the scaled distance of 9.5 for the combinations of eight HDSF (1, 2, 4, 8, 16, 32, 64, and 100) and five FLSF (0.5, 1, 2, 4, and 8) with a methane concentration of 9.5%, were tested and will be presented and discussed in details below.

4.4.2.1 FLSF. Peak overpressures for FLSFs equal 0.5, 1, 5, 4, and 8 when combined with eight HDSFs in a logarithmic coordinate system are shown in Figure 4.12.

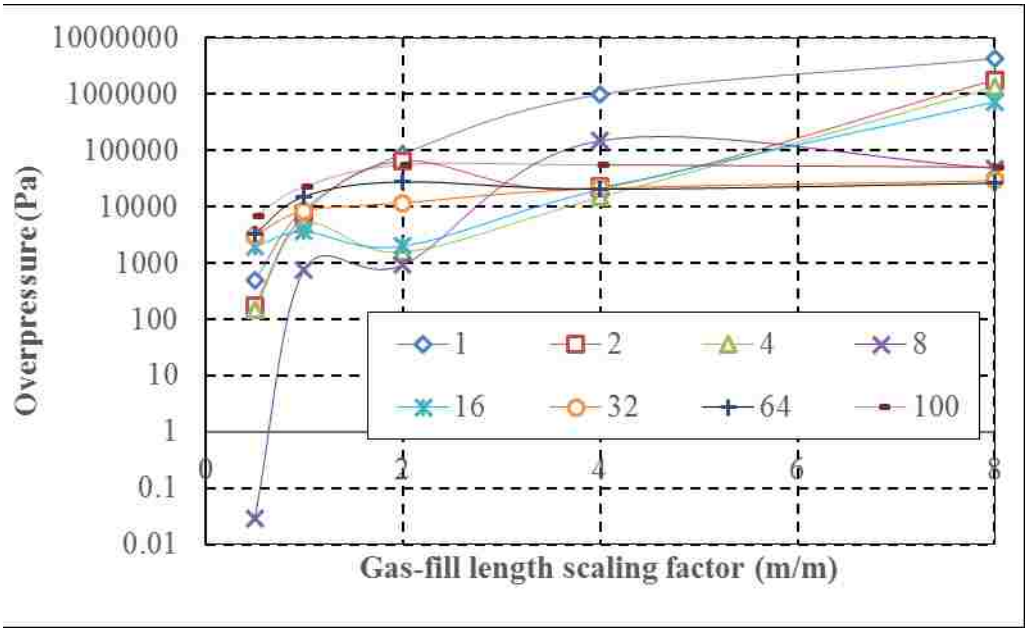

Figure 4.12. Peak overpressures for five FLSFs combined with eight HDSFs for a 9.5% concentration methane explosion

As observed in Figure 4.12, the peak overpressure for all HDSF curves generally increases with FLSFs except when HDSF equals 16 (the cyan curve with * sign). This case shows slightly decrement at FLSF of 8 at the right end of the chart. This suggests the increment of gas-fill length would generally facilitate the overpressure generated by

methane/air explosions regardless of gas-fill space cross-sections. In addition, cases with larger HDSFs reproduced lower peak overpressures than the smaller HDSFs. In #32 and #64 cases with HDSF, significantly low overpressures were detected. This might due to the laminar flame velocity being low (0.42 m/s) and the flame takes longer distance to reach the walls leading to a delay in the laminar -turbulence transition. On the other hand, the space is less confined in cases with larger diameters and thus, the overpressure is attenuated. Note that in the six cases with smaller FLSFs, detonation is triggered instead deflagration, which has higher overpressure than theoretical minimum CJ-detonation pressure. This result is in good agreement with the experimental results that high length-to-diameter ratio is required by DDT (Zipf, et al., 2013).

4.4.2.2 HDSF. The variation of the overpressure with HDSFs when combined with selected FLSFs does not follow the monotonic trend as observed in FLSF cases. Peak overpressures for each FLSF are shown separately in Figure 4.13.

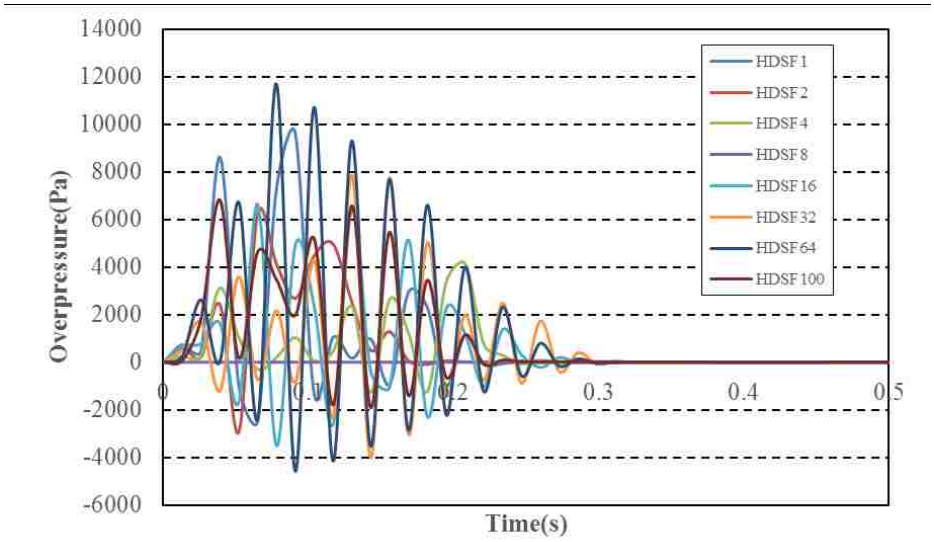

(a)

Figure 4.13. Peak overpressure (Pa) vs eight HDSF (m/m) combined with five FLSFs for 9.5% methane explosion; (a) pressure histories when FLSF=0.5; (b) peak overpressures when FLSF=0.5; (c) pressure histories when FLSF=1; (d) peak overpressures when FLSF=1; (e) pressure histories when FLSF=2; (f) peak overpressures when FLSF=2; (g) pressure histories when FLSF=4; (h) peak overpressures when FLSF=4; (i) pressure histories when FLSF=8; (j) peak overpressures when FLSF=8

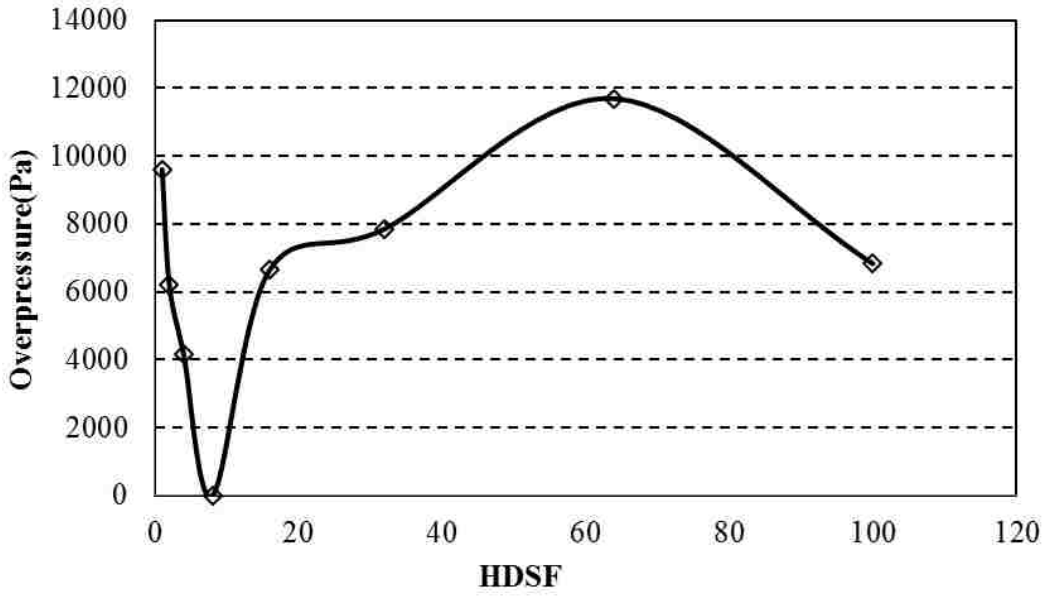

(b)

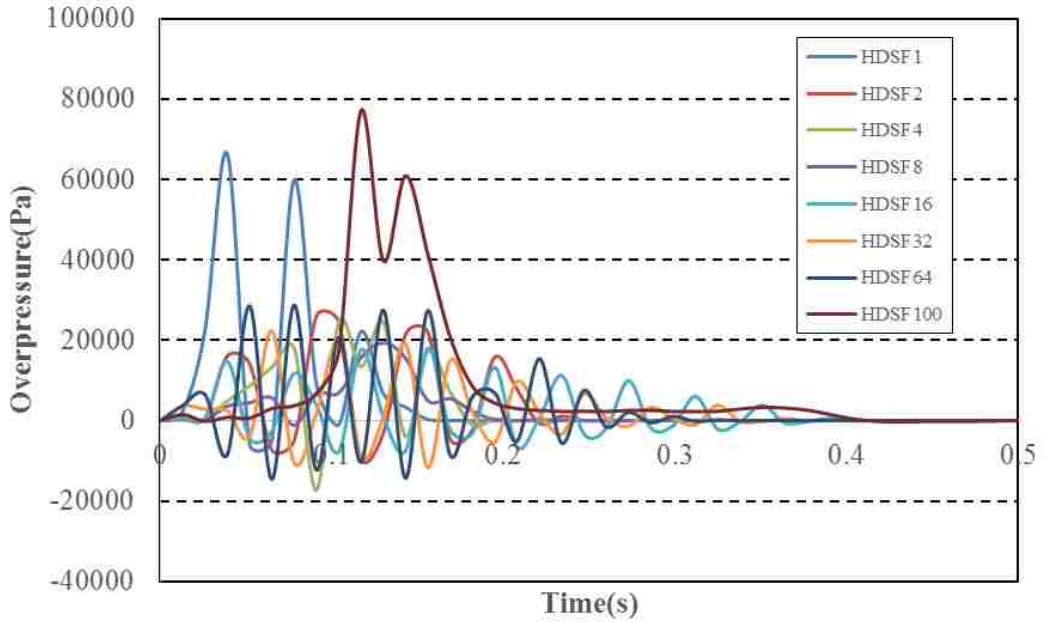

(c)

Figure 4.13. Peak overpressure (Pa) vs eight HDSF (m/m) combined with five FLSFs for 9.5% methane explosion; (a) pressure histories when FLSF=0.5; (b) peak overpressures when FLSF=0.5; (c) pressure histories when FLSF=1; (d) peak overpressures when FLSF=1; (e) pressure histories when FLSF=2; (f) peak overpressures when FLSF=2; (g) pressure histories when FLSF=4; (h) peak overpressures when FLSF=4; (i) pressure histories when FLSF=8; (j) peak overpressures when FLSF=8 (cont.)

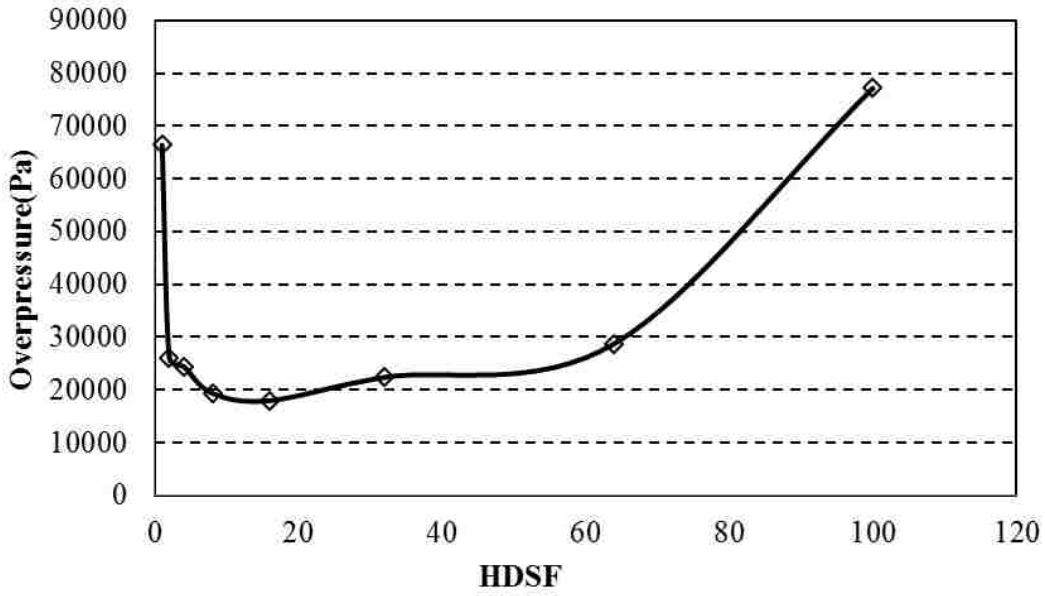

(d)

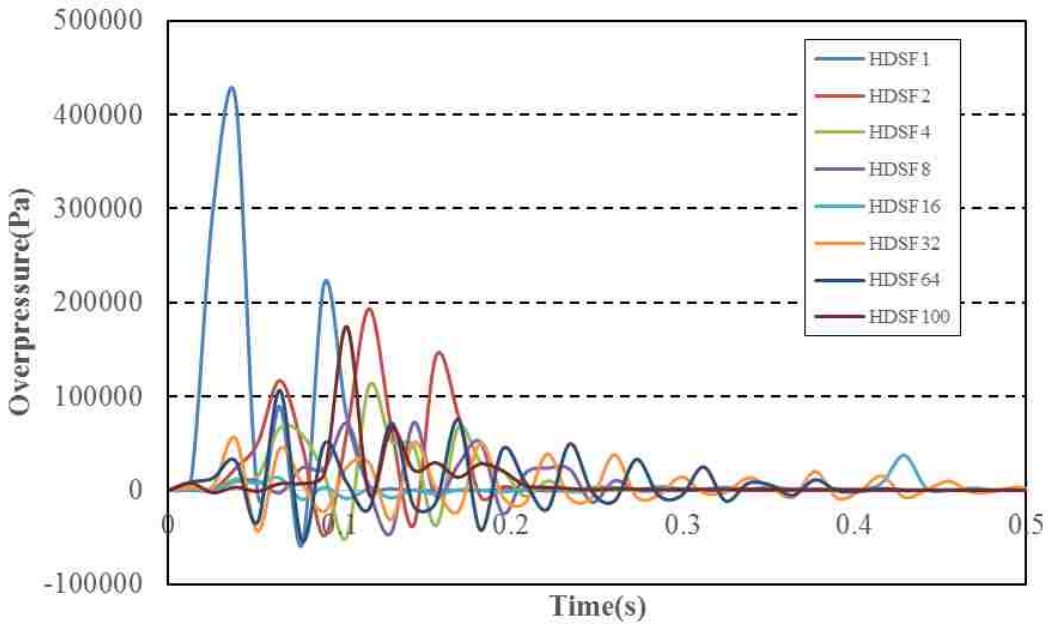

(e)

Figure 4.13. Peak overpressure (Pa) vs eight HDSF (m/m) combined with five FLSFs for 9.5% methane explosion; (a) pressure histories when FLSF=0.5; (b) peak overpressures when FLSF=0.5; (c) pressure histories when FLSF=1; (d) peak overpressures when FLSF=1; (e) pressure histories when FLSF=2; (f) peak overpressures when FLSF=2; (g) pressure histories when FLSF=4; (h) peak overpressures when FLSF=4; (i) pressure histories when FLSF=8; (j) peak overpressures when FLSF=8 (cont.)

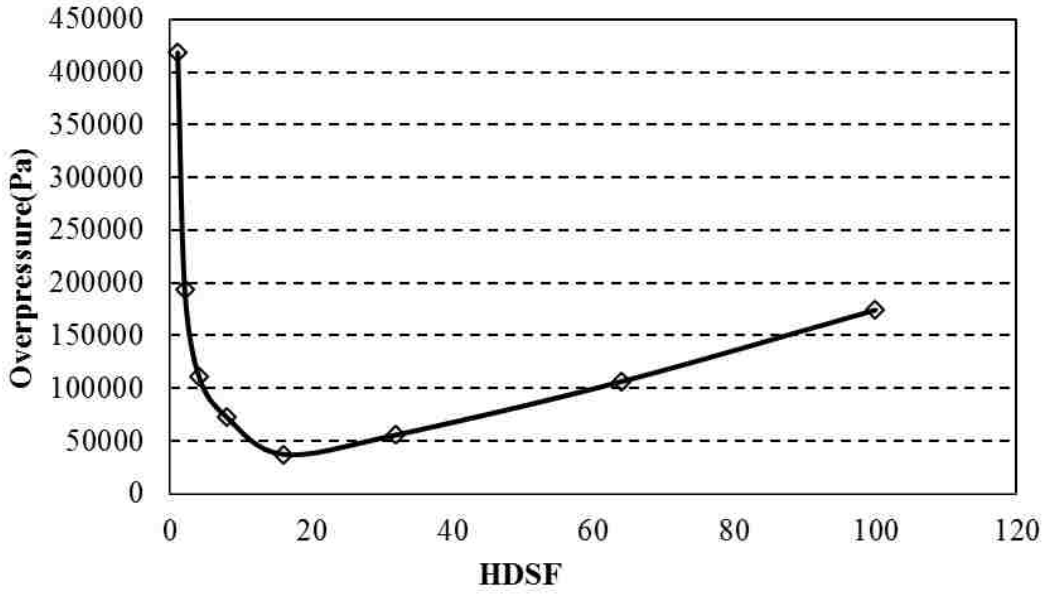

(f)

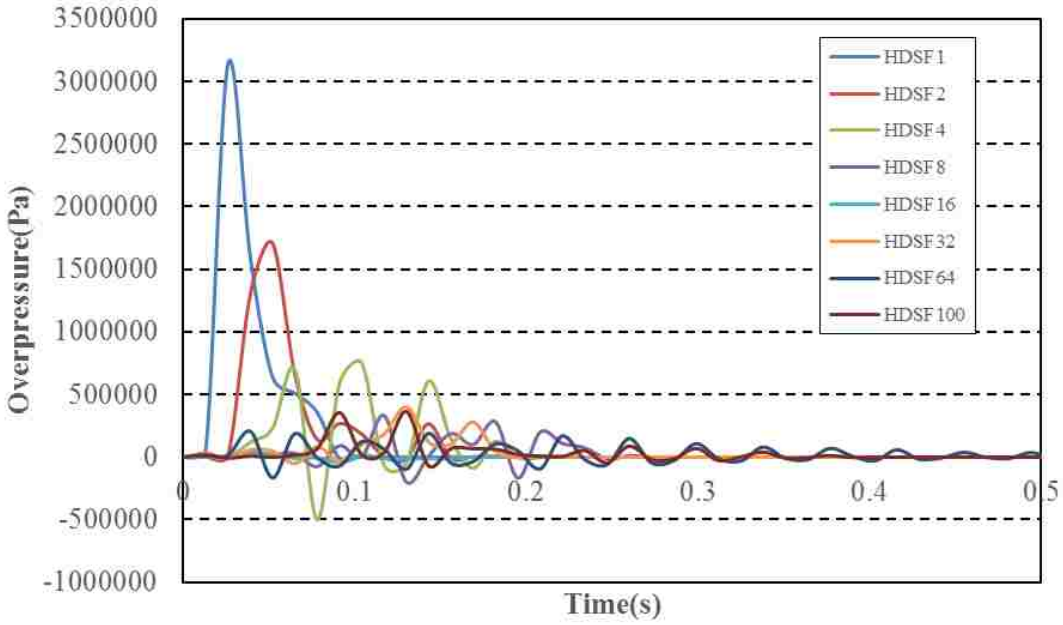

(g)

Figure 4.13. Peak overpressure (Pa) vs eight HDSF (m/m) combined with five FLSFs for 9.5% methane explosion; (a) pressure histories when FLSF=0.5; (b) peak overpressures when FLSF=0.5; (c) pressure histories when FLSF=1; (d) peak overpressures when FLSF=1; (e) pressure histories when FLSF=2; (f) peak overpressures when FLSF=2; (g) pressure histories when FLSF=4; (h) peak overpressures when FLSF=4; (i) pressure histories when FLSF=8; (j) peak overpressures when FLSF=8 (cont.)

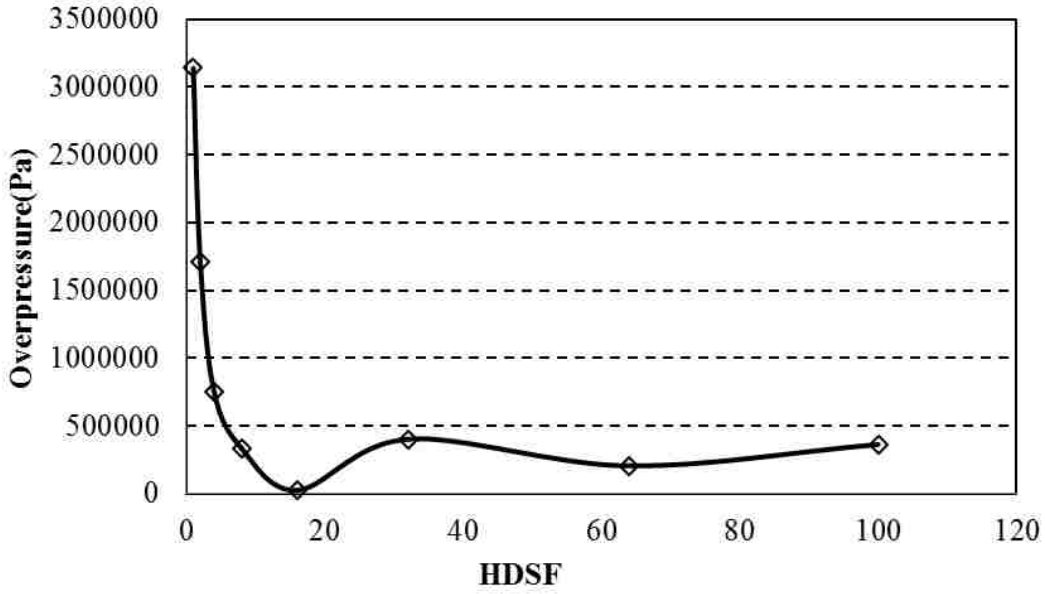

(h)

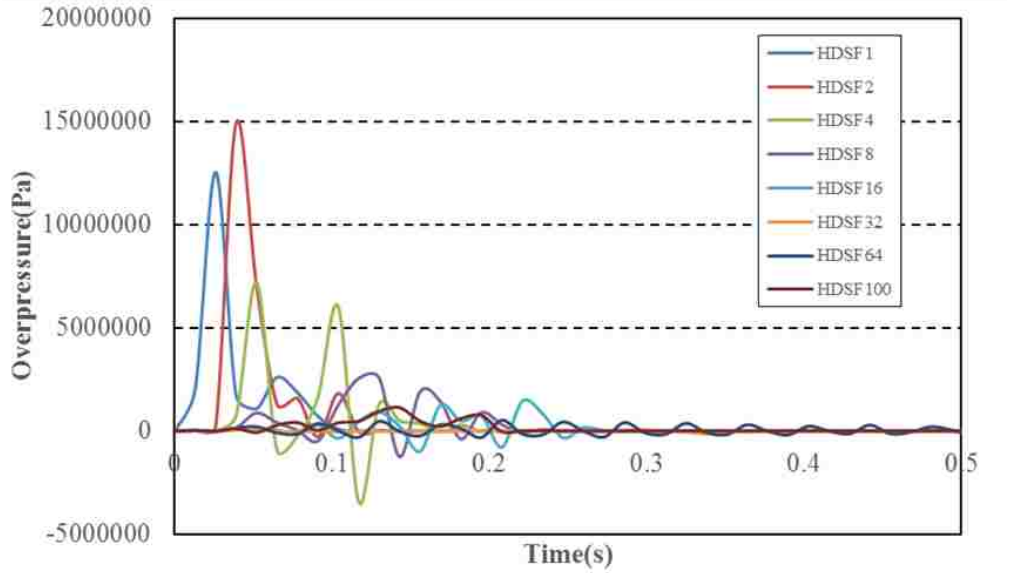

(i)

Figure 4.13. Peak overpressure (Pa) vs eight HDSF (m/m) combined with five FLSFs for 9.5% methane explosion; (a) pressure histories when FLSF=0.5; (b) peak overpressures when FLSF=0.5; (c) pressure histories when FLSF=1; (d) peak overpressures when FLSF=1; (e) pressure histories when FLSF=2; (f) peak overpressures when FLSF=2; (g) pressure histories when FLSF=4; (h) peak overpressures when FLSF=4; (i) pressure histories when FLSF=8; (j) peak overpressures when FLSF=8 (cont.)

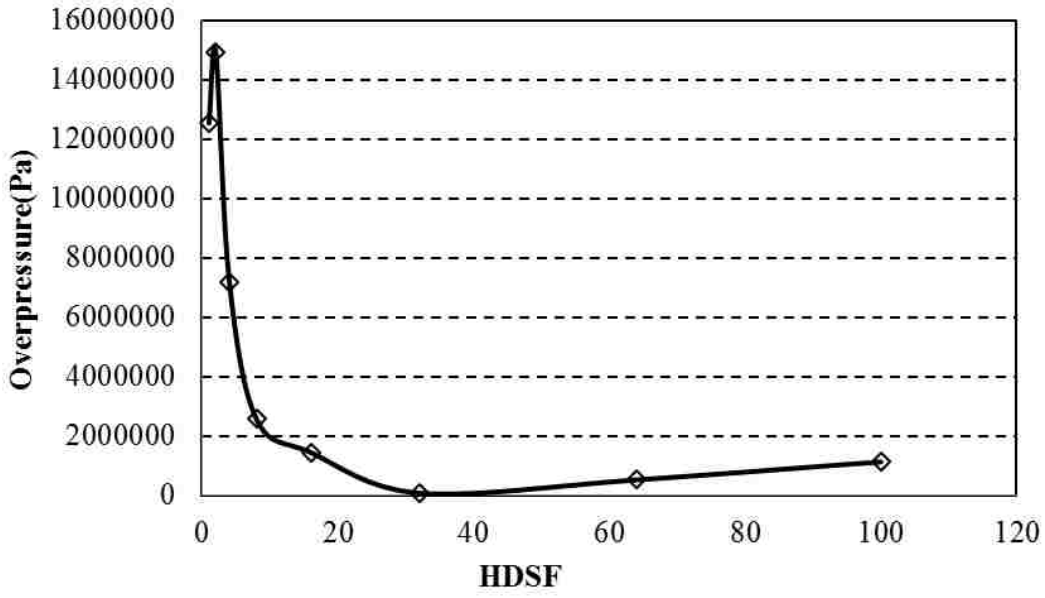

(j)

Figure 4.13. Peak overpressure (Pa) vs eight HDSF (m/m) combined with five FLSFs for 9.5% methane explosion; (a) pressure histories when FLSF=0.5; (b) peak overpressures when FLSF=0.5; (c) pressure histories when FLSF=1; (d) peak overpressures when FLSF=1; (e) pressure histories when FLSF=2; (f) peak overpressures when FLSF=2; (g) pressure histories when FLSF=4; (h) peak overpressures when FLSF=4; (i) pressure histories when FLSF=8; (j) peak overpressures when FLSF=8 (cont.)

Figures 4.13 (a), (c), (e), (g), and (i) show overpressure histories under all eight HDSFs given one selected FLSF. Figures 4.13 (b), (d), (f), (h), and (j) show the peak overpressures under each HDSF. For example, the FLSF 0.5 group (Figure 4.13 (b)), peak overpressure decreases sharply as HDSF increases until it reaches 0, when the HDSF equals to 8. The curve rebounds after HDSF 8 and keeps increasing until the peak value is attained at the HDSF 64. Afterwards, a small decrement is observed. In the FLSFs equal to 1, 2, and 4 groups (Figures 4.13 (d), (f), and (h)), the peak overpressures yield a similar trend and have two local peak values at both ends when HDSFs are equal to 0.5 and 100. Four detonation scenarios are detected close to the left end of the curves. The FLSF 8 group shows a slight incremental change when the HDSF changes from 0.5 to 1 (Figure 4.13 (j)). Then, the peak overpressure decreases to a very low value until it

reaches the minimum, when HDSF equals to 32. This indicates that a larger cross-section of gas-fill space will not always reproduce a larger overpressure and could be opposite in most cases. The overpressure tends to be significant in FLSFs of 2, 4, and 8 groups which depicts that a certain level of gas-fill length is required to produce a violent gaseous explosion. Therefore, detonation is less likely to occur when the length, width, and height of a gas filled space are close to each other in value.

Figure 4.14 summarizes the change of predicted peak overpressures with HDSFs for all five selected FLSFs in a logarithmic coordinate system.

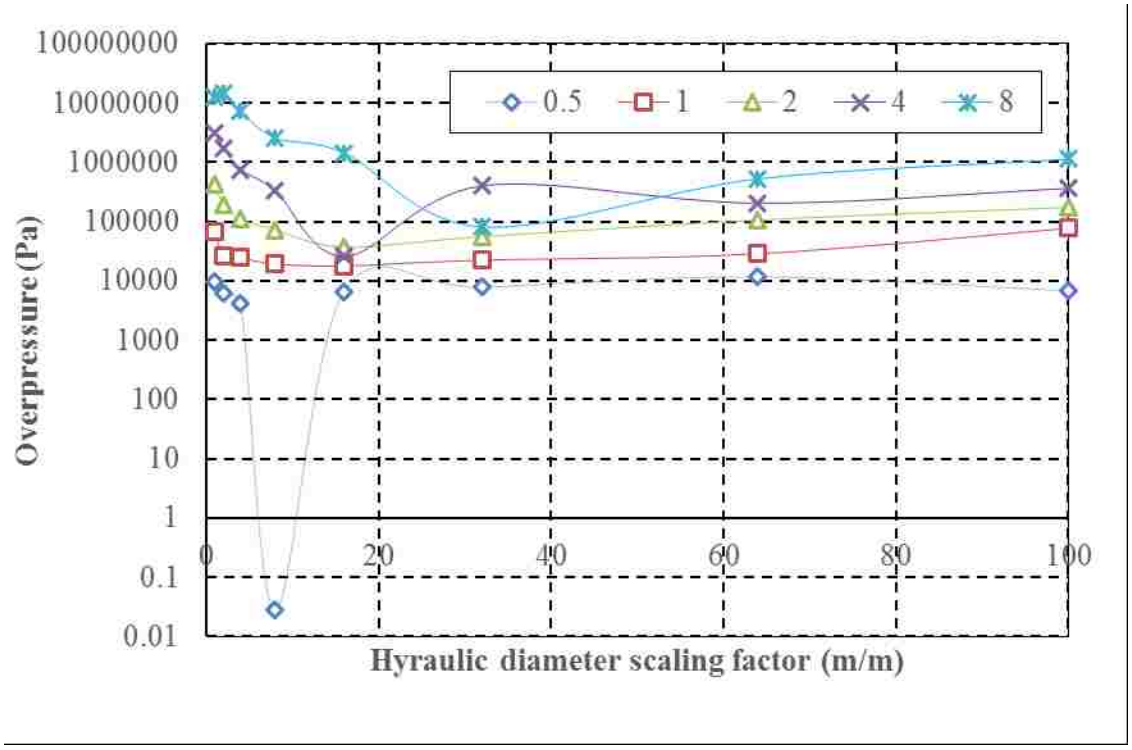

Figure 4.14. Peak overpressure for 9.5% methane explosion change with HDSFs for five FLSFs (curves)

As shown from the chart above, the six data points that transformed to detonation regime are located in small HDSF region close to the left end of the figure. However, larger FLSFs will also give rise to an increment of overpressure which already has been seen in the FLSF analysis.

4.4.2.3 Combined effects. The scaling effect of longitudinal and horizontal directions has been analyzed separately. The combining effect for both FLSFs and HDSFs is illustrated in Figure 4.15.

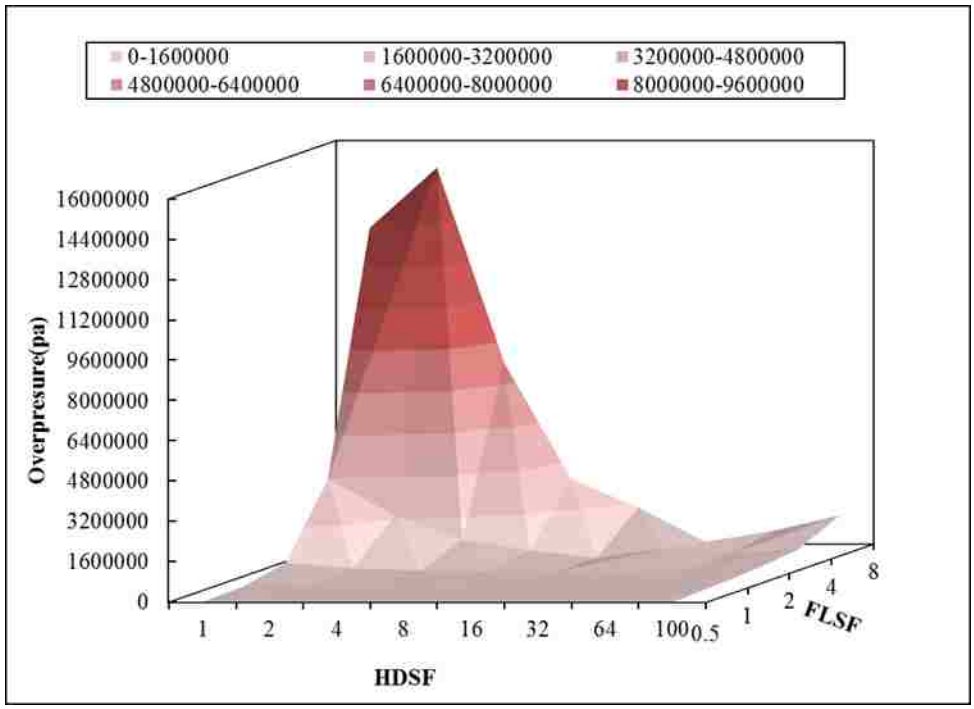

Figure 4.15. Effects of FLSF and HDSF on peak overpressure for 9.5% concentration methane explosion (Pa)

The region with the lightest red color on the bottom of the figure represents the deflagration scenario (0-1,600,000 Pa). Whereas, the region of peak overpressure higher than 1,600,000 Pa is the detonation region (layers with darker red colors). As noticed from the location of the high peak overpressure regions in HDSF/FLSF plane, the detonation regime is located in larger gas-fill length to hydraulic diameter ratios with low HDSFs and high FLSFs at the same time. The minimum value of this ratio is 54 for methane explosions at 9.5% concentration levels. The overpressure also shows a slight increment for larger length to diameter ratios when HDSFs are larger than 64. This is because the enlargement of gas-fill space leads to an increase in fuel quantity. This generates an increase of the total energy of explosives.

Table 4.2 below lists the peak overpressures for selected combinations of eight HDSFs and five FLSFs when methane concentration is at 9.5%. The bold values are detonation cases. As noticed, six detonation cases (with pressures exceeding 1,600,000 Pa) are all located at the right top corner of the table, and the maximum overpressure is 12 MPa when FLSF=8 and HDSD=1. This suggests sustainable detonations were triggered in two of the largest length to diameter ratios.

Table 4.2. Peak overpressure for selected combinations of HDSFs and FLSFs for 9.5% methane explosion (Pa)

FLSF / HDSF	0.5	1	2	4	8
1	9606	66389	418271	**3139192**	**12540373**
2	6219	26094	193489	**1707092**	**14923139**
4	4154	24451	111417	751765	**7199514**
8	1	19348	72218	332517	**2570226**
16	6650	17979	37333	25758	1448854
32	7855	22398	55832	402319	81297
64	11694	28760	106454	205202	525808
100	6829	77150	174292	363850	1132997

4.4.3. Results and Discussion - 8% Concentration. The second methane concentration under analysis is the 8% level which represents a lean fuel case. However, although it deviates from stoichiometry, the laminar flame speed of 8% methane is the largest among all three concentrations under investigation. As a result, the peak overpressures obtained are the largest. Peak overpressure/time relationships at the scaled distance 9.5 for the combinations of eight HDSFs (1, 2, 4, 8, 16, 32, 64, and 100) and five FLSFs (0.5, 1, 2, 4, and 8), with 8% methane concentration were tested and will be presented in the section below.

4.4.3.1 FLSF. Peak overpressures for FLSFs equal to 0.5, 1, 5, 4, and 8 when combined with eight HDSFs are shown in Figure 4.16 in a logarithmic scale.

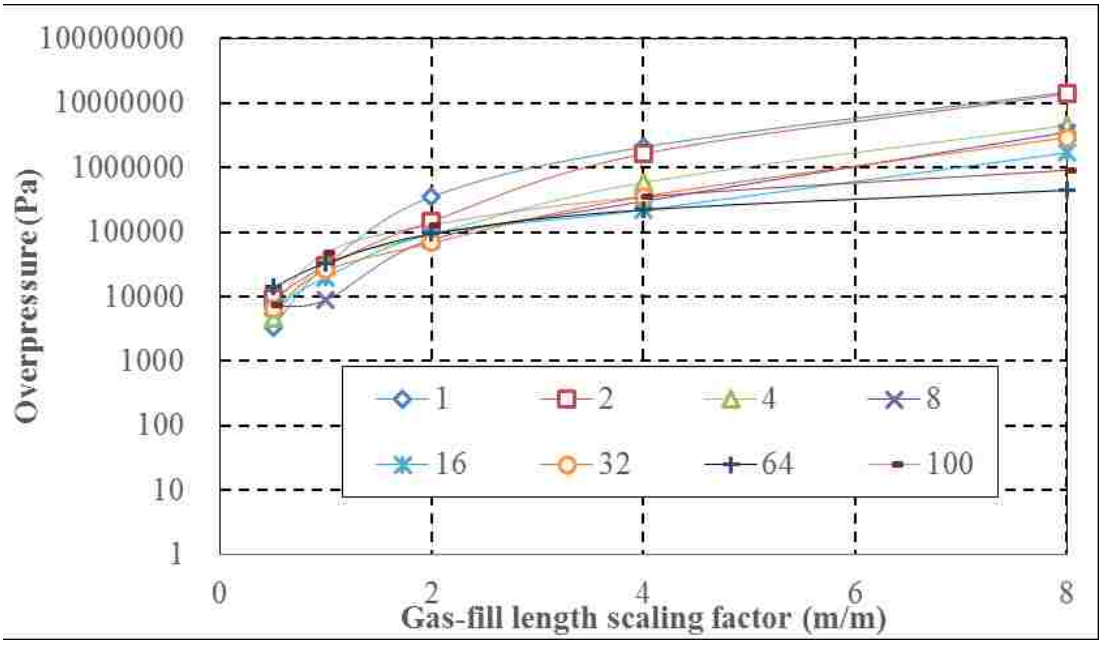

Figure 4.16. Peak overpressures for five FLSFs combined with eight HDSFs for an 8% methane explosion

Similar to the 9.5% concentration level cases, the peak overpressure increases monotonically with the increase of FLSF except when HDSF equals to 8. In this case, a slight decrement is shown at FLSF of 1. Similarly, the larger the HDSF the lower the peak overpressure is observed for the 8% concentration level cases. The lowest peak overpressure among all selected cases is obtained when HDSF equals to 64 and the diameter of duct is 5.12 m. Among the scenarios with 8% methane concentration, eight detonation combinations are found compared to six for an explosion with a 9.5% methane concentration.

4.4.3.2 HDSF. Peak overpressures for each FLSF of an 8% methane explosion is demonstrated in Figure 4.17.

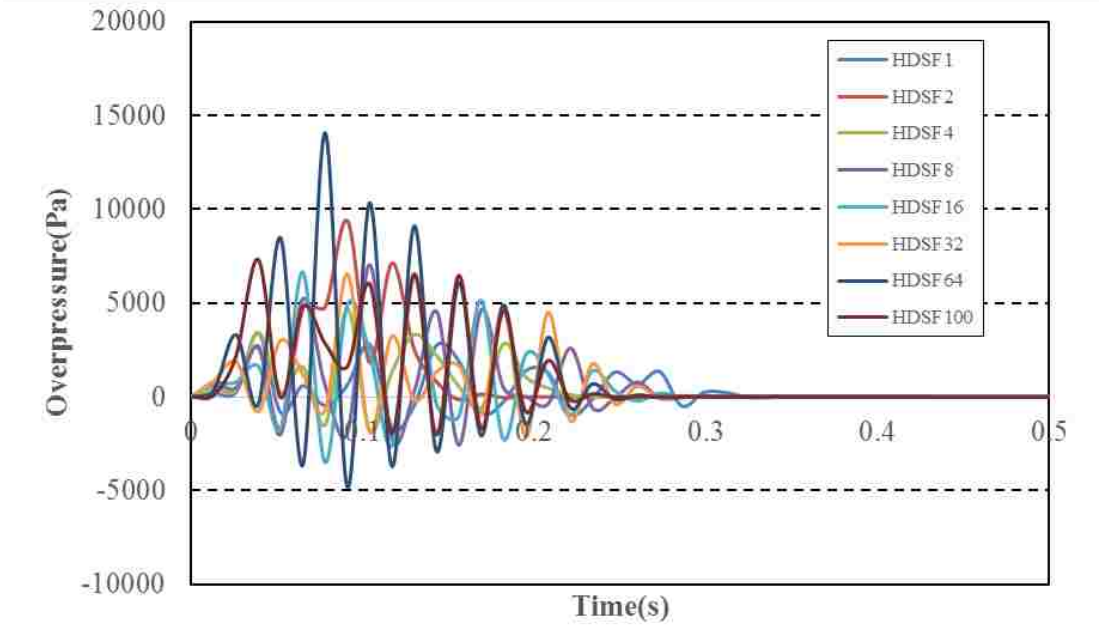

(a)

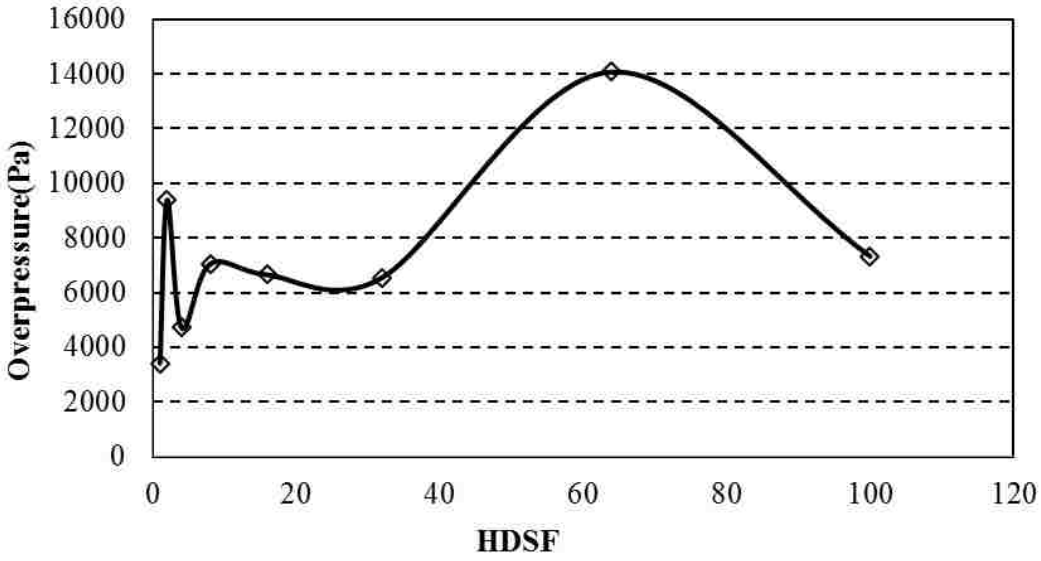

(b)

Figure 4.17. Peak overpressure (Pa) vs eight HDSF (m/m) combined with five FLSFs for 8% methane explosion; (a) pressure histories when FLSF=0.5; (b) peak overpressures when FLSF=0.5; (c) pressure histories when FLSF=1; (d) peak overpressures when FLSF=1; (e) pressure histories when FLSF=2; (f) peak overpressures when FLSF=2; (g) pressure histories when FLSF=4; (h) peak overpressures when FLSF=4; (i) pressure histories when FLSF=8; (j) peak overpressures when FLSF=8

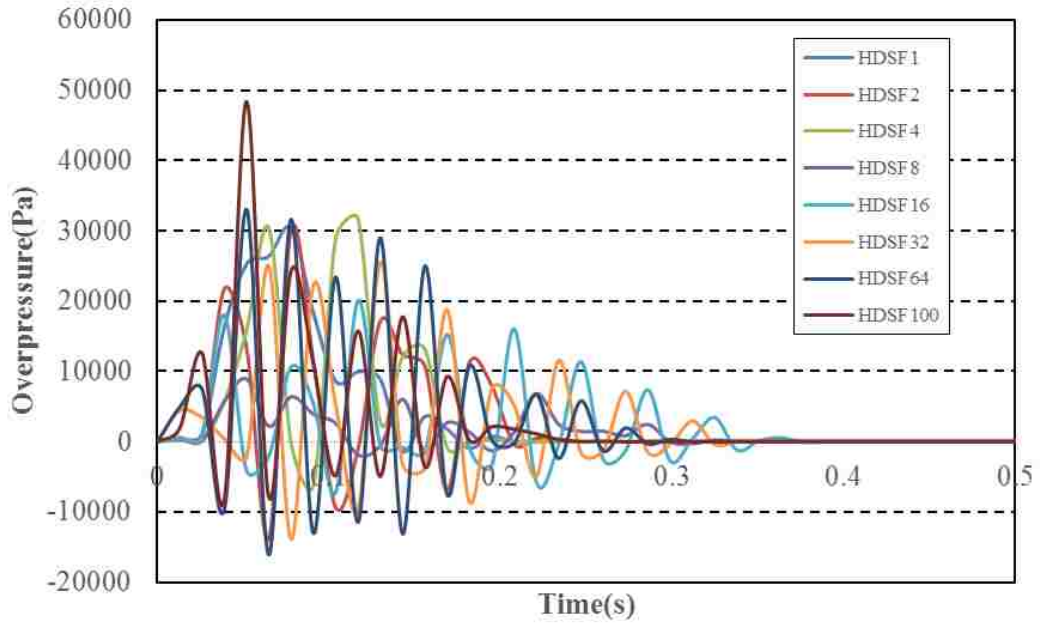

(c)

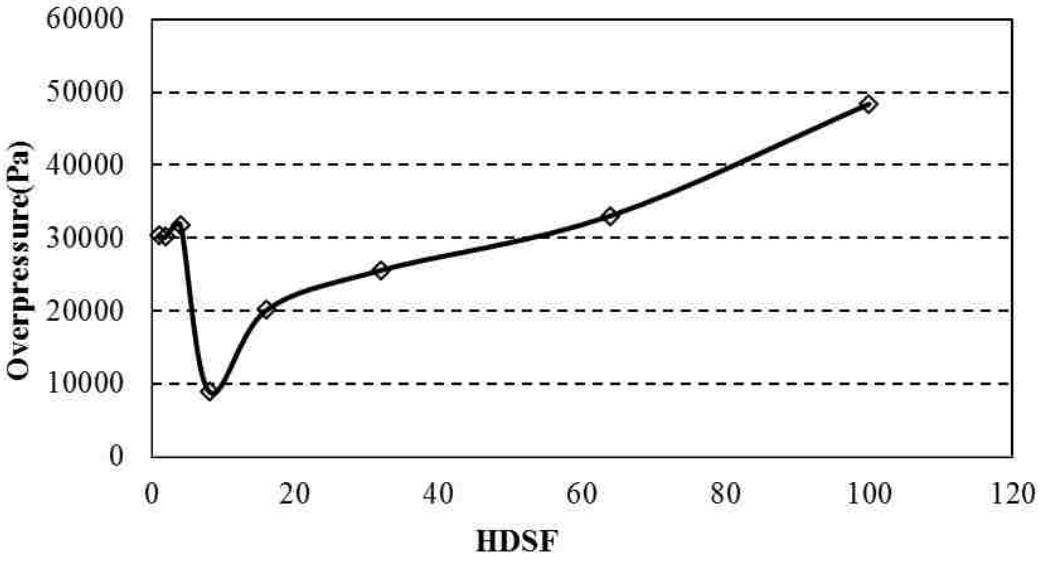

(d)

Figure 4.17. Peak overpressure (Pa) vs eight HDSF (m/m) combined with five FLSFs for 8% methane explosion; (a) pressure histories when FLSF=0.5; (b) peak overpressures when FLSF=0.5; (c) pressure histories when FLSF=1; (d) peak overpressures when FLSF=1; (e) pressure histories when FLSF=2; (f) peak overpressures when FLSF=2; (g) pressure histories when FLSF=4; (h) peak overpressures when FLSF=4; (i) pressure histories when FLSF=8; (j) peak overpressures when FLSF=8 (cont.)

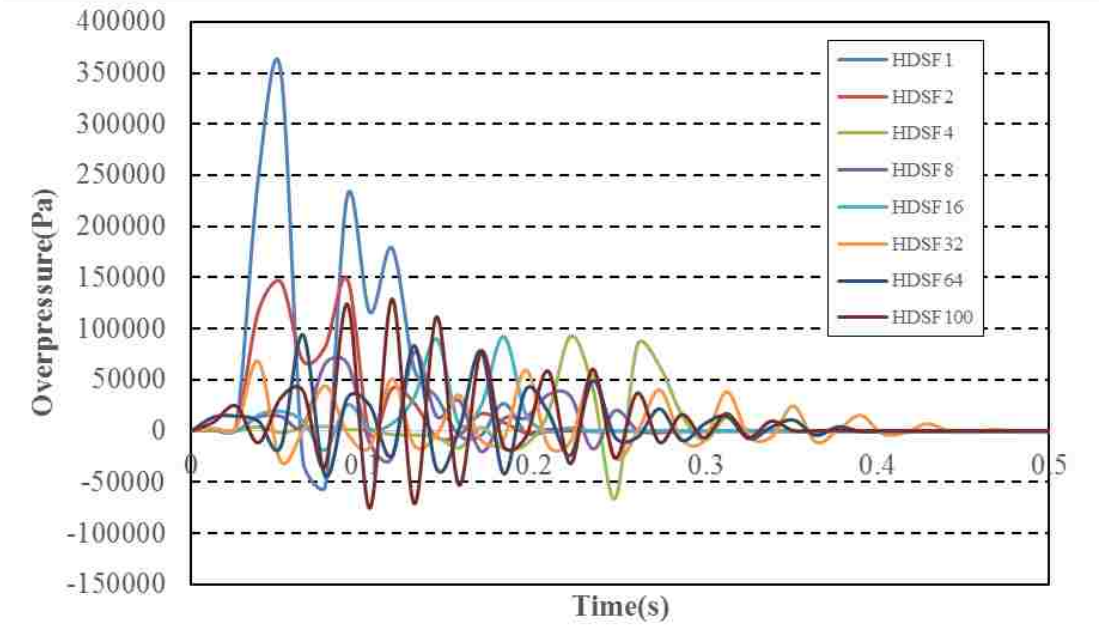

(e)

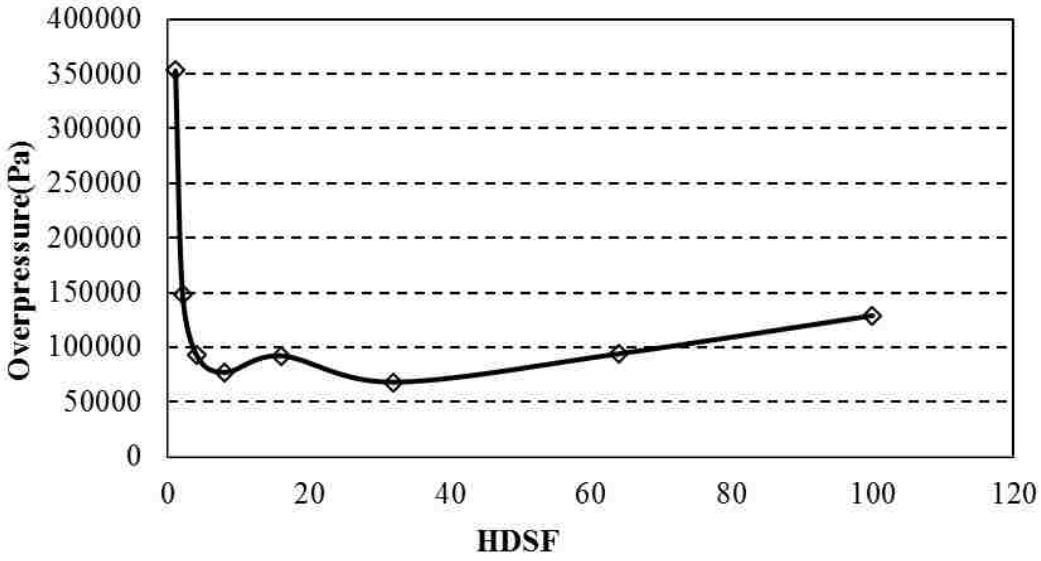

(f)

Figure 4.17. Peak overpressure (Pa) vs eight HDSF (m/m) combined with five FLSFs for 8% methane explosion; (a) pressure histories when FLSF=0.5; (b) peak overpressures when FLSF=0.5; (c) pressure histories when FLSF=1; (d) peak overpressures when FLSF=1; (e) pressure histories when FLSF=2; (f) peak overpressures when FLSF=2; (g) pressure histories when FLSF=4; (h) peak overpressures when FLSF=4; (i) pressure histories when FLSF=8; (j) peak overpressures when FLSF=8 (cont.)

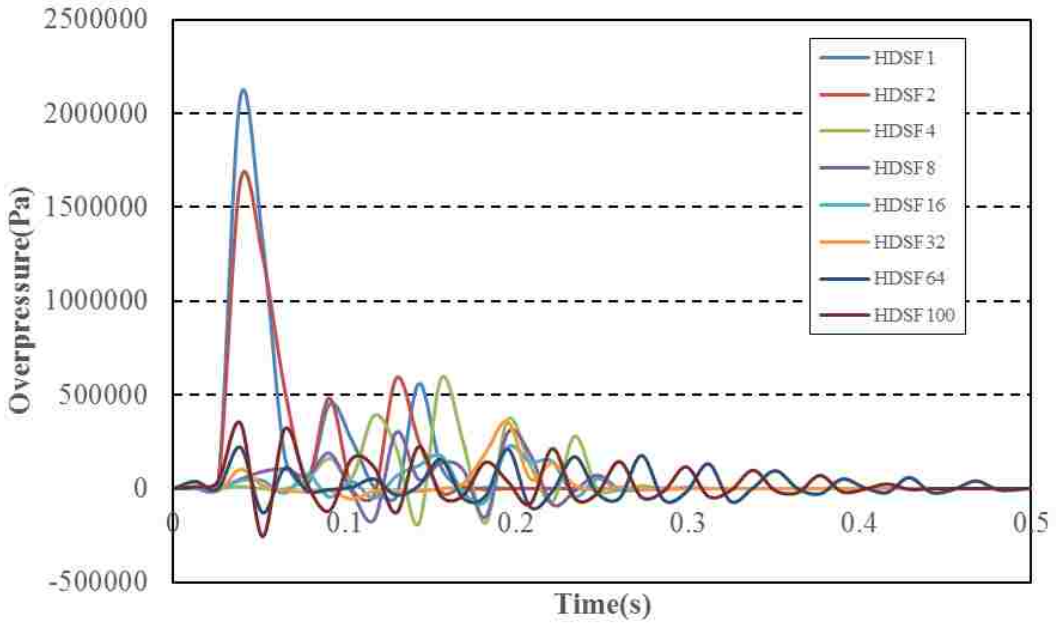

(g)

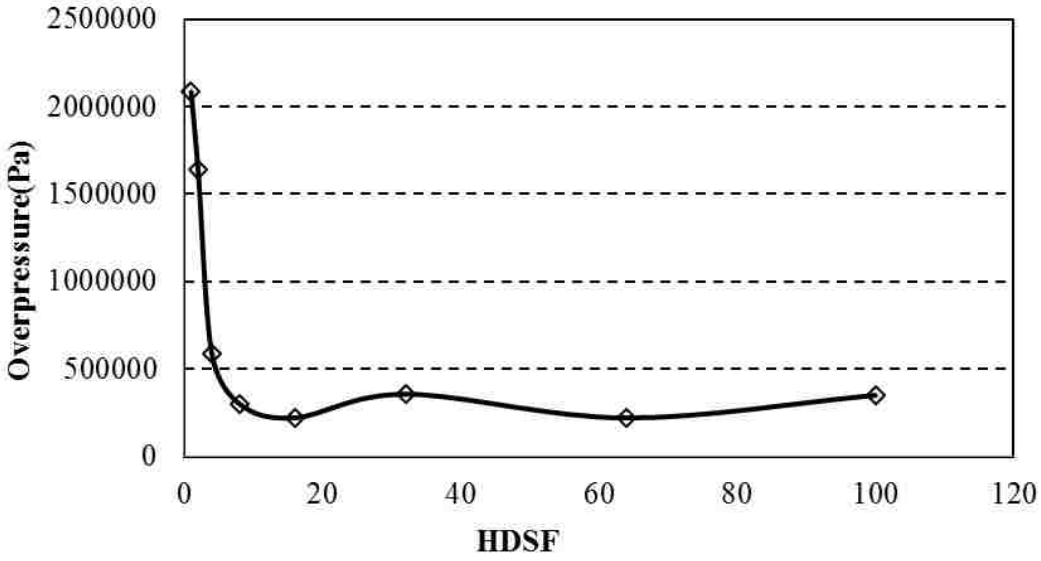

(h)

Figure 4.17. Peak overpressure (Pa) vs eight HDSF (m/m) combined with five FLSFs for 8% methane explosion; (a) pressure histories when FLSF=0.5; (b) peak overpressures when FLSF=0.5; (c) pressure histories when FLSF=1; (d) peak overpressures when FLSF=1; (e) pressure histories when FLSF=2; (f) peak overpressures when FLSF=2; (g) pressure histories when FLSF=4; (h) peak overpressures when FLSF=4; (i) pressure histories when FLSF=8; (j) peak overpressures when FLSF=8 (cont.)

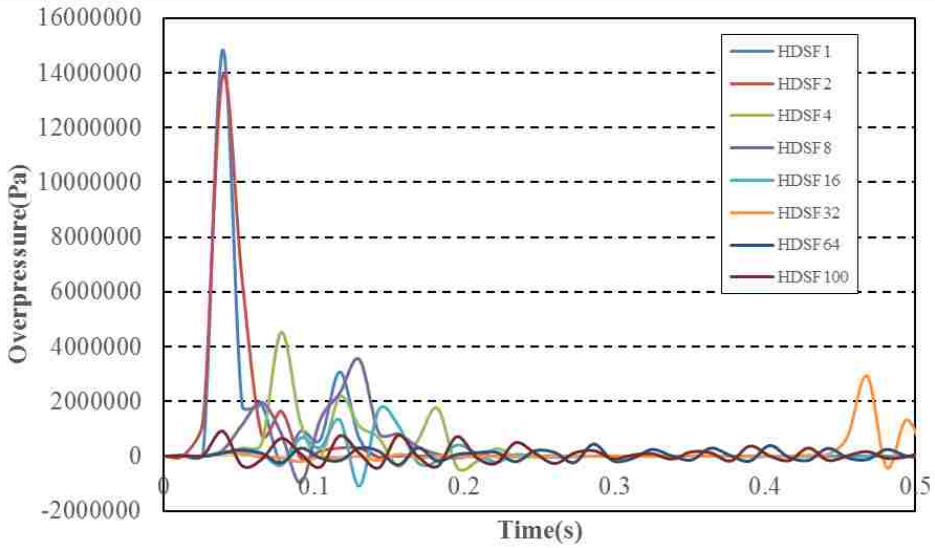

(i)

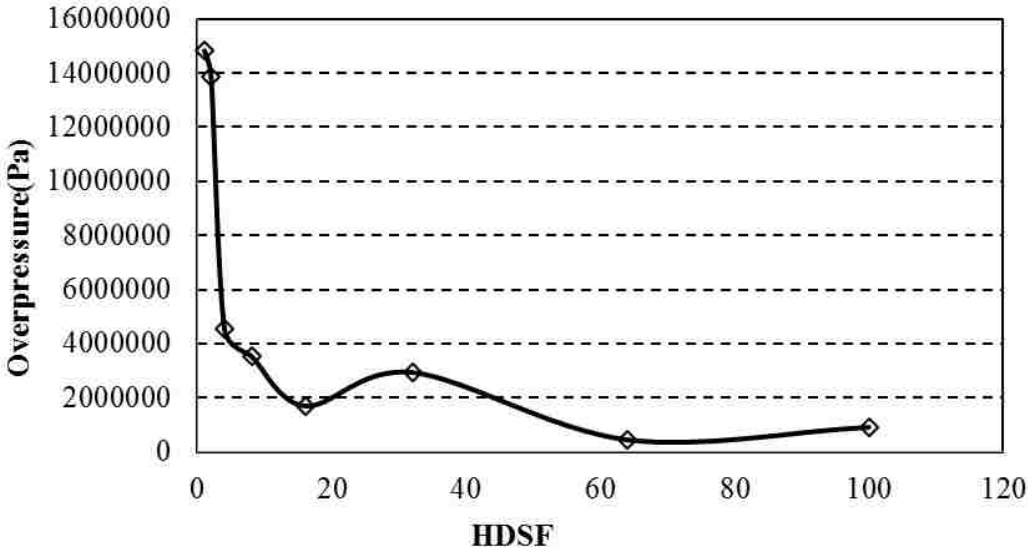

(j)

Figure 4.17. Peak overpressure (Pa) vs eight HDSF (m/m) combined with five FLSFs for 8% methane explosion; (a) pressure histories when FLSF=0.5; (b) peak overpressures when FLSF=0.5; (c) pressure histories when FLSF=1; (d) peak overpressures when FLSF=1; (e) pressure histories when FLSF=2; (f) peak overpressures when FLSF=2; (g) pressure histories when FLSF=4; (h) peak overpressures when FLSF=4; (i) pressure histories when FLSF=8; (j) peak overpressures when FLSF=8 (cont.)

The layout of Figure 4.17 is similar to Figure 4.13 which is below the methane concentration level of 9.5%. Figures 4.17 (a), (c), (e), (g), and (i) show overpressure histories under all eight HDSFs, given one selected FLSF under the 8% concentration level; Figures (b), (d), (f), (h), and (j) show the peak overpressures under each HDSF. As observed in Figure 4.17 (b) when FLSF equals 0.5, the peak overpressure fluctuates at smaller HDSFs then reaches a maximum value around 14,000 Pa, followed by a drop in the overpressure value. When the FLSF equals to one (Figure 4.17 (d)), the peak overpressure decreases slightly and then increases monotonically. Similar trends are found for FLSFs cases of 2, 4 and 8 (Figures 4.17 (f), (h), and (j)). This trend shows a sharply decrement of peak overpressure at the beginning and, after a small fluctuation, it is sustained to a certain level. Similar to 9.5% cases, the detonation cases are found close to the left end of the curves which means that the detonation can only be triggered for a duct with a relatively small cross-sectional dimension.

Figure 4.18 summarizes the interrelationships among predicted overpressure of all five FLSFs in a logarithmic coordinate system.

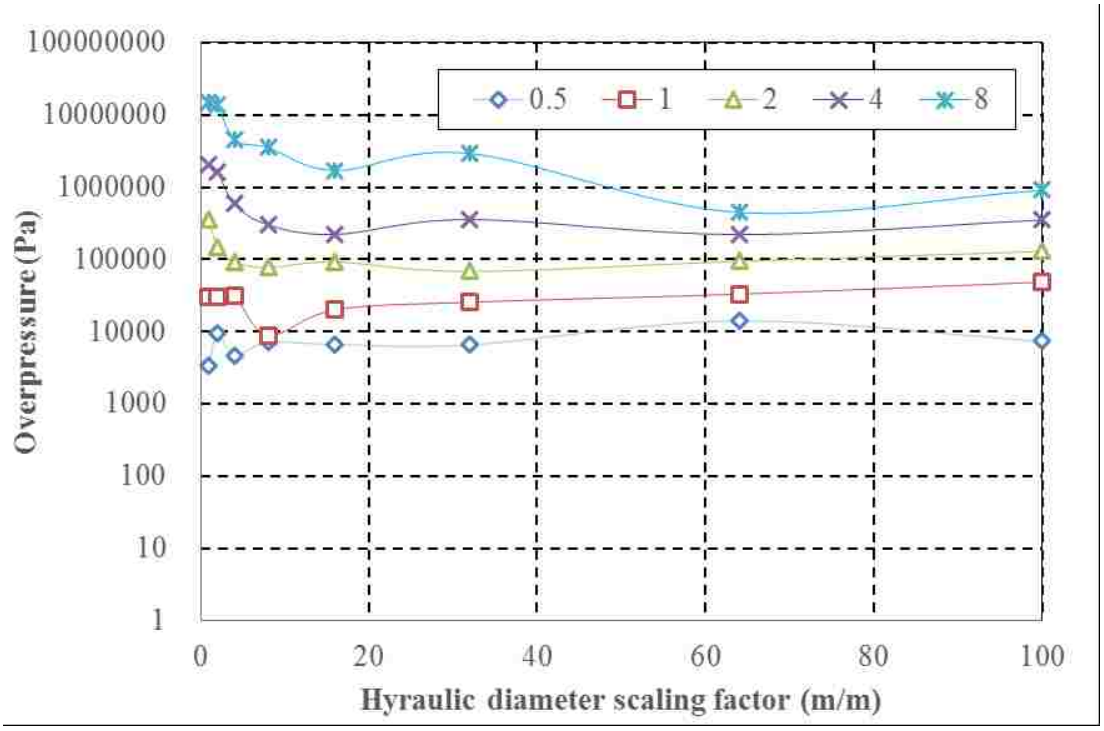

Figure 4.18. Peak overpressure for 8% methane explosion change with HDSFs for five FLSFs (curves)

As can be seen in Figure 4.18, a total of eight data points which are transformed to detonation regime fall into the small HDSF region (close to left end of the figure). An 8% concentration has more detonation cases than the 9.5% concentration level and the maximum peak of the concentration 8% overpressure recorded is also larger (14,829,484) compared to the 9.5% level (12,540,373 Pa).

4.4.3.3 Combined effects. Figure 4.19 illustrated the combined effect of both the FLSFs and HDSFs on overpressures with 8% methane concentration.

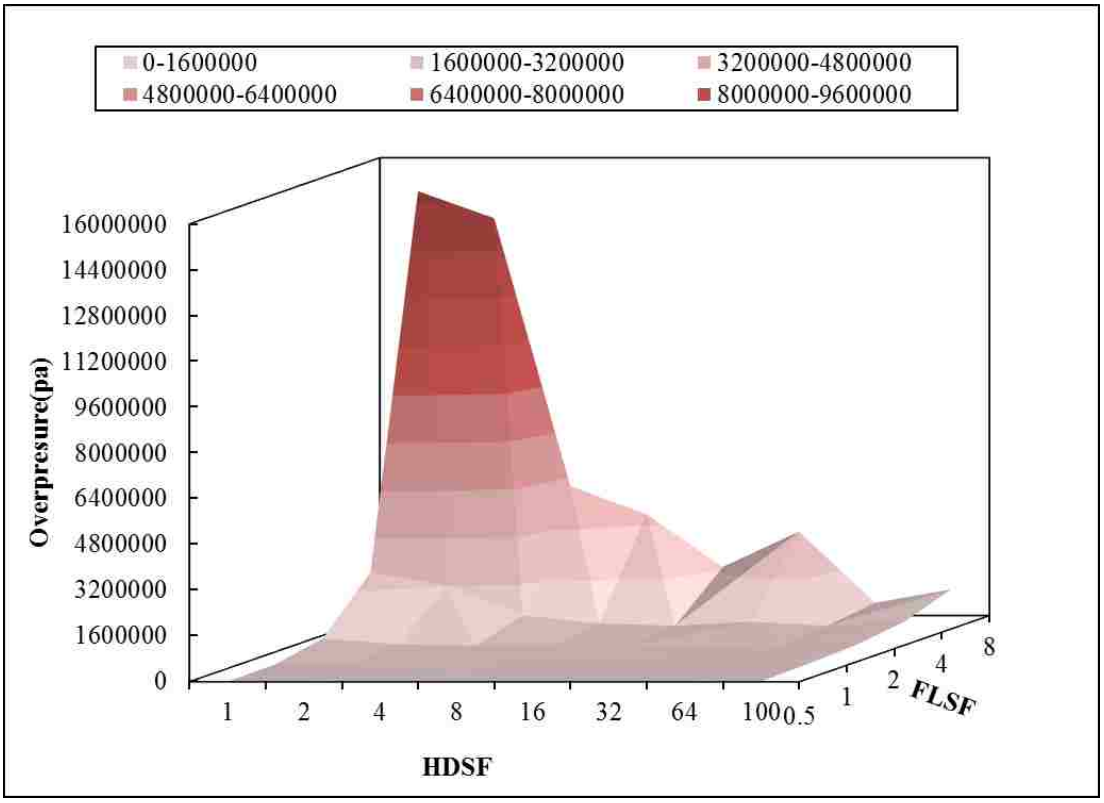

Figure 4.19. Effects of FLSF and HDSF on peak overpressure for 8% concentration methane explosion (Pa)

The region with light red on the bottom represents a deflagration scenario (smaller than CJ-detonation value 1,600,000) and otherwise in a detonation regime. As can be seen, similar to 9.5% concentration level, the detonation regime located in the region with a large gas-fill length to hydraulic diameter ratios on the right top corner of the

HDSF/FLSF plane. The minimum ratio is 13.3 when the methane concentration is 8% compared to a value of 54 with the methane concentration of 9.5%. This result suggests that for a methane concentration of 8%, detonation can be triggered at a relatively lower length to diameter ratio compared to the 9.5% case. The maximum peak overpressure recorded is also the highest among the three (14,829,484 Pa). The shape of the surface shown in Figure 4.19 is similar to that in Figure 4.15. The difference between these two figures is that in the Figure 4.19, the surface shows a fluctuation on the far side of the figure (FLSLs greater than 4) while the peak overpressures increases monotonically with the decrease of HDSF shown in Figure 4.15.

Table 4.3 below illustrates the peak overpressures for each selected HDSF-FLSF combination when the methane concentration is 8%. Bold numbers represent detonation cases. As noticed, eight cases at the right top corner of the table are detonation cases and their peak overpressures are the greatest among the three selected methane concentrations under study. The maximum overpressure recorded is around 14.8 MPa and the second largest is 13.8 MPa. In these two cases, sustainable detonations, which will generate significantly higher overpressures than normal detonations, are triggered. As a consequence, the fuel lean methane explosions actually has higher overpressures than the stoichiometric scenarios.

Table 4.3. Peak overpressure for selected combinations of HDSFs and FLSFs for 8% methane explosion (Pa)

FLSF / HDSF	0.5	1	2	4	8
1	3415	30389	353183	**2084215**	**14829484**
2	9384	30158	147993	**1637268**	**13887314**
4	4712	31733	92466	586447	**4527823**
8	7049	8919	77053	301280	**3533682**
16	6650	20091	92244	221914	**1699870**
32	6552	25569	68172	356974	**2934727**
64	14075	33043	94123	221022	447618
100	7325	48366	129056	350589	912405

4.4.4. Results and Discussion - 12% Concentration. The third methane concentration in this research is the 12% level, which represents fuel lean scenarios. The laminar flame speed is the smallest among the three and, the peak overpressures obtained are the smallest as well. Peak overpressure histories of 12% methane explosion at the scaled distance of 9.5 were tested, under all selected HDSF -FLSF combinations

4.4.4.1 FLSF. Peak overpressure for FLSFs equal 0.5, 1, 5, 4, and 8 when combined with eight HDSFs is shown in Figure 4.20 in a logarithmic coordinate system.

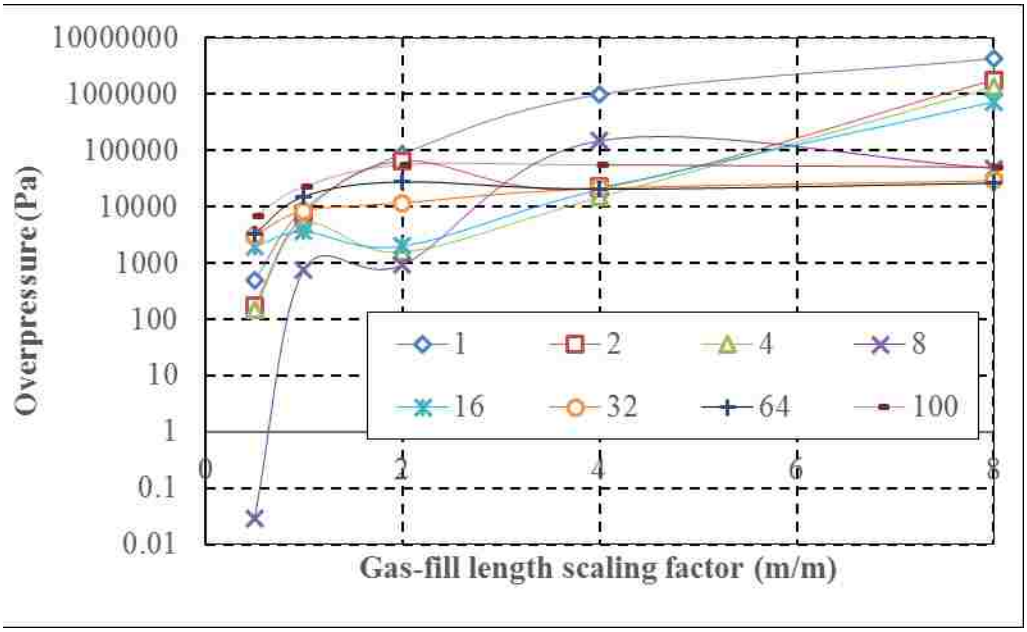

Figure 4.20. Peak overpressures for five FLSFs combined with eight HDSFs for 12% methane explosion

Similar trends of overpressure histories between the 9.5% concentration and the 12% concentration levels are observed. The peak overpressure for all FLSF-HDSF combinations increases monotonically with the increase of FLSF except when HDSF equals to 16 (cyan curve with * sign). In this case, the overpressure history curve shows a slight decrease at the FLSF of 2. The peak overpressures predicted for diverse FLSFs can be divided into two groups. The first group includes HDSFs of 1, 2, 4, and 16 which results of higher peak overpressures. The second group includes HDSFs of 8, 32, 64, and

100, which shows relatively lower peak overpressures. Note that only two detonations are triggered with higher overpressures than the theoretical minimum CJ-detonation pressure. This result suggests that, compared to the 9.5% and 8% cases, the detonation is unlikely to be triggered at 12% methane concentration regardless of geometric dimensions.

4.4.4.2 FLSF. Peak overpressures for each selected FLSF are demonstrated separately in Figure 4.21. The first figure in each FLSF case shows overpressure history under all eight HDSFs while the second figure shows the peak overpressures under each HDSF.

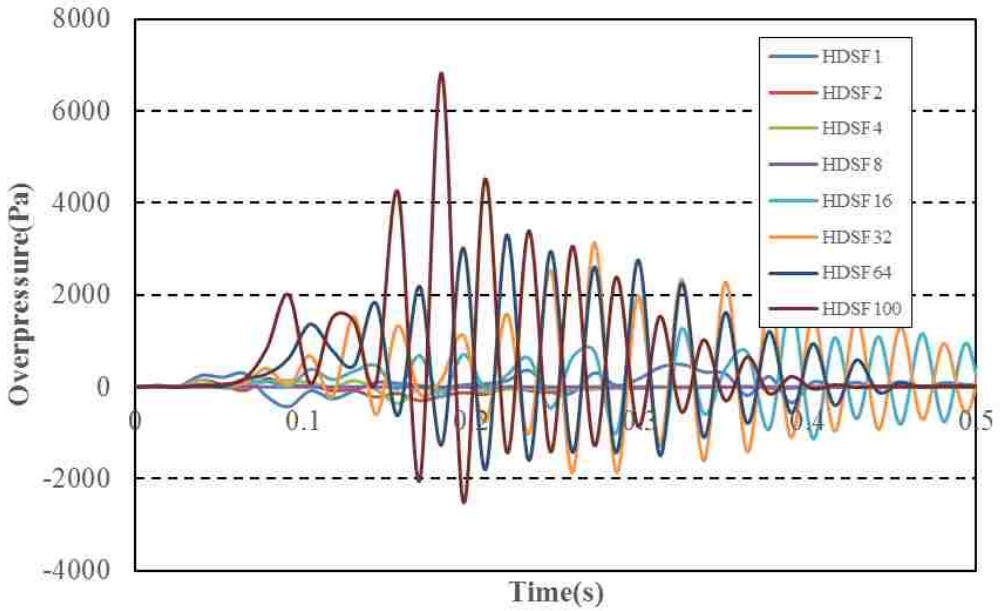

(a)

Figure 4.21. Peak overpressure (Pa) vs eight HDSF (m/m) combined with five FLSFs for 12% methane explosion; (a) pressure histories when FLSF=0.5; (b) peak overpressures when FLSF=0.5; (c) pressure histories when FLSF=1; (d) peak overpressures when FLSF=1; (e) pressure histories when FLSF=2; (f) peak overpressures when FLSF=2; (g) pressure histories when FLSF=4; (h) peak overpressures when FLSF=4; (i) pressure histories when FLSF=8; (j) peak overpressures when FLSF=8

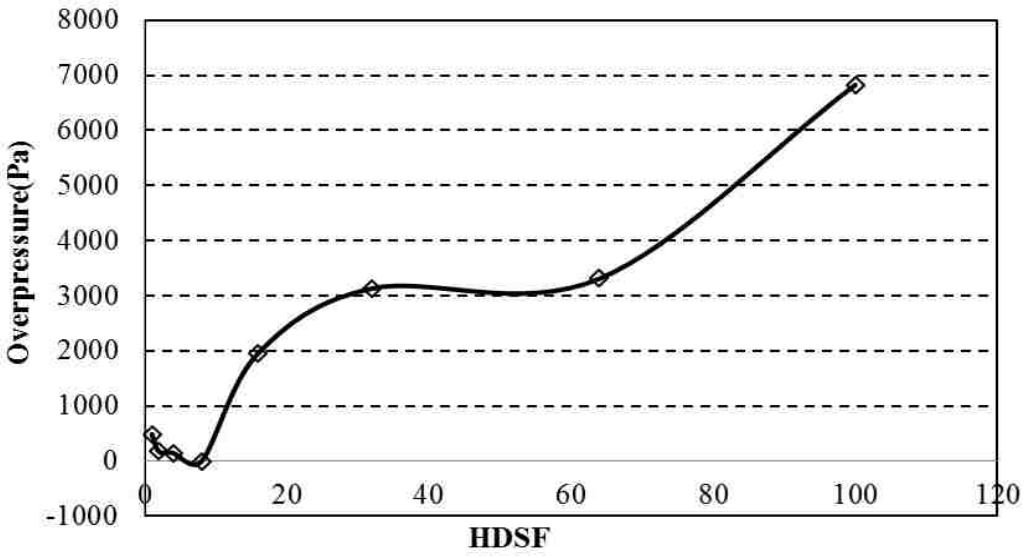

(b)

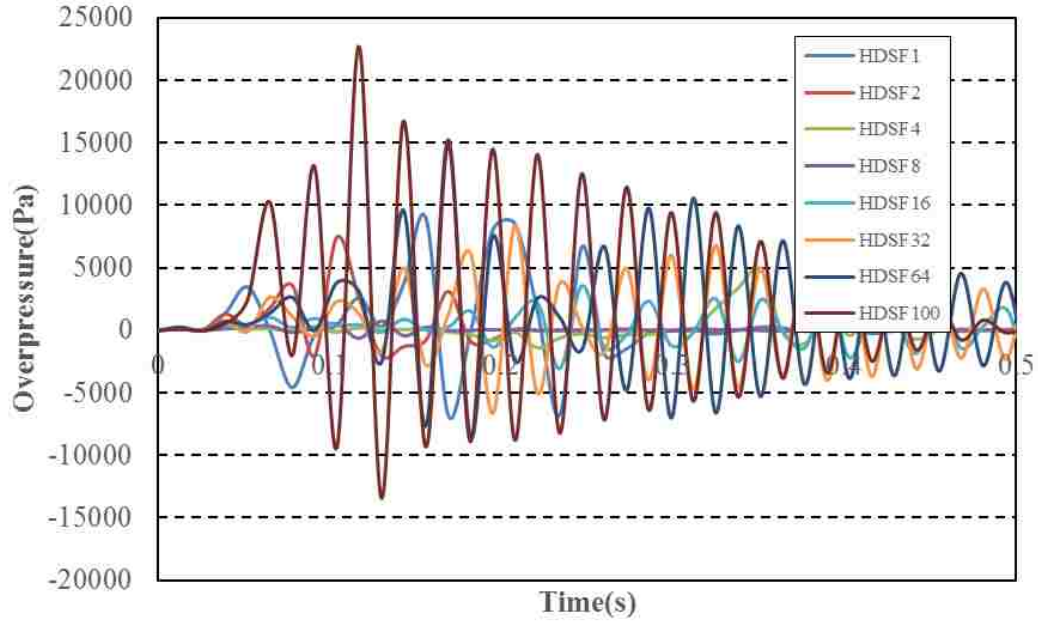

(c)

Figure 4.21. Peak overpressure (Pa) vs eight HDSF (m/m) combined with five FLSFs for 12% methane explosion; (a) pressure histories when FLSF=0.5; (b) peak overpressures when FLSF=0.5; (c) pressure histories when FLSF=1; (d) peak overpressures when FLSF=1; (e) pressure histories when FLSF=2; (f) peak overpressures when FLSF=2; (g) pressure histories when FLSF=4; (h) peak overpressures when FLSF=4; (i) pressure histories when FLSF=8; (j) peak overpressures when FLSF=8 (cont.)

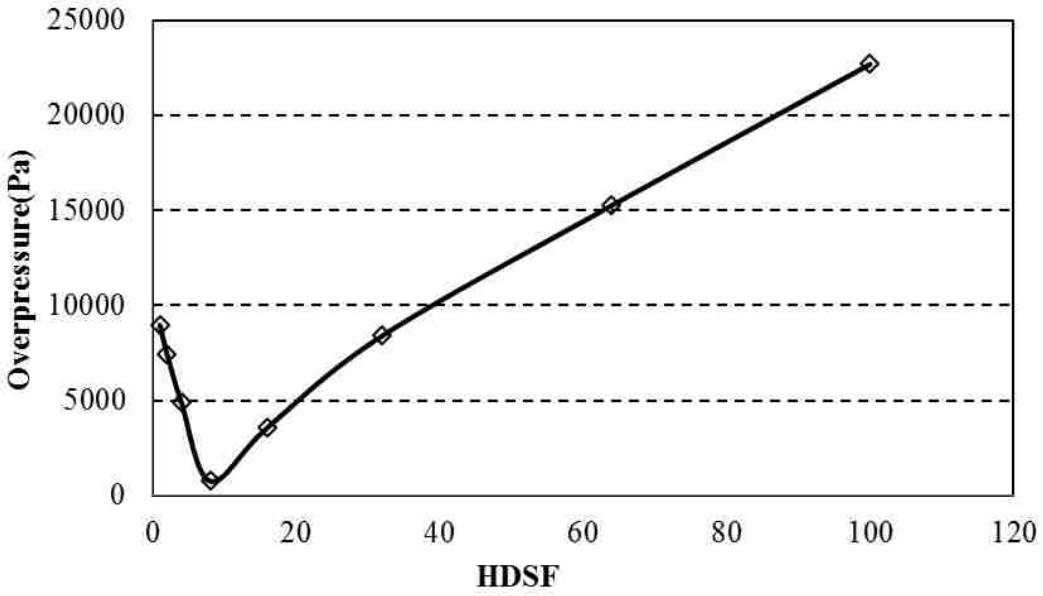

(d)

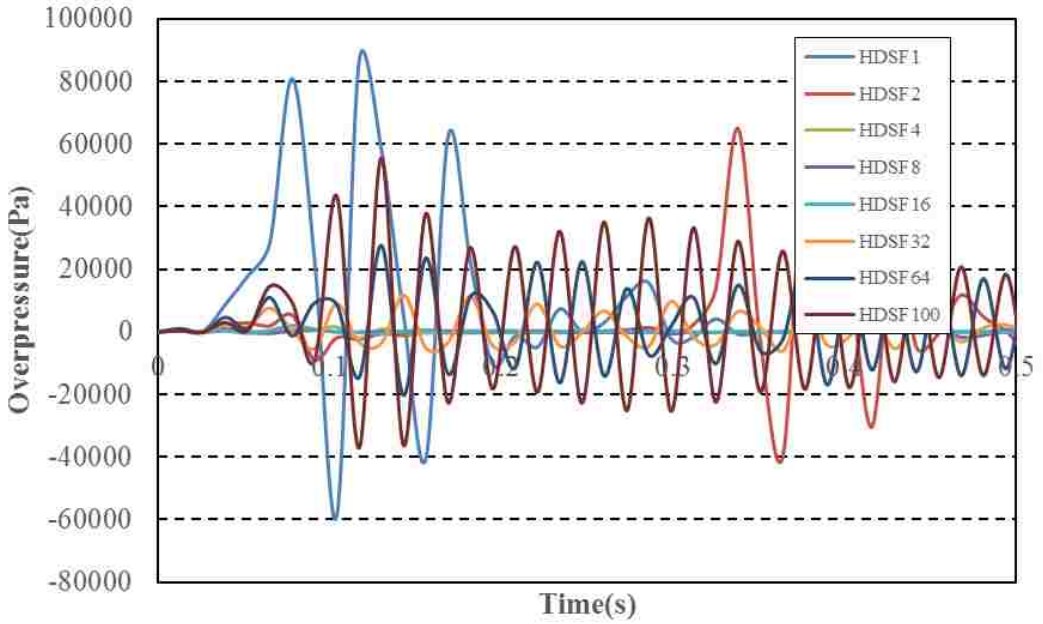

(e)

Figure 4.21. Peak overpressure (Pa) vs eight HDSF (m/m) combined with five FLSFs for 12% methane explosion; (a) pressure histories when FLSF=0.5; (b) peak overpressures when FLSF=0.5; (c) pressure histories when FLSF=1; (d) peak overpressures when FLSF=1; (e) pressure histories when FLSF=2; (f) peak overpressures when FLSF=2; (g) pressure histories when FLSF=4; (h) peak overpressures when FLSF=4; (i) pressure histories when FLSF=8; (j) peak overpressures when FLSF=8 (cont.)

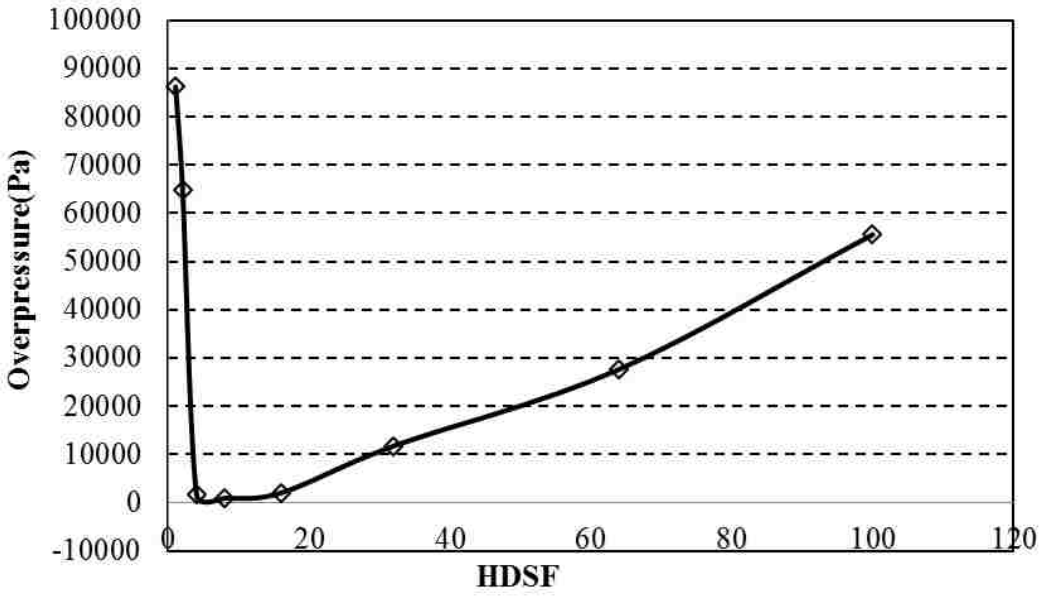

(f)

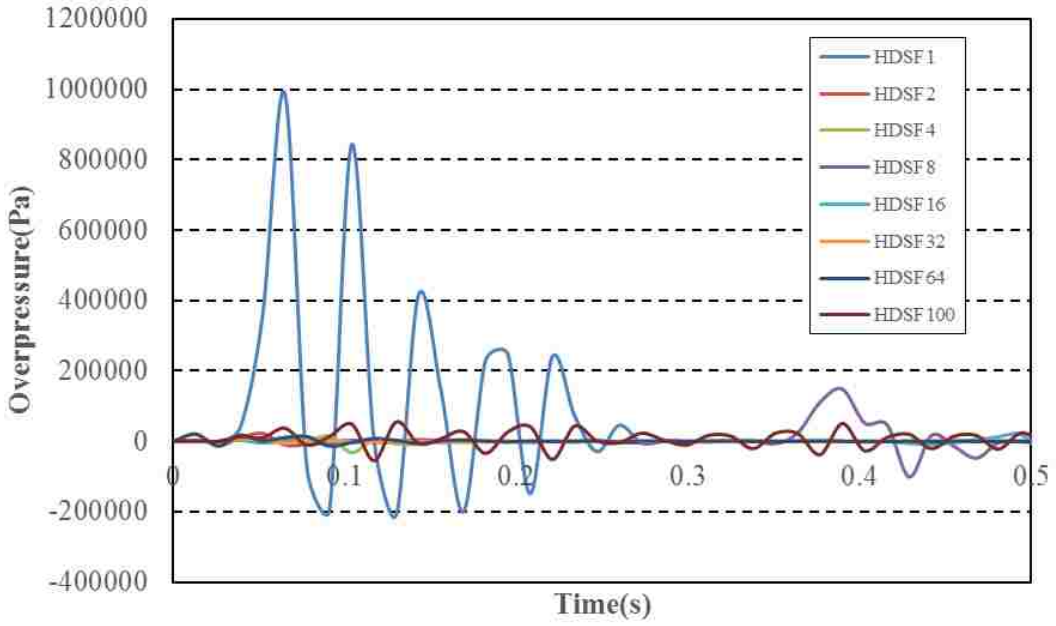

(g)

Figure 4.21. Peak overpressure (Pa) vs eight HDSF (m/m) combined with five FLSFs for 12% methane explosion; (a) pressure histories when FLSF=0.5; (b) peak overpressures when FLSF=0.5; (c) pressure histories when FLSF=1; (d) peak overpressures when FLSF=1; (e) pressure histories when FLSF=2; (f) peak overpressures when FLSF=2; (g) pressure histories when FLSF=4; (h) peak overpressures when FLSF=4; (i) pressure histories when FLSF=8; (j) peak overpressures when FLSF=8 (cont.)

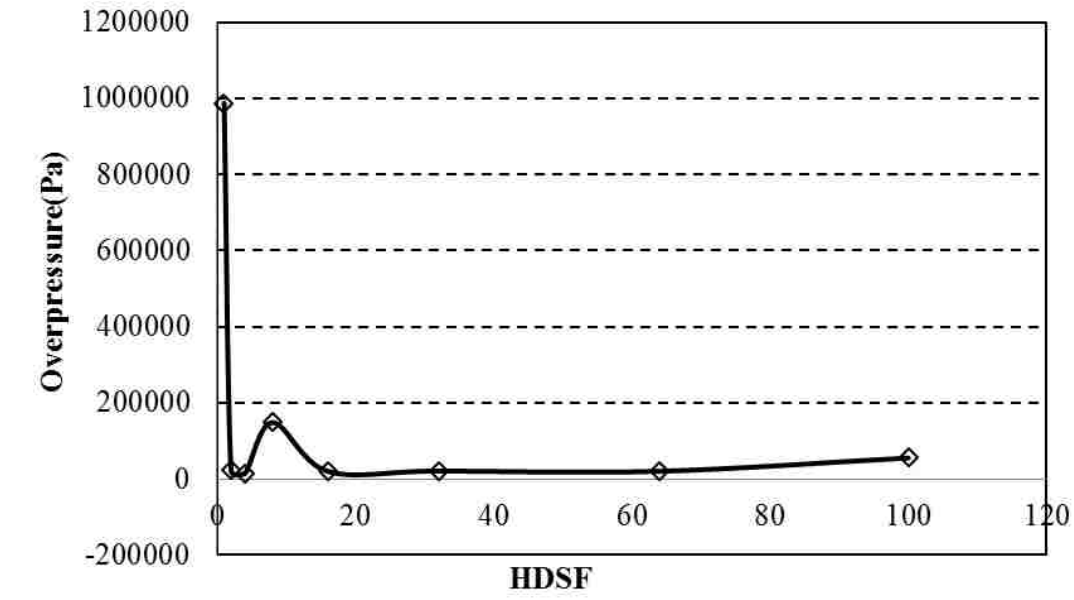

(h)

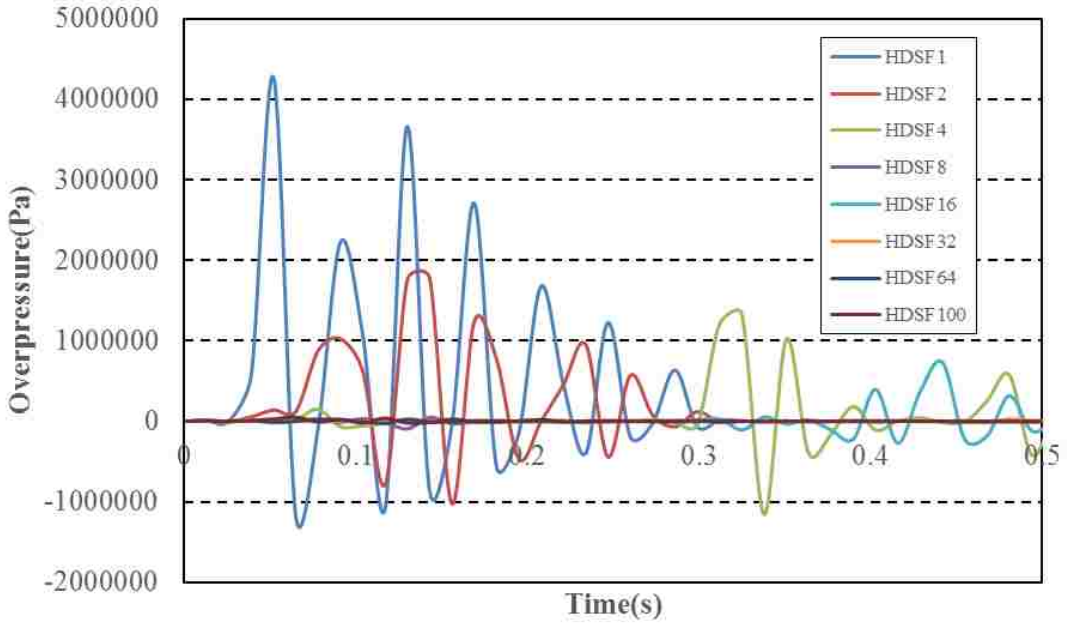

(i)

Figure 4.21. Peak overpressure (Pa) vs eight HDSF (m/m) combined with five FLSFs for 12% methane explosion; (a) pressure histories when FLSF=0.5; (b) peak overpressures when FLSF=0.5; (c) pressure histories when FLSF=1; (d) peak overpressures when FLSF=1; (e) pressure histories when FLSF=2; (f) peak overpressures when FLSF=2; (g) pressure histories when FLSF=4; (h) peak overpressures when FLSF=4; (i) pressure histories when FLSF=8; (j) peak overpressures when FLSF=8 (cont.)

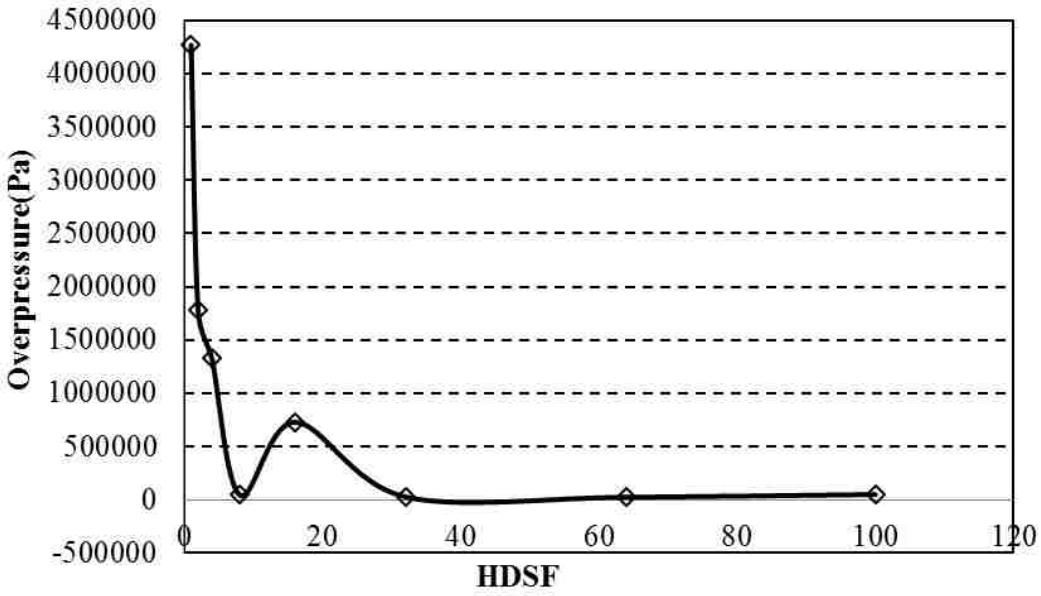

(j)

Figure 4.21. Peak overpressure (Pa) vs eight HDSF (m/m) combined with five FLSFs for 12% methane explosion; (a) pressure histories when FLSF=0.5; (b) peak overpressures when FLSF=0.5; (c) pressure histories when FLSF=1; (d) peak overpressures when FLSF=1; (e) pressure histories when FLSF=2; (f) peak overpressures when FLSF=2; (g) pressure histories when FLSF=4; (h) peak overpressures when FLSF=4; (i) pressure histories when FLSF=8; (j) peak overpressures when FLSF=8 (cont.)

Figure 4.21 uses the same layout as Figure 4.13 and Figure 4.17 where Figures 4.21 (a), (c), (e), (g), and (i) show overpressure histories under eight HDSFs given one selected FLSF and Figures 4.21 (b), (d), (f), (h), and (j) show the peak overpressures under each HDSF. In Figure 4.21 (b), the peak overpressure decreases slightly to around zero and then increases monotonically in cases where FLSF equals to 0.5. In the FLSFs of 0.5, 1, and 2 groups (Figures 4.21 (b), (d), and (f),), the peak overpressures yield the same trend. For the FLSFs of 4 and 8 (Figures 4.21 (h) and (j)), the peak overpressures decrease sharply at first and then, after small fluctuations, sustain to a certain level. In the FLSF of 4 case, the overpressures in HDSF of 1 are much higher than other HDSFs where DDT is about to be triggered. The two detonation scenarios occur when FLSF equals to 8 that are close to left end of the curves shown in Figure 4.21 (j).

Figure 4.22 summarizes the relationships among predicted overpressure of all five FLSFs in a logarithmic coordinate system.

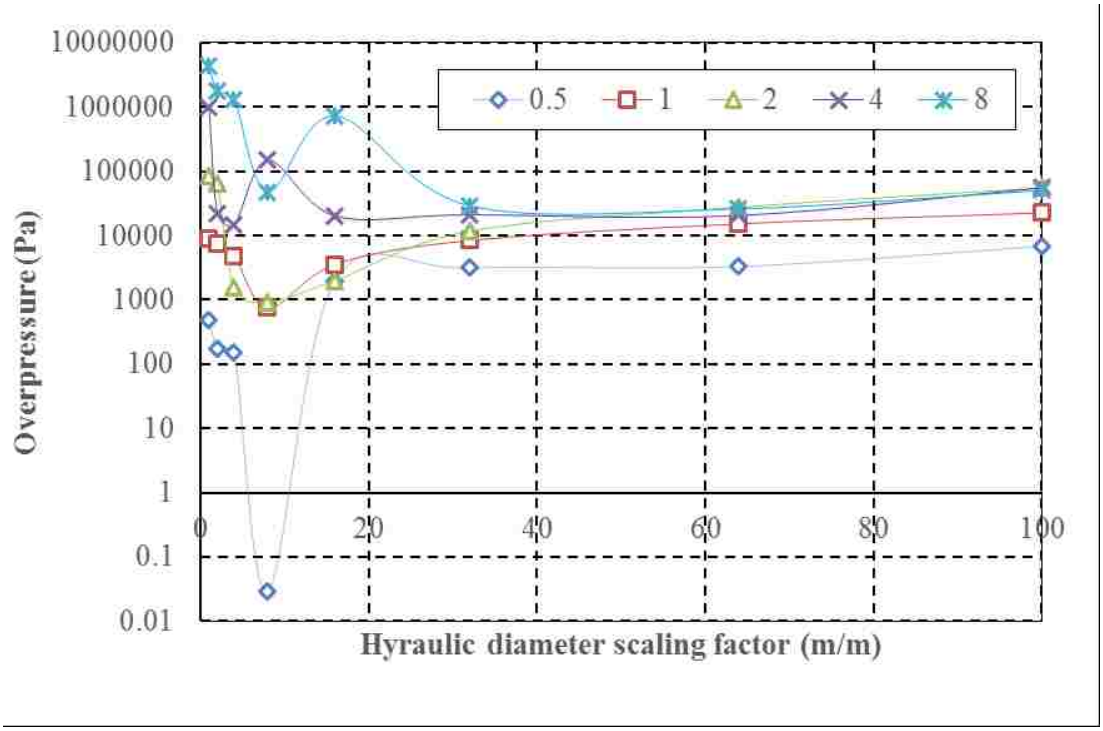

Figure 4.22. Peak overpressure for 12% methane explosion change with HDSFs for five FLSFs (curves)

From Figure 4.22, two data points within detonation regime (peak overpressure larger than 1,600,000 Pa) are found when the HDSF is small. It is located at the left end of the figure. Significant decreases of peak overpressure are found when HDSF is smaller than 16 for all scenarios except when FLSF equals to 4 (see the purple curve with × sign). The FLSF curves rise back to a high level before the HDSF of 20.

4.4.2.3 Combined effects. The combined effects considering both FLSFs and HDSFs are illustrated in Figure 4.23.

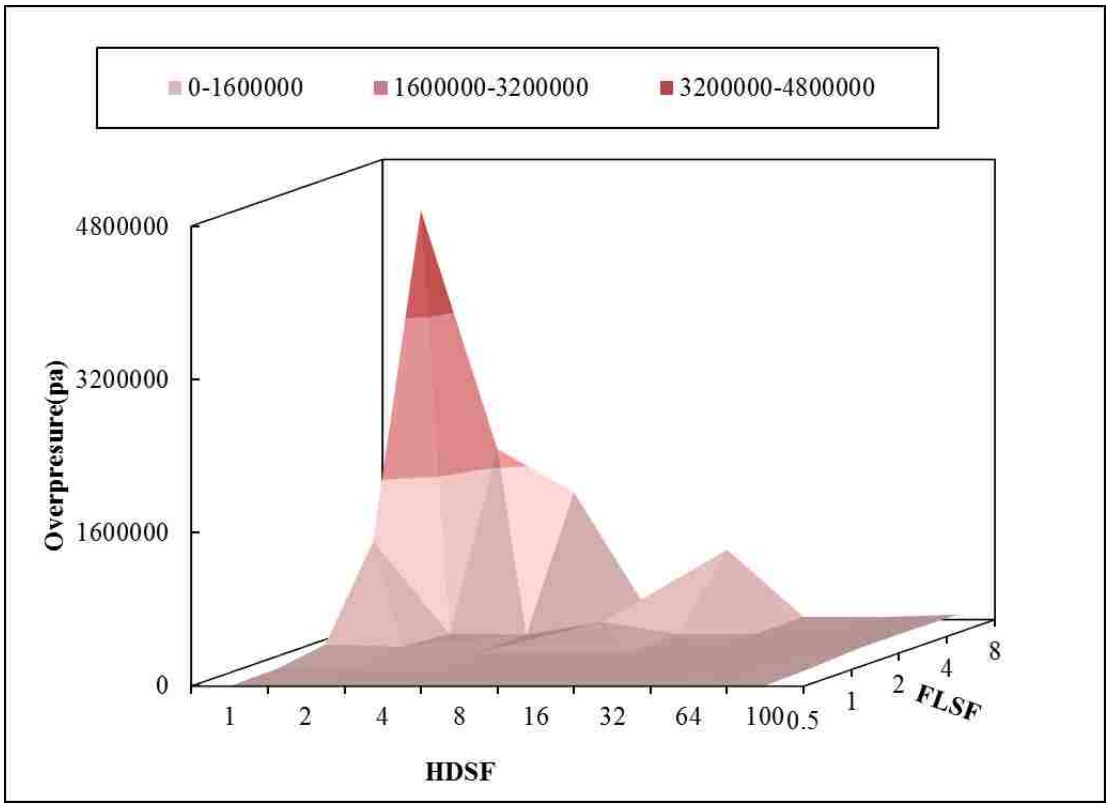

Figure 4.23. Effects of FLSF and HDSF on peak overpressure for 12% concentration methane explosion (Pa)

The bottom layer of the surface with light red in Figure 4.23 shows the peak overpressures for the 12% methane concentration within a deflagration regime (0-1,600,000 Pa). The part of the surface above the bottom layer is in the detonation regime. As can be seen in this figure, the detonation regime is located in the right-top corner of the FLSS-HDSF plane, where large gas-fill length to hydraulic diameter ratio is reached. The minimum length to diameter ratio for a detonation is 212.5 in the 12% concentration. This result suggests DDT is the most unlikely to happen under the 12% methane concentration among the three selected concentrations.

Table 4.4 below shows the peak overpressures for all selected HDSF-FLSF combinations when the methane concentration equals to 12%. The detonation cases are

represented in bold numbers. As observed from this table, only two detonation cases at the right top corner are recorded. Compared to 8% (14.8 MPa) and 9.5% (12.5 MPa) methane concentrations, smaller maximum peak overpressure is generated by the 12% (4.2 MPa) concentration methane explosions.

Table 4.4. Peak overpressure for selected combinations of HDSFs and FLSFs for 12% methane explosion (Pa)

HDSF \ FLSF	0.5	1	2	4	8
1	490	8959	86233	987772	**4268920**
2	175	7439	64934	22446	**1778456**
4	149	4876	1566	14752	1326657
8	1	751	923	148550	48136
16	1963	3573	1996	20263	729814
32	3134	8403	11732	21117	29052
64	3310	15258	27637	20592	26178
100	6828	22690	55580	55525	50531

Results can be drawn from the analysis above as follows: at the concentration of 8%, DDT is most readily to be triggered among three selected concentrations. The maximum detonation overpressure for 8% methane explosion is also the largest. The 12% concentration level, however, has the most stringent requirement to trigger DDT. The detonation pressures at the 12% level are also significantly smaller than those observed for the 8% and 9.5% concentration levels.

4.5. CONCENTRATION INFLUENCE

Figure 4.24 compares the overpressure histories for 8%, 9.5%, and 12% when their maximum overpressures are reached.

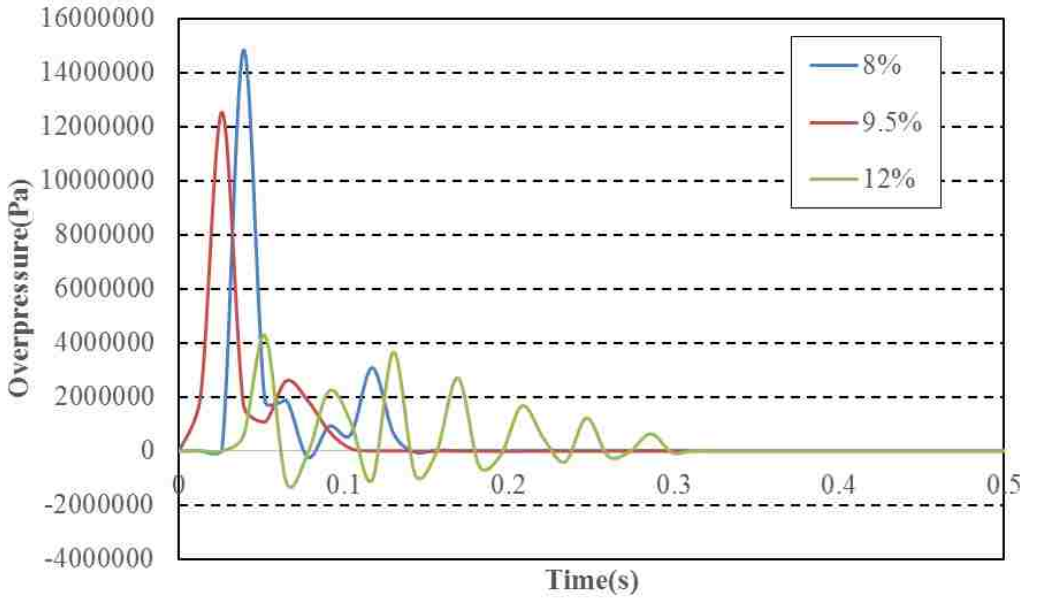

Figure 4.24. Overpressure histories for 8%, 9.5%, and 12% (curves in blue, red, and green) under maximum cases

Figure 4.24 shows the overpressure fluctuation curves recorded in a length to diameter ratio of 9.5 of the explosion duct with methane concentrations of 8%, 9.5%, and 12%, respectively. As can be seen in this figure, the 8% case (blue curve) has the largest peak overpressure which is larger than 14 MPa; while the 9.5% case reaches around 12 MPa (red curve). As for the 12% concentration (green curve), no sustainable detonation has been found. The maximum overpressure within the range of dimensions under all three concentration levels is around 4 MPa which is the smallest among the three. Additionally, the blast-wave under a concentration of 9.5% has a smaller arrival time than do the other two concentrations. The compressive wave takes the longest time under the 12% concentration level to reach the pressure sensor at about 0.04 s when the green curve start to go up.

4.6. SUMMARY

In order to develop the explosion source database, the methane explosion characteristics in the driver section were first investigated. Methane concentration and

explosion site geometry are considered two of the major factors to affect the explosion overpressure. As shown, methane explosion has three possible conditions: deflagration, detonation, and sustainable detonation, with different explosion mechanisms. From the simulation results, three methane concentrations provided different orders of magnitude of peak overpressures. In this Section, methane explosion characteristics have been examined for three methane concentration levels (8%, 9.5%, and 12%) and specific site geometries by using scaling-factors. Detonation and sustainable detonation cases were obtained in large length to diameter ratios for the 8% and 9.5% cases.

Based on the preceding analysis in this Section, four main conclusions can be drawn: (1) detonation occurs more easily in a methane accumulated space which has large length-to-diameter ratio. (2) For the concentration of 8%, DDT is most readily triggered at the lowest length-to-diameter ratio of 13.3, compared to 54 for the 9.5%, and 212 for the 12%. (3) An 8% methane concentration level has the largest peak overpressure of more than 14 MPa, while the 9.5% has around 12 MPa. Finally, (4) one sustainable detonation is detected for 9.5% case while two are found in the case of 8%. For the concentration of 12%, no sustainable detonation was found within the dimensions covered in this research.

5. EFFECT OF GEOMETRIC CHANGES

5.1. INTRODUCTION

The influences of geometric changes of airways on blast-wave propagation should not be neglected while studying gaseous explosions. This section will provide quantificational analysis of these influences on mechanics of blast-wave propagation. The results will be used to include the attenuation effect of a specific geometric change in the network-based 1D simulation introduced and discussed in Section 6.

5.1.1. Problem Statement. The most common types of geometric changes in underground coal mines are bends, branches, obstacles, and cross-sectional changes. Empirically speaking, their presence could result in attenuations of the blast-wave. However, as it has been discussed in Section 1.3.2, geometric changes such as bends could also strengthen a blast-wave in some circumstances. Numerical tools are used to quantify the attenuation effects of selected types of geometric changes. Lab-scaled experiment has been done to validate the numerical model used. This quantificational study could provide mine planners a better understanding of the range and propagation of an explosion by considering the geometrical characteristics of an underground airway layout. The effect of a geometric change is quantified by employing a coefficient, called an Attenuation Factor. The Attenuation Factor is the ratio of the peak overpressure upstream to a geometric change and peak overpressure downstream. Attenuation Factors will be calculated for selected types of geometric change throughout this section. They have proven useful to adjustments of overpressure distributions when conducting network-based simulations (more than two airways are included in an airway system).

5.1.2. Governing Equations. The elementary governing equations of fluid dynamic were introduced in Section 2. In the numerical studies of the driver section, 3D NS (Navier-Stokes) conservation equations, turbulence, and chemical reactions were used. However, when attempting to model a blast-wave propagating through a geometric change, a 2D Euler model is considered appropriate if turbulence and reaction are no longer factors. The flow should be considered as both transient and compressible since a blast-wave is highly time dependent and of high-speed propagation. According to the above assumptions, the trimmed equations used are demonstrated as following.

$$\frac{D\rho}{Dt} + \rho(\frac{\partial u}{\partial x} + \frac{\partial v}{\partial y})=0 \quad (5.1)$$

$$\rho\frac{Du}{Dt} = -\frac{\partial P}{\partial x} \quad (5.2)$$

$$\rho\frac{Dv}{Dt} = -\frac{\partial P}{\partial y} \quad (5.3)$$

$$\rho\frac{De}{Dt} + \rho\left(\frac{\partial u}{\partial x} + \frac{\partial v}{\partial y}\right) = \frac{DQ}{Dt} - \left(\frac{\partial q}{\partial x} + \frac{\partial q}{\partial y}\right) \quad (5.4)$$

$$p = \rho RT \quad (5.5)$$

The equations above are called Euler equations, and are assumed to be inviscid. Note that in the Euler equations, the viscous terms in momentum equations are eliminated due to turbulent shear and are ignored in blast-wave section. The unsteady terms are retained to capture the transient nature of blast-wave propagation. All the terms in z direction are also eliminated due to the 2D assumption.

5.1.3. Density Based Solver. The density-based method was used for simulations including geometric changes. A density-based solution is an alternative to the pressure-based solution employed by *ANSYS Fluent*. It solves Equations (5.1) to (5.4) simultaneously in vector forms. The advantage of it is to resolve transient flows when density changes significantly with respect to time, such as blast-wave propagation. Specifically, the primitive flow parameters are solved by the following four steps listed below:

(1) To update the primitive flow parameters from the last solution or given initial conditions

(2) To solve the continuity, momentum, and energy equations simultaneously to get flow parameters for the next time step.

(3) To use the updated flow parameters to solve separate scalars if appropriate.

(4) To check the convergence of the solution

Another feature of this numerical scheme is the usage of an explicit temporal scheme. An explicit scheme is different from the implicit schemes used by the 3D and 1D models, respectively. Its expression can be shown as:

$$\phi^{n+1} = \phi^n + \Delta t F(\phi^n) \quad (5.6)$$

where the superscripts represent the time level a flow parameter belongs to. n means the current time step while n+1 means the next time step.

5.2. NUMERICAL DETAILS

5.2.1. Meshing. To model the blast wave propagation through a geometric change, geometrical models should be developed and meshed (spatially discretized) before implementing a numerical simulation. The pre-process software *ANASYS Gambit* version 2.4.6 is used to develop the geometric models and mesh them. Unstructured quadrilateral meshing is used in all bends except for the 90° geometric change which requires a quadrilateral mapping structural mesh. For the Blockage Ratio (BR) cases, T-branching, and cross-sectional change cases, quadrilateral mapping is used.

5.2.1.1 Bends. The meshed geometrical models for computational domain of bends with angles of 30°, 40°, 50°, 90°, 120°, 140°, and 160°can be shown in Figures 5.1 to 5.7:

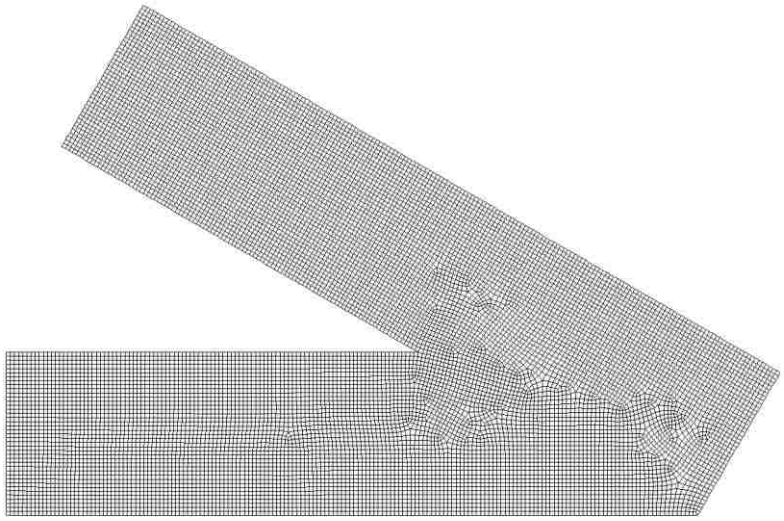

Figure 5.1. Meshed geometrical model of 30°bend

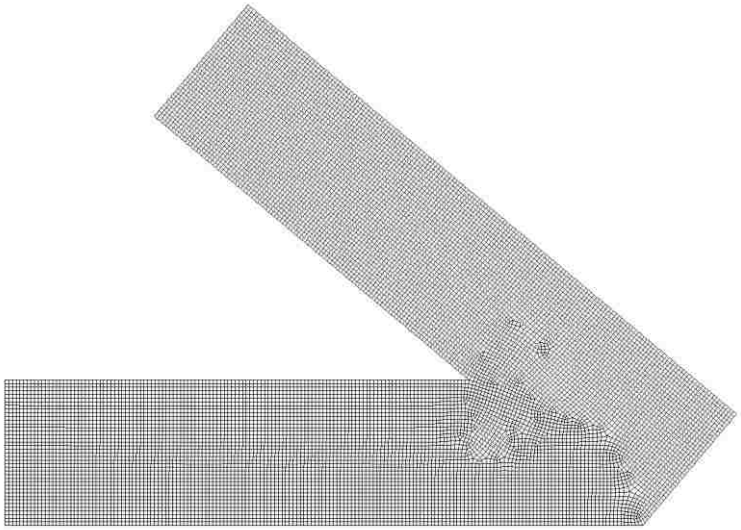

Figure 5.2. Meshed geometrical model of 40°bend

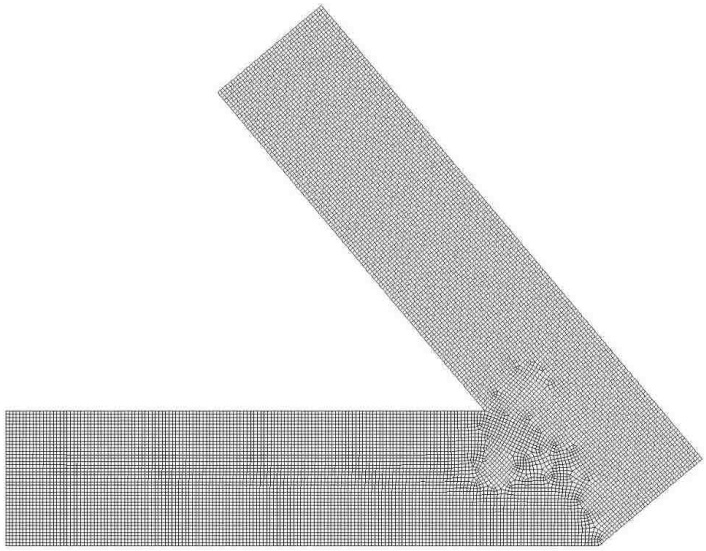

Figure 5.3. Meshed geometrical model of 50°bend

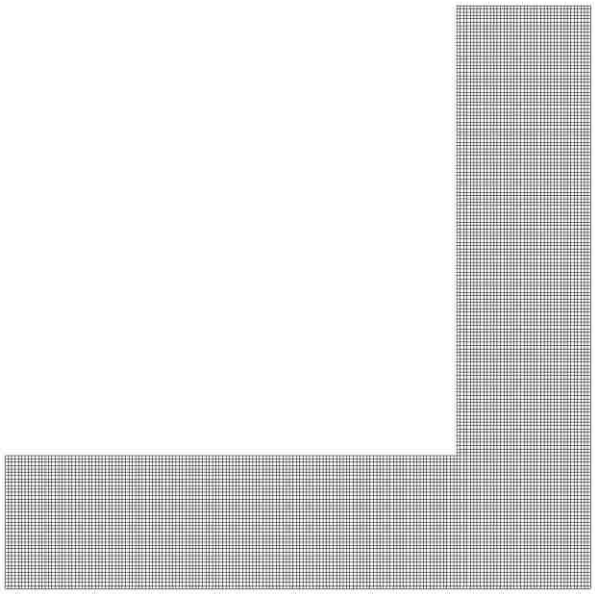

Figure 5.4. Meshed geometrical model of 90°bend

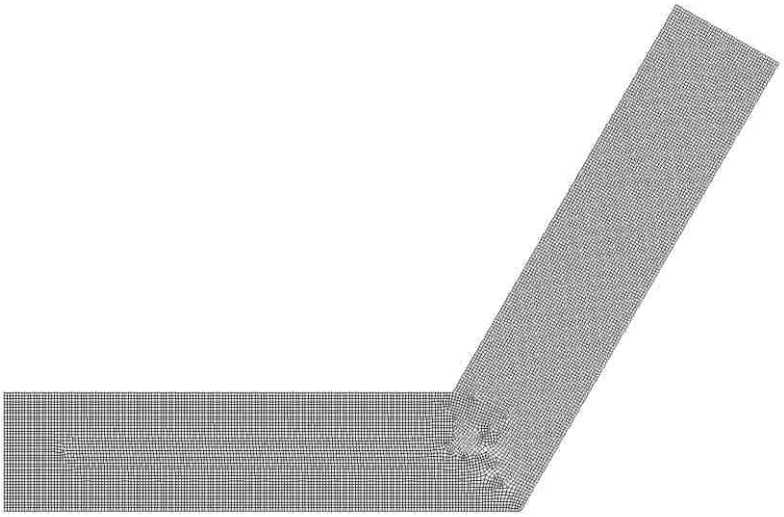

Figure 5.5. Meshed geometrical model of 120°bend

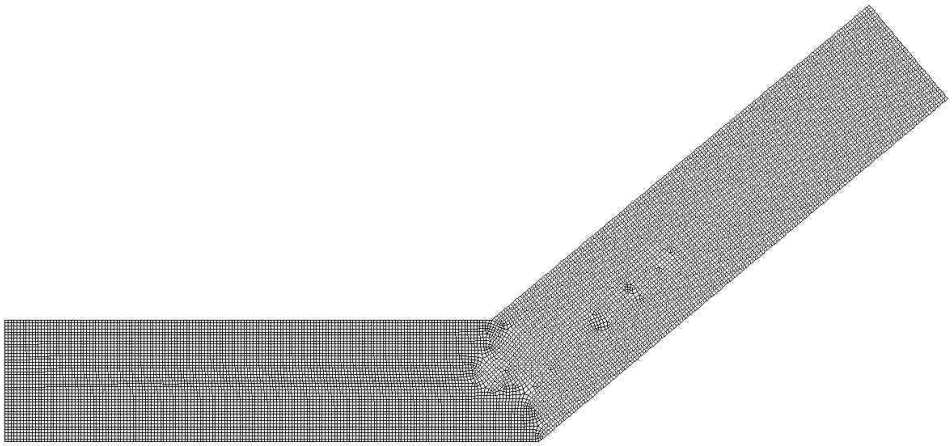

Figure 5.6. Meshed geometrical model of 140°bend

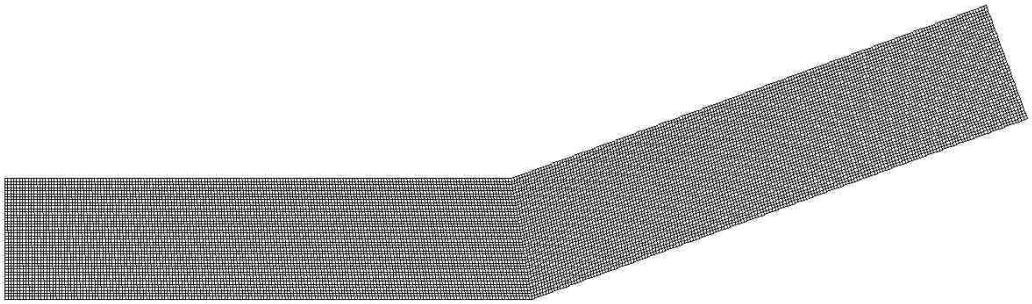

Figure 5.7. Meshed geometrical model of 160°bend

The length of a single arm of each bend is 0.35 m. The diameter of the ducts is 0.08 m. The bending angles are assigned to be 30°, 40°, 50°, 90°, 120°, 140°, and 160° as shown in Figures 5.1 to 5.7, respectively.

Detailed information regarding meshes and their quantity for the selected bends is summarized in Table 5.1.

Table 5.1. Information on meshes for bending cases

	30°	**40°**	**50°**	**90°**	**120°**	**140°**	**160°**
Number of cells	12,622	13,215	13,344	12,400	12,945	13,411	14,000
Number of Faces	25,580	26,867	27,055	25,150	25,523	26,446	28,390
Number of Nodes	12,959	13,654	13,712	12,751	13,313	13,788	14,391
Minimum Orthogonal Quality	0.881	0.895	0.898	1.000	0.884	0.881	0.985
Maximum Aspect Ratio	2.159	2.205	2.174	1.414	2.141	2.160	1.601

A mesh with Minimum Orthogonal Quality close to one is considered ideal quality, whereas a Maximum Aspect Ratio smaller than five is considered reasonable for analysis.

5.2.1.2 Obstacles. The meshed geometrical models for computational domain of obstacles with blockage-ratios of 25%, 50%, and 75% are shown in Figures 5.8 to 5.10:

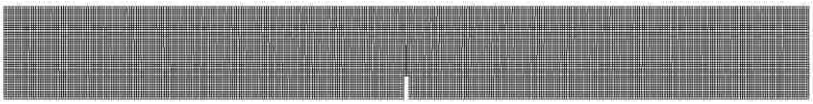

Figure 5.8. Meshed geometrical model of BR of 25%

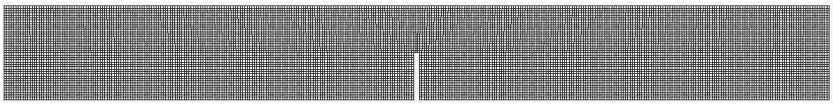

Figure 5.9. Meshed geometrical model of BR of 50%

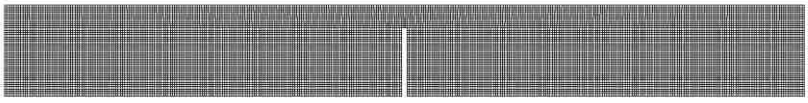

Figure 5.10. Meshed geometrical model of BR of 75%

The length of the selected duct is 0.705 m. The obstacle is located at 0.35 m downstream the inlet and is 0.005 m thick. The diameter of the duct is 0.08m.

5.2.1.3 T-branches and cross-sectional change. The meshed geometrical models are used for computational domain of the t-branches when air flows from the main and branch inlets. These are shown in Figures 5.11 and 5.12:

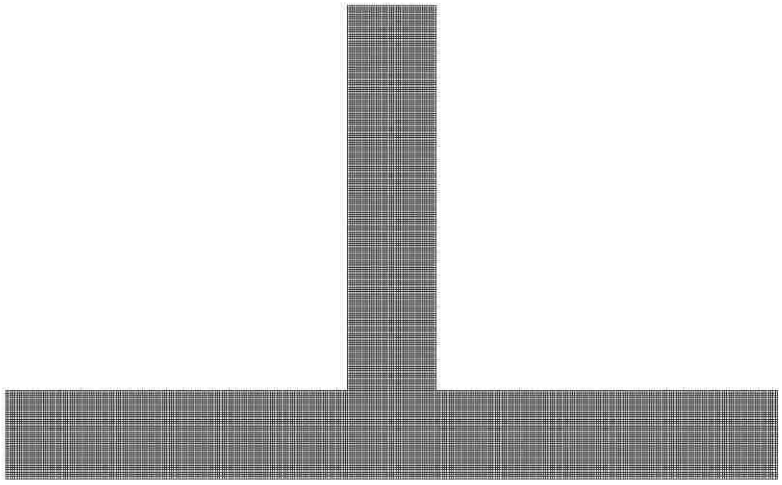

Figure 5.11. Meshed geometrical model of T-branch flow from main stream

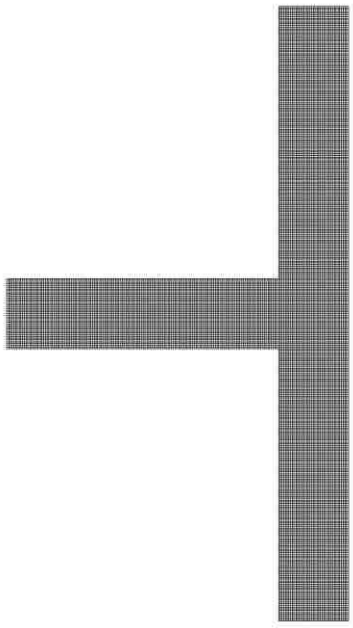

Figure 5.12. Meshed geometrical model of T-branch flow from branch stream

The meshed geometrical models for computational domain of cross-sectional change are shown in Figure 5.13:

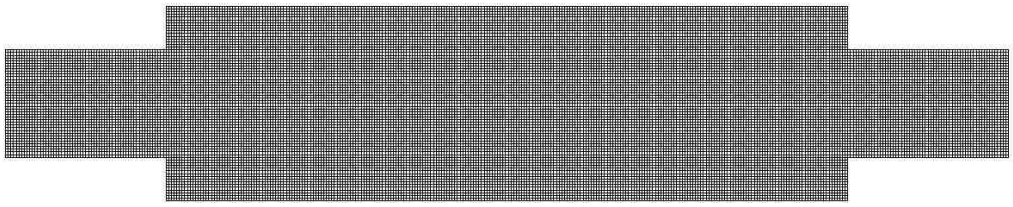

Figure 5.13. Meshed geometrical model of cross-sectional change

In the t-branch cases, the length of the three arms of t-branches is 0.35 m. The diameter of the duct is 0.08 m. For the cross-sectional change case, two segments of duct with smaller diameter are 0.12 m long and 0.08 m in diameter. In the expanded part, the length and diameter are 0.51 m and 0.145m, respectively.

The information about meshes and their mesh quantity for blockage-ratios, branches, and cross-sectional change case is summarized in Table 5.2.

Table 5.2. Information on meshes for obstacles with varying blockage-ratios (BR), branch, and cross-sectional change cases

	BR25%	**BR50%**	**BR75%**	**T_{branch}**	**T_{mian}**	**Cross-**
Number of cells	14,090	14,060	14,030	21,000	20,200	23,160
Number of Faces	28,583	28,533	28,483	42,565	40,945	46,767
Number of Nodes	14,494	14,474	14,454	21,566	20,746	23,608

Table 5.2. Information on meshes for obstacles with varying blockage-ratios (BR), branch, and cross-sectional change cases (cont.)

Minimum Orthogonal Quality	1.000	1.000	1.000	1.000	1.000	1.000
Maximum Aspect Ratio	1.564	1.566	1.570	1.414	1.414	1.425

5.2.2. Numerical Details. After the meshing process is completed, the governing equations can be solved in the discretized domains. The CFD general code *ANSYS Fluent* Cortex Version: 14.5.0 was employed as the solver. A density-based solution was used in all selected scenarios. Explicit schemes were used to discretize the computational domain and the time duration as well. Courant number (CFL) is set to be one to ensure that numerical calculations are stable for an explicit temporal discretization. Least squares cell based method is used for gradient treatment and third-order Monotonic Upstream-Centered Scheme for Conservation Laws (MUSCL) method is used for flow parameters. The time step size can be calculated by Equation (5.7) given that CFL equals to 1.

$$\Delta t = \frac{CFL \cdot V}{\Delta x} \tag{5.7}$$

where V is characteristic flow velocity magnitude and CFL is Δx is characteristic cell size.

CFD calculations were conducted using computer with quad-core i7 3770K and 16 Gb raw. Two parallel processes were used. The residuals are generally at e^{-01} level.

5.3. RESULTS

In this research study, the blast-wave passing through twelve different geometric considerations was simulated. The overpressures from experimental results were assigned to the numerical models where the upstream pressure sensors are located. For example, in

the t-branch case shown in Figure 5.14, if the experimental result of the eleventh pressure sensor (P11) of is 0.05 MPa, the region upstream of it will be assigned to be 0.05 MPa in the corresponding numerical model.

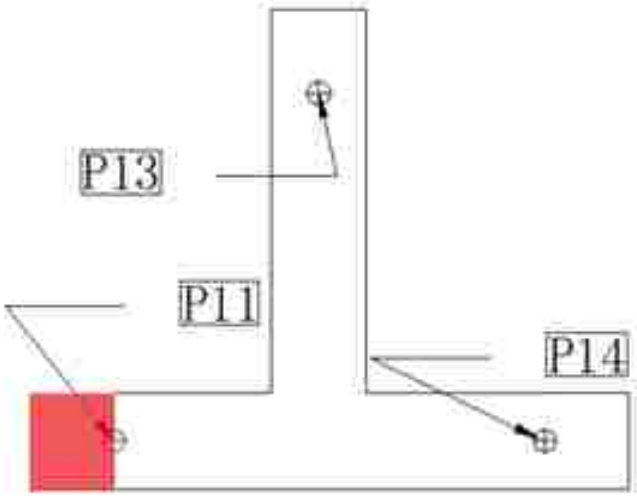

Figure 5.14. Pressure sensor layout and high over-pressure region

The inlet at the left end will be considered to be a pressure-inlet which has a constant pressure of 0.05 MPa to represent a sustainable blast-wave. In such setup, a simplification from a real blast-wave to the ideal blast-wave is made. Real blast-wave will decay after its wave front, while an ideal blast-wave does not decay. Under this assumption, the predicted pressure will be relatively higher than real cases. The simulation results for all five cases will be provided in this section.

To quantify the attenuation effect of a geometric change, the Attenuation Factor η is employed as expressed in Equation (5.8) (Jia, Liu, & Jing, 2011):

$$\eta = \frac{P_0}{P_1} \tag{5.8}$$

where P_0 and P_1 are the overpressure upstream and downstream of a selected geometric change, respectively. As stated, for a case of η greater than one, the blast-wave is

attenuated, since overpressure upstream is greater than that of downstream, and vice versa.

5.3.1. Bending. In this subsection, blast-waves propagating though seven bend scenarios; i.e., 30°, 40°, 50°, 90°, 120°, 140°, and 160°, are simulated. Their overpressure contours during propagation and overpressure histories, upstream and downstream of the bend will be demonstrated. The length of the arms of each bend is 0.35 m. Its diameter (width of the duct) is 0.08 m. The pressure sensor upstream is placed a distance of 0.12 m from the inlet, along the centerline of the duct. The sensor downstream the bend is placed 0.12 m from the outlet, along the duct centerline.

30° Bend. The predicted overpressure gradient contours after 25, 100, 200, and 300 time steps when blast-wave is passing through the 30° bend are shown in Figure 5.15 (make sure the numbers are correct) (a) through (d). Figure 5.15 (e) and (f) illustrate the overpressure contour at 0.000682 sec and 0.00137 sec when maximum overpressure of the first impulse is obtained by upstream and downstream sensors, respectively. The convergence is normally of a magnitude of e^{-1} for the continuity equation, and e^{-3} for other equations.

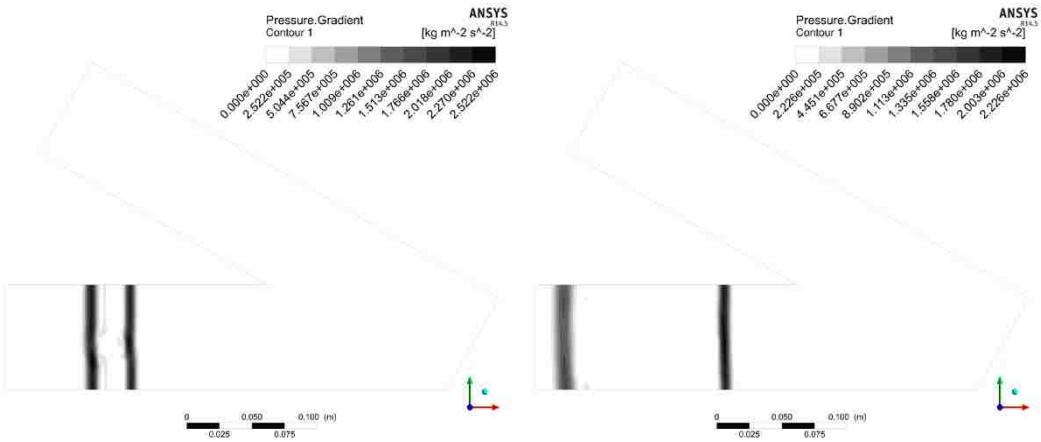

(a) (b)

Figure 5.15. Overpressure gradient contours for blast-wave propagating through 30° bend after (a) 25 time steps, (b) 100 time steps, (c) 200 time steps, (d) 300 time steps, and at (e) 0.000682 sec, and (f) 0.00137 sec

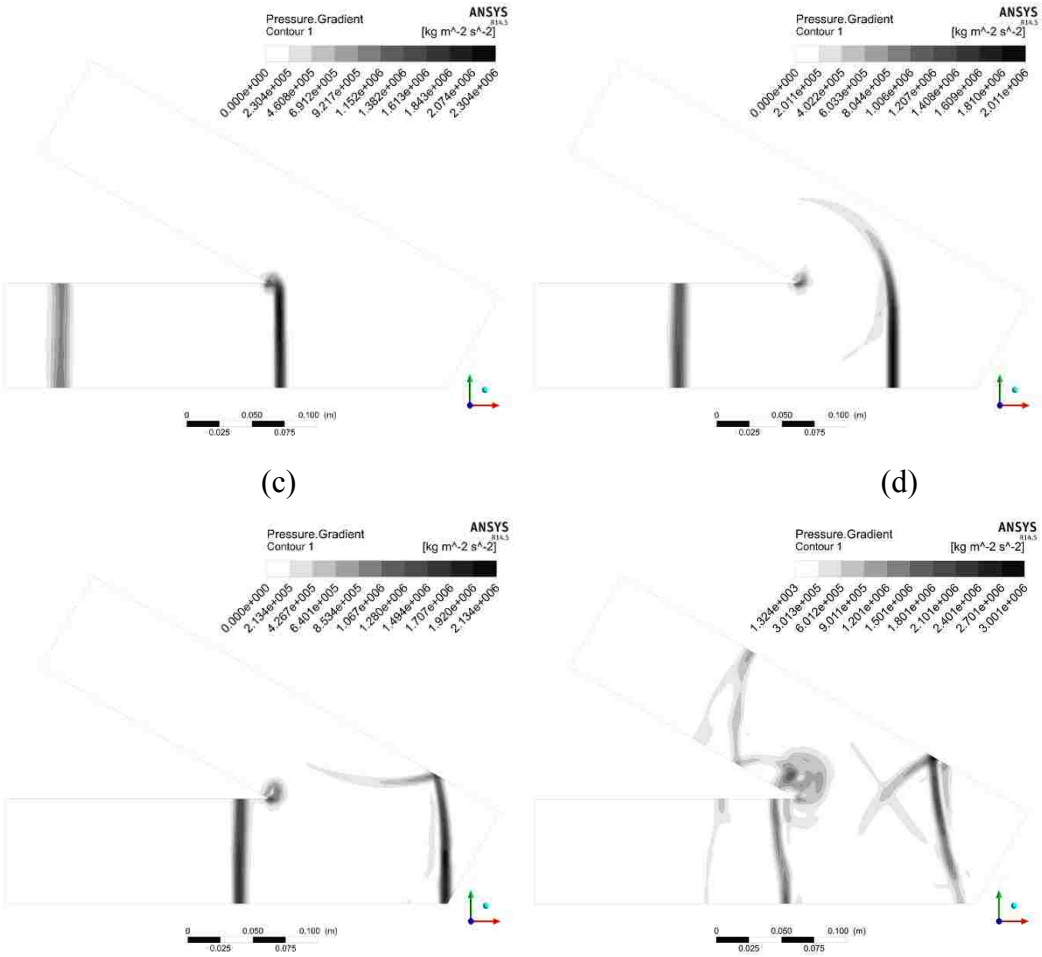

Figure 5.15. Overpressure gradient contours for blast-wave propagating through 30° bend after (a) 25 time steps, (b) 100 time steps, (c) 200 time steps, (d) 300 time steps, and at (e) 0.000682 sec, and (f) 0.00137 sec (cont.)

The overpressure histories upstream and downstream of the bend are demonstrated in Figure 5.16. The maximum overpressure for the first impulse upstream the bend is 24,616 Pa at 0.000682 sec, while the attenuated maximum overpressure for the first impulse downstream the bend is 21,400 Pa at 0.00137 sec, the Attenuation Factor η is 1.15.

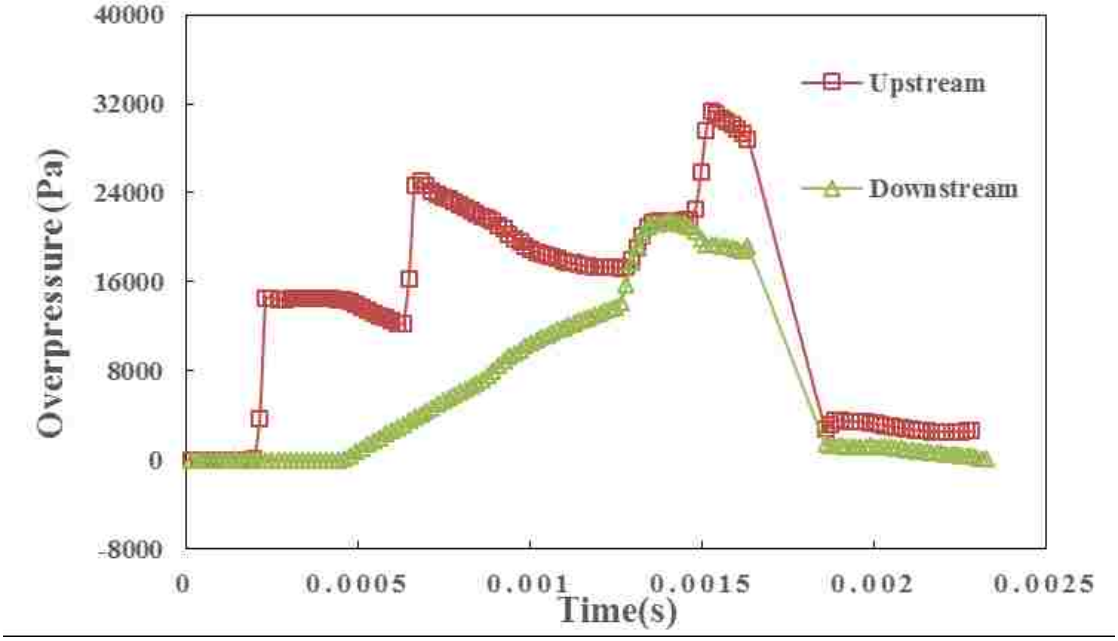

Figure 5.16. Overpressure histories upstream and downstream of the 30° bend

40° Bend. The predicted overpressure gradient contours after 25, 100, 200, and 300 time steps when blast-wave is passing through the 40° bend are shown in the Figure 5.17 (a) through (d). Figure 5.17 (e) and (f) show the overpressure contour at the time of 0.000691 sec and 0.00158 sec when maximum overpressures of the first impulse were obtained by upstream and downstream sensors, respectively.

It should be noted that, the bend with bending angles smaller than 40° are not included in this numerical research. The attenuation effect is assumed to be infinity when bending angle equals to 0° due to the duct being blocked. The design of ventilation airway with bending angle smaller than 40° needs to be avoided due to safety concerns.

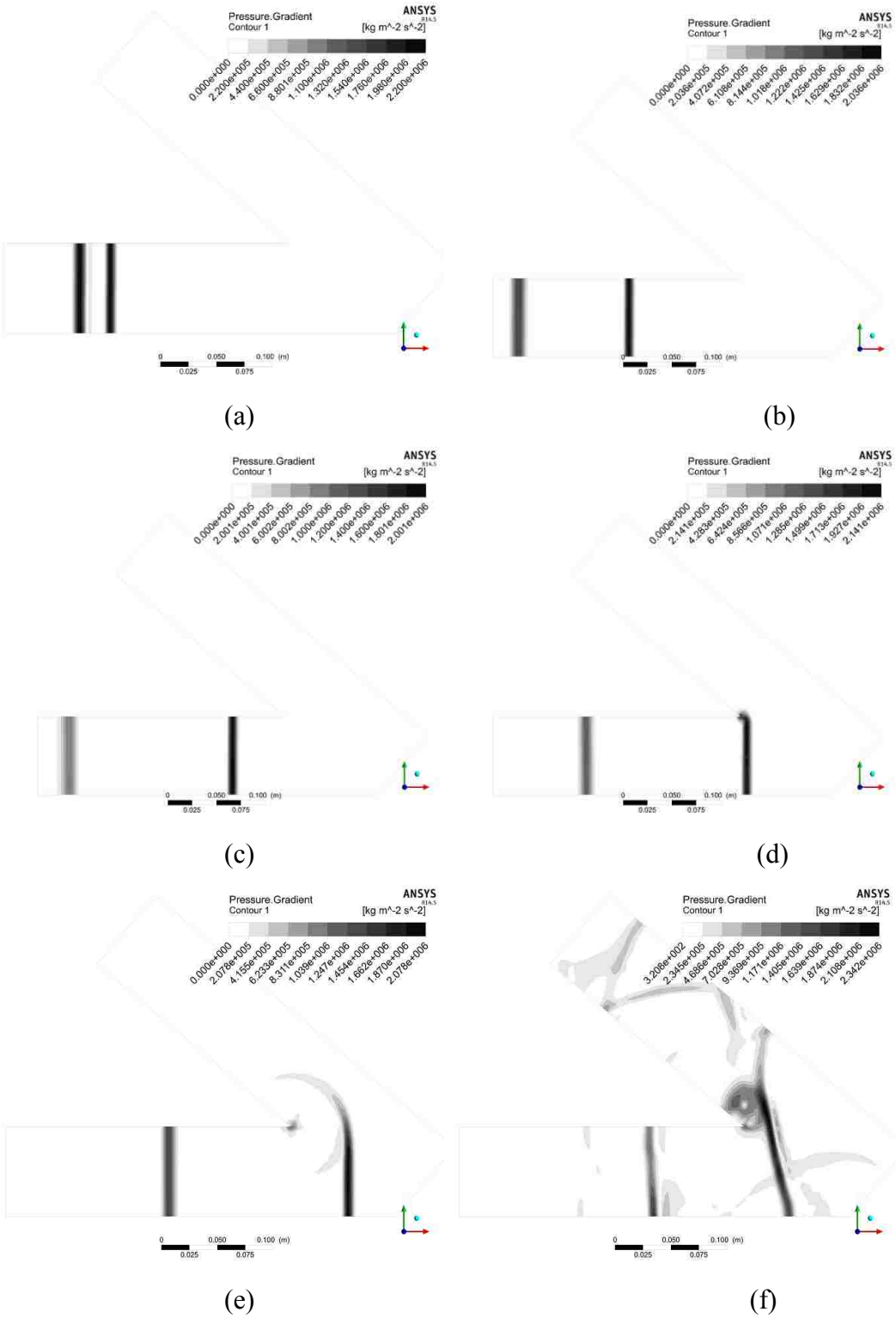

Figure 5.17. Overpressure gradient contours for blast-wave propagating through 40° bend at (a) 25 time steps, (b) 100 time steps, (c) 200 time steps, (d) 300 time steps; and at (e) 0.000691 sec and (f) 0.00158 sec

The overpressure histories upstream and downstream of the bend are demonstrated in Figure 5.18. The maximum overpressure for the first impulse upstream the bend is 28,422 Pa at 0.000691 sec, while the attenuated maximum overpressure for the first impulse downstream the bend is 23,418 Pa at 0.00158 sec, the Attenuation Factor η is 1.214.

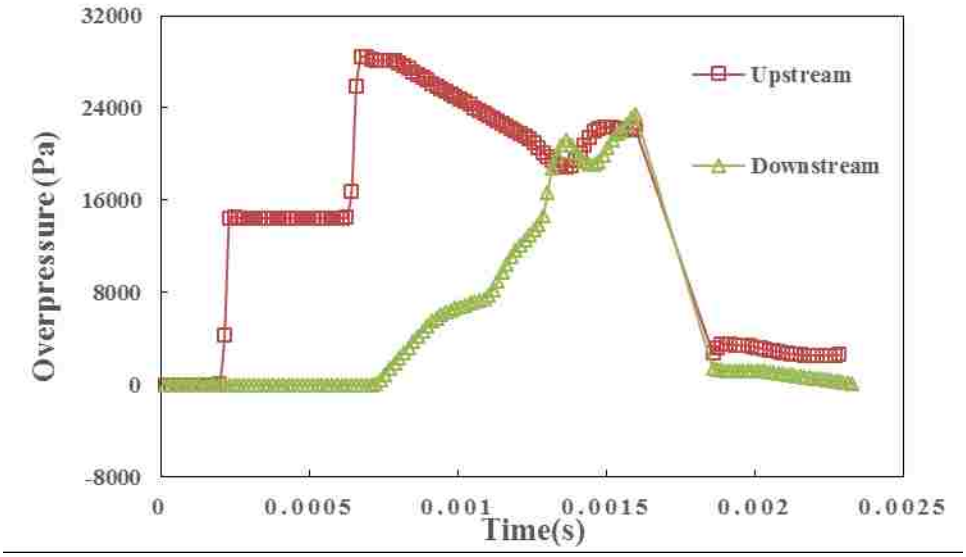

Figure 5.18. Overpressure histories upstream and downstream of the 40° bend

50° Bend. The predicted overpressure gradient contours after 25, 100, 200, and 300 time steps when blast-wave is passing through the 50° bend are shown in the Figure 5.19 (a) through (d). Figure 5.19 (e) and (f) show the overpressure contour at the time of 0.000595 sec and 0.00149 sec when maximum overpressures of the first impulse were obtained by upstream and downstream sensors, respectively.

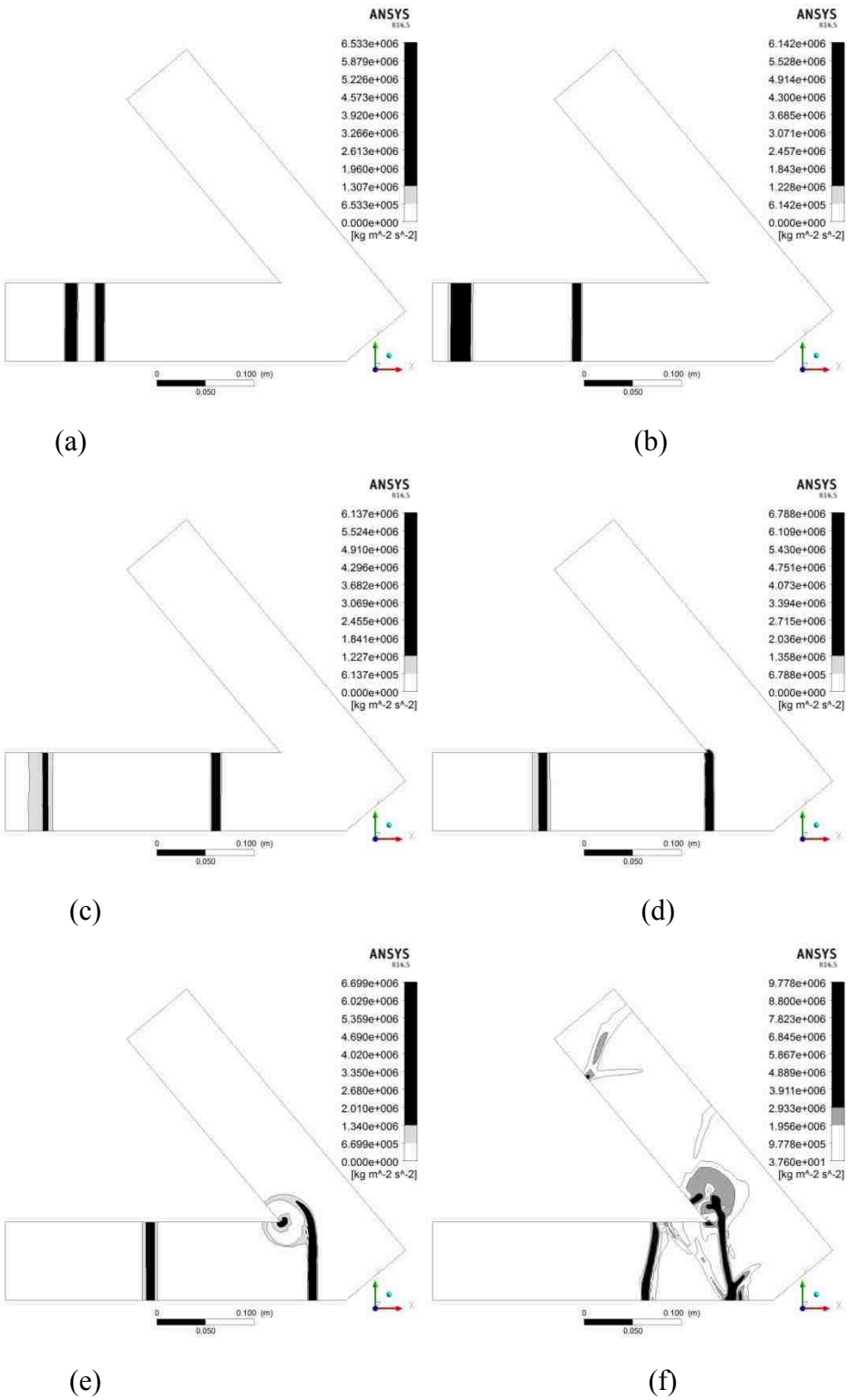

Figure 5.19. Overpressure gradient contours for blast-wave propagating through 50° bend at (a) 25 time steps, (b) 100 time steps, (c) 200 time steps, (d) 300 time steps; and at (e) 0.000595 sec and (f) 0.00149 sec

The overpressure histories upstream and downstream of the bend are demonstrated in Figure 5.20. The maximum overpressure for the first impulse upstream the bend is 70,100 Pa at 0.000595 sec, while the attenuated maximum overpressure for the first impulse downstream the bend is 45,703 Pa at 0.00149sec, the Attenuation Factor η is 1.534.

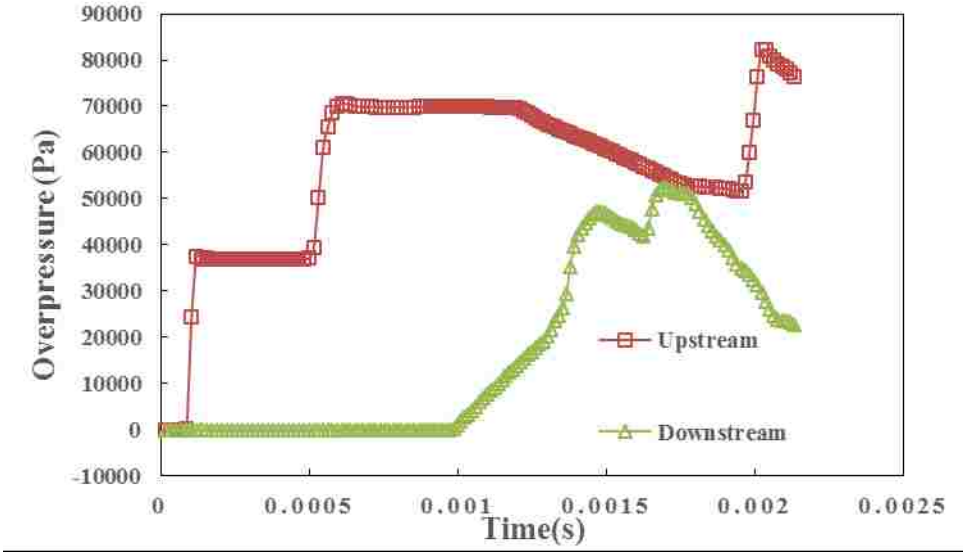

Figure 5.20. Overpressure histories upstream and downstream of the 50° bend

90° Bend. The predicted overpressure gradient contours after 25, 100, 200, and 300 time steps when blast-wave is passing through the 90° bend are shown in the Figure 5.21 (a) through (d). Figure 5.21 (e) and (f) show the overpressure contour at the time of 0.00136 sec and 0.00161 sec when maximum overpressures of the first impulse were obtained by upstream and downstream sensors, respectively.

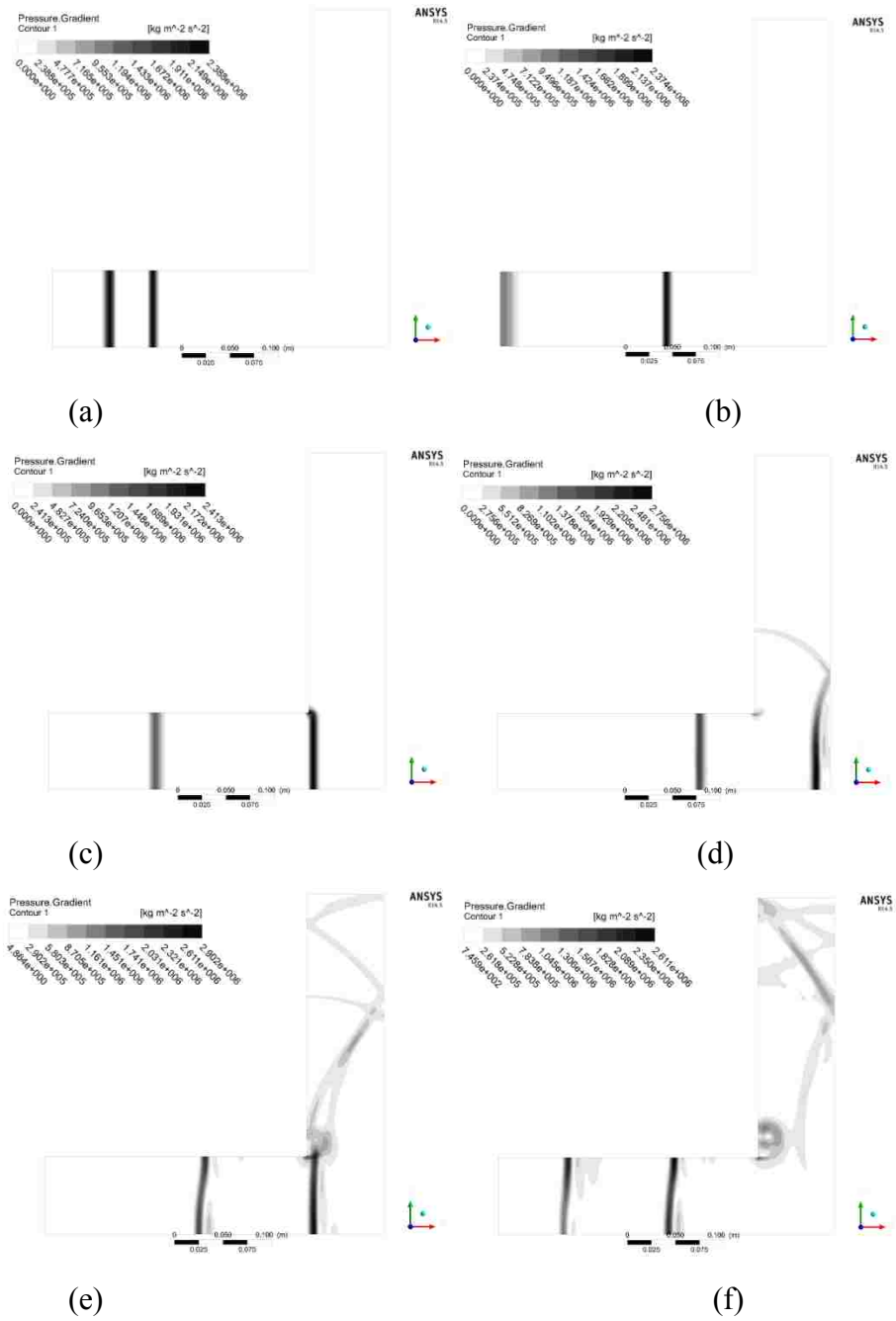

Figure 5.21. Overpressure gradient contours for blast-wave propagating through 90° bend after (a) 25 time steps, (b) 100 time steps, (c) 200 time steps, (d) 300 time steps; and at (e) 0.00136 sec and (f) 0.00161 sec

The overpressure histories upstream and downstream of the bend are demonstrated in Figure 5.22. The maximum overpressure for the first impulse upstream

the bend is 37,886 Pa at 0.00136 sec, while the attenuated maximum overpressure for the first impulse downstream the bend is 32,356 Pa at 0.00161 sec, the Attenuation Factor η is 1.171.

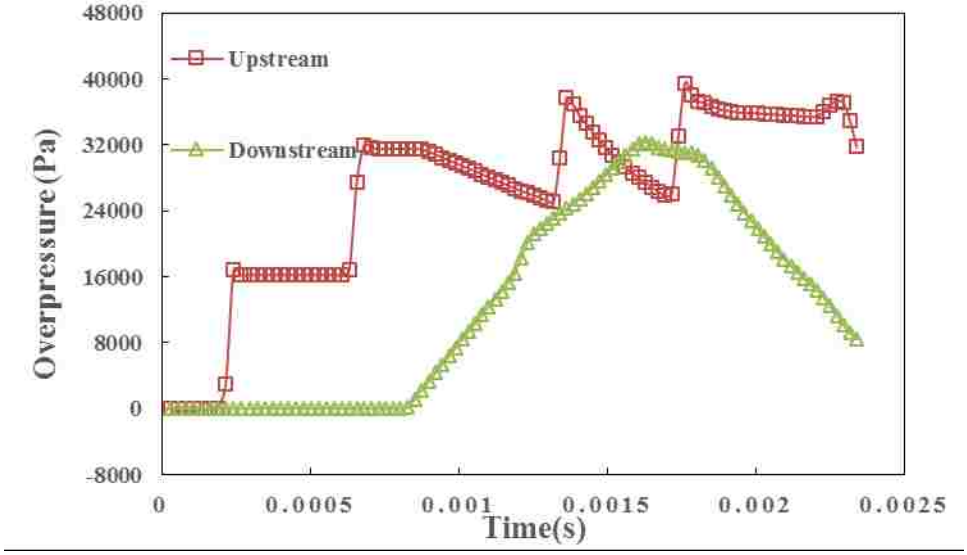

Figure 5.22. Overpressure histories upstream and downstream of the 90° bend

120° Bend. The predicted overpressure gradient contours after 25, 100, 200, and 300 time steps when blast-wave is passing through the 120° bend are shown in the Figure 5.23 (a) through (d). Figure 5.23 (e) and (f) show the overpressure contour at the time of 0.000679 sec and 0.00158 sec when maximum overpressures of the first impulse were obtained by upstream and downstream, sensors, respectively.

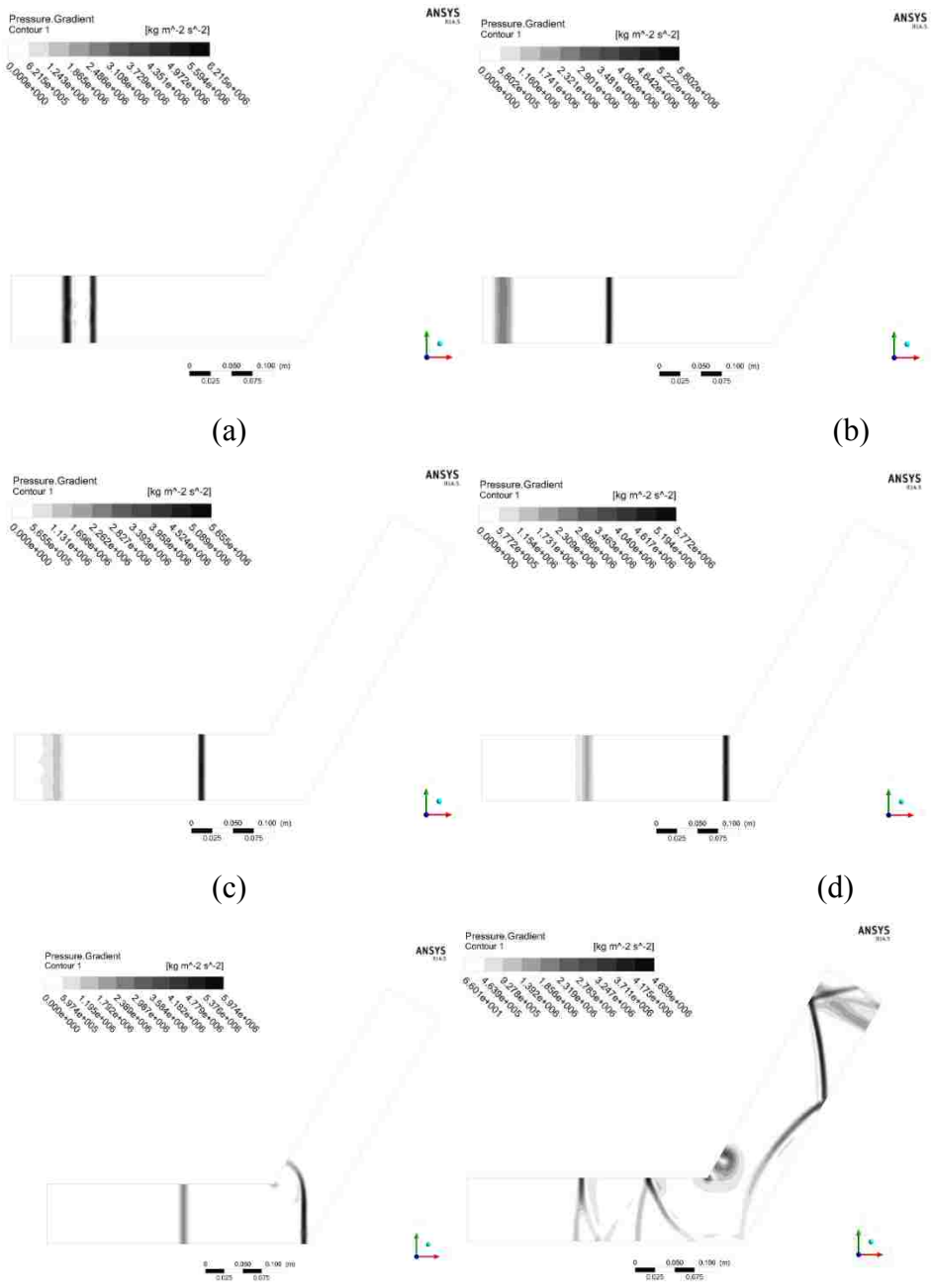

Figure 5.23. Overpressure gradient contours for blast-wave propagating through 120° bend after (a) 25 time steps, (b) 100 time steps, (c) 200 time steps, (d) 300 time steps; and at (e) 0.000679 sec and (f) 0.00158 sec

The overpressure histories upstream and downstream of the bend are demonstrated in Figure 5.24. The maximum overpressure for the first impulse upstream

the bend is 65,850 Pa at 0.000679 sec, while the attenuated maximum overpressure for the first impulse downstream the bend is 66,476 Pa at 0.00158 sec, the Attenuation Factor η is 0.991.

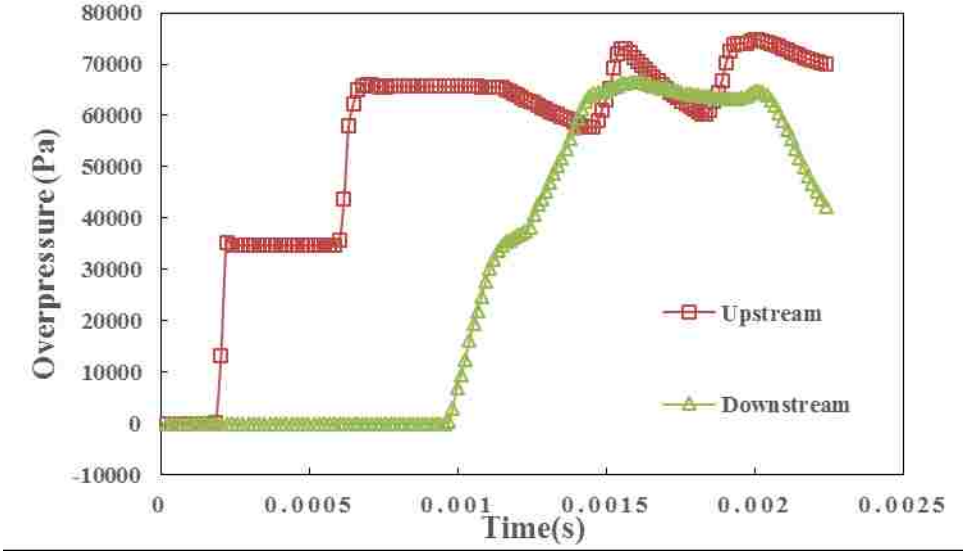

Figure 5.24. Overpressure histories upstream and downstream of the 120° bend

140° Bend. The predicted overpressure gradient contours after 25, 100, 200, and 300 time steps when blast-wave is passing through the 140° bend are shown in the Figure 5.25 (a) through (d). Figure 5.25 (e) and (f) show the overpressure contour at the time of 0.000692 sec and 0.00164 sec when maximum overpressures of the first impulse were obtained by upstream and downstream sensors, respectively.

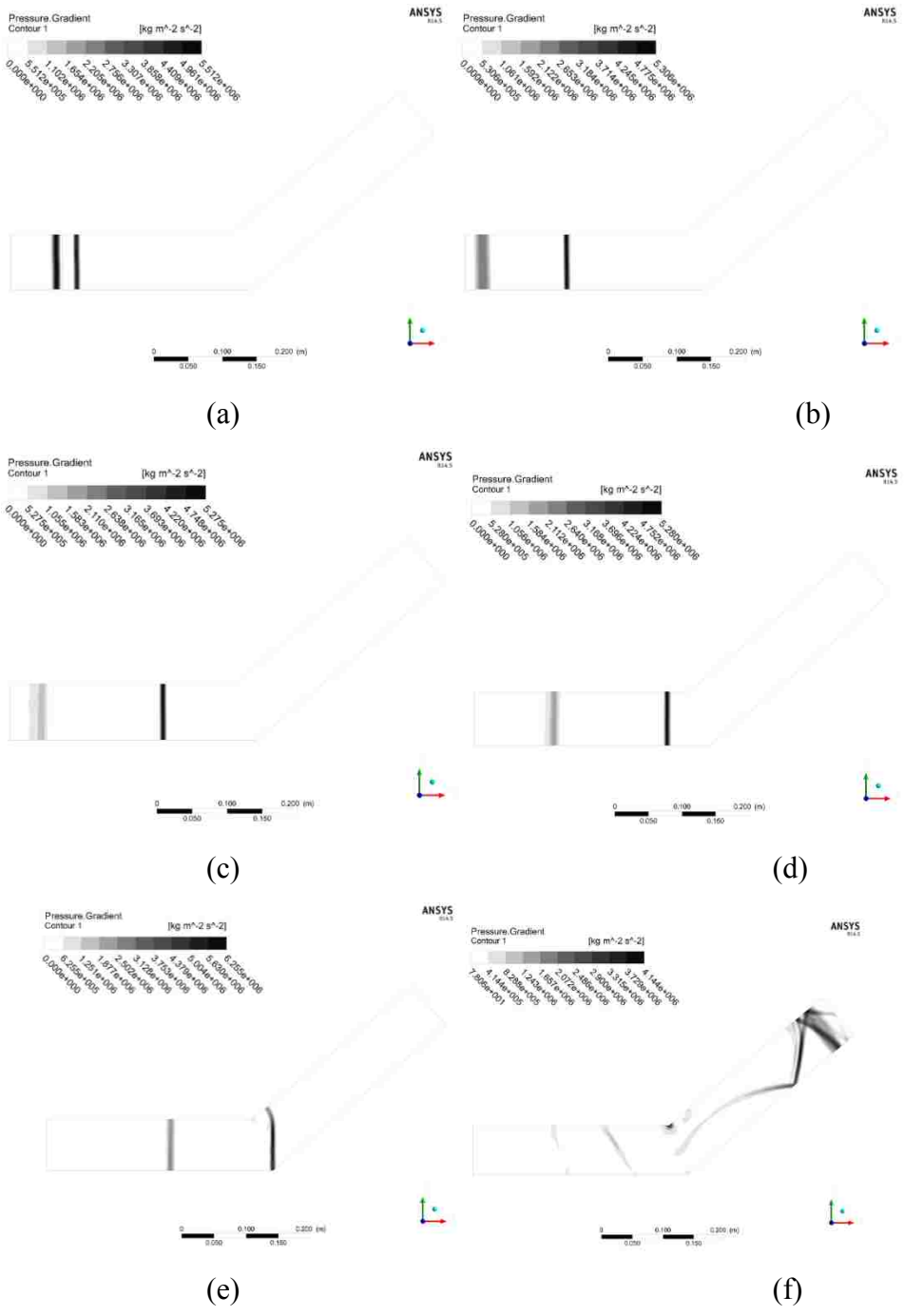

Figure 5.25. Overpressure gradient contours for blast-wave propagating through 90° bend after (a) 25 time steps, (b) 100 time steps, (c) 200 time steps, (d) 300 time steps; and at (e) 0.000692 sec and (f) 0.00164 sec

The overpressure history upstream and downstream of the bend is demonstrated in Figure 5.26. The maximum overpressure for the first impulse upstream the bend is

62,272 Pa at 0.000692 sec, while the attenuated maximum overpressure for the first impulse downstream the bend is 62,581 Pa at 0.00164 sec, the Attenuation Factor η is 0.995.

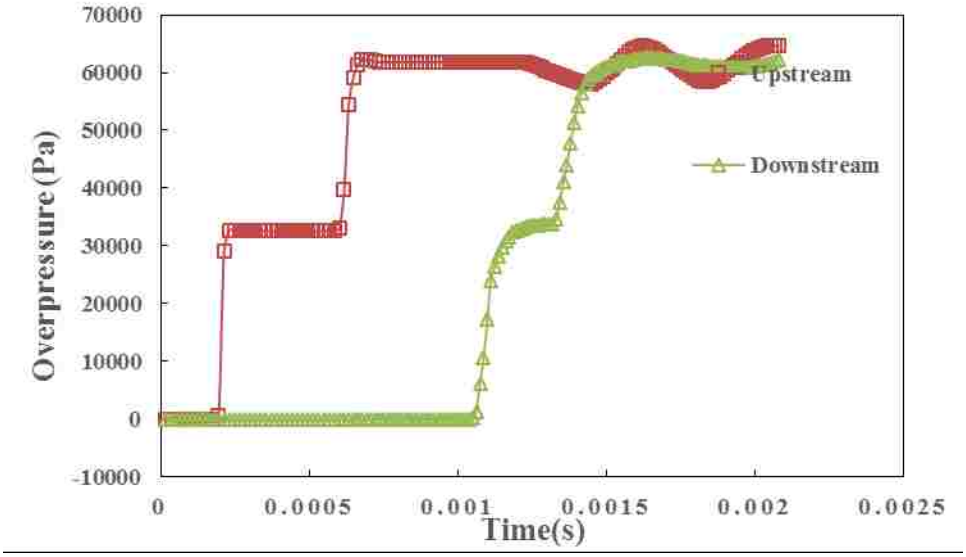

Figure 5.26. Overpressure history upstream and downstream of the 140° bend

160° Bend. The predicted overpressure gradient contours after 25, 100, 200, and 300 time steps when blast-wave is passing through the 160° bend are shown in the Figure 5.27 (a) through (d). Figure 5.27 (e) and (f) show the overpressure contour at the time of 0.000695 sec and 0.00159 sec when maximum overpressures of the first impulse were obtained by upstream and downstream sensors, respectively.

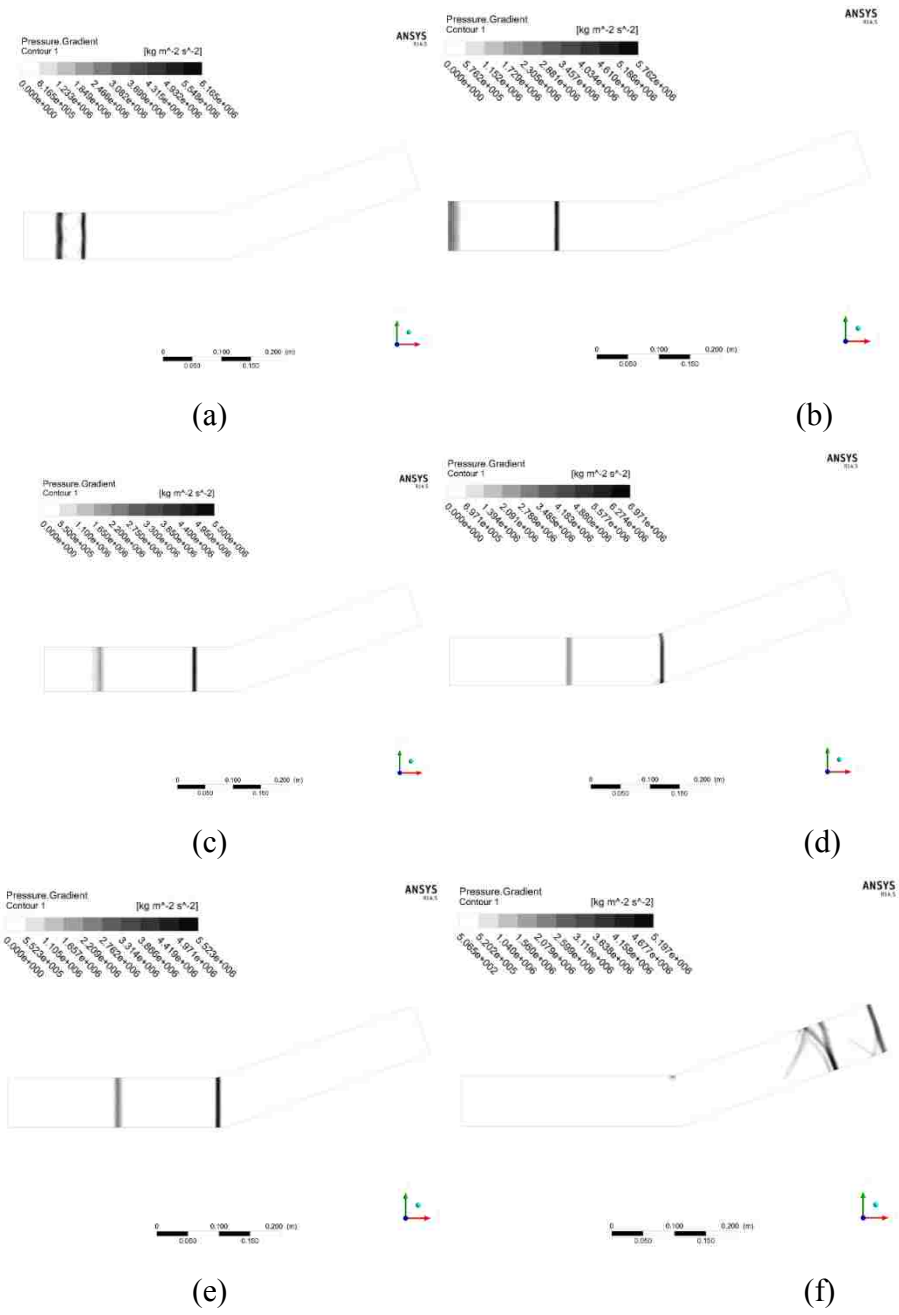

Figure 5.27. Overpressure gradient contours for blast-wave propagating through 160° bend after (a) 25 time steps, (b) 100 time steps, (c) 200 time steps, (d) 300 time steps; and at (e) 0.000695 sec and (f) 0.00159 sec

The overpressure histories upstream and downstream of the bend are demonstrated in Figure 5.28. The maximum overpressure for the first impulse upstream the bend is 62,366 Pa at 0.000695 sec, while the attenuated maximum overpressure for

the first impulse downstream the bend is 62,224 Pa at 0.00159 sec, the Attenuation Factor η is 1.002.

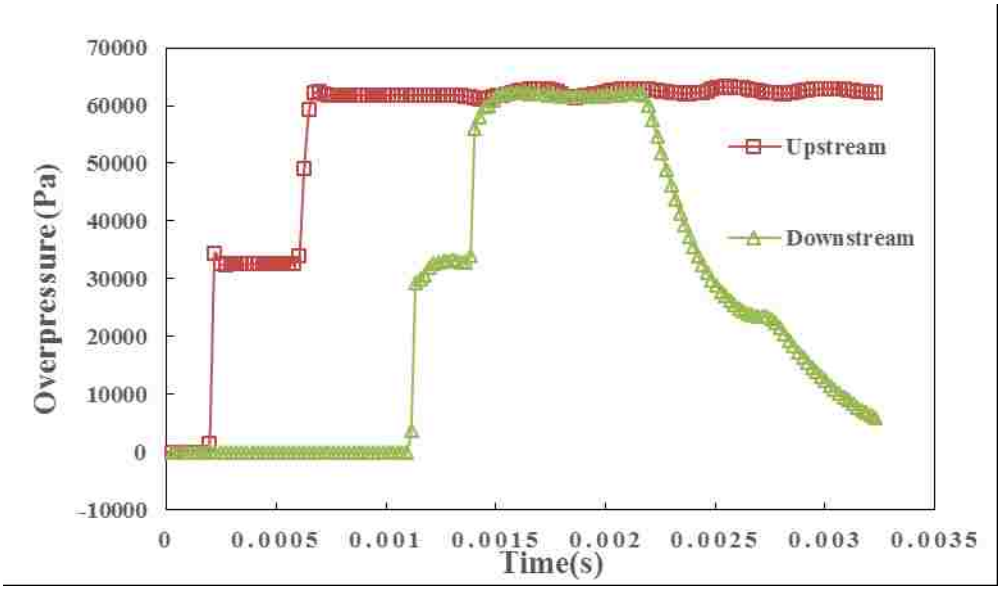

Figure 5.28. Overpressure histories upstream and downstream of the 160° bend

5.3.2. Obstacles. Blast-waves propagating through obstacles with blockage-ratios (BR) of 25%, 50%, and 75% were simulated. BR is calculated such as the blocked area is divide by the total area of the cross-section. The total length of the selected ducts was 0.705 m. The obstacle was located at 0.35 m downstream the inlet and was 0.005 m thick. The diameter of the duct was 0.08m. The pressure sensor upstream of the bend was placed along the centerline of the duct, 0.12m apart from the inlet. The sensor downstream the bend was placed along the duct centerline, 0.12m from the outlet.

BR 25%. The predicted overpressure gradient contours after 25, 100, 200, and 300 time steps when blast-wave was passing through an obstacle with blockage-ratio of 25% are shown in the Figure 5.29 (a) through (d). Figure 5.29 (e) and (f) show the overpressure contour at the time of 0.00183 sec and 0.00215 sec when maximum overpressures of the first impulse were obtained by upstream and downstream sensors, respectively.

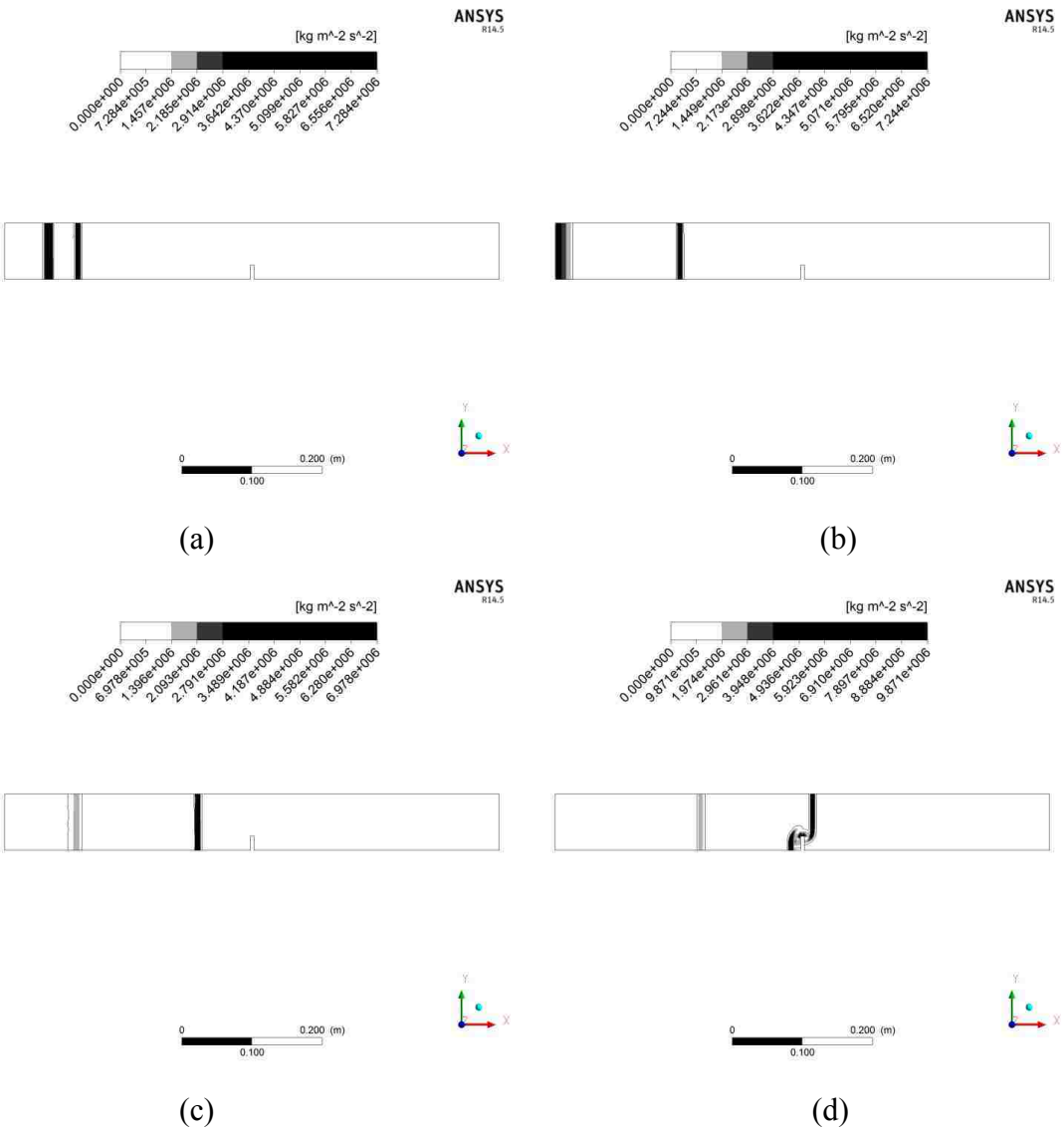

Figure 5.29. Overpressure gradient contours for blast-wave propagating through obstacle of BR25% after (a) 25 time steps, (b) 100 time steps, (c) 200 time steps, (d) 300 time steps; and at (e) 0.00183 sec and (f) 0.00215 sec

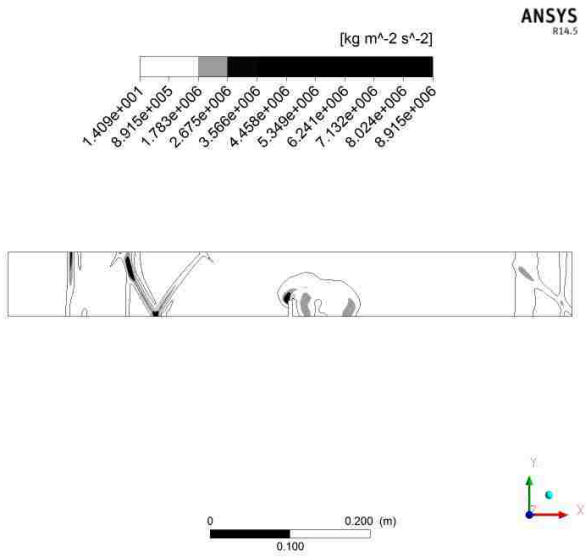

(e)

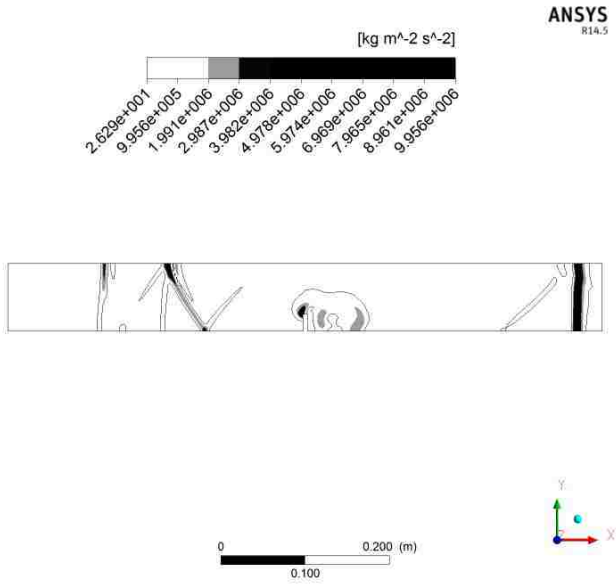

(f)

Figure 5.29. Overpressure gradient contours for blast-wave propagating through obstacle of BR25% after (a) 25 time steps, (b) 100 time steps, (c) 200 time steps, (d) 300 time steps; and at (e) 0.00183 sec and (f) 0.00215 sec (cont.)

The overpressure histories upstream and downstream of an obstacle with BR 25% are demonstrated in Figure 5.30. The maximum overpressure for the first impulse

upstream the bend is 103,392 Pa at 0.00183 sec, while the attenuated maximum overpressure for the first impulse downstream the bend is 77,866 Pa at 0.00215 sec, the Attenuation Factor η is 1.328.

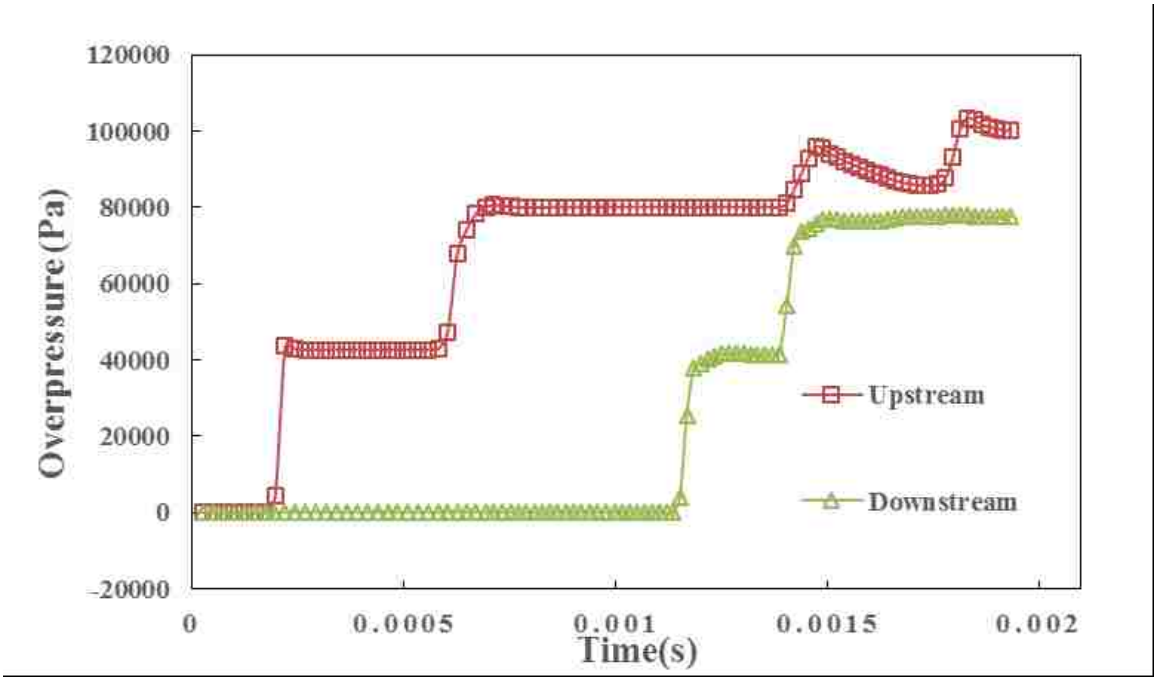

Figure 5.30. Overpressure histories upstream and downstream of BR 25%

BR 50%. The predicted overpressure gradient contours after 25, 100, 200, and 300 time steps when blast-wave is passing through an obstacle with blockage-ratio of 50% are shown in the Figure 5.31 (a) through (d). Figure 5.31 (e) and (f) show the overpressure contour at the time of 0.00144 sec and 0.00162 sec when maximum overpressures of the first impulse were obtained by upstream and downstream sensors, respectively.

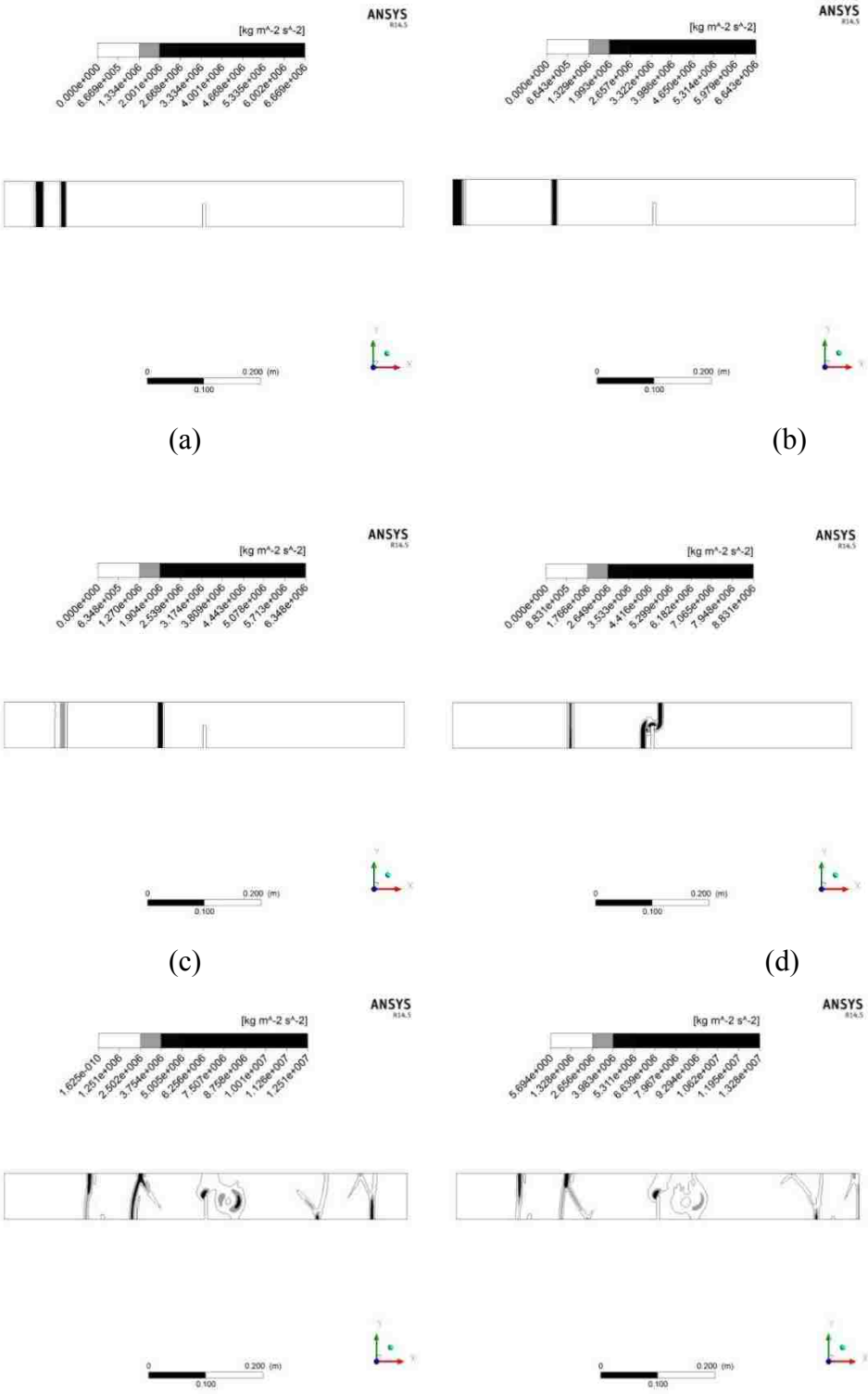

Figure 5.31. Overpressure gradient contours for blast-wave propagating through an obstacle of BR 50% after (a) 25 time steps, (b) 100 time steps, (c) 200 time steps, (d) 300 time steps; and at (e) 0.00144 sec and (f) 0.00162 sec

The overpressure histories upstream and downstream of an obstacle with BR 50% are demonstrated in Figure 5.32. The maximum overpressure for the first impulse upstream the bend is 103,969 Pa at 0.00144 sec, while the attenuated maximum overpressure for the first impulse downstream the bend is 66,711 Pa at 0.00162 sec, the Attenuation Factor η is 1.559.

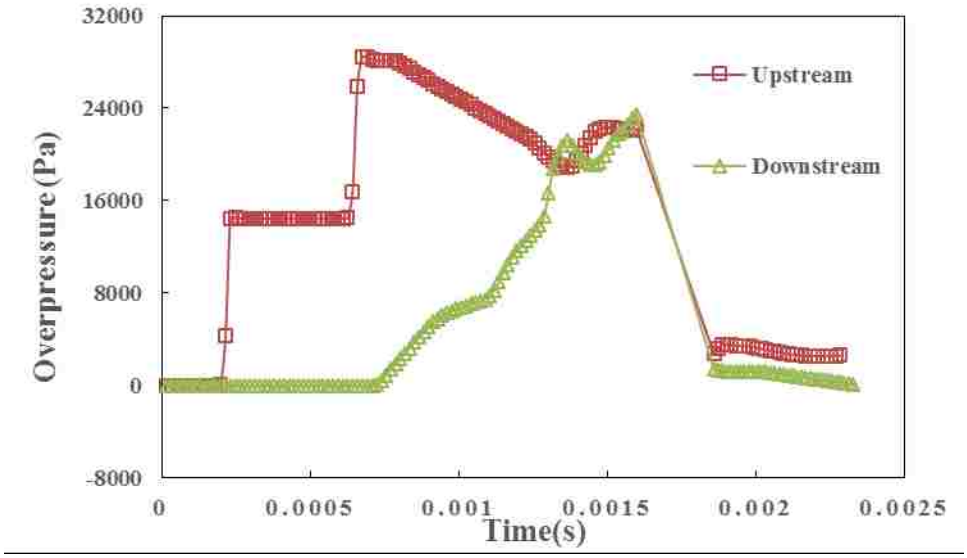

Figure 5.32. Overpressure histories upstream and downstream of BR 50%

BR 75%. The predicted overpressure gradient contours after 25, 100, 200, and 300 time steps when blast-wave is passing through an obstacle with blockage-ratio of 75% are shown in the Figure 5.33 (a) through (d). Figure 5.33 (e) and (f) show the overpressure contour at the time of 0.00130 sec and 0.00192 sec when maximum overpressures of the first impulse were obtained by upstream and downstream sensors, respectively.

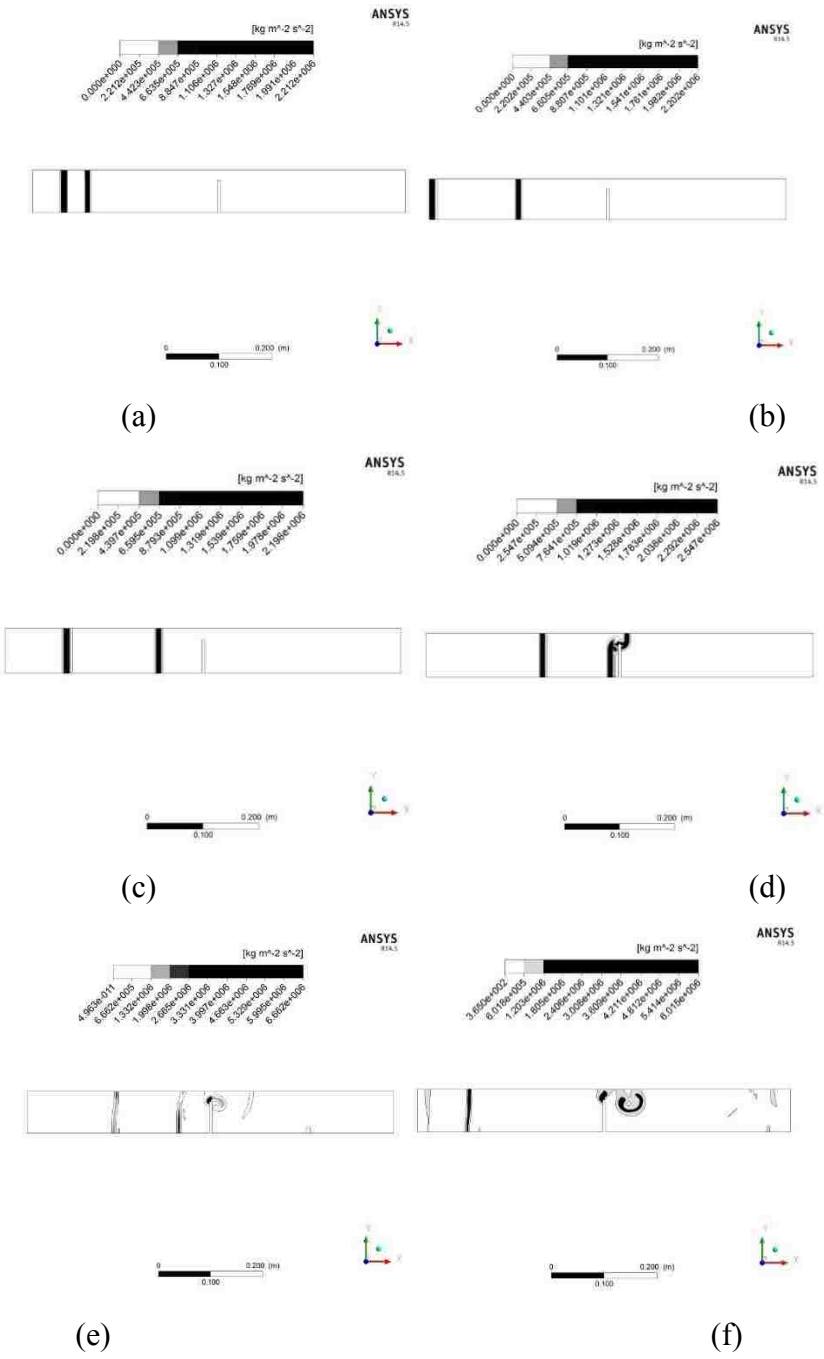

Figure 5.33. Overpressure gradient contours for blast-wave propagating through an obstacle of BR 75% after (a) 25 time steps, (b) 100 time steps, (c) 200 time steps, (d) 300 time steps; and at (e) 0.00130 sec and (f) 0.00192 sec

The overpressure histories upstream and downstream of an obstacle with BR 75% are demonstrated in Figure 5.34. The maximum overpressure for the first impulse

upstream the bend is 42,717 Pa at 0.00130 sec, while the attenuated maximum overpressure for the first impulse downstream the bend is 21,766 Pa at 0.00192 sec, the Attenuation Factor η is 1.96.

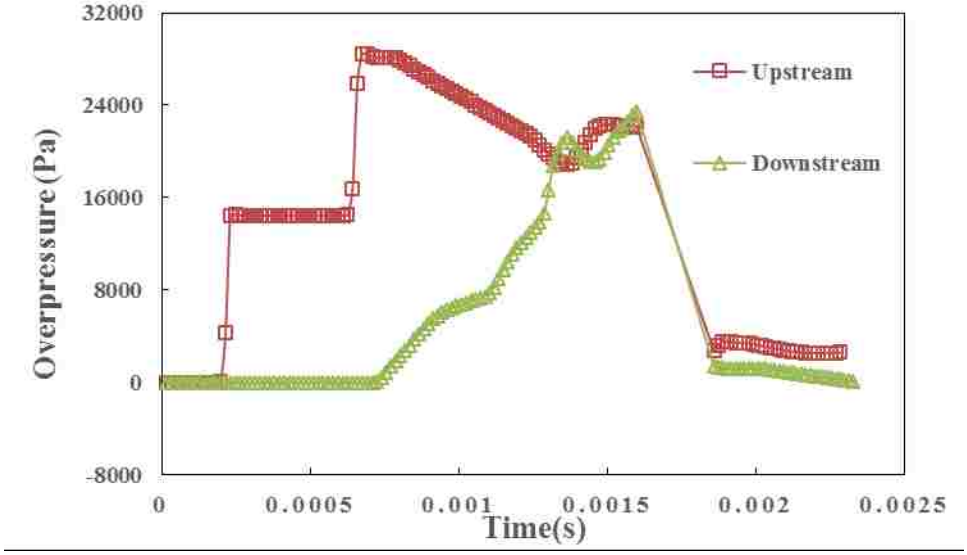

Figure 5.34. Overpressure histories upstream and downstream of BR 75%

5.3.3. Branches and Cross-sectional Change. The last category of geometric changes selected for this research included two t-branch cases and one cross-sectional change case. For the t-branch cases, the length of the three arms of a t-branch is 0.35 m. The diameter of the duct was 0.08 m. The pressure sensor upstream of the t-branch was placed along the centerline of the duct, 0.12 m apart from the inlet. The sensors downstream were placed along the duct centerline, 0.12 m from the outlet. For the cross-sectional change case, two segments of duct with smaller diameter are 0.12 m long and 0.08 m in diameter. The expanded part is 0.51 m in length and 0.145 m in diameter.

T-branch flow from main arm. The predicted overpressure gradient contours after 25, 100, 200, and 300 time steps when blast-wave passed through a t-branch, and where it flowed from the main arm, are shown in the Figure 5.35 (a) through (d). Figure 5.35(e),

(f), and (g) show the overpressure contours at the time of 0.000658 sec, 0.00147 sec and 0.00177 sec when maximum overpressures of the first impulse were obtained by upstream, downstream-top , and downstream-bottom sensors, respectively.

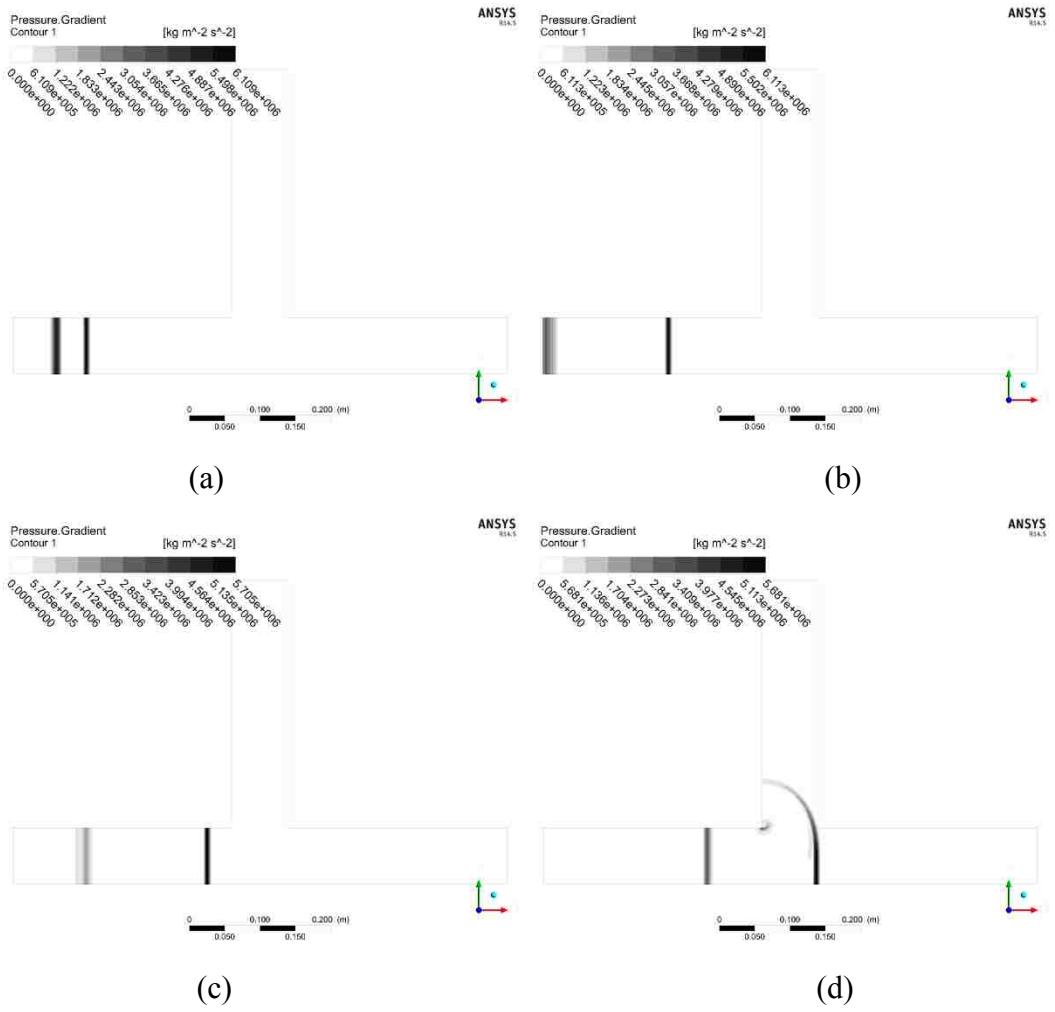

Figure 5.35. Overpressure gradient contours for blast-wave propagating through the t-branch (flow from the main arm) after (a) 25 time steps, (b) 100 time steps, (c) 200 time steps, (d) 300 time steps, and at (e) 0.000658 s, (f) 0.00147 sec, and (g) 0.00177 sec

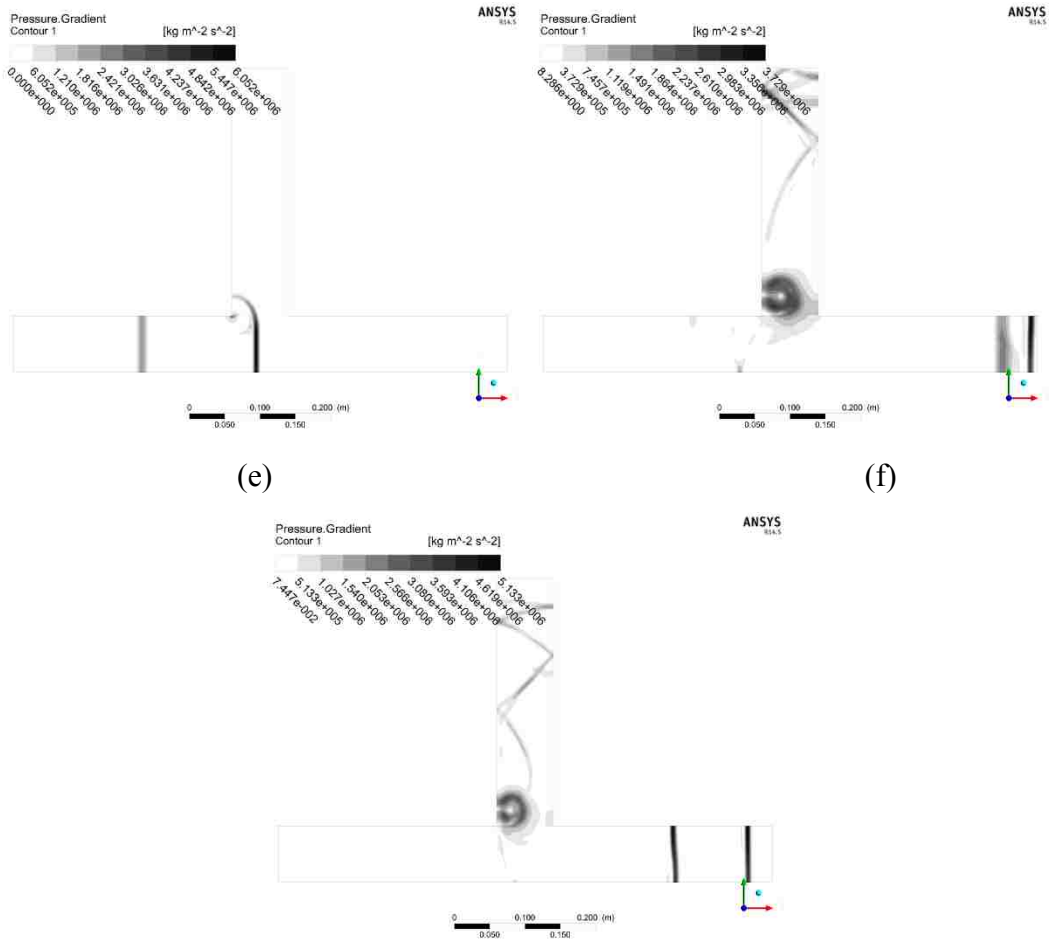

Figure 5.35. Overpressure gradient contours for blast-wave propagating through the t-branch (flow from the main arm) after (a) 25 time steps, (b) 100 time steps, (c) 200 time steps, (d) 300 time steps, and at (e) 0.000658 s, (f) 0.00147 sec, and (g) 0.00177 sec (cont.)

The overpressure histories upstream and downstream of the t-branch are demonstrated in Figure 5.36. The maximum overpressure for the first impulse upstream the bend was 69,651 Pa at 0.000658 sec, while the attenuated maximum overpressure for the first impulse of the downstream-top and downstream-bottom were 41,383 Pa at 0.00177s and 53,974 Pa at 0.00147 sec. The Attenuation Factor η for the top branch is 1.683 while for the bottom main arm is 1.29.

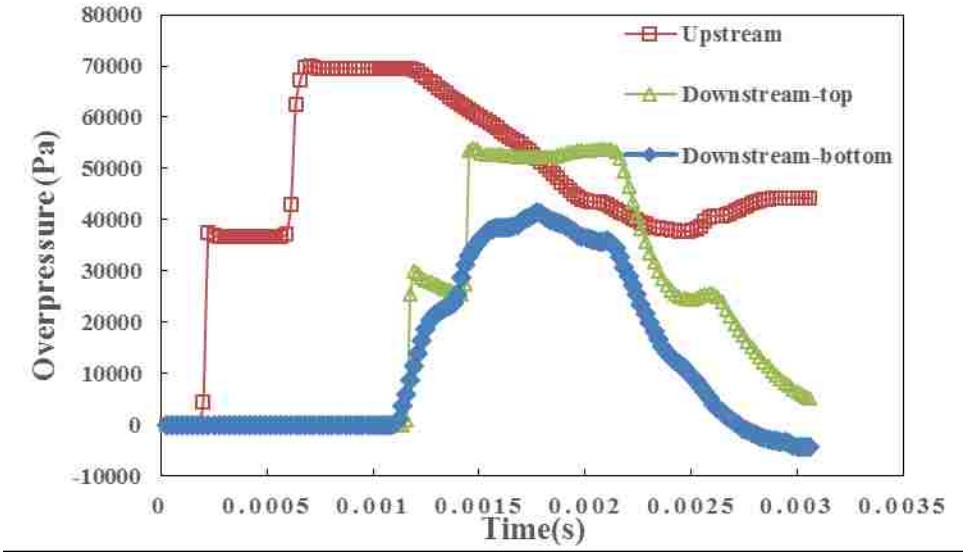

Figure 5.36. Overpressure histories upstream and downstream of the t-branch flows from main arm

T-branch flow from branch arm. The predicted overpressure gradient contours after 25, 100, 200, and 300 time steps when blast-wave passed through a t-branch, and when it flowed from the branch arm, are shown in the Figure 5.37 (a) through (d). Figure 5.37 (e), (f), and (g) show the overpressure contours at the time of 0.000702 sec and 0.00171 sec when maximum overpressures of the first impulse were obtained by upstream, downstream-top, and downstream-bottom sensors respectively (downstream-top and downstream-bottom reach their maximum overpressure simultaneously).

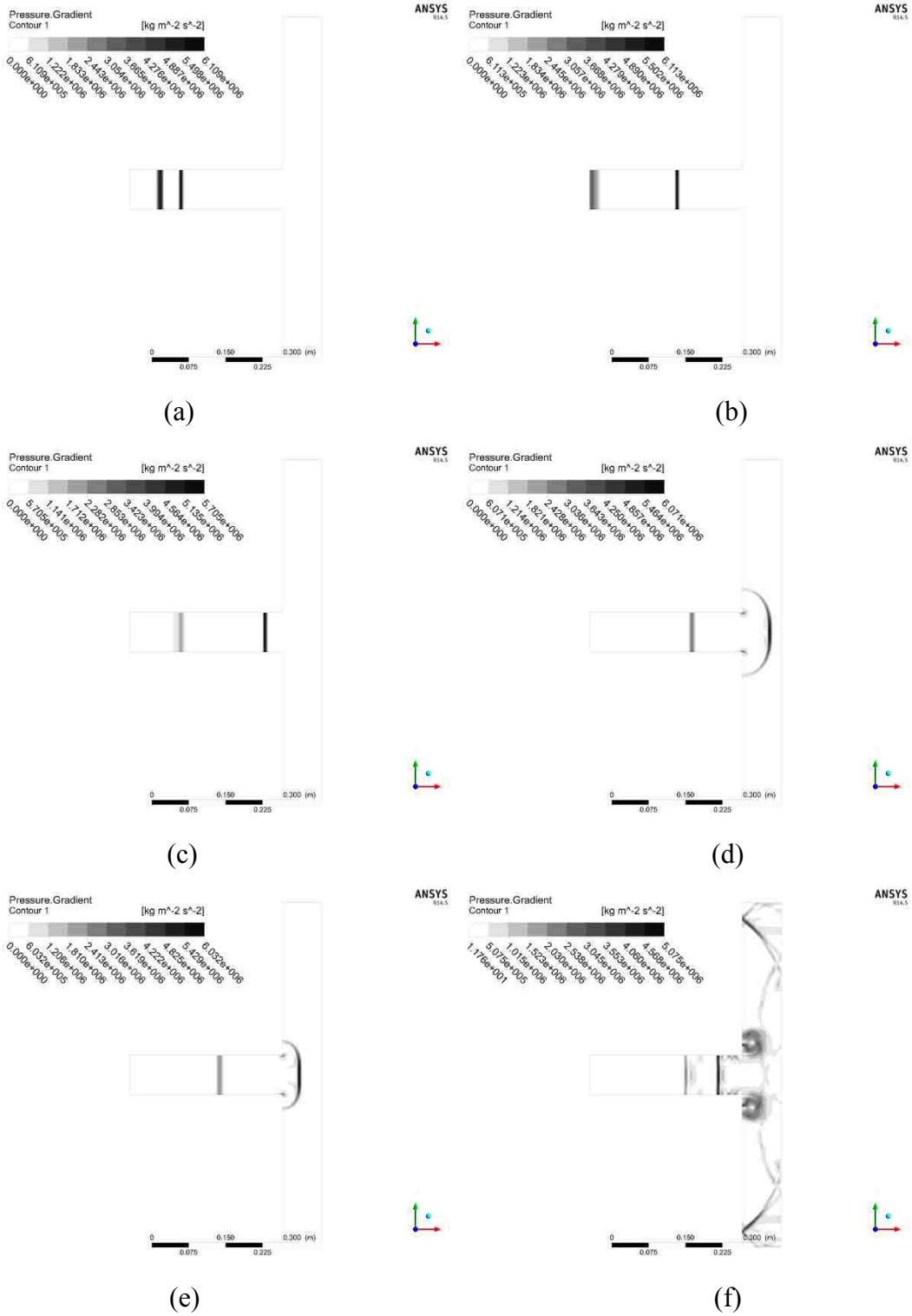

Figure 5.37. Overpressure gradient contours for a blast-wave propagating through the t-branch (flow from the branch arm) after (a) 25 time steps, (b) 100 time steps, (c) 200 time steps, (d) 300 time steps, and at (e) 0.000701 sec, and (f) 0.00170 sec

The overpressure histories upstream and downstream of the t-branch are demonstrated in Figure 5.38. The maximum overpressure for the first impulse upstream the bend was 70,037 Pa at 0.000702 sec, while the attenuated maximum overpressure for the first impulse of the downstream-top and downstream-bottom were 47,353 Pa at 0.00171s and 473,285 Pa at 0.00171 sec. Attenuation Factors η for the top branch are 1.479 while 1.481 for the bottom branch arm.

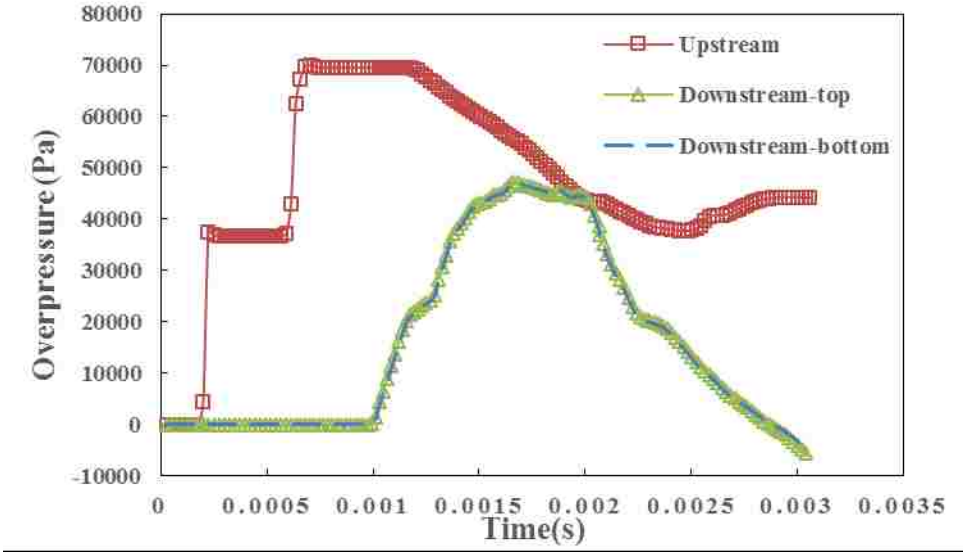

Figure 5.38. Overpressure histories upstream and downstream of the t-branch flows from branch arm

Cross-sectional change. The predicted overpressure gradient contours after 25, 100, 200, and 300 time steps when blast-wave passed through the cross-sectional change are shown in the Figure 5.39 (a) through (d). Figure 5.39 (e), (f), and (g) show the overpressure contour at the time of 0.000382 sec, 0.00244 sec and 0.00196 sec when maximum overpressures of the first impulse were obtained by upstream, middle of the expended area , and downstream sensors, respectively.

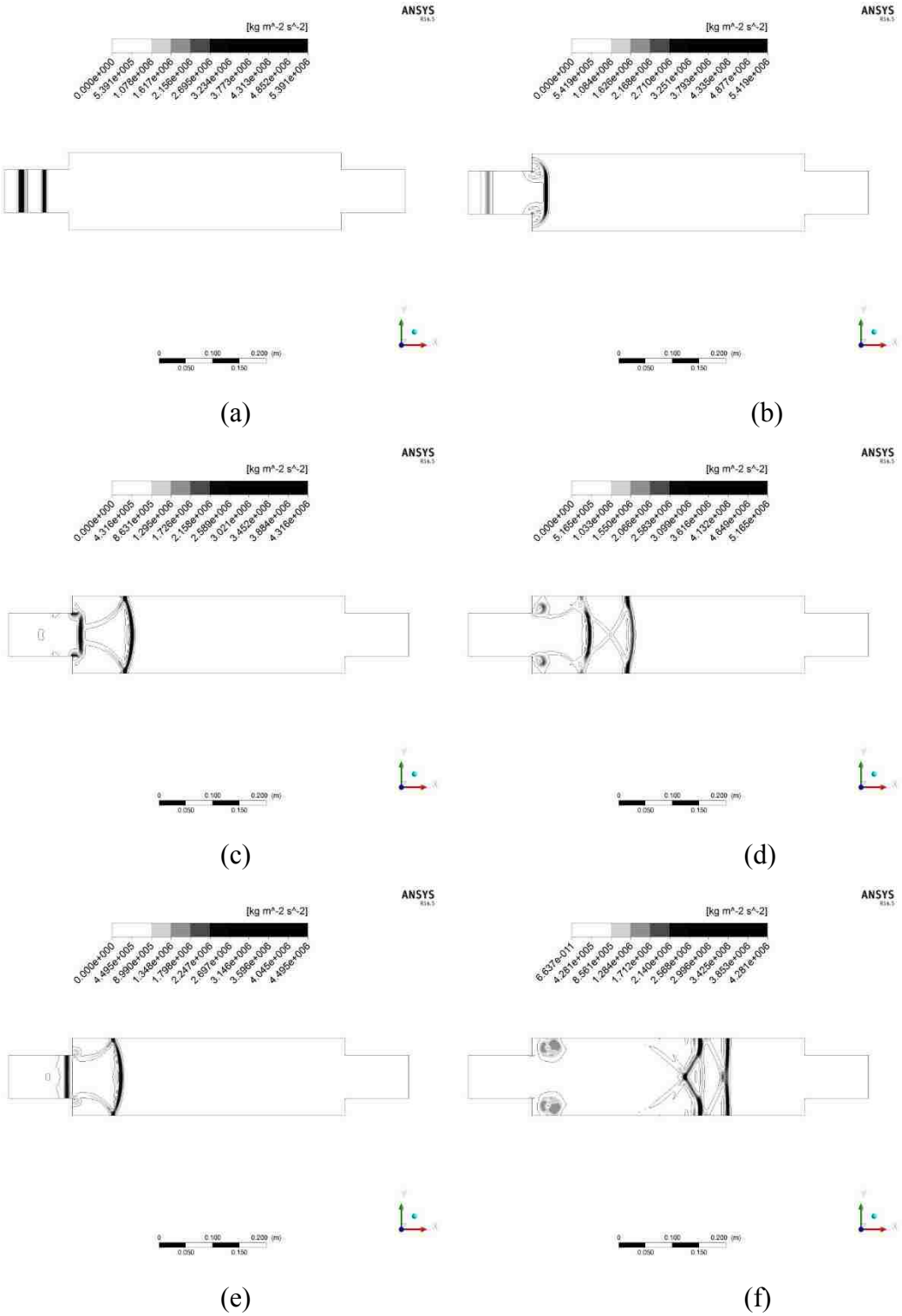

Figure 5.39. Overpressure gradient contours for blast-wave propagating through the cross-sectional change after (a) 25 time steps, (b) 100 time steps, (c) 200 time steps, (d) 300 time steps, and at (e) 0.000382 sec, (f) 0.00244 sec, and (g) 0.00196 sec

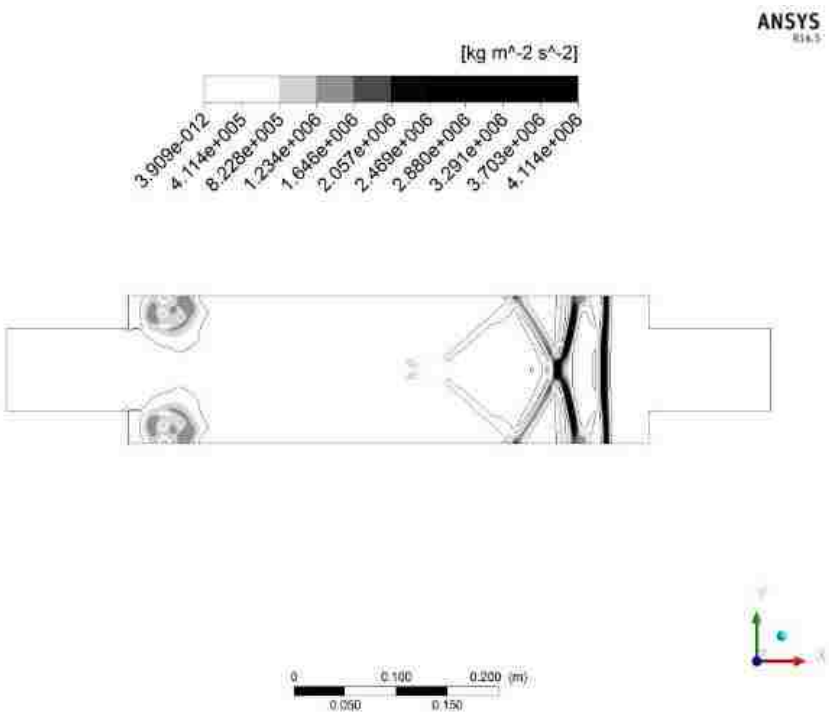

(g)

Figure 5.39. Overpressure gradient contours for blast-wave propagating through the cross-sectional change after (a) 25 time steps, (b) 100 time steps, (c) 200 time steps, (d) 300 time steps, and at (e) 0.000382 sec, (f) 0.00244 sec, and (g) 0.00196 sec (cont.)

The overpressure histories upstream, middle of the expended area, and downstream of the cross-sectional change are demonstrated in Figure 5.40. The maximum overpressure for the first impulse upstream the bend was 60,365 Pa at 0.000382 sec, while the attenuated maximum overpressure for the first impulse of the downstream and middle of the expended area were 45,487 Pa at 0.00114 sec and 47,804 Pa at 0.00142 sec. The Attenuation Factor η for the expended area was 1.269 while for the contracted-back area is 1.207.

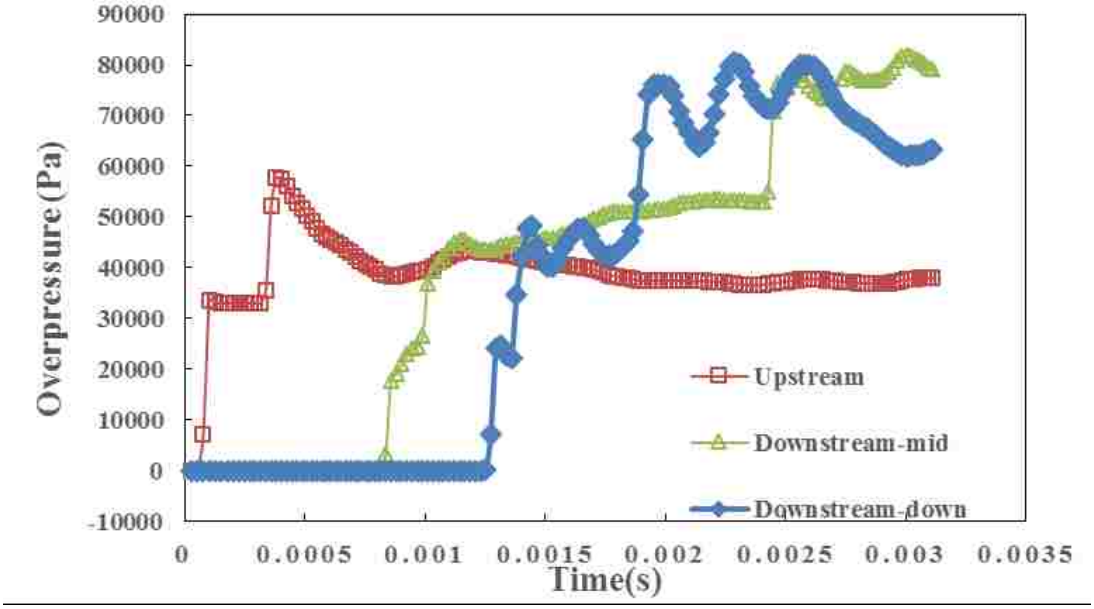

Figure 5.40. Overpressure histories upstream and downstream of the cross-sectional change

5.3.4. Discussion. Conclusions can be drawn from the simulation results. The trends and characteristics of the blast-wave propagation through bends, obstacles, t-branches, and cross-sectional change will be discussed, below, based on the observations from the simulation results.

5.3.4.1 Bends. As can be observed from the Figures 5.15, 5.17, 5.19, 5.21, 5.23, 5.25, and 5.27 which shown pressure gradient contours, the blast-wave fronts are clear when propagating through the straight duct upstream the bends. In each case, a strong blast-wave (compressive wave) is followed by a weak rarefaction wave due to the expansion by the compressive wave front. The rarefaction wave propagates to the opposite direction as the compressive wave. At the duct downstream of a bend, reflections and diffractions occur. As can be seen from the overpressure histories (Figures 5.16, 5.18, 5.20, 5.22, 5.24, 5.26, and 5.28), the overpressures first fluctuate and then decrease immediately after the reflection passed through the pressure sensor.

The Attenuation Factor increases from 30° until it meets the maximum value at 50°. Then, it decreases to around 1.14 at the 90°. The bends with obtuse angles greater

than 90° seams to strengthen the blast-wave, with the magnitude remaining small. All three of the angle angles greater than 90° cases have Attenuation Factors close to one. The total energy is not considerably reduced by the reflections.

5.3.4.2 Obstacles. Unlike the bends, a very clear trend can be found in the case of obstacles. The Attenuation Factor increases with blockage ratio, monotonically. The larger the area being blocked, a greater overpressure decrease downstream of an obstacle is observed. In the case of BR 75%, η reaches as high as 1.92 which is the greatest value recorded in all selected scenarios. As can be observed from the pressure gradient contours (Figures 5.29, 5.31, and 5.33), the maximum values of both upstream sensors and downstream sensors are obtained when the reflected wave passes by them instead of main blast-wave fronts. The overpressures decrease rapidly afterward.

5.3.4.3 T-branch and cross-sectional change. Two cases of t-branches with blast-waves from the different aims are simulated. The first case consists of blast-wave propagation from the main arm of the t-branch. As can be seen from Figure 5.35 (g), after the blast-wave has been propagated through the joint, it maintains a clear wave front in upstream. In Figure 5.36 (d), diffraction occurs at the edge of the joint and causes reflections of the blast-wave to the branch duct. The momentum transported to the branch duct is less than that to the main duct. This fact leads to the Attenuation Factor for the branch duct is greater than the main duct by 30%.

The second case is a blast-wave that propagates from the branch duct to two main ducts. The geometry is perfectly symmetric. A highly symmetric wave propagation pattern is observed in Figure 5.38. As a consequence, the Attenuation Factors for two main ducts are almost identical. Reflection is the major fact contributing to the overpressure decreases in both arms.

In the selected cross-sectional change case, the attenuation effect in the middle of the expended area and the part of the duct downstream is investigated. The overpressure is greater within the expended area compared to the overpressure downstream the sectional change due to the decrease of the velocity and reflection. As can be seen in Figure 5.40, large fluctuations are observed in both overpressure curves. Their peak overpressures from the first impulse, when the blast-wave front has passed by, are significantly smaller than are those caused by reflections. This occurs since reflections

between walls are more significant in this highly confined area. Momentum cannot be transported through this constrained area smoothly, in this selected geometry, as had been possible in other geometric change cases.

5.4. COMPARISON

The predicted Attenuation Factors are compared with experimental values to examine the accuracy of the numerical predictions in this section of the research study. Specifically, the comparison study of bends, obstacles, t-branches, and cross-sectional change will be demonstrated in this subsection.

5.4.1. Bends. The Attenuation Factors η for the predicted values and the experimental results are listed in Table 5.3. Bends with angles of 30°, 40°, and 160° are not covered by the experiment in this study.

Table 5.3. Predicted and experimental Attenuation Factors for bends

Bending	Predicted η	Experimental η
30°	1.150	Na
40°	1.214	Na
50°	1.534	1.726
90°	1.140	1.131
120°	0.991	0.703
140°	0.995	0.945
160°	1.002	Na

The comparison of predicted and experimental values is shown in Figure 5.41. The red curve represents simulation results while the blue curve represents experimental data.

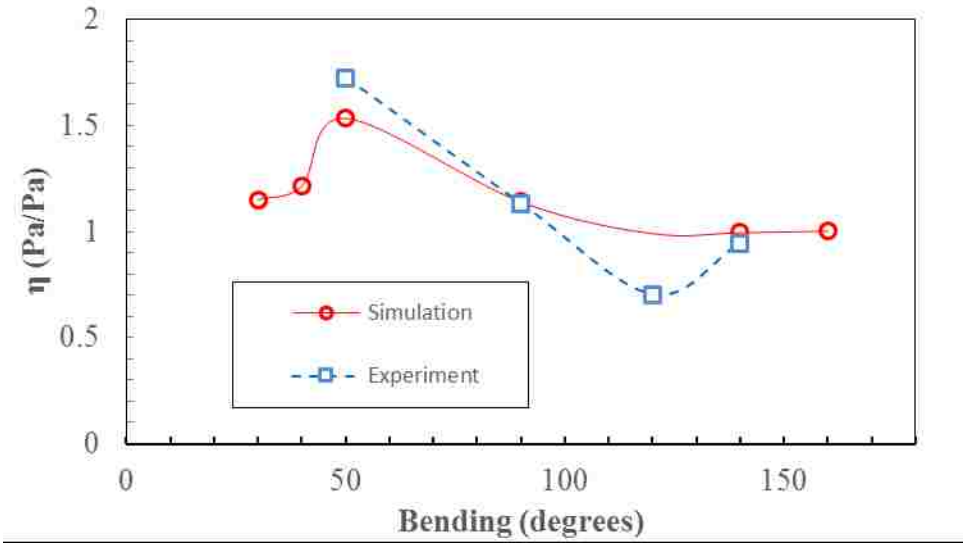

Figure 5.41. Comparison of simulation and experimental Attenuation Factors for the bends

As illustrated in Figure 5.41, the predicted η is in agreement with experimental values in the 50°, 90°, and 150° cases, with a relative error of 0.8%, 5%, and 11%, respectively. In the 120° case, however, the prediction overestimates the attention factor by 29%. In the discussion of experimental results, it was explained that the bend with a 120° angle tends to strength the blast-wave further than predicted. However, this strengthening effect is not observed at the level of 140°. This large difference might due to leakage during experiment and shear heating for the 120° case, which is neglected in numerical simulation. This effect is weakened in the 140° case due to a slight change of wave propagating direction.

5.4.2. Obstacles. Attenuation Factors of three selected BRs from experiments and simulations are shown in Table 5.4 and Figure 5.42.

Table 5.4. Predicted and experimental Attenuation Factors for obstacles with three BRs

BR (%)	Predicted η	Experimental η
25	1.329	1.1
50	1.559	1.326
75	1.959	1.759

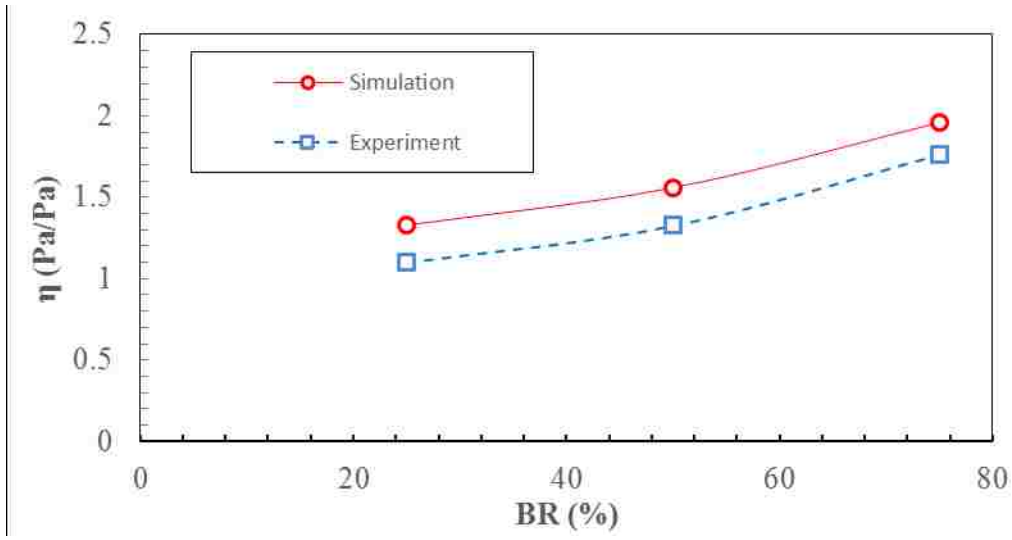

Figure 5.42. Comparison of simulation and experiment Attenuation Factors for obstacles

As seen in both Table 5.4 and Figure 5.42, the predicted values are commonly larger than experimental by around 15%. This is due to the ideal blast-wave simplification applied in numerical simulation that ignores the overpressure decrement after the first impulse. To use this model for predicting more BR cases, a 15% adjustment factor should be applied on the each of the simulation results.

5.4.3. T-branch and Cross-sectional Change. The experiment includes one t-branch and one cross-sectional change. The corresponding scenarios with the same dimensions of experimental setup are simulated by the selected numerical scheme. The predicted and experimental Attenuation Factors for these two cases are listed in Table 5.4. The upper two rows of Table 5.5 show the Attenuation Factor of the branch arm and the main arm downstream of the t-branch. The lower two rows show the Attenuation Factor located in the middle of the expended area and downstream of it.

Table 5.5. Predicted and experimental Attenuation Factors for t-branch and cross-sectional change (CSC)

	Predicted η	Experimental η
Branch arm of t-branch	1.683	1.615
Main arm of t-branch	1.290	0.998
Middle expended region of CSC	1.269	1.232
Main duct downstream of CSC	1.207	0.984

As seen in Table 5.5, in the case of the t-branch, the numerical model successfully predicted the Attention Factor for the branch arm while overestimating the value at the downstream main arm. In the cross-sectional change case, the prediction of the attenuation effect within the expended area is accurate; but a relative error of 17% was observed when it was used to predict η downstream of the expended area. The experiments showed an Attention factor close to one in the main duct downstream the expended area. That is to say, the blast-wave was not attenuated significantly after it passed through an expend-contract structure.

The prediction, however, indicated that the blast-wave will be attenuated and energy will be lost. As the Attenuation Factor can only show the difference of peak overpressure between two ends (three ends in the case of the t-branch), it is also important to consider the impact of geometric changes based on overpressure histories, instead of assuming that the peak pressures are the only concern.

5.5. SUMMARY

In this section, the attenuation effect of seven types of bends, three obstacles with varying BRs, two t-branch cases, and one cross-sectional change case are investigated. Five main conclusions have been drawn from the preceding discussions: (1) as a bending angle increases from 0° to 180° the Attenuation Factor increases at 30° until the maximum value is obtained at 50°. Then, it decreases to around 1.14 in the 90° case. The bends with angles greater than 90° tend to strengthen blast-waves. (2) For the obstacles with different Blockage Ratios, the Attenuation Factor increases as BR increases. (3) In

the case of the t-branch, when a blast-wave is brought from the main arm, the Attenuation Factor for the branch duct is greater than the main duct by 30%. (4) In the cross-sectional change case, the overpressure is greater inside the expended area compared to the overpressure downstream, due to the constrained reflections. (5) The inviscid, changing density, and unstable numerical scheme used in this research tends to overestimate the Attenuation Factors in the 120° bend; and the obstacles with BR 25%, BR 50%, BR 75% were comparable to the experimental results.

The Attenuation Factor is a rudimentary indicator of the influence of a geometric change. It has been suggested that the overpressure history curve should also be considered when dealing with practical problems. In addition, the numerical schemes used in this Section are simplified. The results of this research that deviated from the experimental values should be used with extra care.

6. NUMERICAL MODELING IN BLAST WAVE SECTION

6.1. INTRODUCTION

According to the two-section theory discussed in details in Section 2, the methane explosion space has been divided into two segments, a driver section and a blast-wave section. The explosion in the driver section has been modeled in Section 4. This Section will focus on the numerical modeling for the blast-wave section, where turbulence and combustion modeling are ignored. Since the geometric model in the blast-wave section has been simplified to one-dimensional model (1D), it could significantly reduce computational cost without compromising accuracy. The explosion source database developed in Section 4 can provide initial and boundary conditions for the 1D model analyzed here. The attenuation due to geometric changes is also included in the analysis by modifying factors of specific components in the 1D network geometry.

In the numerical research on blast-wave, one dimensional CFD code *Flowmaster* is selected as the platform to perform network-based predictions. *Flowmaster* is a 1D CFD commercial package based on implicit Finite Difference Method. It has been widely used in simulating the fluid dynamics behavior in gas or water pipelines. However, its behavior when predicting blast-wave propagation needs to be investigated and its attenuation models need to be modified for this particular research. The modifications will be introduced in Section 6.2.

The governing equations for the blast-wave section were briefly introduced in Section 2.2.2. The form of the 1D governing equations is modified specifically to meet the needs of *Flowmaster*. Based on the 1D, inviscid, and compressible assumptions, the full description of conservation of mass, momentum, and energy equations used in the blast-wave section are shown as (Anon, 2012):

$$\frac{\partial p}{\partial t} + V\frac{\partial V}{\partial x} + \rho a^2 \frac{\partial V}{\partial x} = \frac{a^2}{C_P T}\left[1 + \frac{T}{Z}\left(\frac{\partial Z}{\partial T}\right)_T\right]\frac{\Omega + WV}{A} \tag{6.1}$$

$$\frac{\partial V}{\partial t} + V\frac{\partial V}{\partial x} + \frac{1}{\rho}\frac{\partial p}{\partial x} = \frac{W}{A\rho} - g\sin\theta \tag{6.2}$$

$$\frac{\partial T}{\partial t} + V\frac{\partial T}{\partial x} + \frac{a^2}{C_P}\left[1 + \frac{T}{Z}\left(\frac{\partial Z}{\partial T}\right)_p\right]\frac{\partial V}{\partial x} = \frac{a^2}{C_P p}\left[1 - \frac{p}{Z}\left(\frac{\partial Z}{\partial p}\right)_T\right]\frac{\Omega + WV}{A} \tag{6.3}$$

$$W = f\frac{A}{D}\rho\frac{V|V|}{2} \tag{6.4}$$

where V is velocity, in m/s, x is axial distance, in m, a is speed of sound, in m/s, C_P is specific heat in J/gC°, Z is gas compressibility, A is flow area in m^2, Ω is heat input per unit length, g is gravity acceleration, and θ is pipe angle to horizontal in degrees. f is Darcy Frictional Factor which will be discussed in Section 6.2.2. Note that Equation (6.2) now takes gravitational acceleration and bearing angle into consideration, however, they were not used when developing the explosion source database. This is only true in horizontal or nearly horizontal airways as the effect of gravity acceleration may be ignored under these conditions. The propagation of a blast-wave is also considered as an adiabatic process. Therefore, the heat input terms Ω in Equations (6.1) and (6.3) was dropped out.

Before conducting a network-based 1D simulation, *Flowmaster* requires adjustments on pressure losses and initial/boundary condition inputs. The adjustment of pressure losses due to the friction and geometric changes will be introduced in Section 6.2 while the incorporation of initial and boundary conditions will be discussed in Section 6.3. The last two subsections of this section will provide two applications of decoupled methane explosion prediction method: predictions of methane explosions in a sample parallel network and in a full-scale Experimental Mine.

6.2. PRESSURE LOSSES

6.2.1. Pressure Losses. The 1D CFD code *Flowmaster* is used as the platform to simulate the blast-wave propagation within an underground network. Pressure losses would occur along the way of the blast-wave propagation. Two categories of pressure losses are considered by *Flowmaster*, namely, frictional loss and loss due to geometric changes. The effect of frictional loss is treated by incorporating the Darcy Friction Factor f into the analysis. Frictional loss is also determined by the length and the absolute roughness of each pipe component. The pressure loss due to geometric changes is accounted for by the governing equations for the different components employed by *Flowmaster*. The simulation results in Section 5 can provide validated attenuation factor data. These attenuation factors can be substituted into corresponding component equations. The component equations for bend, obstacles, t-branch, and cross-sectional change will be introduced in the following subsections.

6.2.2. Frictional Loss. Frictional loss is the pressure loss generated by shear heating that occurs in near-wall areas. The mechanical energy of the blast-wave is thus, transferred to heat and then dissipated. Darcy Friction Factor f in Equation (6.4) varies with the Reynolds number $Re = V\rho D/\mu$ differed by three flow scenarios. μ is dynamic viscosity equals to 1.983e^{-5} for air under 25ºC. According to Colebrook-White's Approximation (Colebrook and White, 1937):

For laminar flow (Re < 2000):

$$f = f_l = \frac{64}{Re} \tag{6.5}$$

For transition zone (2000 < Re < 4000):

$$f = xf_t + (1 - x)f_l;\ \mathrm{x} = \frac{Re-2000}{2000} \tag{6.6}$$

For turbulent flow (Re> 4000):

$$f = f_t = \frac{0.25}{\left[log\left(\frac{k}{0.37D}+\frac{5.74}{Re^{0.9}}\right)\right]^2} \tag{6.7}$$

where f_l and f_t are laminar and turbulent friction factors, respectively. k is absolute roughness in mm.

6.2.3. Bends and Obstacles. Pressure loss due to geometric changes is another type of energy loss within the process of the blast-wave propagation. The study on the attenuation effect of four geometric changes, which can be commonly found in underground coal mines, was provided in details in Section 5. These geometric changes are bends, obstacles, branches, and cross-sectional changes. In *Flowmaster*, the bend component can usually be ignored when building a geometric network in long-distance water pipes. However, in the case of methane explosion, the attenuation effect related to bends cannot be ignored as discussed in Section 5.1. To account for this effect, a Cd Discrete Loss component is utilized in the analysis.

The *Flowmaster* accounts for the pressure loss led by including a Cd Discrete Loss component as shown in the equation below. The attenuation factors η can be substituted in the expression by adjusting the factor C_d.

$$\Delta p = \frac{8Lf}{\rho^2 \pi d^5} \left(\frac{C_d \cdot A_t \cdot P_{t1} \cdot \psi \cdot \sqrt{\frac{2}{R_S \cdot T_{t1} \cdot Z_1}}}{m_{t1}} \right)^2 \tag{6.8}$$

where P_{t1}, m_{t1}, and T_{t1} are total pressure in Pa, mass flow rate in kg/s, and total temperature upstream of the Cd Discrete Loss. Darcy Friction Factor f can be calculated using Equation (6.7). ψ is flow function while Z_1 is compressibility factor for upstream flow and R_s is a gas constant. The pressure loss due to a bend δp can be correlated to attenuation factor η as $\delta p = P_{t1}(1-\eta)/\eta$. For a given η. The change of discharge coefficient due to a bend $C_d{}'$ can be back calculated by a given δp. The total C_d is assigned to be a flow property for a discrete loss. Note that, C_d should be calculated from η and P_{t1}, the latter is always assigned to be the input peak overpressure of the explosion source. The reason is, according to the experiments conducted, the pressure upstream of a bend always has the same order of magnitude as the input peak overpressure. The effect of obstacles will be treated the same way that bends are treated in this research. The only difference is their designated attenuation factors. The incorporation of obstacles will not be further detailed.

6.2.4. T-branches. Propagation of blast-waves through a t-branch was discussed in Section 5.3.3. Similar to the bend case, the t-branch component (called t-joint in *Flowmaster*) has an insignificant effect on a long water pipe in *Flowmaster*. Therefore, the attenuation coefficient should be modified when simulating blast-wave propagation.

The pressure loss of t-branches is calculated by *Flowmaster* using the following equation:

$$\Delta p = \frac{C_{Re} K \dot{m_c} |\dot{m_c}|}{2\rho A_c} \tag{6.9}$$

where C_{Re} is correction for Reynolds number and K is the loss coefficient for one of the arms. To account for the extra pressure loss due to the geometric change, the total pressure loss $\Delta p'$ for an arm of a t-branch can be expressed by $\Delta p' = \Delta p + P_{t1}(1-\eta)/\eta V$.

Attenuation factors for t-branches with flows from the main arm and the branch arm are predicted in Section 5.4.3. The loss coefficient K could be calculated by a given η and P_{t1}.

6.2.5. Cross-sectional Change. According to Bernoulli's theory, the expansion of a duct would increase the overpressure of a blast-wave while its velocity decreases. The kinetic energy is transferred into volumetric energy, which in turn, increases overpressure inside the section. To account for this effect, *Flowmaster* employs Transition Component, governed by the equation shown below:

$$\frac{P_{t1}}{P_{t2}} = 1 - K\left(1 - \frac{P_{s2}}{P_{t2}}\right) \tag{6.10}$$

where P_{s2} is the static pressure downstream of the expanded area before it contracts back again. The selected expand-contract structure does not have significant effect on the blast-wave propagation. The only concern should be that the overpressure increases inside the expanded area due to reflections between the duct walls. This mechanism leads to a notable overpressure increase inside the expended area.

6.3. METHANE EXPLOSION DATABASE

The 1D simulation using *Flowmaster* requires initial and boundary conditions such as ambient temperature, ambient pressure, and overpressure (static pressure) history. The working temperature and gauge pressure can be measured at the work site. The pre-developed explosion source database can provide the overpressure histories based on numerical predictions with specific methane concentration levels and geometry. The development of the methane explosion database was introduced in Section 4; this database includes three methane concentrations and 13 scaling factors for each concentration, which covers a wide range of commonly encountered conditions in underground coal mine operations. The cases with concentrations and dimensions between two data points can be linearly interpolated. To store and manage the collected data, *Flowmaster* requires a standard and accessible database tool, *Microsoft SQL server* system was selected for this purpose.

Microsoft SQL server is a database tool developed by Microsoft that can build, manage, and store data. It is an industry standard database that can easily be shared with

other users. The version of the software used in this research is *SQL Express* 2008. The overpressure histories in selected conditions are stored in *Microsoft SQL Express* by the form of overpressure/time curves. In the setting of each 1D simulation, the curves can be retrieved from the pre-built database when specific concentration and dimension are requested by a specific methane explosion simulation.

6.4. CASE STUDY-PARALLEL NETWORK

6.4.1. Problem Statement. A methane explosion that occurred in a sample parallel airway was simulated using the1D CFD code *Flowmaster*. The schematic of the network is shown in Figure 6.1:

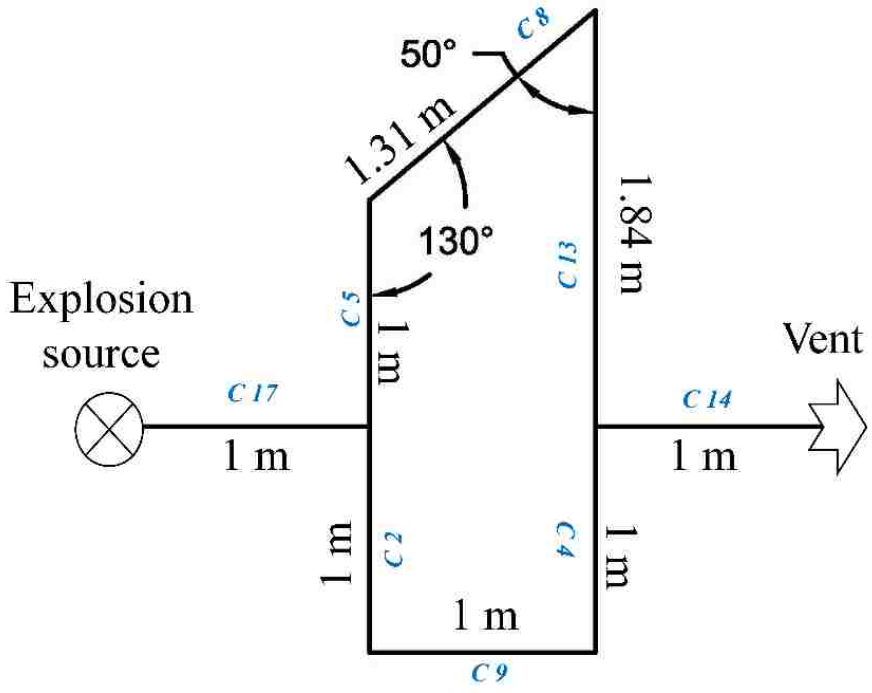

Figure 6.1. Schematic of the Parallel Sample Network showing the top view

The explosion source was set to the left hand side of the network where a pressure source was placed. In this test, all pipes were 1 m long except C8 and C13, which were 1.31 m and 1.84 m, respectively. The diameter of all components used in this network model was 0.08 m. A methane explosion was set close to the dead end on the left hand side and a blast-wave propagated through the duct before reaching the t-branch and then separated by two parallel ducts between two bends. In the branch with C5, C8, and C3 in series, the first and second bends are 130˚ and 50˚, respectively. In the C2, C9, and C4 branches, both angles were at 90˚. The attenuation factors η for each bend can be calculated using Equation (5.8). Two ducts merge at a t-branch and then are vented to atmosphere (a pressure source on the right side that has constant total pressure of one bar).

The geometric model of the parallel network for *Flowmaster* is shown in Figure 6.2. The numbers next to each component are their component number and will be expressed as C_i (i denotes the component number).

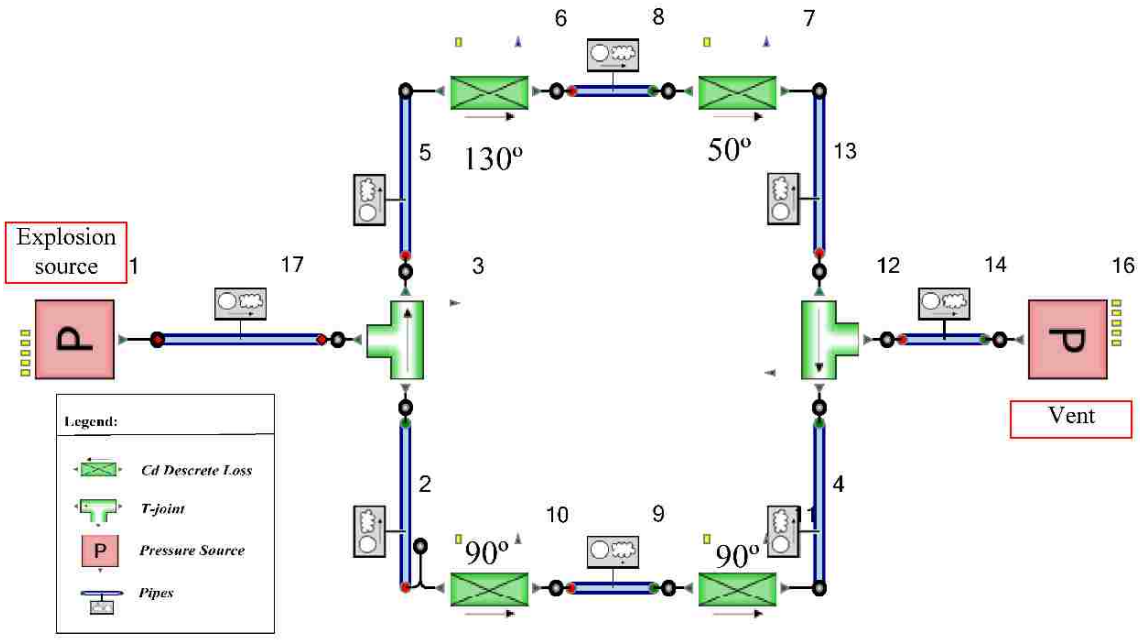

Figure 6.2. Geometric model for Flowmaster of the Sample Parallel Network from the top view

Figure 6.2 shows the geometric model developed in *Flowmaster* that represent the same network shown in Figure 6.1. The ducts used in Figure 6.2 are not to scale. Their lengths are assigned to be corresponding values as shown in Figure 6.1. Four bends are replaced by Cd Discrete Loss components as stated in Section 6.2.3. The Calculated C_d based on the four angles (two at 90º, one at 130º, and one at 50º) are assigned to four Discrete Loss components to incorporate the attenuation effects made by four bends with different angles as shown Figure 6.1.

6.4.2. Results. The blast-wave propagation can be clearly demonstrated by the pressure history (in bar) of each pipe component changing with their local length (from 0 m to 1 m in this case). The peak values in each chart are obtained when blast-waves are passing by a specific pipe. The waves are attenuated on the way of propagation by friction along a pipe and by each geometric change.

The initial condition for the 1D simulation is input by retrieving the overpressure history of the 8% concentration methane explosion with FLSF=1 and HDSF=1 from the pre-developed methane explosion database. The pressure, local pipe length (distance starts from one end to another for each pipe), and time relationships of all pipe components are shown in Figures 6.3 to 6.10. The component numbers and locations of a selected pipe refer to Figure 6.2.

Figures 6.3 through 6.10 illustrate interrelationships among pressures in bar, local pipe length in m, and time in s, for pipe components C17, C2, C5, C8, C9, C4, C13, and C14 shown in Figure 6.1. The blast-waves propagating through each pipe component are demonstrated by surfaces with obvious pressure changes over time and slight pressure changes with local pipe length. The detailed discussion of these figures will be provided in Section 6.4.3.

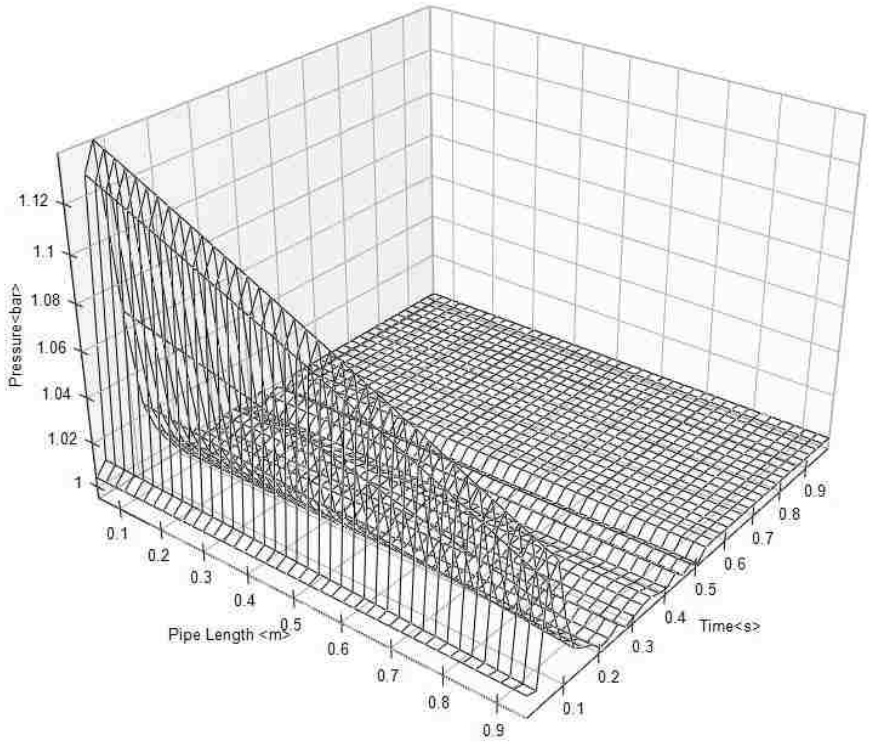

Figure 6.3. Surface of pressure, pipe length, and time for C17

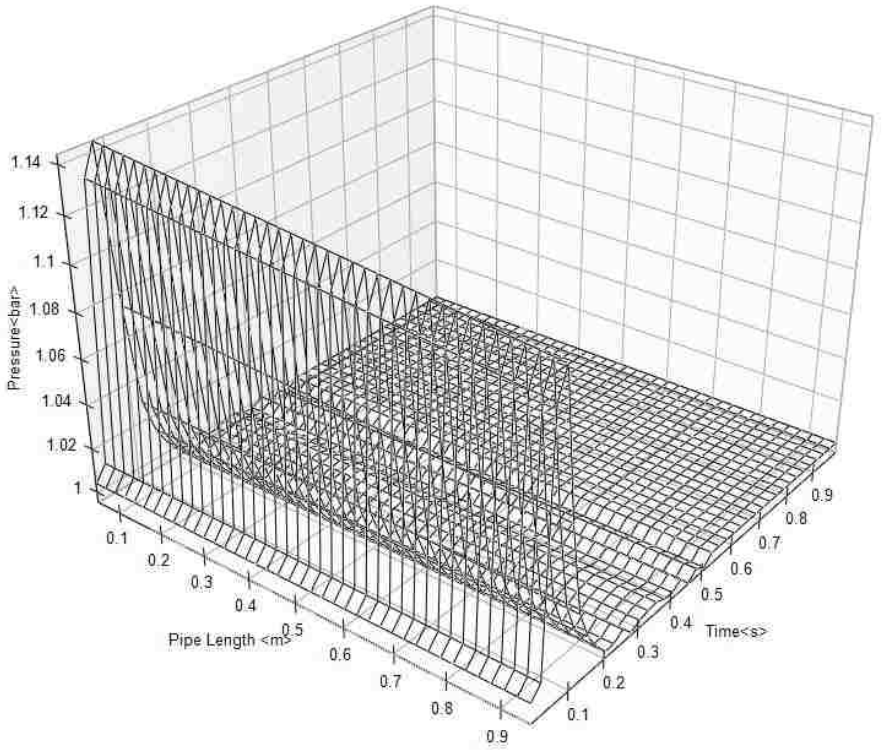

Figure 6.4. Surface of pressure, pipe length, and time for C2

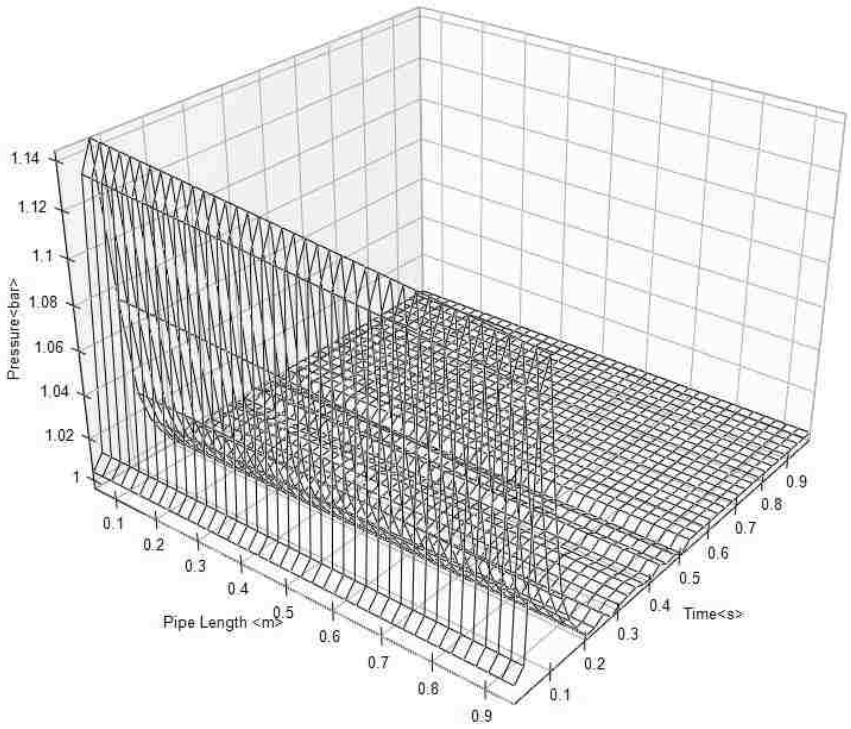

Figure 6.5. Surface of pressure, pipe length, and time for C5

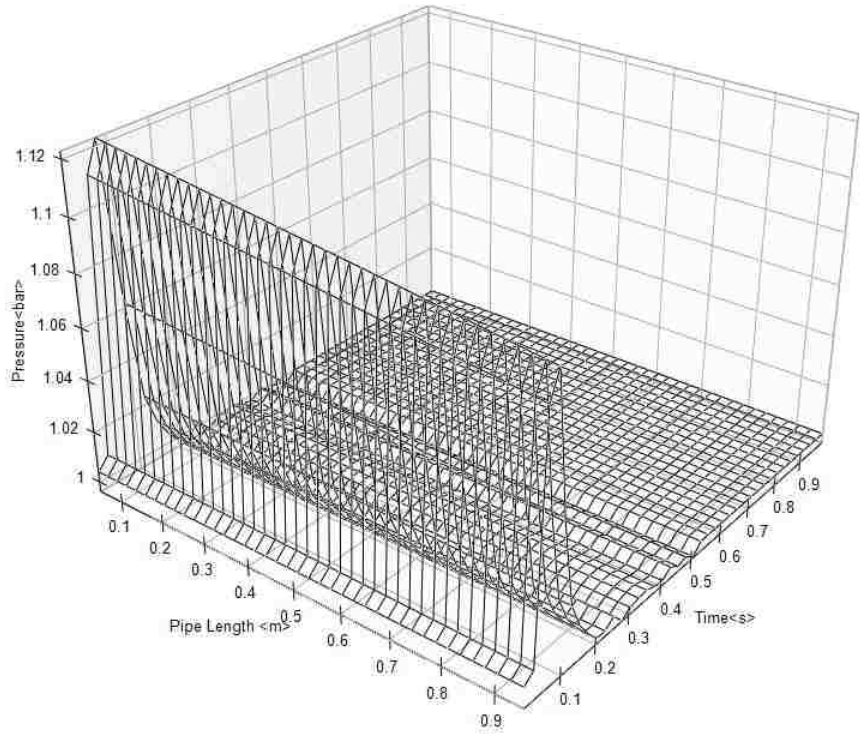

Figure 6.6. Surface of pressure, pipe length, and time for C8

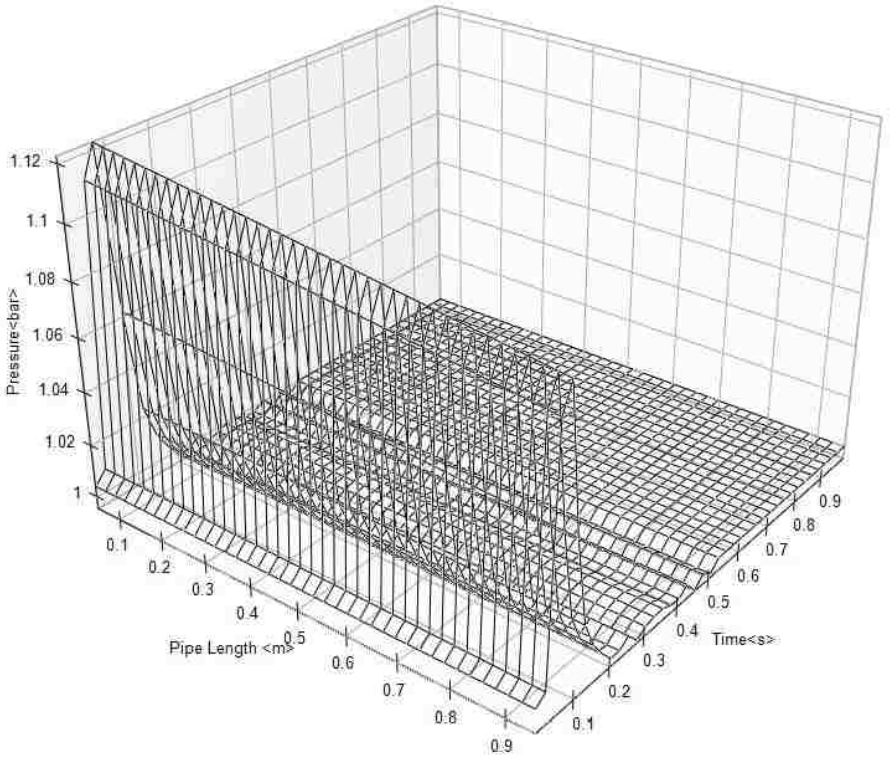

Figure 6.7. Surface of pressure, pipe length, and time for C9

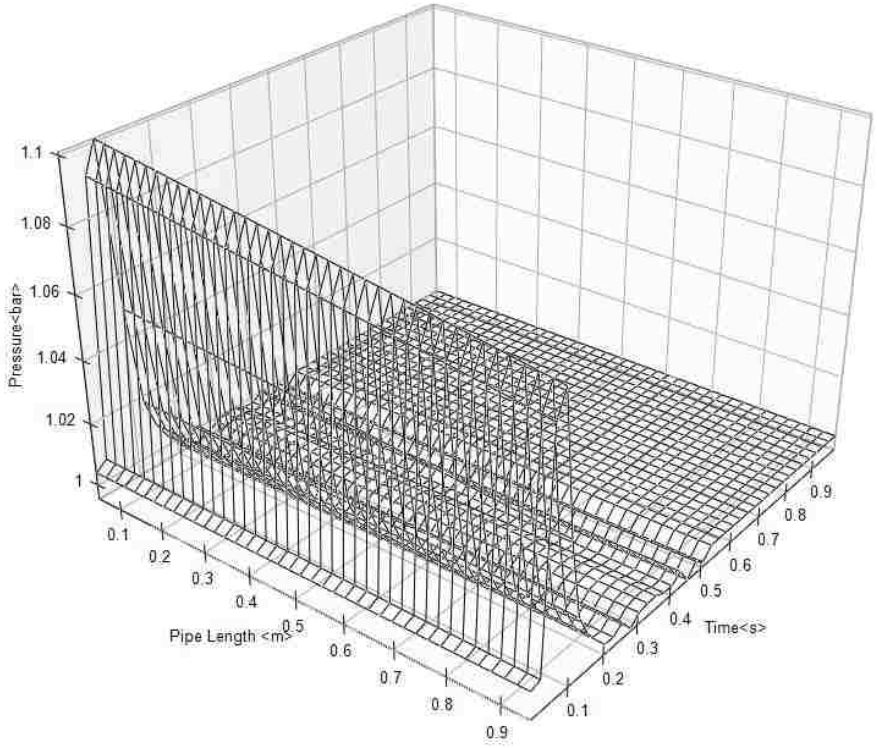

Figure 6.8. Surface of pressure, pipe length, and time for C4

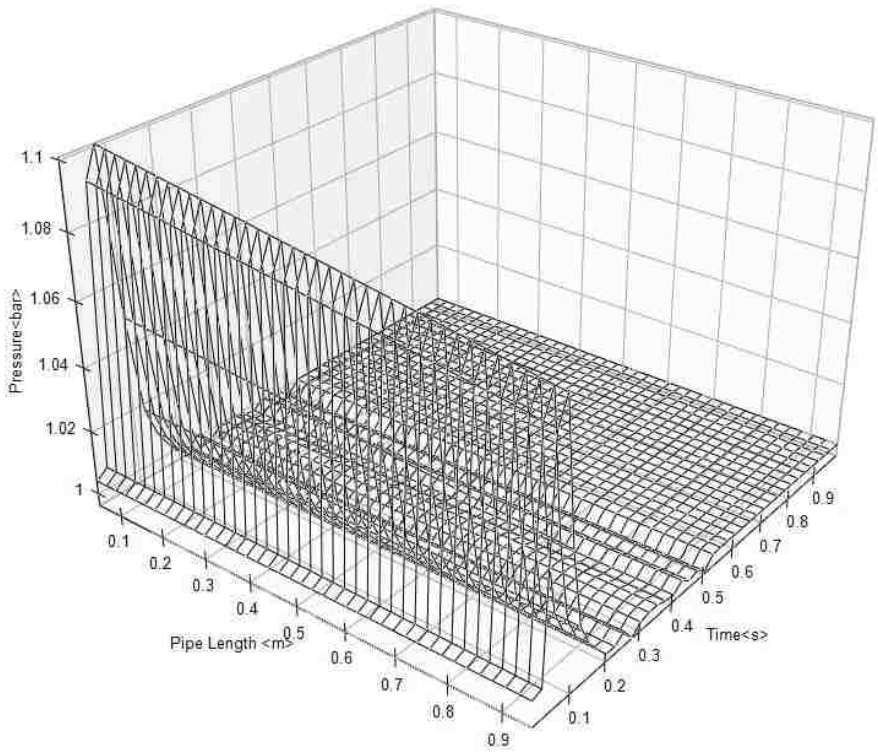

Figure 6.9. Surface of pressure, pipe length, and time for C13

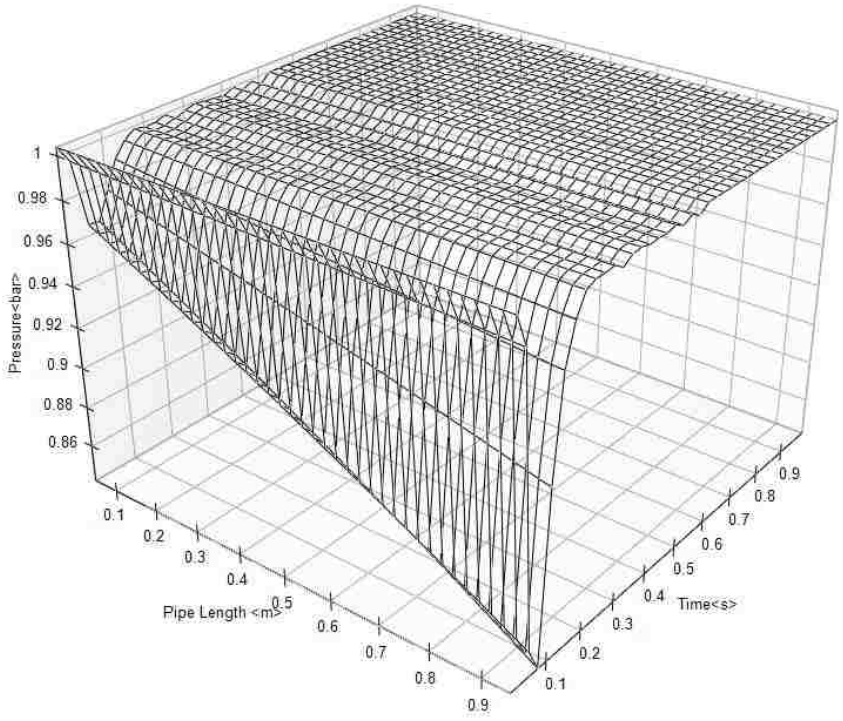

Figure 6.10. Surface of pressure, pipe length, and time for C14

Figure 6.11 shows the pressure distribution for each pipe component at 0.065 sec. The numbers next to the pipes are the pressure level in bar with two significant numbers. As can be seen in this figure, the difference is relatively small between the upper branch and lower branch. The pressure loss is around 0.1 bar for both branches. This is partly because the simulated explosion is in deflagration state and the peak overpressure assigned at explosion source is relatively low (less than 0.3 bar), the amount of attenuation is therefore small.

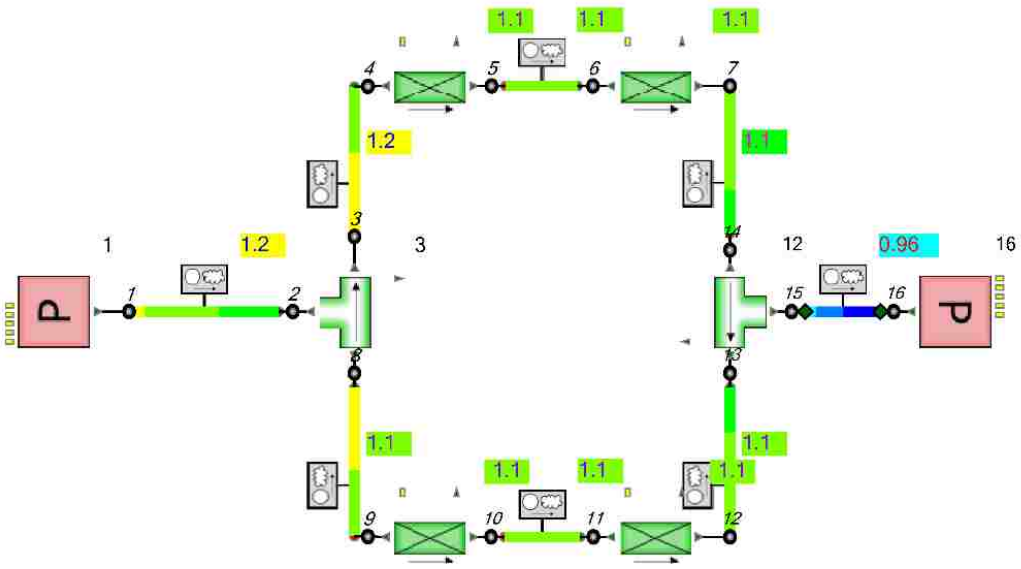

Figure 6.11. Pressure distribution in pipe components at 0.065 sec

6.4.3. Discussion. As observed in Figures 6.3 through 6.9, the peak overpressures are achieved around 0.065 sec. C14 is connected to the atmosphere and shows a rarefaction wave (dilatation wave) with a magnitude around 0.91 bar (0.09 bar below atmospheric pressure). Beyond that, the pressure of the pipe gradually approaches atmospheric pressure. The peak pressures in the bar recorded by each pipe component are shown in Table 6.1.

Table 6.1. Peak overpressures of pipe components in the sample parallel network

Component #	Peak Overpressures (bar)	Arrival Time (sec)
C17	0.20862	0.065
C2	0.18832	0.065
C5	0.21908	0.065
C8	0.20935	0.065
C9	0.13642	0.065
C13	0.05882	0.065
C4	0.06313	0.065
C14	0	Na

Table 6.1 shows that geometric changes have smaller impact on the overpressure than it has been measured in a single duct. This occurs because there is an interaction between the geometric changes in underground airways. For example, the presence of a bend downstream of the first one will weaken the attenuation effect generated by the upstream bend (Anon, 2012).

From the observations on pressure/pipe length relationships (exclude the effect of time on pressure) shown on Figures 6.3 to 6.10, pressure decreases slightly as the length of each pipe increases in each case. This type of pressure loss is most significant in C17 (shown in Figure 6.3) which is the closest to the explosion source. These pressure decreases are due to friction as discussed in Section 6.2.2. The frictional loss would be more significant as the pipe length increases.

In addition, the position of vents has influence on the attenuation effect of geometric changes, especially for those close to them. An obvious decrease of overpressure is observed in C13 and C4 pipes that are closest to the vent.

6.5. CASE STUDY: EXPERIMENTAL MINE

6.5.1. Problem Statement. Another case study was conducted by applying the decoupled simulation method for a methane explosion in a full-scale Experimental Mine. Compared to the sample parallel network model, the network at the Experimental Mine is much more complex. The dimensions of airways in this test are also more representative than were the lab-scale network model.

The Experimental Mine used in the study is an underground mine with room-and-pillar layout at the Mining and Nuclear Engineering Department, Missouri University of Science and Technology, Rolla, Missouri. An imaginary methane explosion at the Experimental Mine was simulated using the 1D CFD code *Flowmaster*. The simulation results, namely, pressure distribution and arrival time of blast-wave, will be discussed in Section 6.5.3.

The network model for the *Flowmaster* was based on a geometric model built in the ventilation commercial package *VentSim*[1]. The schematic of the network and the bending angles between underground airways are shown in Figure 6.12. The layout and dimensions of the airways for the geometric model can be found in Appendix A2.

[1] A ventilation network simulation software developed by Chasm Consulting, Queensland, Australia (http://www.ventsim.com/contact/).

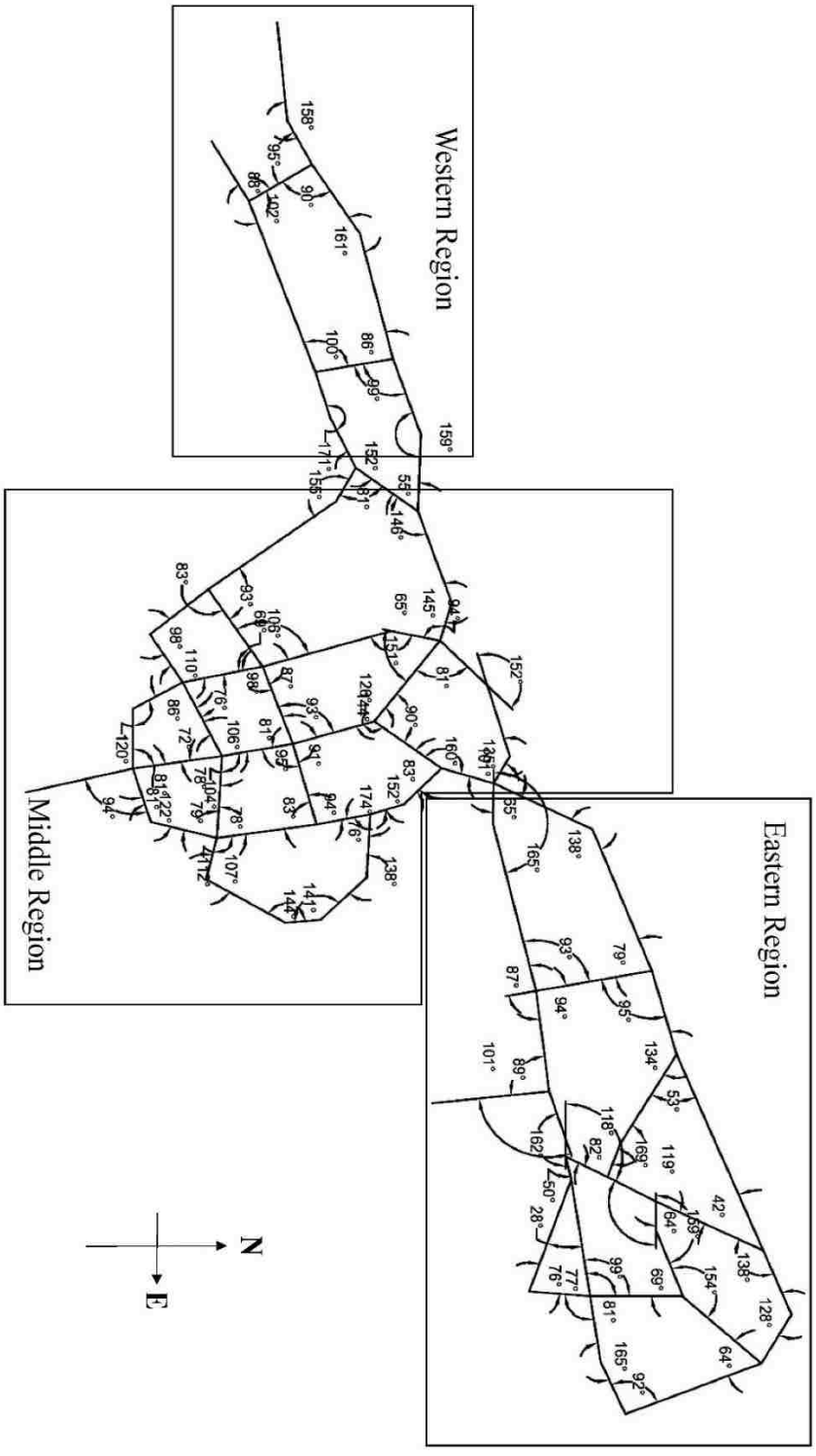

Figure 6.12. Map showing underground airways at the Experimental Mine, Missouri S&T, Rolla, MO

The network at the Experimental Mine is relatively complex, and reasonable simplifications needed to be applied to ensure convergences of calculations. As observed from Figure 6.12, the Eastern Region of the mine is connected to the Middle and Western Regions by a single airway with relatively small dimensions (2.9 m by 2.8 m, width, and height). Therefore, the designated methane explosion which occurred in the middle part of the mine had limited influence on the Eastern part. For simplification purposes, the Eastern portion was removed from the simulation. In addition, two adjacent airways, which have an angle greater than 165º, were merged into one long airway with a length equal the summation of the two. The simplified geometric model with Western and Middle Regions for *Flowmaster* is shown in Figure 6.13.

As illustrated in Figure 6.13, the Middle and Western Regions of the Experimental Mine were divided into eight sub-regions based on individual airway circuits in the network except Region 6 (marked by a blue rectangle), which connects Middle and Western Regions by three pipes in series. The airways shared by two sub-regions belong to both regions. In order to investigate the impact of the explosion on each region, one airway is selected from each region; i.e. C59, C9, C24, C11, C31, C29, C43, and C50 for Regions 1 to 8, respectively.

An imaginary explosion occurs between pipes C59 and C21. The locations of selected airways and their corresponding regions are marked with red rectangles and the angles of bend in degrees are shown next to each Cd Discrete Loss. In addition to the eight selected airways, two additional airways (C2 and C53) connected to portals were also included in measurement. The blast-waves that exhaust from two portals (the “P” in red on the left top corner represents portal number 1 which is a pressure source with constant pressure of 1 bar; and the “P” on the button represents portal number 2 also with constant pressure of 1 bar) provided the data collected.

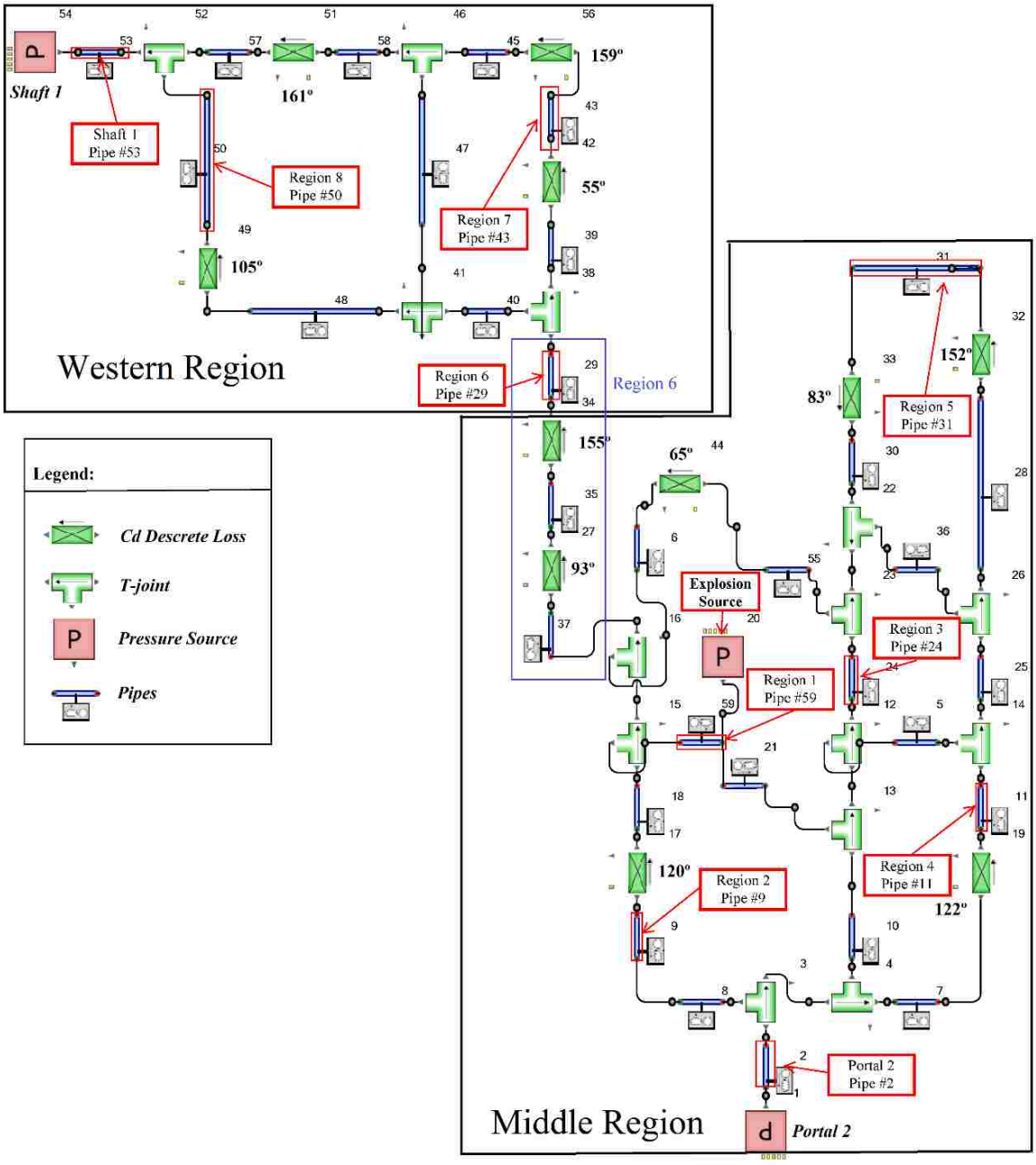

Figure 6.13. Geometric model Experimental Mine used in Flowmaster

The pressure source in Figure 6.13 (the "P" in red in the middle of the figure near Region 1) was the location of the explosion source with a methane concentration of 8%,

FLSF of 2, and HDSF of 32. The selected methane explosion source can be found in the pre-developed database described in Section 4. The gas-filled space is 8.5 m by 2.56 m and 2.56 m for length, width and height, respectively, and its equivalent hydraulic diameter is similar to airways C59 and C21. The time step size was assigned to be 0.0013 s, which was the same value given in the 3D simulations.

Similar to the sample parallel network, the bends in the network of the Experimental Mine are represented by discrete pressure loss components. The double t-branch structure used to represent a joint has more than three arms. The effect of smooth cross-sectional change is accounted for by assigning different dimensions to the adjacent airways. No abrupt cross-sectional change is found in the network; the transition component is not used.

6.5.2. Results. Simulation results are shown as 3D surfaces coordinated by local airway length, pressure, and time. Figures 6.14 through 6.24 demonstrate the simulation results of selected airways from eight regions as well as, areas close to the portals.

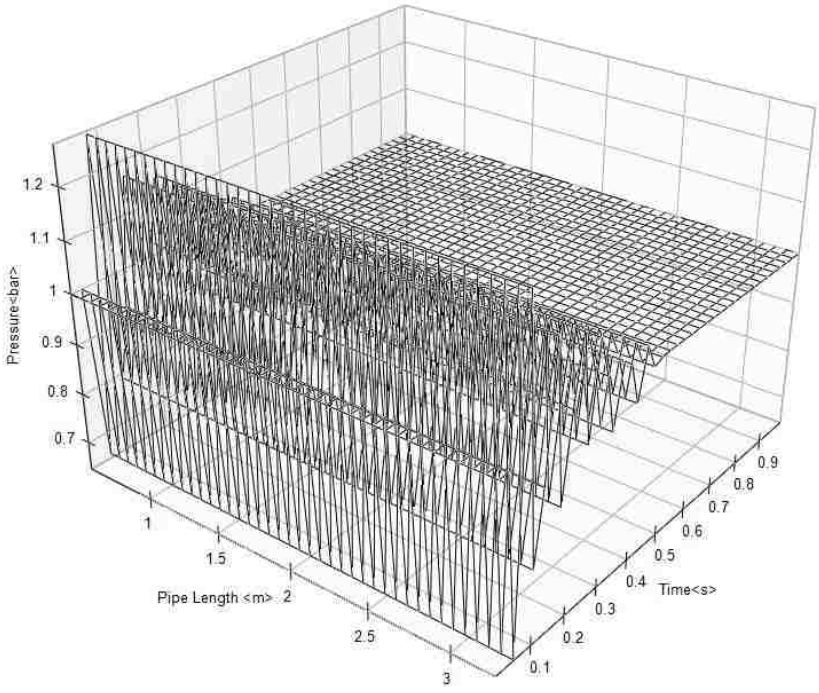

Figure 6.14. Surface of pressure, pipe length, and time for C59 for Region 1

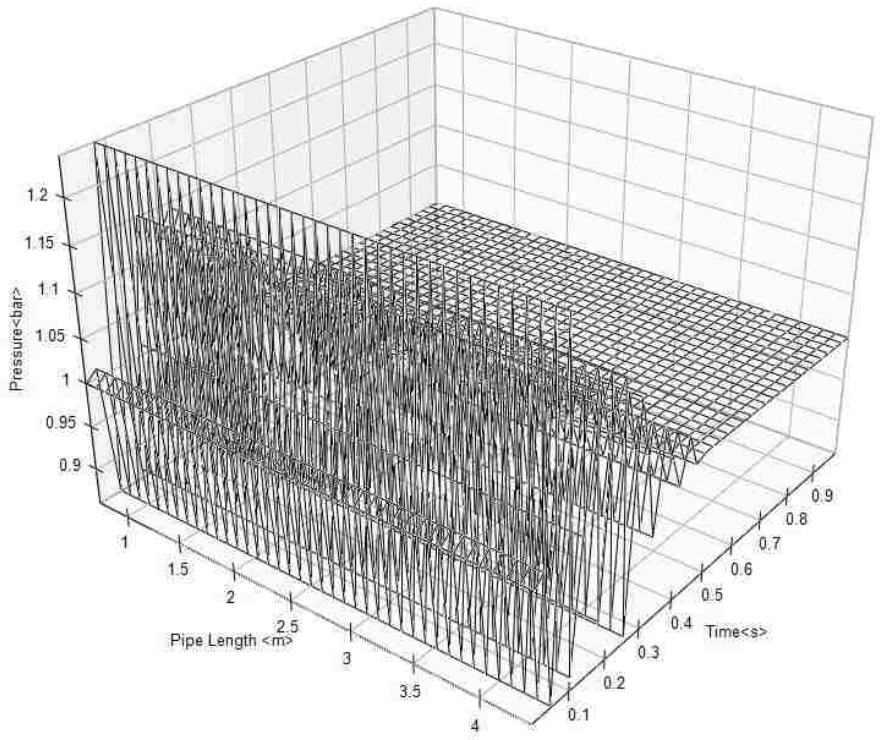

Figure 6.15. Surface of pressure, pipe length, and time for C9 for Region 2

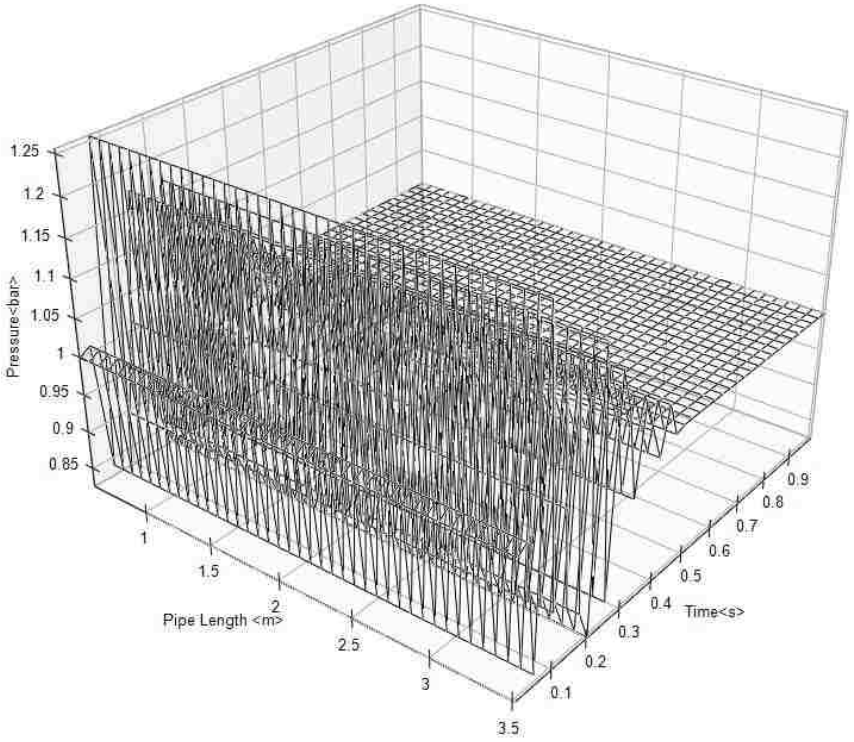

Figure 6.16. Surface of pressure, pipe length, and time for C24 for Region 3

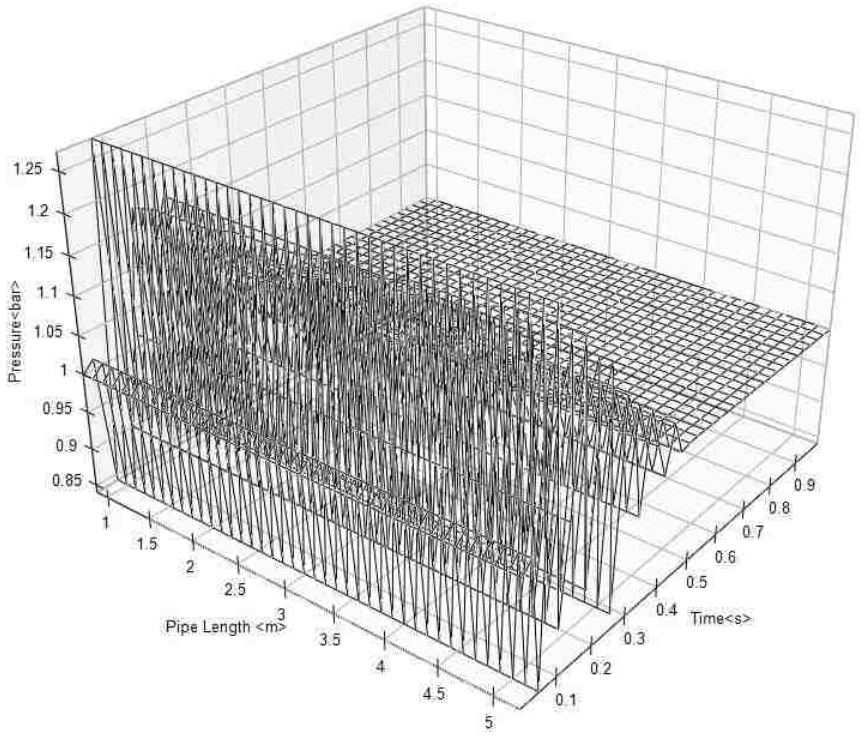

Figure 6.17. Surface of pressure, pipe length, and time for C11 for Region 4

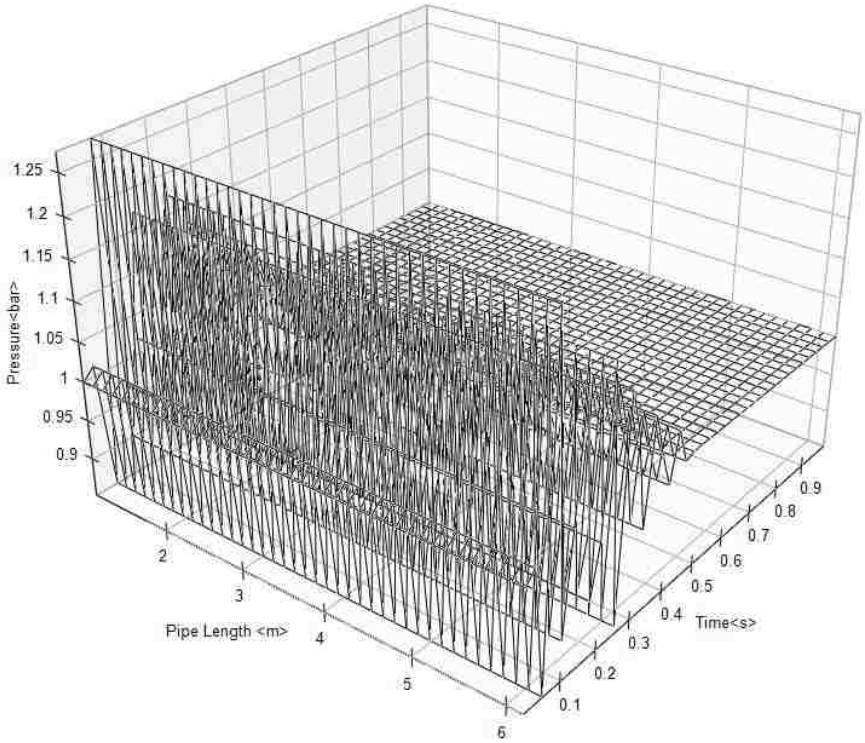

Figure 6.18. Surface of pressure, pipe length, and time for C31 for Region 5

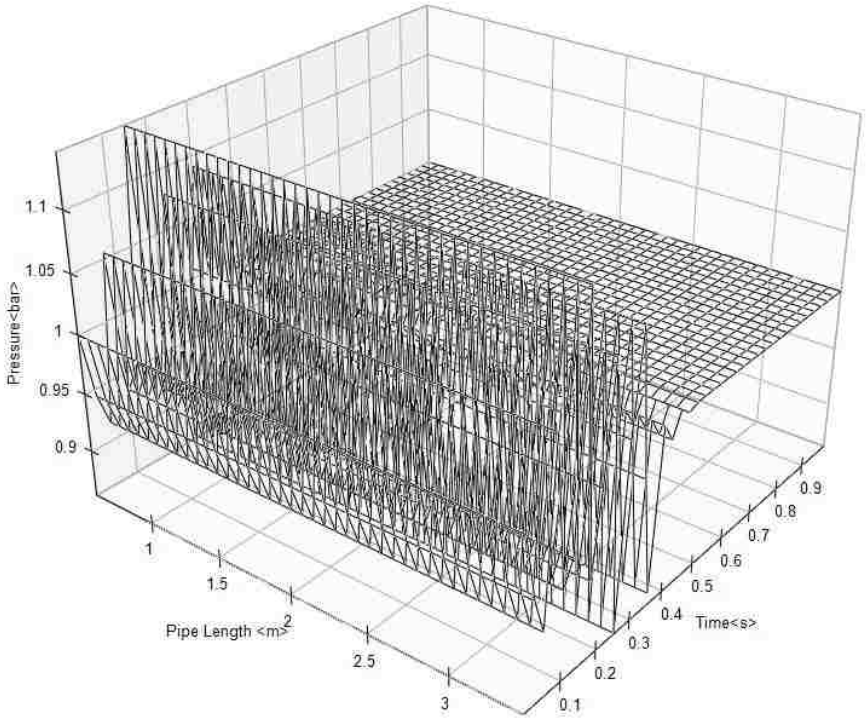

Figure 6.19. Surface of pressure, pipe length, and time for C29 for Region 6

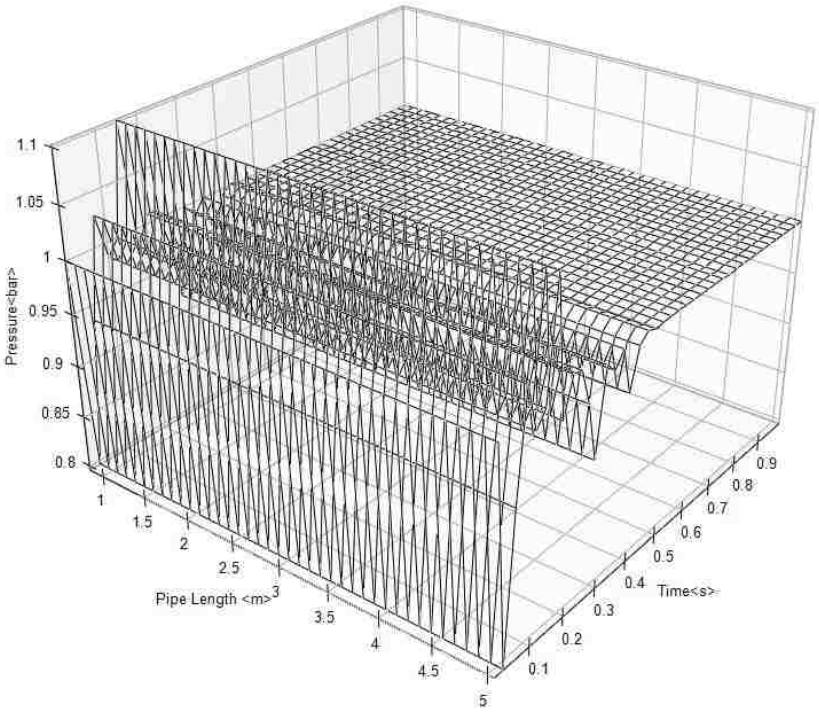

Figure 6.20. Surface of pressure, pipe length, and time for C43 for Region 7

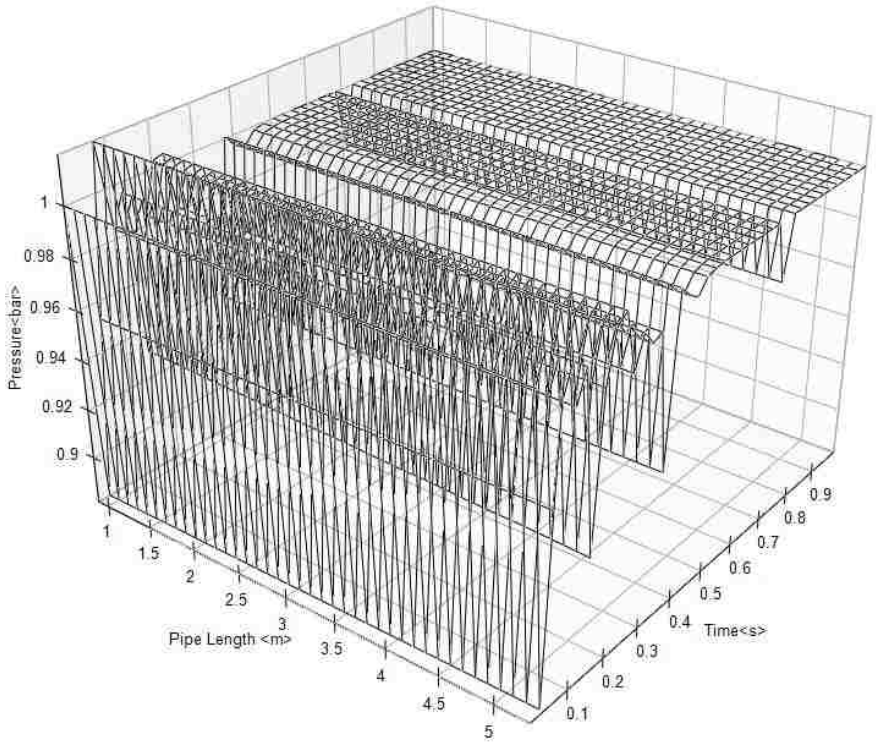

Figure 6.21. Surface of pressure, pipe length, and time for C50 for Region 8

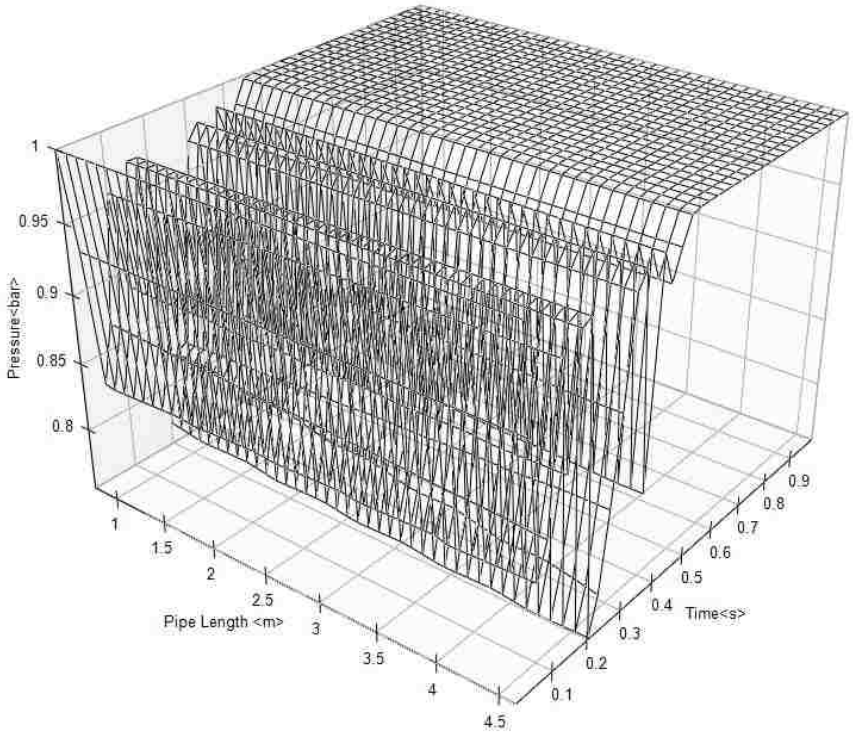

Figure 6.22. Surface of pressure, pipe length, and time of C53 for Shaft 1

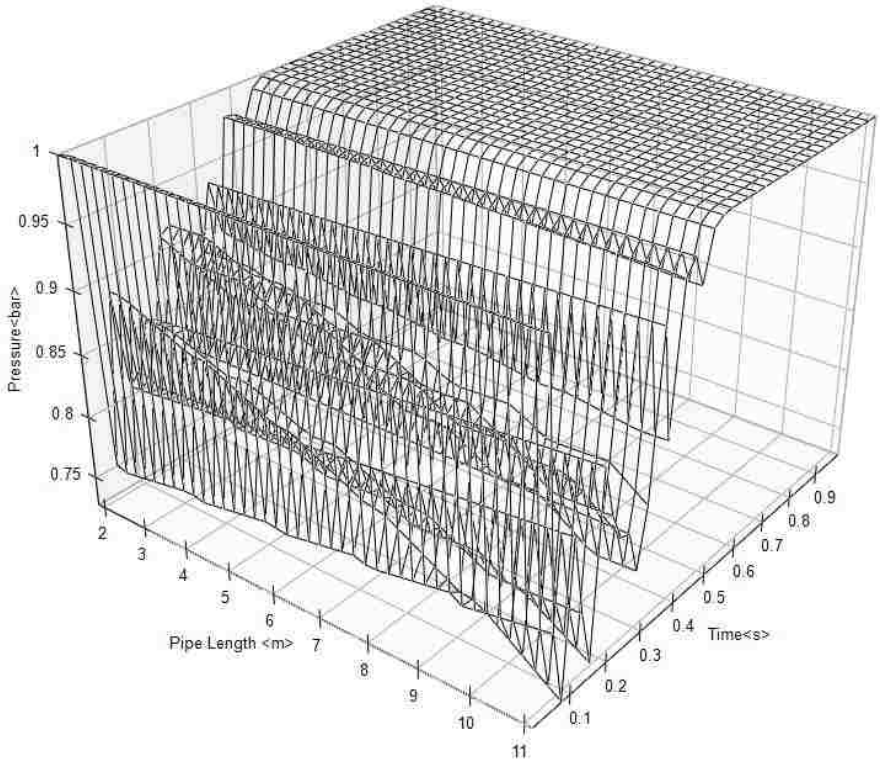

Figure 6.23. Surface of pressure, pipe length, and time of C2 for Portal 2

Figures 6.14 through 6.23 show the pressure variations of the blast-waves with time and local pipe length for selected pipe components. As observed from Figures 6.14 to 6.23, oscillations of pressure magnitude are found when the simulation time is smaller than 0.5 sec. In addition, a decrease in the pressure with an increase in the local pipe length (to observe the change of pressure from pressure/pipe length plane) is less obvious than those observed in the parallel models from Figures 6.3 through 6.9. This is because the friction plays a less significant role to attenuate a blast-wave in ducts with larger dimensions. A detailed discussion about the Figures above will be provided in Section 6.5.3.

The pressure distributions in the network at 0.039 sec, 0.117 sec, and 0.195 sec are shown in Figures 6.24 through 6.26 to demonstrate the influence of explosion source on the entire mine when three peak pressure values (peaks of blast-wave) are obtained.

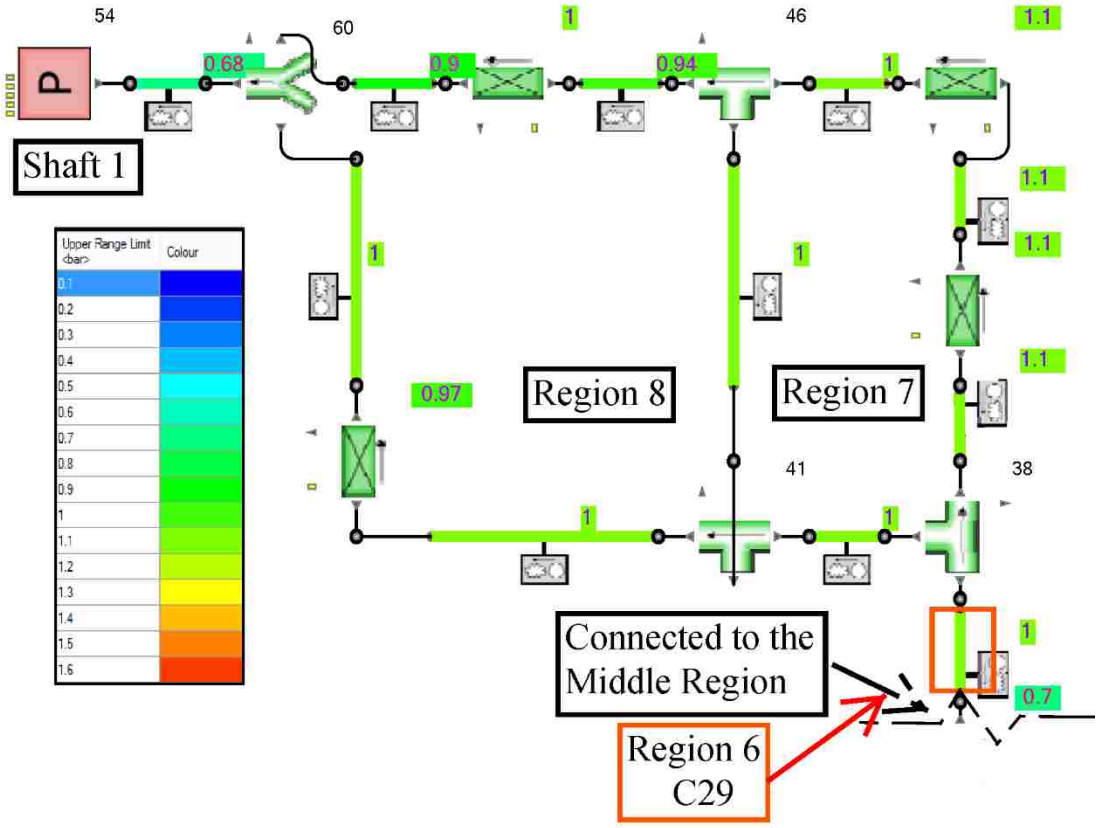

(a)

Figure 6.24. Pressure distribution of airway network at 0.039 sec in the (a) Western Region and in the (b) Middle Region of the Experimental Mine

For Figures 6.24 through 6.26, the color map on the left hand side of panel (a) for each figure shows the upper range of the pressure obtained in bar. The small number highlighted by sample colors shown in the color map represents the peak pressure obtained by the corresponding components (i.e. pipes, T-Junctions, and Cd Discrete losses).

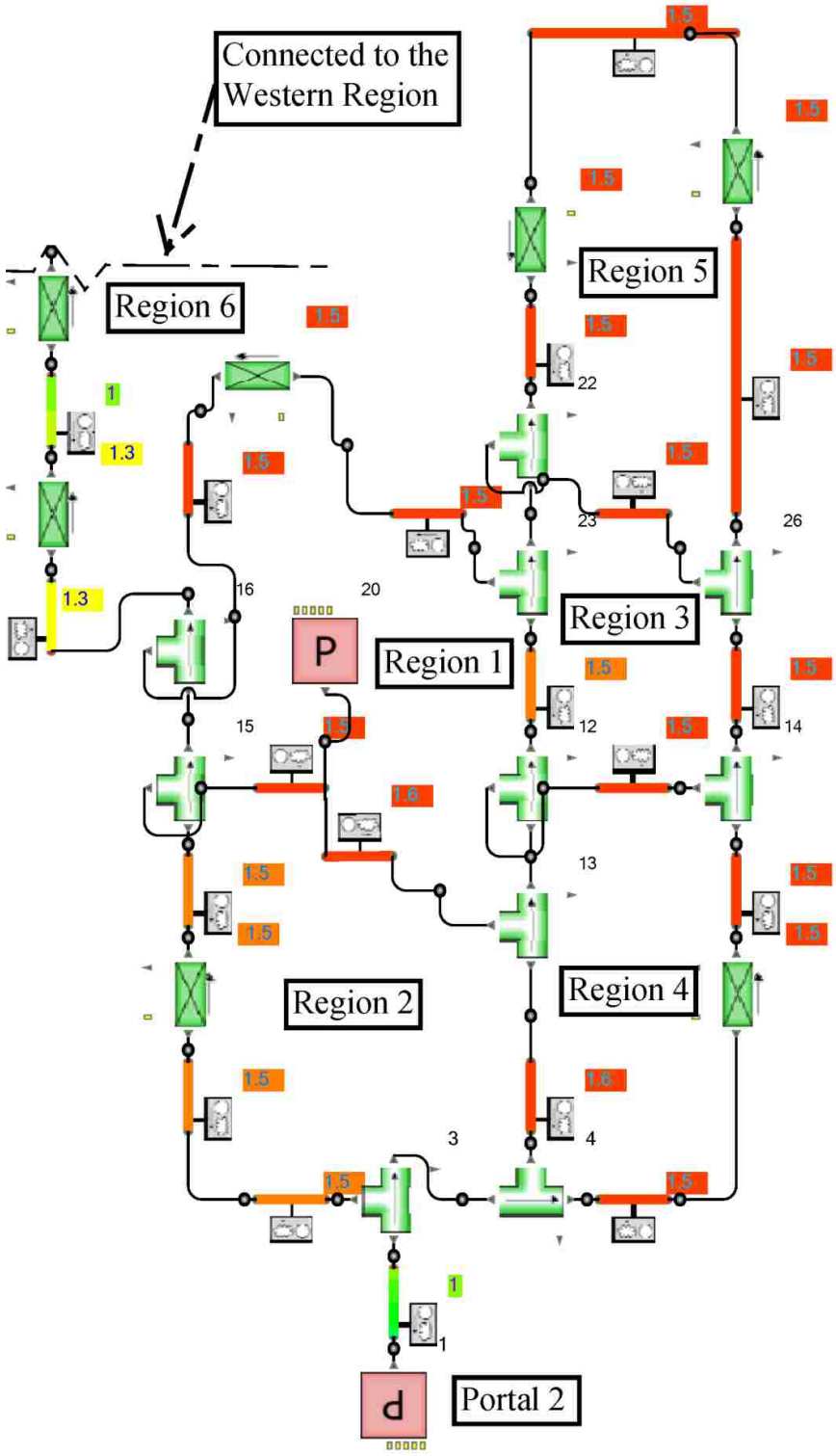

(b)

Figure 6.24. Pressure distribution of airway network at 0.039 sec in the (a) Western Region and in the (b) Middle Region of the Experimental Mine (cont.)

Figure 6.24 demonstrates the pressure distribution for the Western Region (6.24 (a)) and Middle Region (6.24 (b)) of the network impacted by the imaginary explosion at 0.039 s. The Middle Region and Western Region are displayed separately. Small figures in green, yellow, or red next to each component denote its peak pressure values in bar. As noticed from the peak pressure values in Figure 6.24 (b), the pressure values for Regions 1 to 5 are almost identical. However, from Figure 6.24 (a), the blast-wave seems to have a limited influence on Region 6 and 7; and almost has no impact on Region 8. The detailed discussion of this phenomenon will be provided in Section 6.5.3.

Figures 6.25 and 6.26 illustrate the pressure distribution of the network at 0.117 sec and 0.195 sec when the second and third peaks of the blast-wave arrive at explosion source.

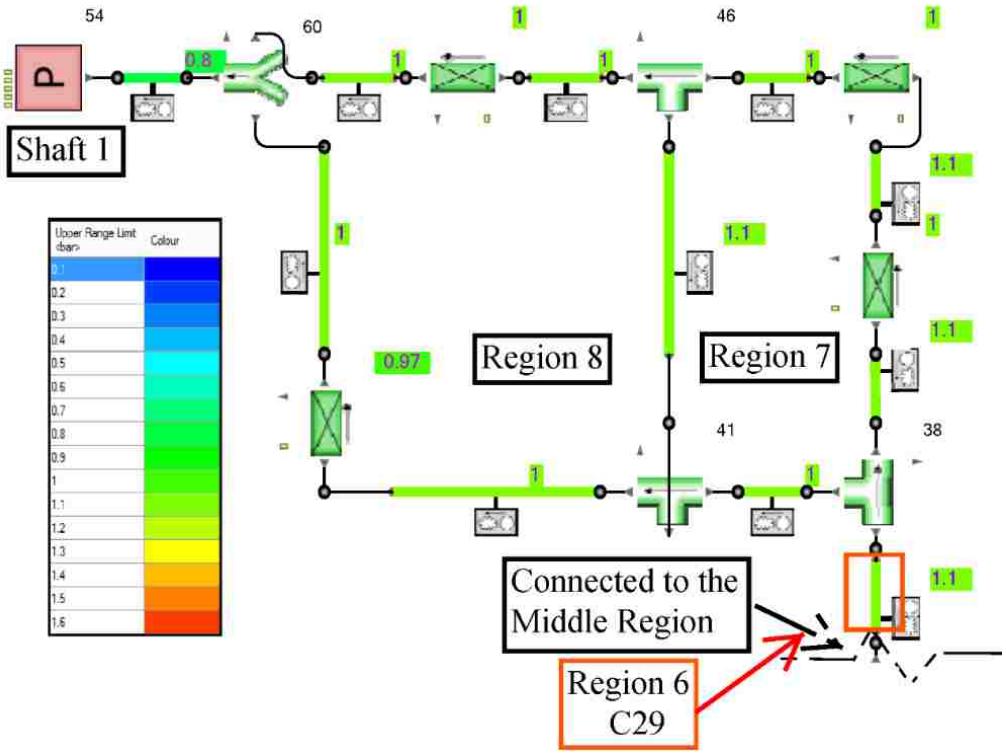

(a)

Figure 6.25. Pressure distribution of airway network at 0.117 sec in the (a) Western Region and in the (b) Middle Region of the Experimental Mine

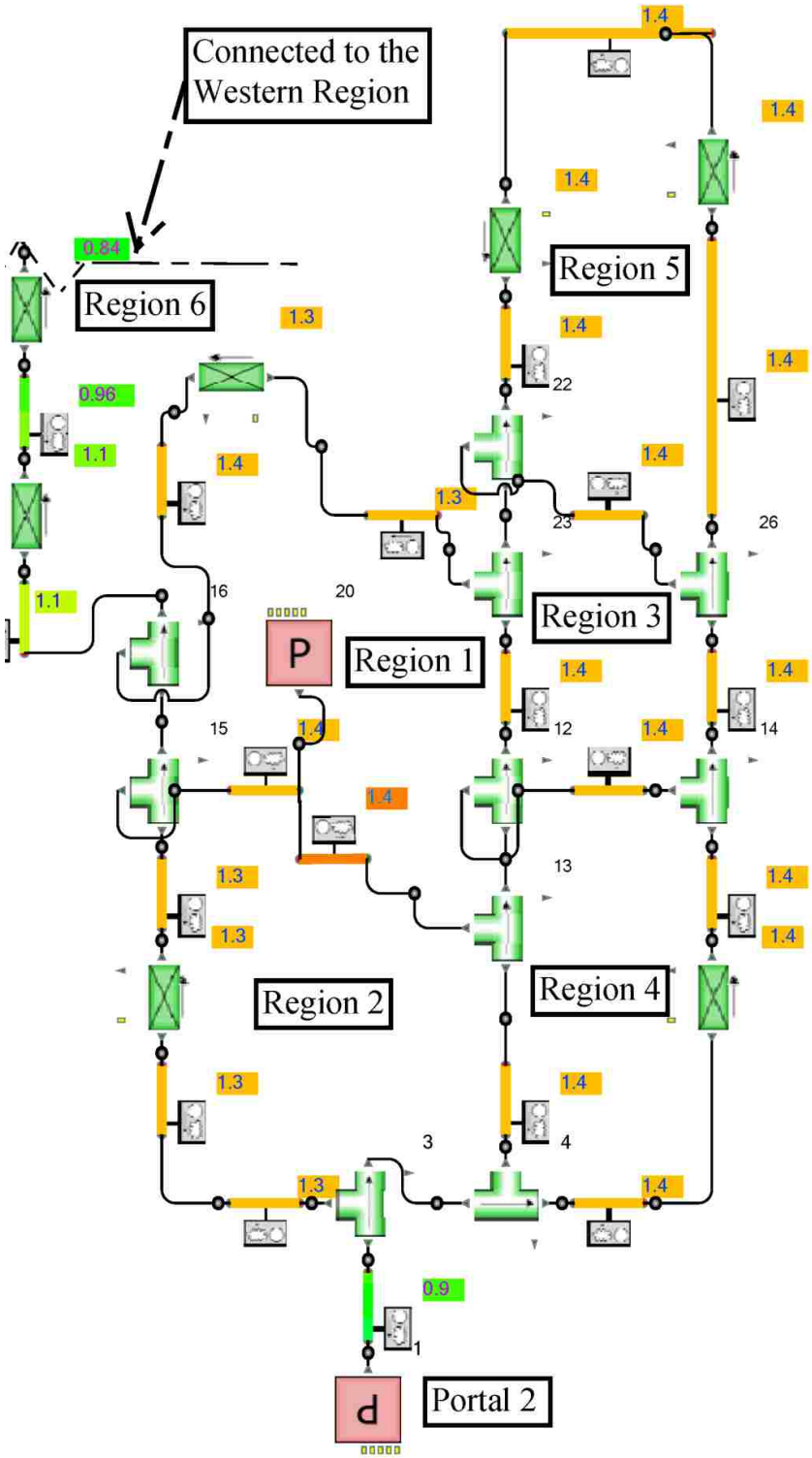

(b)

Figure 6.25. Pressure distribution of airway network at 0.117 sec in the (a) Western Region and in the (b) Middle Region of the Experimental Mine (cont.)

Figure 6.25 shows the pressure distribution when the second peak of the blast-wave reaches the network at 0.117sec. Similar patterns of the pressure distribution as Figure 6.24 are illustrated in Figure 6.2. Thus, the blast-wave influence on Regions 6 through 8 is still limited. Both pipes close to Shaft 1 and Portal 2 (C2 and C53) show negative overpressures.

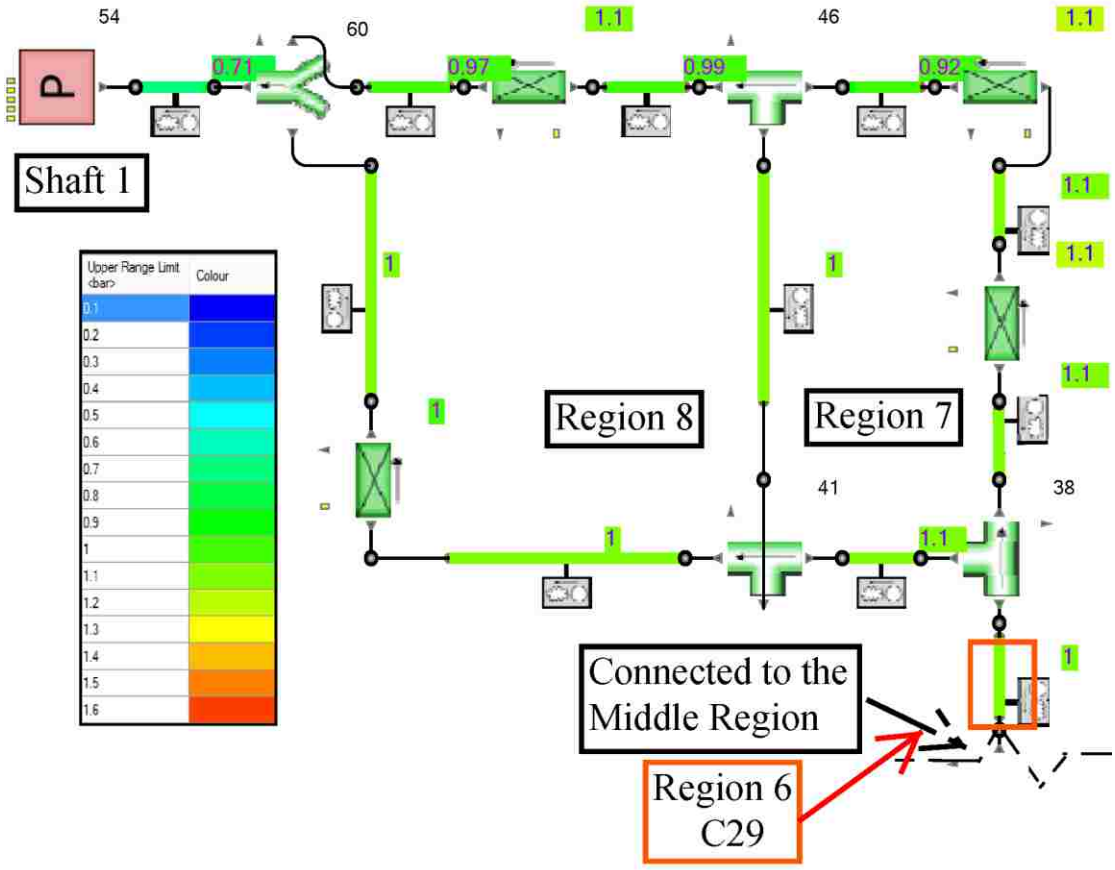

(a)

Figure 6.26. Pressure distribution of airway network at 0.195 sec in the (a) Western Region and in the (b) Middle Region of the Experimental Mine

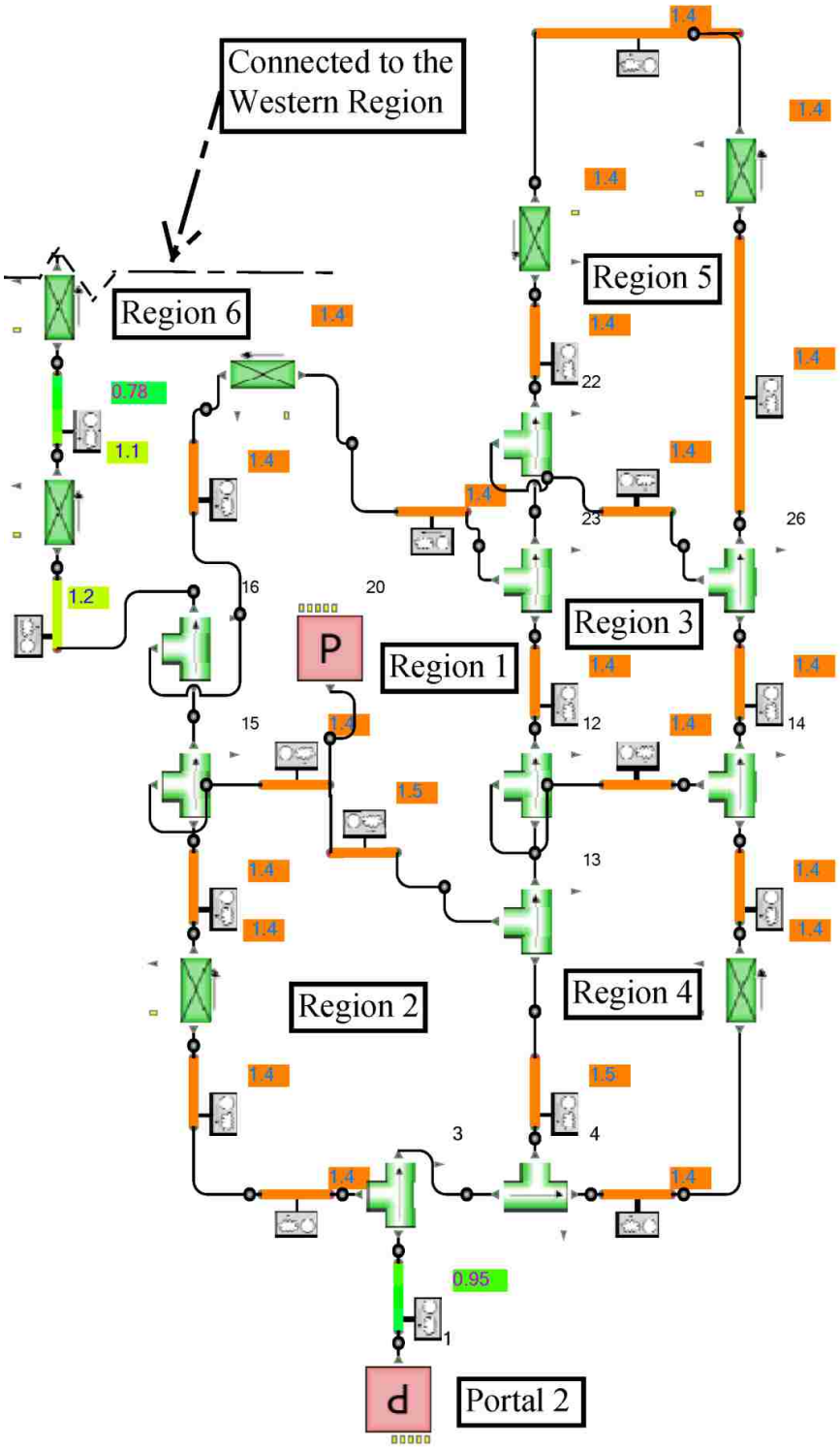

(b)

Figure 6.26. Pressure distribution of airway network at 0.195 sec in the (a) Western Region and in the (b) Middle Region of the Experimental Mine (cont.)

Figure 6.26 shows the pressure distribution when the third peak of the blast-wave reaches the network. As seen in Figure 6.26 (a), the pressure values reached 1.1 bar for four of the airways in Region 7 at 0.195 sec, which had a relatively greater impact from the methane explosion than did the other two time instances. This implies that the blast-wave arrived later in Region 7 and Region 8 than in the other sub-regions. The pressure values obtained in the Western Region (around 1.1 bar) are still much smaller than those in the Middle Region (normally 1.4 to 1.5 bar).

6.5.3. Discussion. The network-based simulations for a hypothetical methane explosion at the Experimental Mine were conducted. Figures 6.14 to 6.23 show the pressure-time-length relationships of selected pipe components from eight regions of the Mine together with two pipes connected to the surface (Shaft 1 and Portal 2). As seen in Figures 6.14 to 6.18, the pressure oscillation patterns were found to be similar in Regions 1 to 6. At Regions 7 and 8, however, oscillations with a magnitude around 0.2 bar are observed (See the pressure surfaces in Figures 6.20 and 6.21). The absolute values of negative impulses were larger than positive ones, which had magnitudes around 0.1 bar. This phenomenon suggests that a rarefaction wave can propagate a greater distance than a compressive wave. Negative pressure impulses were found in airways connected to the Shaft 1 and Portal 2 (Figures 6.22 and 6.23). They might be attributed to the rarefaction waves led by the exhausting process of blast-wave occur in close-to-surface areas.

The peak pressures were obtained at 0.039 sec., 0.117 sec., and 0.195 sec., respectively. These pressure distributions are shown in Figures 6.24 to 6.26. At 0.117sec., the influence of a methane explosion does not show substantially attenuated in Regions (airway circuits) 2, 3, 4, and 5 connected to each other in parallel (Figure 6.25(b)). By contrast, the blast-wave was significantly attenuated in Region 6, 7, and 8, when 6 and 7 are connected in series (Figure 6.25 (a)). The Western Region is directly connected to the explosion source by three airways in series that belong to Region 6. The geometric changes and friction become critical when attenuating the blast-waves. A similar pressure distribution pattern was also found at the 0.195 sec. case (Figure 6.26).

The peak overpressures for each selected pipe component and their arrival times are listed in Table 6.2.

Table 6.2. Peak overpressures and arrival times of selected pipes at the Experimental Mine

Regions	Component#	Peak Overpressure (bar)	Arrival Time (sec)
R1	C59	0.522	0.039
R2	C9	0.492	0.039
R3	C24	0.512	0.039
R4	C11	0.375	0.117
R5	C31	0.443	0.195
R6	C29	0.144	0.156
R7	C43	0.151	0.156
R8	C50	0.04	0.195
Shaft 1	C53	0.001	Na
Portal 2	C2	0	Na

Table 6.2 suggests that the peak overpressure decreases as the distance from explosion source increases. The attenuation effect of geometric change is insignificant when airway cells are connected to each other with more than one airway as in Regions 2, 3, 4, and 5. By contrast, the geometric changes become critical on the propagation of the blast-wave when two regions are connected by only one airway. The decrease of the overpressure is obvious from Regions 6 to 7, and 7 to 8.

6.6. SUMMARY

This section introduced applications of the decoupled network-based method and methane explosion simulations. The initial and boundary conditions were provided by the pre-built explosion source database using *Microsoft SQL Express server.* The pressure

losses during the blast-wave propagation were captured using the frictional loss for pipes in the *Flowmaster*, Cd Discrete Loss for bends and obstacles, T-Junction component for branches, and transition component for cross-sectional changes.

This research seeks to improve the prediction efficiency of gaseous explosions and realized numerical simulations of gaseous explosions in a full-scale, underground network using a decoupled numerical method. To provide quick predictions of overpressure distribution of methane explosions in underground airway networks, a two-section theory was employed. The explosion space was divided into a driver section and a blast-wave section. Governing equations including the conservation of mass, momentum, and energy, together with chemical reaction and turbulence models were solved for the driver section and the blast-wave section by using computational fluid dynamics (CFD) solver ANSYS Fluent (3D-based) and *Flowmaster* (1D-based), respectively. Imaginary methane explosions with a lab-scale sample parallel network and a full-scale Experimental Mine were simulated. Six major conclusions are summarized, below, from the results analyses provided in the preceding subsections. These conclusions are as follows: (1) geometric changes in an airway network have a less significant impact on the overpressure compared when they are measured alone in a single duct; (2) the position of a vent has a positive impact on the attenuation effect due to geometric changes; (3) rarefaction waves can propagate a longer distance than compressive waves in airways; (4) oscillations are found in the pipes connected to the surface due to their large velocity gradient; (5) the peak overpressure decreases as the distance from the explosion source increases, regardless of the network layout; (6) the attenuation effect due to geometric changes is more significant when airways are connected to each other by more than one airway.

7. CONCLUSIONS

7.1. SUMMARY

The initial motivation for this research study was to solve a major safety problem in mining operations. However, the simulation cost of methane explosions as they occur in a full scale underground mine is unaffordable using the available numerical techniques. The current study attempted to solve this problem by employing a decoupled numerical method and provide quick predictions of overpressure distributions of methane explosions in a complex network. According to the two-section theory introduced in Section 2, the explosion space can be divided into a driver section and a blast-wave section. Governing equations including the conservation of mass, momentum, and energy, together with chemical reaction and turbulence models were incorporated in the calculations of the driver section. Numerical calculation results for the driver section were stored in a database tool *Microsoft SQL Server Express* which resulted in a methane explosion source database. The development of the database is introduced in Section 4. To validate the selected combustion and turbulent models, a series of lab-scale methane explosion experiments were conducted. The experiment design and result analysis are provided in details in Section 3.

A set of simplified governing equations were used in the simulation of the blast-wave section and, a one-dimensional (1D) numerical simulation based on transient implicit method was used. The details of the simulations in the blast-wave section are discussed in Section 6. The influences of geometric changes were investigated by using 2D Euler equations and the results were discussed in Section 5. In reaching a major goal of this research to develop a decoupled methane explosion numerical prediction method, some key findings in each part of the research will be introduced in the following subsection.

The use of a decoupled method can reduce the calculation time significantly by using 1D simplification in the blast-wave section. Specifically, a geometrical model with FLSF=1 and HDSF=1 is useful for such analysis. The geometry is 0.08 m in width and height, and 4.25 m in length. Hexahedral cells with a width of 0.5 mm are used to mesh the geometry. The meshed geometrical model has 217,600 cells and 245,939 nodes.

Governing equations including turbulence and combustion models were introduced in Section 2.2 and would need to be solved 217,600,000 times if 1000 time steps were applied. The calculation time using a computer model with the appropriate software was approximately 21 minutes using a powerful personal computer with INTEL quad-core i7 3770K and 16 Gb of raw using eight parallel processes with *ANSYS Fluent*. In addition, the 1D simplification with a four node linear element for the same geometry took approximately 1.8 seconds using the same computer with *Flowmaster* ,as the governing equations were solved 4,000 times using 1,000 time steps. In addition, the computational cost was further reduced by eliminating two momentum equations in x and y directions, as well as combustion and turbulence modeling from the governing equation system. The calculation time reduction for the 1D simplification in the blast-wave section could be more considerable if larger and more complex geometries were used compared to the selected case of geometry for airways commonly encountered in mines.

7.2. SIMULATION AND LAB FINDINGS

In the process of developing the decoupled prediction method for methane explosion, twenty major conclusions were drawn from the analysis of the experimental and numerical results in each part of the research. Detailed discussions can be found in the last subsection in Sections 3, 4, 5, and 6. They are grouped and summarized below as follows:

Methane Explosion Experiment. The experimental study on methane explosion aimed to investigate the capability of selected combustion and turbulence models used in simulations in the driver section. From the analysis in Section 3.4, three key findings were identified, which are:

(1) In a case where there are bends in airways, the attenuation factor decreases with the bending angle between 50° and 120°; and the Attenuation Factor drops to less than 1 from angles 90° to 120° and then increases back to 1 before 180°

(2) In the t-branching case, the overpressure distributed at the bottom branch is higher than the overpressure at the top branch

(3) The selected cross-sectional change geometries have no notable impact on the propagation of blast-waves

Simulations in the driver section. Turbulence and chemical reaction play key roles in a methane explosion in the driver section and can be recaptured in numerical modeling as well. From the simulation results, four conclusions have been drawn in Section 4.5 as follows:

(1) Detonation is more likely to occur in a methane accumulated space with large length-to-diameter ratios

(2) In an 8% methane concentration level, the detonation is easily triggered at the lowest length-to-diameter ratio of 13.3 compared to 54 for the 9.5% level and 212 for the 12% level

(3) Airway with an 8% methane concentration level has the largest peak overpressures of more than 14 MPa, while for the 9.5% level it is around 12 MPa. Therefore, overpressure was inversely proportional to concentration

(4) One sustainable detonation was detected for the case of 9.5% methane concentration level while two detonations were detected for the 8% case. For the 12% methane concentration level, no sustainable detonation is found within the dimensions covered in this research

Influences of geometric changes. From numerical research on the influence of geometric changes on the blast-wave propagation in Section 5.4, five major conclusions were identified as follows:

(1) As the bending angle changes, the Attenuation Factor increases from 30° until the maximum value obtained at 50°. Then, it decreases to a value around 1.14 at 90°. Bends with angles greater than 90° tends to strengthen the compressive wave with Attenuation Factors smaller than one

(2) For obstacles with different blockage ratio, the Attenuation Factor increases when the Blockage Ratio (BR) increases

(3) In a t-branch section, when blast-wave is input from the main arm, the Attenuation Factor for the branch duct is greater than the main duct by 30%

(4) In the cross-sectional change case, the overpressure is greater inside the expended area compared to the downstream overpressure due to constrained reflections

(5) The selected numerical scheme overestimates the Attenuation Factors in 120° bend case as well as all obstacles cases

Simulations in blast-wave section. The numerical study for the blast-wave section is based on 1D, transient, and compressible flow assumptions. The required initial and boundary conditions were provided by pre-developed explosion database and pressure losses due to friction and geometric changes, which were included using the results of the study in Section 5. The decoupled network-based prediction method was applied for two case studies. Six conclusions illustrate the result analysis stated in Sections 6.4 and 6.5 as follows:

(1) The geometric changes have relatively less significant impact on the overpressure in a network compared to being measured separately in a single duct

(2) The position of the vent has impact on the attenuation effect of geometric changes, especially for those close to the location of the vent

(3) In a methane explosion, rarefaction wave can propagate through larger regions compared to compressive wave

(4) Oscillations are found in the pipes connected to the surface

(5) The peak overpressure commonly decreases as the distance from explosion source increases regardless of network layout

(6) The attenuation effect of geometric changes is more significant when airway cells are in series rather than in parallel

According to the key findings above, this work has made four major contributions to the experimental and numerical research on methane explosions in a confined space. These major contributions are:

(1) Evaluated the capability of LES turbulence model on methane explosion

(2) Investigated the scaling effects of gas accumulated space on peak overpressure of explosions

(3) Investigated the impact of geometric changes normally encountered in underground mines on blast-wave propagation

(4) Applied decoupled numerical methods on two case studies. These studies enable numerical simulation of methane explosion in complex networks without the sacrifice of accuracy by considering different features of two separate sections

7.3. FUTURE WORK

This research provided an analytic tool for methane explosions influence on underground airway networks. This tool can be improved by the following four aspects: (1) the completion of explosion source database with the incorporation of complex scenarios; (2) validation of the 1D model by using a full scale methane explosion test in airway networks; (3) investigation of various turbulent and combustion models to improve accuracy; and (4) development of a statistical model based on degree of confidence to account for the DDT randomness.

One of the major goals of this study is to highlight the importance of methane explosions in mines and push for further scientific research in this field. There are still gaps in knowledge in this field, and research has to further investigate this problem to eventually eliminate the major safety hazards associated with the underground mining industries. In addition, coal production is still a vital industry and could not be easily substituted by other energy sources. Thus, miners will still spend their working lives beneath the earth in mines and be exposed to such hazard that should be urgently explored and solved.

APPENDIX A.

LAYOUT OF METHANE EXPLOSION EXPERIM

Appendix A shows the locations of pressure sensors (○ sign) and flame sensors (⊕ sign) on the explosion duct. The layout of the pre-duct (straight duct before the presence of geometric changes). The total length of pre-duct is 11 m and diameter is 0.08 m. The full length of pre-duct is divided into five parts shown in Figures A1.1-A1.5. In all figures, Pi represent pressure sensors and Fi represent flame sensors, i is sensor number. The unit shown in annotations is meter.

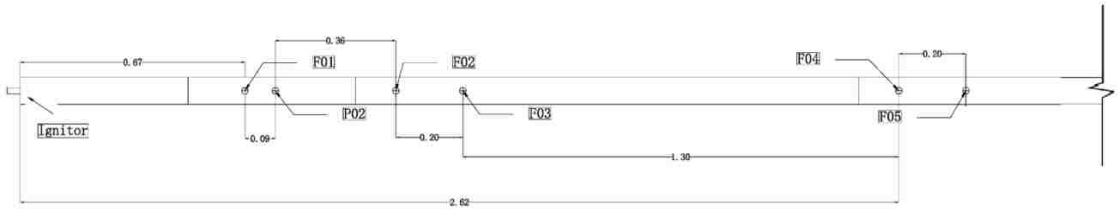

A1. Pressure sensor and flame sensor layout from the total length of 0 m to 2.62 m (from igniter to F04 2.62 m in length)

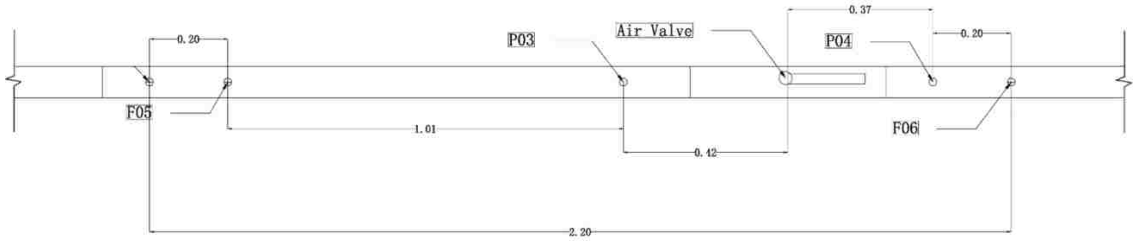

A2. Pressure sensor and flame sensor layout from the total length of 2.26 m to 4.82 m (from F04 to F06, 2.2 m in length)

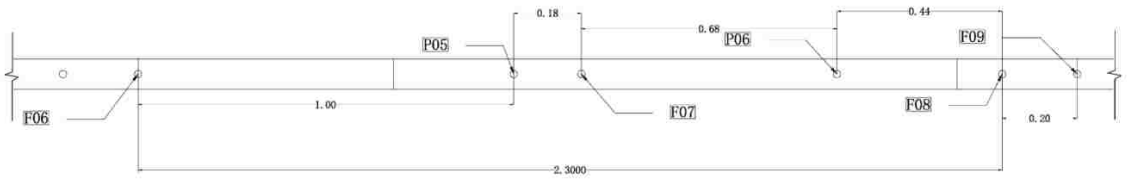

A3. Pressure sensor and flame sensor layout from the total length of 4.82 m to 7.12 m (from F06 to F08, 2.3 m in length)

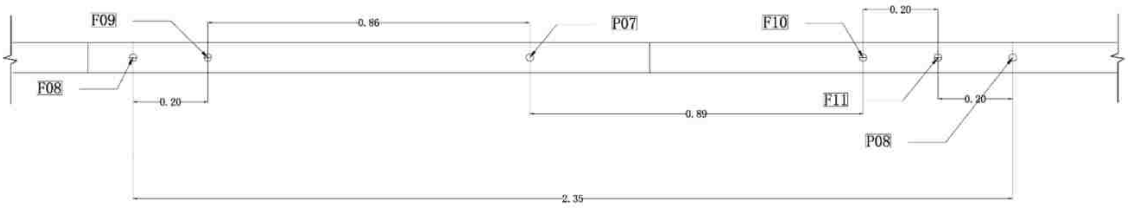

A4. Pressure sensor and flame sensor layout from the total length of 7.12 m to 9.4 (from F08 to P08, 2.35 m in length)

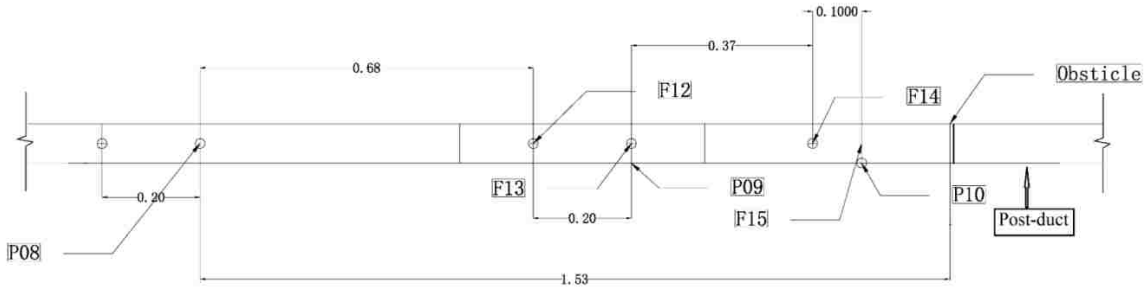

A5. Pressure sensor and flame sensor layout from the total length of 9.47 m to 11 m (from P08 to right end, 1.53 m in length)

The pressure and flame sensor lay out on the post-ducts with five geometric changes are demonstrated in Figures A1.6 to A1.11.

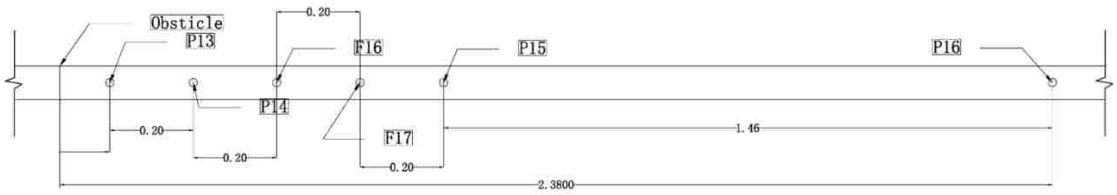

A6. Pressure sensor and flame sensor layout for post-duct, straight duct for obstacles (BR25, BR50, and BR75)

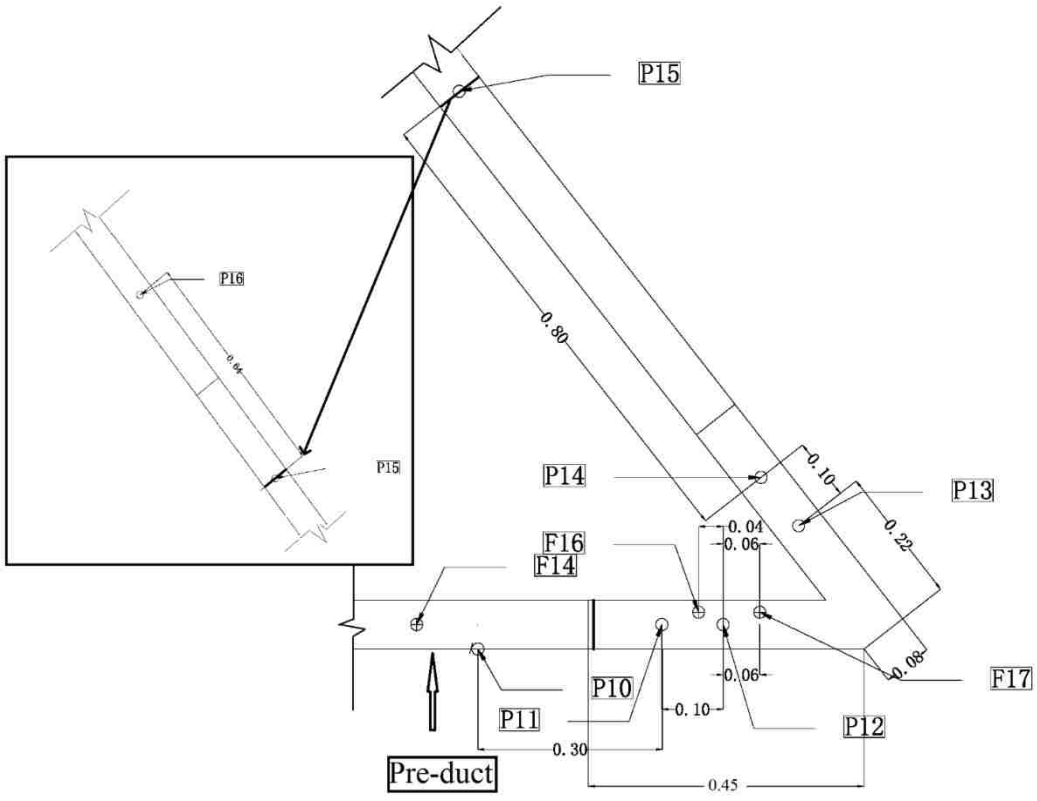

A7. Pressure sensor and flame sensor layout for post-duct with 50 ºbend

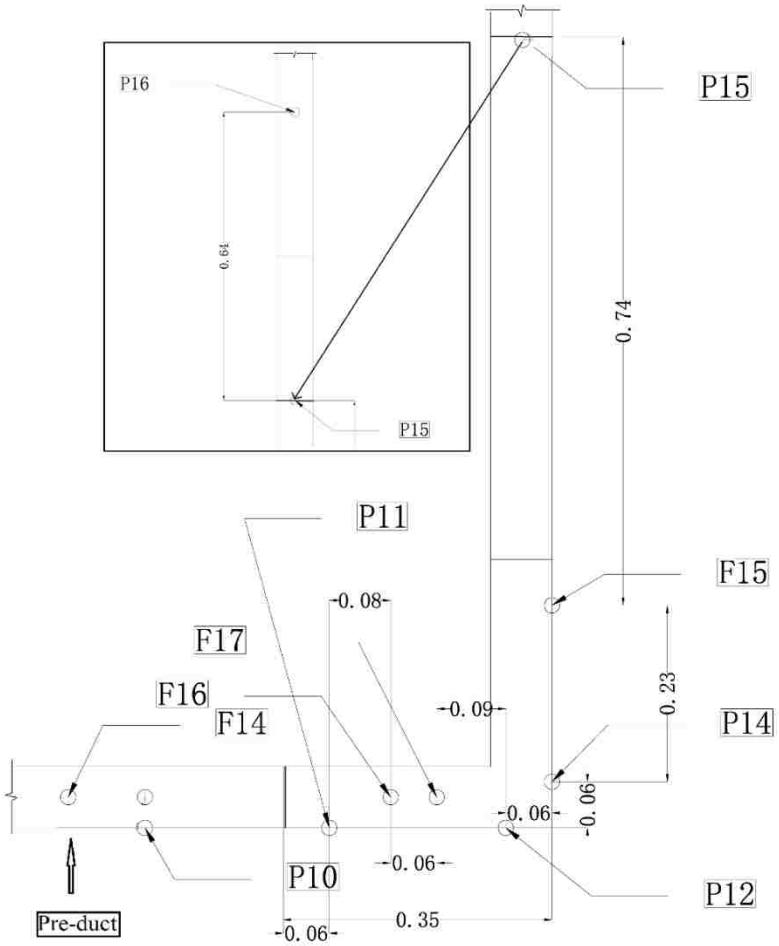

A8. Pressure sensor and flame sensor layout for post-duct with 90 ºbend

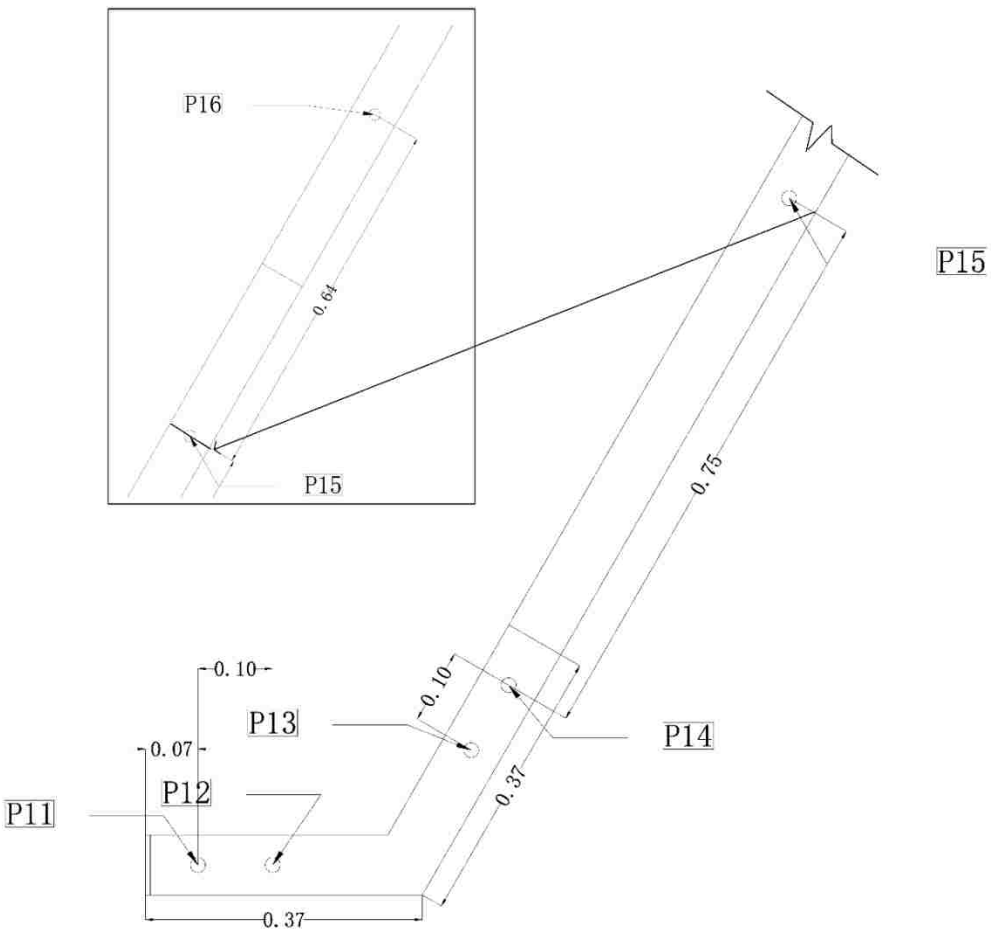

A9. Pressure sensor and flame sensor layout for post-duct with 120 ºbend

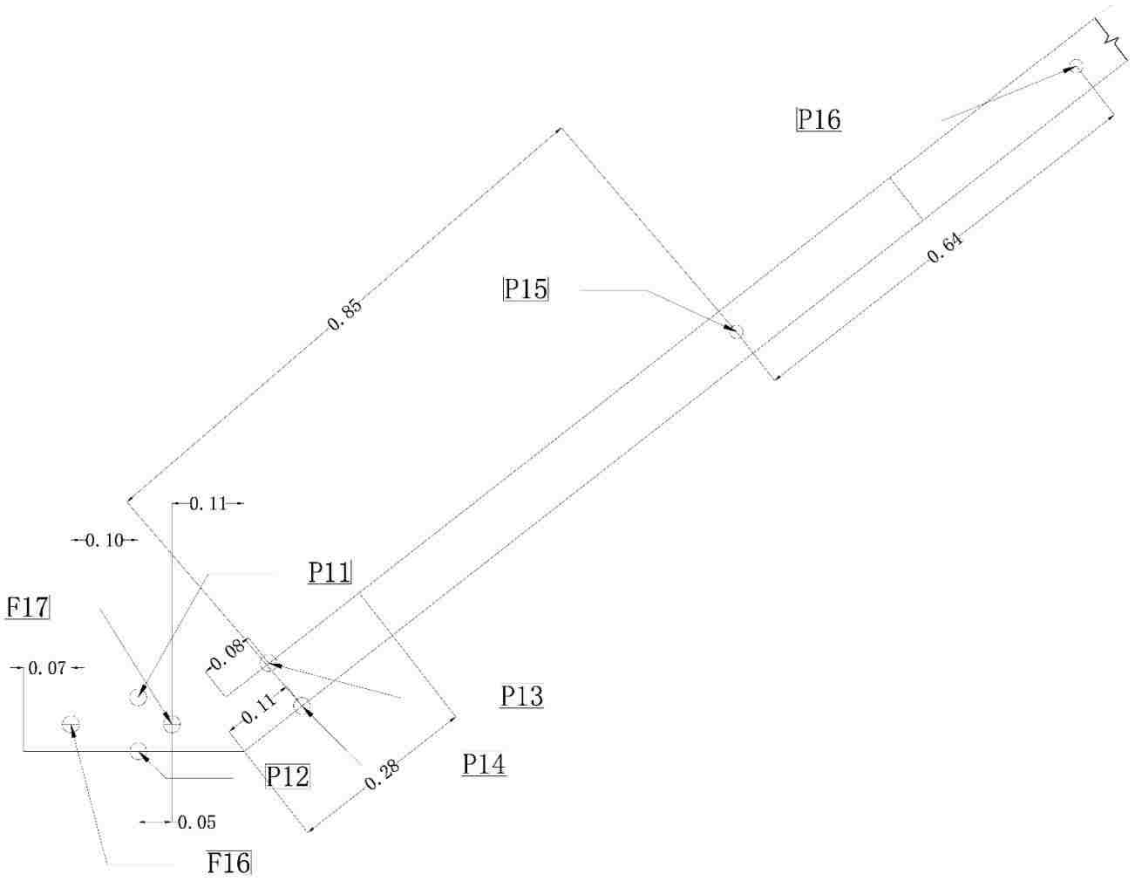

A10. Pressure sensor and flame sensor layout for post-duct with 140 ºbend

A11. Pressure sensor and flame sensor layout for post-duct with a cross-sectional change

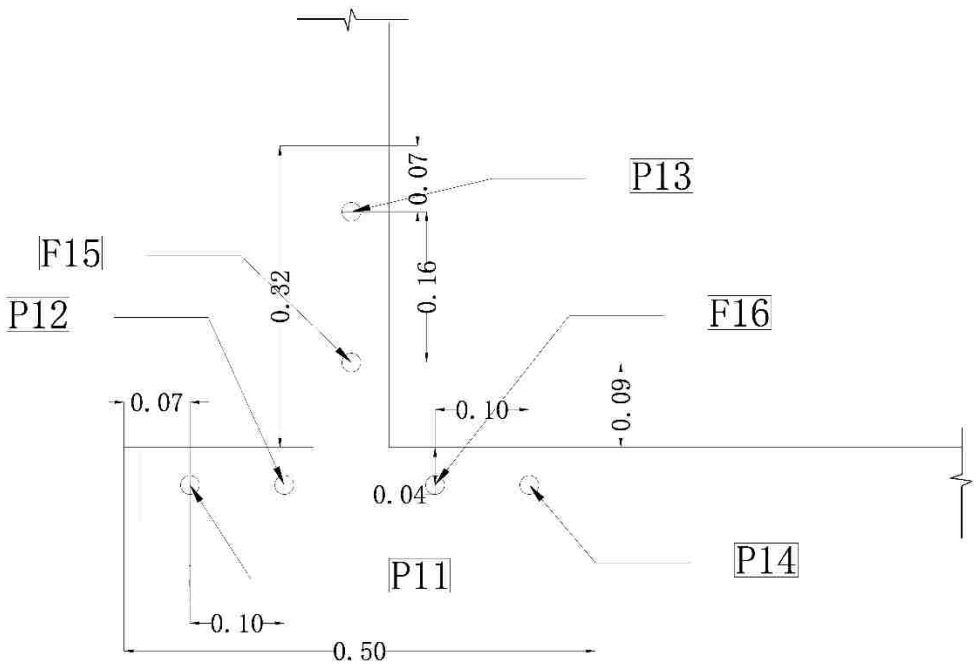

A12. Pressure sensor and flame sensor layout for post-duct with a t-branch

APPENDIX B

DIMENSIONS OF AIRWAYS OF EXPERIMENTAL MINE

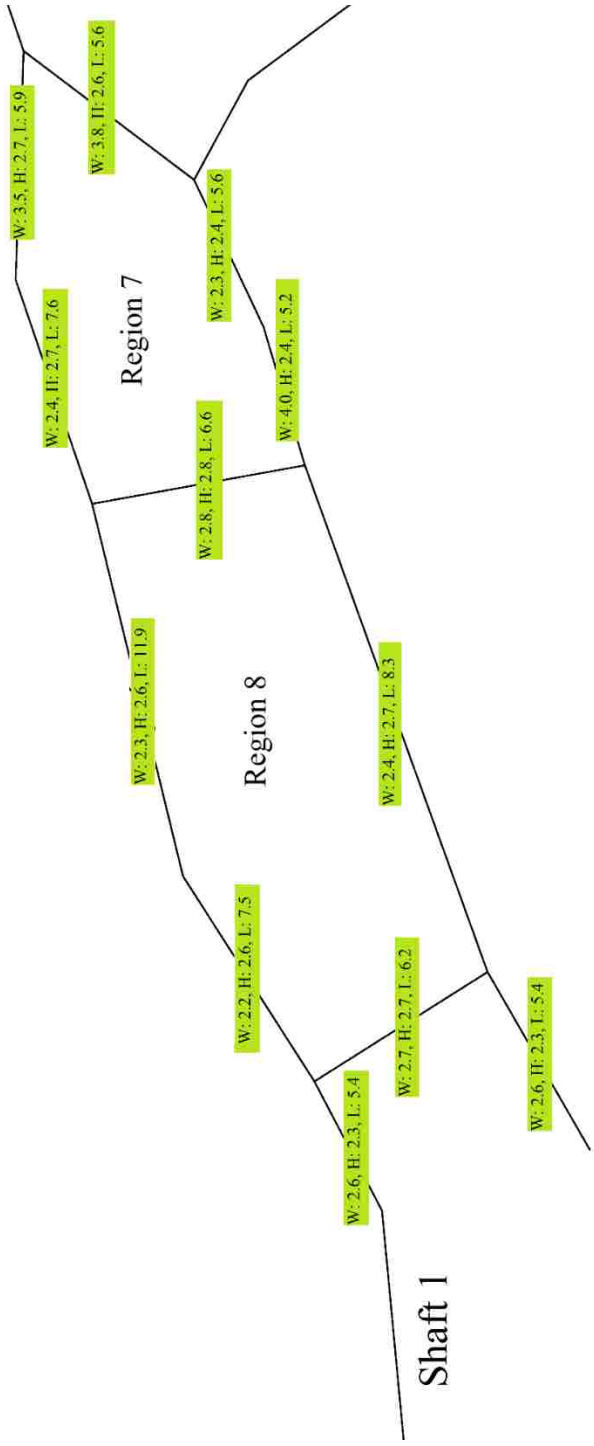

B1. Width, Height, and Length of airways in meter in the Western Region of Experimental Mine

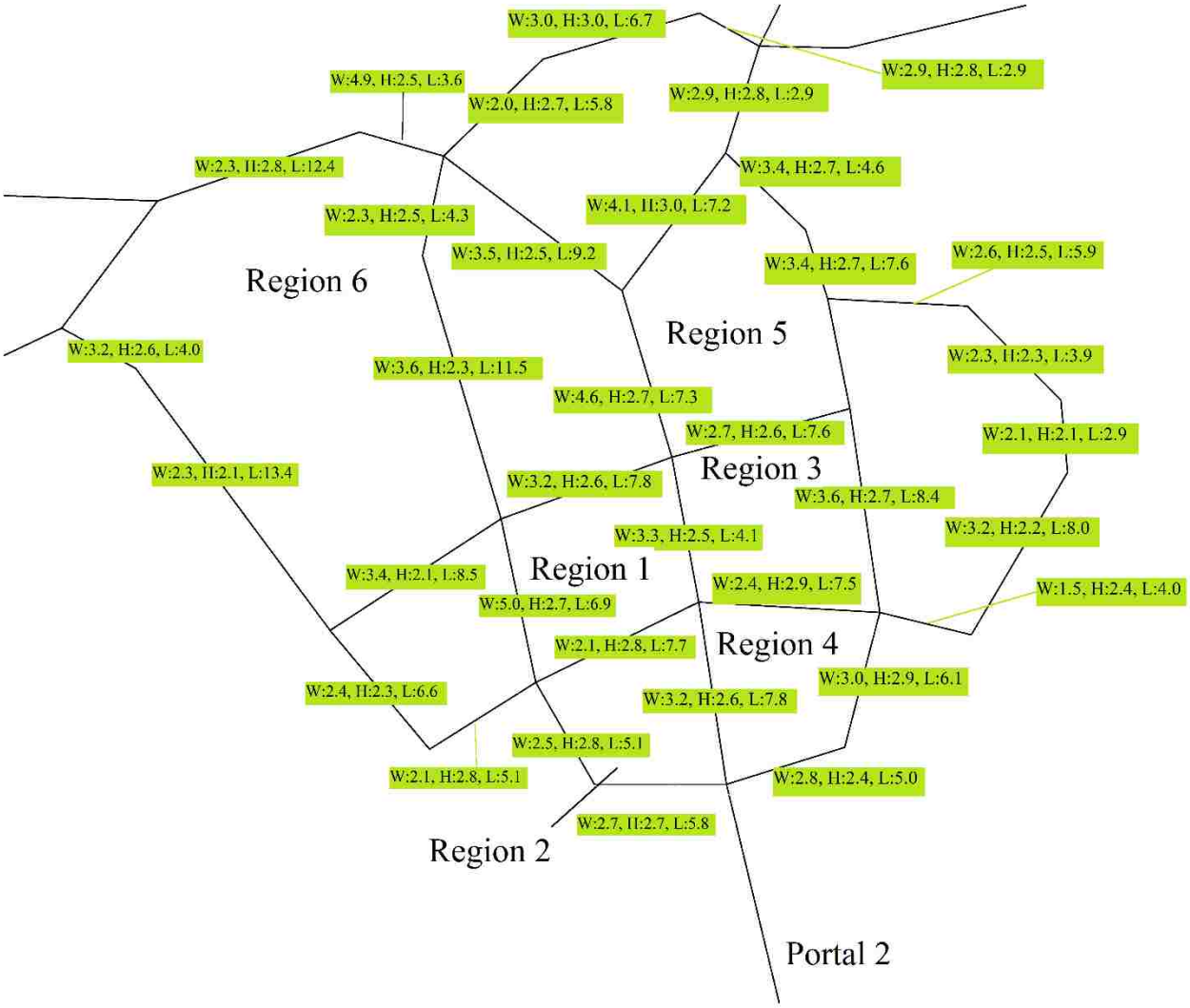

B2. Width, Height, and Length of airways in meter in the Middle Region of Experimental Mine

BIBLIOGRAPHY

Alla, G.H. (2002) "Computer Simulation of a Four Stroke Spark Ignition Engine," *Energy Conversion and Management*, Vol. 43, pp. 1043-1061.

Anon., (1978) "30 CFR § 75.323," *in Code of Federal Regulations, online source: http://www.msha.gov/30cfr/75.323.htm,* last accessed on 11/18/2105.

Anon., (1994) "Spacecraft Maximum Allowable Concentrations for Selected Airborne Contaminants, Volume 1," *by National Research Council Washington, DC: The National Academies Press*, p. 143.

Anon. (2011) "ANSYS FLUENT Theory Guide," Source: http://www.ansys.com, pp. 41-138; 197-224; 263-281.

Anon, (2012) "Flowmaster V7 Introduction," Flowmaster help document. *Sections: components categories; introduction of basic flow in pipes; Cd Discrete Loss; Bends; T-Junctions; and Transition Component.*

Barth, T. J. and Jespersen, D. (1989) "The Design and Application of Upwind Schemes on Unstructured Meshes Technical Report," *AIAA-89-0366. AIAA 27th Aerospace Sciences Meeting, Reno, Nevada,* pp. 1-4.

Bauwens, C. R., Chaffee, J., Dorofeev, S. (2008). "Experimental and numerical study of methane-air deflagrations in a vented enclosure," *Fire Safety Science–Proceedings of the Ninth International Symposium*, pp.1043-1054.

Bayraktar, H. and Durgun, O. (2003) "Mathematical Modeling of Spark Ignition Engine Cycles," *Energy Conversion and Management*, pp.651-666.

Bayraktar, H. and Durgun, O. (2004) "Investigating the Effects of LPG on Spark Ignition Engine Combustion and Performance," *Energy Conversion and Management*, pp. 2317-2333.

Brnich, M. J. and Kowalski-Trakofler, K. M. (2010) "Mining Publication: Underground Coal Mine Disasters 1900-2010: Events, Responses, and a Look to the Future," *Society of Mining, Metallurgy, and Exploration, 2010 Jan,* pp. 363-372.

Candel, S. and Poinsot, T. (1990) "Flame Stretch and the Balance Equation for the Flame Area," *Combustion Science and Technology*. Vol.70, pp.1-15.

Catlin, C. A. (1991) "Scale Effect on the External Combustion Caused by Venting of a Confined Explosion," *Combustion and Flame*, 83, pp. 399-411.

Catlin, C. A. and Johnson, D. M. (1992) "Experimental Scaling of the Flame Acceleration Phase of an Explosion by Changing Fuel Gas Reactivity," *Combustion and Flame*, 88, pp. 15-27.

Chen, X. J. and Hou, H. M., (2008) "Methane Explosion and Protection," *Coal*, Vol. 17-2, pp. 53-55.

Chilton, J.E., Taylor, C.D., Hall, E. and Timko, R.J. (2006) "Effect of Water Sprays on Airflow Movement and Methane Dilution at the Working Face," *11th US/North American Mine Ventilation Symposium, University Park, PA.* pp. 1-7

Colebrook, C. F. and White, C. M. (1937) "Experiments with Fluid Friction in Roughened Pipes," Proceedings of the Royal Society of London. Series A, Mathematical and Physical Sciences, 161 (906), pp.367-381.

Courtney, W.G. (1990) "Frictional Ignition with Coal Mining Bits," *Bureau of Mines IC 9251.*pp. 5-11.

Dai, L.C., Zhao, C.H., Liu, Z. and Hu, T.Z. (2011) "Numerical Simulation Study of Gas Explosion Propagation Law in the Pipe," *Mineral Engineering Research*, Vol. 26, No. 1, pp. 31-32.

Dalzell, R.W. (1966) "Face Ventilation in Underground Bituminous Coal Mines, Performance Characteristics of Common Jute Line Brattice," *Bureau of Mines RI 6725,* pp. 2-12

Diamond, P.W. (1994) "Methane Control for Under-Ground Coal Mines," *Bureau of Mines, IC 9395,* pp. 9-35

Döring, W. (1943) "On Detonation Processes in Gases". *Annalen der Physik* (in German) Vol. 43 (6-7): pp. 421-436.

Escanciano, J., Kotchourko, A., Lelyakin, A., Gavrikov, A., Efimenko, A., Zbikowski, M., Makarov, D. and Molkov, V. (2011) "Comparison Exercise on the CFD Detonation Simulation in Large Scale Confined Volumes," *International Journal of Hydrogen Energy*, Vol. 36, Issue 3, pp. 2613–2619.

Ewald, J. (2006) "A Level Set Based Flamelet Model for the Prediction of Combustion in Homogeneous Charge and Direct Injection Spark Ignition Engines," *PhD Thesis. Aachen University,* pp. 122-143.

Fieldner, A.C. (1950) "Achievements in Mine Safety Research and Problems Yet to Be Solved," *Bureau of Mines IC 7573,* pp. 1-6.

Heywood, J.B. (1998) "Internal Combustion Engine Fundamentals," *McGraw-Hill, New York, rev. edition*, pp. 371-470.

Hjertager, B. H., (1984) "Influence of Turbulence on Gas Explosions," *J. Hazardous Mater.,* Vol. 9, pp. 315-346.

Hjertager, B.H. (1993) "Computer Modelling o Turbulent Gas Explosion in Complex 2D and 3D Geometries," *Journal of Hazardous Materials*, Vol. 34, pp.173-197.

Hustad, J. E. and Sonju, O. K., (1988) "Experimental Studies of Lower Flammability Limits of Gases and Mixtures of Gases at Elevated Temperatures," *Combustion and Flame,* Vol. 71-3, pp. 283-294.

Jia, Z.W., Liu, Y.W. and Jin, X.G. (2011) "Propagation Characteristic about Shock Wave of Gas Explosion at Laneway Corner," *Journal of China Coal Society*, Vol. 36 No.1, pp. 97-100. (in Chinese)

Jia, Z.Z. and Lin, B.Q. (2009) "Analysis on Flame Acceleration Mechanism and Affecting Factors of Methane Explosion Propagation in Duct," *Mineral Engineering Research*, Vol. 24, No. 1, pp.57-61. (in Chinese)

Jiang, B.Y., Lin, S.L., Zhu, C.J. and Zhai, C. (2011a) "Numerical Analysis on Propagation Characteristics and Safety Distance of Gas Explosion," *Procedia Engineering*, Vol. 26 pp. 271-280.

Jiang, B.Y., Lin, S.L., Zhu, C.J., Zhai, C. and Li, Z.W. (2011b) "Numerical Simulation on Shock Wave Propagation Characteristics of Gas Explosion in Parallel Roadway," *Journal of Combustion Science and Technology*, Vol. 17 pp. 250-254.

Jing, G.X., Shi, G. and Jia, Z.W. (2011) "Experimental Study on the Propagation Regulation of Gas Explosive Shock Wave at the Turning Point of Pipeline," *Journal of China Coal Society*，Vol. 1 pp.1-6. (in Chinese)

Karacan, C.Ö., Diamond, W.P. and Schatzel, S.J. (2007) "Numerical Analysis of the Influence of In-Seam Horizontal Methane Drainage Boreholes on Longwall Face Emission Rates," *International Journal of Coal Geology*, Vol. 72, p. 15.

Karacan, C.Ö. (2007) "Development and Application of Reservoir Models and Artificial Neural Networks for Optimizing Ventilation Air Requirements in Development Mining Of Coal Seams," *International Journal of Coal Geology*, Vol. 72, p. 221.

Kindracki, J., Kobiera, A., Rarata G. and Wolanski, P. (2007) "Influence of Ignition Position and Obstacles on Explosion Development in Methane-Air Mixture in Closed Vessels," *Institute of Heat Engineering, Warsaw University of Technology, 00-665 Warsaw*, pp. 21-25.

Kordylewski, W. and Wach, J. (1988) "Influence of Ducting on Explosion Pressure: Small Scale Experiments," *Combustion and flame*, Vol. 71, pp. 51-61.

Lea, C.J. (2002) "A Review of the State of the Art in Gas Explosion Modeling," *Project report of health and safety laboratory, Fire and Explosion Group,* pp. 7-31.

Lin, B.Q., Jiang, C.G. and Zhou, S.N. (2003) "Inducement of Turbulence and Its Effect on Fire Transmission in Gas Explosion," *Journal of China University of Mining & Technology*, Vol. 32, No. 2, pp. 107-110. (in Chinese)

Lin, B.Q., Qing, Y., Jian, C. G. and Zhai, C. (2008) "The Flame Propagation of Methane Explosion in Bifurcation Duct," *Journal of China Coal Society*, Vol.2, pp.1-7. (in Chinese)

Lin, B.Q., Zhou, S.N. and Zhang, R.G. (1999) "Influence of Barriers on Flame Transmission and Explosion Wave in Gas Explosion," *Journal of China University of Mining & Technology*, Vol. 28, No. 2, pp. 104-106.

Lin, B.Q. and Zhu, C. J. (2009) "The Influences of Bend on Methane Explosion Propagation in Underground Coal Mines," *China National Occupational Safety and Health Association Annual Conference Paper Collection 2009*, pp. 312-318.

Londoño, L. F., López, C. E. and Cadavid, F. (2013) "Hugo Burbano Determination of Laminar Flame Speed of Methane/Air Flames at Sub-Atmospheric Conditions Using the Cone Method and CH Emission," *Dynamics.,* 80(180), pp. 130-135.

Luxner, J. V. (1969) "Face Ventilation in Underground Bituminous Coal Mines: Airflow and Methane Distribution Patterns in Immediate Face Area-Line Brattice," *University of Michigan Library.*

McPherson, M. J. (1993) "Subsurface Ventilation Engineering," *Mine Ventilation Services,* pp. 21.45-21.46.

Makarov, D.A, Verbecke, F. and Molkov, V. (2007) "Numerical Analysis of Hydrogen Deflagration Mitigation by Venting through a Duct," *Journal of loss prevention*, Vol. 20, pp. 433-438.

Makarov, D.A, Verbecke, F. and Molkov, V. (2008) "LES of Hydrogen-Air Deflagrations in a 78.5-m Tunnel," *Combustion Science and Technology*, Vol. 180, pp. 37-41.

Maksimovic, S.D., Elder, C.H. and Kissell, N. (1977) "Hydraulic Stimulation of a Surface Borehole for Gob Degasification," *Bureau of Mines RI 8228*, pp. 5-8.

McAteer, J. D., Bethell, T.N., Monforton, C., Pavlovich, J.W., Roberts, D. and Spence, B. (2006) "The Sago Mine Disaster-a Preliminary Report to Governor Joe Manchin III," in report from Buckhannon, West Virginia, pp. 4-5.

Moureaua, V., Fiorinab, B. and Pitscha, H. (2009) "A Level Set Formulation for Premixed Combustion LES Considering the Turbulent Flame Structure," *Combustion and Flame*, Vol.156, Issue 4, pp. 801-812.

Needham, C.E. (2010) "Shock Wave and High Pressure Phenomena-blast Wave," Springer Express, pp. 9-15, 87-99, 293-302.

Neumann. V. (1963) "Theory of Detonation Waves," *Progress Report to the National*, *A. H. John von Neumann: Collected Works, 1903-1957.*

Peluso, R.G. (1968) "Face Ventilation in Underground Bituminous Coal Mines, Airflow Characteristics of Flexible Spiral-Reinforced Ventilation Tubing," *Bureau of Mines RI 7085,* p. 9.

Petrov, T. and Wala, A. (2013) "CFD Analysis of Line Brattice Face Ventilation Systems Ability for Methane Dilution during Extended Cut," *2013 SME Annual Meeting. Denver, Colorado,* pp. 2-22.

Qu, Z.M., Quan, Z.X., Wang, H.Y. and Ma, H.L. (2008) "Overpressure Attenuation of Shock Wave during Gas Explosion," *Journal of China Coal Society*, Vol. 33, No. 4, pp. 410-414.

Ruban, A. D. Zaburdyaev, V.S. and Kharchenko, A.V. (2012) "Coal Bed Methane Drainage with Long Directional Boreholes," *Journal of Mining Science*, Vol. 48, No. 3, pp. 436-439.

Sarli, V. D., Benedettoa, A. D. and Russob, G. (2010) "Sub-Grid Scale Combustion Models for Large Eddy Simulation of Unsteady Premixed Flame Propagation Around Obstacles," *Journal of Hazardous Materials,* Vol. 180, pp. 71-78.

Schwerer, F.C. (1984) "Methane Modeling-Predicting the Inflow of Methane Gas into Coal Mines," *Bureau of Mines research contract report, No. J0333952,* pp. 5-22.

Smagorinsky, J. (1963) "General Circulation Experiments with the Primitive Equations. I-the Basic Experiment," *Monthly .Weather Review. Rev.*, Vol. 91. pp. 99-164.

Spalding, D. B. (1970) "Mixing and Chemical Reaction in Steady Confined Turbulent Flames," *In 13th Symp. (Int'l.) on Combustion. The Combustion Institute*, pp. 649-657.

Spindler, M.L. and Poundstone, W.N. (1960) "Experimental Work in the Degasification of the Pittsburgh Coal Seam by Horizontal and Vertical Drilling," *AIME, Preprint 60F106,* pp.37-46.

Steidl, P.F. (1978) "Foam Stimulation to Enhance Production from Degasification Wells in the Pittsburgh Coal Bed," *Bureau of Mines RI 8286,* pp.4-5.

Tannehill, J.C., Anderson, D.A. and Pletcher, R.H. (1997) "Computational Fluid Mechanics and Heat Transfer," *2nd edition, ISBN 1-56032-046-X, Taylor & Francis*, pp. 299-316.

Taylor, C.D., Rider, J.P. and Thimons, E.D. (1997) "Impact of Unbalanced Intake and Scrubber Flows on Methane Concentrations," *6th International Mine Ventilation Congress, Pittsburgh, PA,* pp. 1-4.

Taylor, C.D., Thimons, E.D. and Zimmer, J.A. (2001) "Factors Affecting the Location of Methanometers on Mining Equipment," *7th International Mine Ventilation Congress, Krakow, Poland,* pp.1-5.

Van Wingerden, C. J. (1989) "On the Scaling of Vapour Cloud Explosion Experiments," *Chemical Engineering Research and Design*, (67-4), pp. 339-347.

Zel'dovich and Ya, B. (1940) "On the Theory of the Propagation of Detonations on Gaseous," *Zh. Eksp. Teor. Fiz.,* Vol. 10, pp. 542-568.

Zhang, B., Bai, C. H., Xiu, G. L., Liu, Q. M. and Gong, G. D., (2014) "Explosion and Flame Characteristics of Methane/Air Mixtures in a Large-Scale Vessel," *Wiley Online Library*. DOI 10.1002/prs.11670.

Zhang, Q., Li, W., Huang, Y. and Duan, Y. (2011) "Influence of Spark Duration on Deflagration Characteristics of Methane-Air Mixtures" *wileyonlinelibrary.com*, DOI 10.1002/prs.10506

Zhang, Q. and Li, W. (2013) "Ignition Characteristics for Methane-Air Mixtures at Various Initial Temperatures," *wileyonlinelibrary.com*, DOI 10.1002/prs.11561.

Zhang, Q., Pang, L. and Liang, H.M. (2011) "Effect of Scale on the Explosion of Methane in Air and Its Shockwave," *Journal of Loss prevention in the Process Industries*, Vol. 24, pp.43-48.

Zhang, Q., Pang, L. and Zhang, S. X. (2011) "Effect of Scale on Flame Speeds of Methane-Air," *Journal of Loss prevention in the Process Industries*, 24, 705-712.

Zhen, W.R. and Chow, W.K. (2006) "Reaction Mechanisms of Methane for Modelling Combustion and Suppression," *Asian Journal of Chemistry,* Vol. 18, No. 3, pp. 1719-1745.

Zimont, V., Polifke, W., Bettelini, M. and Weisenstein, W. (1998) "An Efficient Computational Model for Premixed Turbulent Combustion at High Reynolds Numbers Based on a Turbulent Flame Speed Closure," *J. of Gas Turbines Power*. Vol.120. pp. 526-532.

Zipf, R.K., Jr., D.D., Gamezo, Sapko, M.J., Marchewka, W.P., Mohamed, K.M., Oran, V.N., Kessler, D.A. Weiss, E.S., Addis, J.D., Karnack, F.A. and Sellers, E.S. (2010) "Mining Publication: Methane-Air Detonation Experiments at NIOSH Lake Lynn Laboratory," *Proceedings of the Eighth International Symposium on Hazards, Prevention, and Mitigation of Industrial Explosions,* pp. 1-11.

Zipf, R.K., Jr., Sapko, M.J., Marchewka, W.P., Mohamed, K.M., Weiss, E.S., Addis, J.D., Karnack, F.A., Sellers, D.D., Gamezo, V.N., Oran, E.S. and Kessler, D.A. (2013) "Methane-Air Detonation Experiments at NIOSH Lake Lynn Laboratory," *Journal of Loss Prevention in the Process Industries,* Vol. 26, Issue 2, pp. 295–301.

VITA

The author Liang Wang, earned a bachelor's degree in Mining Engineering from Recourse and Environmental Science College, Chongqing University, China in June 2005; a master's degree in Mining Engineering in Recourse and Environmental Science College, Chongqing University in June, 2008; a master's degree in Civil Engineering from New Mexico State University in May 2011; In May, 2015 he received his Ph.D. degree in Mining Engineering from Missouri University of Science and Technology.

The author's aspect of research during Ph.D. study was mine ventilation. The topics include mine ventilation optimization, mine fire simulation, methane combustion simulation, and refuge chamber purging optimization. The author specializes in computational fluid dynamics (CFD) and optimization methods.